PRECISION MEASUREMENT OF THE β-ENERGY SPECTRUM IN ^{6}HE DECAY

By

Xueying Huyan

A DISSERTATION

Submitted to
Michigan State University
in partial fulfillment of the requirements
for the degree of

Physics – Doctor of Philosophy

2019

ABSTRACT

PRECISION MEASUREMENT OF THE β-ENERGY SPECTRUM IN ^{6}HE DECAY

By

Xueying Huyan

Precision measurements of the β-energy spectrum in nuclear and neutron decays have a high potential to find possible signatures of new physics beyond the standard electroweak model. Such signatures would produce a distortion to the β-energy spectrum relative to the Standard Model prediction. In Gamow-Teller transitions, these distortions would indicate the presence of the exotic tensor type interactions. An attractive candidate for this study is ^{6}He because the simplicity of its decay and its other nuclear properties allow an accurate theoretical description of the spectral shape.

At the National Superconducting Cyclotron Laboratory, we measured the β-energy spectrum in ^{6}He decay using a calorimetric technique. The radioactive ions were implanted into the active volume of a detector, eliminating the critical instrumental effect related to the backscattering of β particles. The goals of the experiment are to provide the first measurement of the weak magnetism form factor (b_{WM}) in ^{6}He decay and the first direct measurement of the Fierz interference term (b_{GT}) in Gamow-Teller decay.

This work summarizes the efforts on this experiment, focusing on the data analysis of the main systematic effects and the projected sensitivities to the observables. The estimates of b_{WM} and b_{GT} are $b_{WM} = ? \pm 4.9_{\text{stat}} \pm 11_{\text{sys}}$ and $b_{GT} = \left[? \pm 3.1_{\text{stat}} \pm 4.7_{\text{sys}}\right] \times 10^{-3}$, where the central values of b_{WM} and b_{GT} will be determined in the future analysis. The predicted uncertainty of b_{GT} satisfies the precision goal of $O(10^{-3})$, a level which allows new constraints on tensor couplings beyond the Standard Model.

ACKNOWLEDGMENTS

I want to express my highest appreciation to my thesis advisor, Oscar Naviliat-Cuncic. You have trained me to become a scientist with both high requirement and enormous support. You have continuously motivated me to come up with creative solutions when the research gets challenging. This uphill journey has been a rewarding experience for me. And thank you for the great patience teaching me how to communicate science.

I want to offer my special thanks to my Ph.D. guidance committee members. Vladimir Zelevinsky, you are one of the first persons who introduced me the uniqueness of the low-energy high-precision experiments and you have a special appreciation for my research. You have been a mentor to me since I took your quantum mechanics class. Wayne Repko, you have provided invaluable insight into the theoretical part of my research, particularly the radiative correction calculations. Thank you for giving me a 4.0 in your enjoyable quantum physics class, without which I would have been kicked out of graduate school after the first year. Kei Minamisono, thank you for the constructive suggestions about my data analysis, for challenging me to think harder, and for reminding me of the big picture of my research. Stuart Tessmer, thank you for your constant encouragement and support when I was lost. It was great to know that you were backing me up.

My thesis experiment has been a team effort of at least sixteen people at NSCL. I want to acknowledge the contributions of Shumpei Noji, Alexandra Gade, Anna Simon, Sean Liddick, Daniel Bazin, Dirk Weisshaar, Mike Bowry, Walter Buhro, Vincent Bader and Saul Beceiro-Novo during the experiment. I am particularly grateful to Max Hughes, Stan Paulauskas, Elisabeth George, and Paul Voytas for our many discussions during the data analysis.

I want to thank Scott Pratt. You provided me the essential support during my difficult transition from a non-physics major to physics in my first year. I did not know if I could survive graduate school at that time.

Thanks to my friends in graduate school who shared our vulnerabilities and optimism. It has been a great experience growing up with your company.

I appreciate my parents for the persistent strong support for my education. Thank you for understanding my many decisions that broke the traditions. I hope I have made you proud.

My special thanks to my spouse, Sam Marinelli. Thank you for believing me more than I believe in myself. You have been encouraging me to explore my full potential. You have empowered me.

TABLE OF CONTENTS

LIST OF TABLES

LIST OF FIGURES

CHAPTER 1

INTRODUCTION

This chapter provides the background for the precision measurement of the β-energy spectrum in ^{6}He decay. We will start with the physics motivations and the precision goals for the new physics. We will provide a list of relevant physics observables. It will be shown that one of the observables, the Fierz interference term (b_{GT}), could manifest itself through the shape of the β-energy spectrum. We will explain why the nuclear β decay of ^{6}He is an attractive candidate. In addition, we will provide a brief history of the ^{6}He β-spectrum measurement. A few recent measurements of the β-energy spectra in other decay systems will be reviewed, focusing on the common instrumental challenges.

1.1 Motivation

The Standard Model (SM) of particle physics describes the building blocks of nature and their interactions. It has been an enormous success since its discovery, particularly with the encouraging discovery of the Higgs boson. However, today, it is believed that the SM is not the ultimate description of nature. In the past few decades, a pandora box of puzzles has been opened, such as:

- The SM includes 18 free parameters that are not predicted by theory and are solely determined by experiments.
- The SM does not include gravity. The unification of gravity with the rest of the fundamental interactions requires the quantization of gravity.
- The SM does not explain the origin of matter-antimatter asymmetry. The CP violations observed in hadronic sectors so far are insufficient to describe the amount of matter in the universe. Extensive searches for new CP violations are taking place.
- The SM suggests that the masses of neutrinos are zero. However, the discovery of the

neutrino oscillation indicates non-zero neutrino masses. Besides, the exact masses of the three neutrino flavors and the neutrino mass hierarchy remain unknown.

- The total mass and energy of the universe include roughly 4.9% of the ordinary matter described by the SM, 26.8% dark matter, and 68.3% dark energy. The natures of dark matter and dark energy remain to be cosmological puzzles.

The above open questions motivate physicists to search for a new theoretical framework that involves new physics beyond the SM. Currently, there exist two frontiers to search for new physics: the energy frontier, which directly searches for new particles with particle colliders; and the precision frontier, which indirectly searches for signatures of new physics that manifest in low and intermediate energy processes. Such signatures would result in small deviations from the SM predictions and are accessible through high-precision measurements. This work belongs to the latter category.

1.1.1 Phenomenology of Semileptonic Weak Processes

Historically, the neutron and nuclear β decays have played an essential role in the development of the electroweak interactions in the SM. For example, the fact that the β-energy spectra are continuous, rather than discrete, has inspired Wolfgang Pauli to propose a new particle, neutrino, as a "desperate remedy" to save the law of energy conservation. β decays have also lead to the discovery of parity violation by Chien Shiung Wu and collaborators through a measurement of the asymmetry in β emission by polarized ^{60}Co nuclei. In addition, soon after the discovery of parity violation, β decays have played a prominent role in shaping the $V-A$ structure of weak interactions, which eventually became part of the SM framework.

Today, there is strong motivation to search for the deviation from the $V-A$ structure of weak interactions. Despite that the $V-A$ theory has been consistent with data, the existence of other interactions, i.e., the "exotic" interactions beyond the SM, have not yet been excluded. These "exotic" interactions would manifest themselves through the scalar or tensor terms in semi-leptonic

weak processes. These processes can be studied with an Effective Field Theory (EFT) approach, which makes a connection between the observables in low-energy and high-energy processes and allows a comparison between the sensitivities of these observables to new physics. The general expression of the low-energy (O(1 GeV)) effective Lagrangian for semi-leptonic transitions is [19]

$$\begin{aligned}\mathcal{L}_{eff} = &-\frac{G_F^{(0)}V_{ud}}{\sqrt{2}}[(1+\epsilon_L)\bar{e}\gamma_\mu(1-\gamma_5)\nu_l\cdot\bar{u}\gamma^\mu(1-\gamma_5)d+\tilde{\epsilon}_L\bar{e}\gamma_\mu(1+\gamma_5)\nu_l\cdot\bar{u}\gamma^\mu(1-\gamma_5)d\\&+\epsilon_R\bar{e}\gamma_\mu(1-\gamma_5)\nu_l\cdot\bar{u}\gamma^\mu(1+\gamma_5)d+\tilde{\epsilon}_R\bar{e}\gamma_\mu(1+\gamma_5)\nu_l\cdot\bar{u}\gamma^\mu(1+\gamma_5)d\\&+\epsilon_S\bar{e}(1-\gamma_5)\nu_e\cdot\bar{u}d+\tilde{\epsilon}_S\bar{e}(1+\gamma_5)\nu_e\cdot\bar{u}d\\&-\epsilon_P\bar{e}(1-\gamma_5)\nu_e\cdot\bar{\mu}\gamma_5 d-\tilde{\epsilon}_P\bar{e}(1+\gamma_5)\nu_e\cdot\bar{\mu}\gamma_5 d\\&+\epsilon_T\bar{e}\sigma_{\mu\nu}(1-\gamma_5)\nu_e\cdot\bar{u}\sigma^{\mu\nu}(1-\gamma_5)d+\tilde{\epsilon}_T\bar{e}\sigma_{\mu\nu}(1+\gamma_5)\nu_e\cdot\bar{u}\sigma^{\mu\nu}(1+\gamma_5)d]+\text{h.c.},\end{aligned}\tag{1.1}$$

where $G_F^{(0)}$ is the Fermi constant, V_{ud} is the Cabibbo-Kobayashi-Maskawa (CKM) matrix element describing the weak mixing of the up and down quarks. l represents the weak flavor. $\epsilon_i (i = V, A, S, T, P)$ stands for quark-level couplings for vector, axial-vector, scalar, tensor, and pseudoscalar type interactions. With the focus on the linear order of the couplings, we neglect the terms related to right-handed neutrinos by setting $\tilde{\epsilon}_{L,R,S,P,T} = 0$, which are of the second order. In addition, we drop the pseudoscalar terms. As the pseudoscalar bilinear is $O(1/M)$, where M is nucleon mass, the pseudoscalar contributions are strongly suppressed in the nonrelativistic limit. Thus the linear-order low-energy effective Lagrangian for neutron and nuclear β decay has the form [20]

$$\begin{aligned}\mathcal{L}_{eff} = &-\frac{G_F^{(0)}V_{ud}}{\sqrt{2}}(1+\epsilon_L+\epsilon_R)\left\{\bar{e}\gamma_\mu(1-\gamma_5)\nu_e\cdot\bar{u}\gamma^\mu[1-(1-2\epsilon_R)\gamma_5]d\right.\\&\left.+\epsilon_S\bar{e}(1-\gamma_5)\nu_e\cdot\bar{u}d+\epsilon_T\bar{e}\sigma_{\mu\nu}(1-\gamma_5)\nu_e\cdot\bar{u}\sigma^{\mu\nu}(1-\gamma_5)d\right\}+\text{h.c.},\end{aligned}\tag{1.2}$$

where the factor $(1 + \epsilon_L + \epsilon_R)$ affects the overall normalization and can be absorbed into V_{ud}. The couplings related to new physics are:

- The right-handed coupling, ϵ_R, which can be extracted by measuring $(1 - 2\epsilon_R)g_A/g_V$ in

neutron decays and determining g_A/g_V from lattice QCD calculations, where g_V and g_A are vector and axial form factors.

- The quark-level scalar and tensor couplings, ϵ_S and ϵ_T. They are accessible in both low-energy precision measurement experiments and high-energy collider experiments. We will discuss the current limits on ϵ_S and ϵ_T from low-energy and high-energy experiments and compare their sensitivities in Sec. 1.2.3.

In order to make connections with the nuclear and neutron β decay observables, one could match the quark-level effective Lagrangian (Eq. 1.2) with a nucleon-level effective Lagrangian obtained by Lee and Yang [21, 22], who introduced the Lee-Yang effective couplings $C_i, C_i'(i \in V, A, S, T)$, where the primed coefficients correspond to parity non-conserving interactions. Once again, we neglect the right-handed neutrinos, i.e., setting $\tilde{\epsilon}_{L,R,S,T} = 0$, the Lee-Yang effective couplings are related to the quark-level couplings in the following expressions [19]

$$\overline{C}_V = g_V(1 + \epsilon_L + \epsilon_R + \tilde{\epsilon}_L + \tilde{\epsilon}_R) \qquad \overline{C}'_V = g_V(1 + \epsilon_L + \epsilon_R - \tilde{\epsilon}_L - \tilde{\epsilon}_R) \tag{1.3}$$

$$\overline{C}_A = -g_A(1 + \epsilon_L - \epsilon_R - \tilde{\epsilon}_L + \tilde{\epsilon}_R) \qquad \overline{C}'_A = -g_A(1 + \epsilon_L - \epsilon_R + \tilde{\epsilon}_L - \tilde{\epsilon}_R) \tag{1.4}$$

$$\overline{C}_S = g_S(\epsilon_S + \tilde{\epsilon}_S) \qquad \overline{C}'_S = g_S(\epsilon_S - \tilde{\epsilon}_S) \tag{1.5}$$

$$\overline{C}_P = g_P(\epsilon_P - \tilde{\epsilon}_P) \qquad \overline{C}'_P = g_P(\epsilon_P + \tilde{\epsilon}_P) \tag{1.6}$$

$$\overline{C}_T = 4g_T(\epsilon_T + \tilde{\epsilon}_T) \qquad \overline{C}'_T = 4g_T(\epsilon_T - \tilde{\epsilon}_T), \tag{1.7}$$

where $C_i = \frac{G_F}{\sqrt{2}} V_{ud} \overline{C}_i$. It is useful to express the effective couplings in terms of their sums and differences, $C_i \pm C_i'$ [1]:

$$\overline{C}_V + \overline{C}'_V = 2g_V(1 + \epsilon_L + \epsilon_R), \qquad \overline{C}_V - \overline{C}'_V = 2g_V(\tilde{\epsilon}_L + \tilde{\epsilon}_R), \tag{1.8}$$

$$\overline{C}_A + \overline{C}'_A = -2g_A(1 + \epsilon_L - \epsilon_R), \qquad \overline{C}_A - \overline{C}'_A = 2g_A(\tilde{\epsilon}_L - \tilde{\epsilon}_R), \tag{1.9}$$

$$\overline{C}_S + \overline{C}'_S = 2g_S\epsilon_S, \qquad \overline{C}_S - \overline{C}'_S = 2g_S\tilde{\epsilon}_S, \tag{1.10}$$

$$\overline{C}_P + \overline{C}'_P = 2g_P\epsilon_P, \qquad \overline{C}_P - \overline{C}'_P = -2g_P\tilde{\epsilon}_P, \tag{1.11}$$

$$\overline{C}_T + \overline{C}'_T = 8g_T\epsilon_T, \qquad \overline{C}_T - \overline{C}'_T = 8g_T\tilde{\epsilon}_T, \tag{1.12}$$

where the sums and differences are sensitive to left-handed and right-handed neutrinos, respectively. The motivation for separating the contributions of the left-handed and right-handed neutrinos is that the constraints on the former is much more accessible experimentally. The constants $g_i (i \in V, A, S, P, T)$ are hadronic form factors, among which $g_V = 1$ is predicted by the Conserved Vector Current (CVC) hypothesis, and the others are precisely determined with lattice QCD calculations. The current most precise values are summarized in Table. 1-1 [1]:

Table 1-1: Current most precise values of the hadronic form factors determined with lattice QCD calculations from Ref. [1].

	g_A	g_S	g_P	g_T
Value	1.278(21)(26)	1.02(11)	349(9)	0.987(51)(20)
Reference	[23]	[24]	[24]	[25]

1.1.2 Current Limits on the Scaler and Tensor Couplings

The current strongest constraints on the exotic couplings are provided in Ref. [1], where the exotic couplings are extracted by fitting 17 experimental input data, including the $\mathcal{F}t$ values from $0^+ \rightarrow 0^+$ transitions and selected neutron data. These fits assume that the right-handed neutrinos are absent, i.e., $C'_i = C_i$, and that all couplings are real, i.e., $C_A/C_V = (C_A + C'_A)/(C_V + C'_V)$, $C_S/C_V = (C_S + C'_S)/(C_V + C'_V)$, $C_T/C_A = (C_T + C'_T)/(C_A + C'_A)$. The results are shown in Fig. 1-1, where the extracted exotic couplings are

$$C_S/C_V = 0.0014 \pm 0.0012, \tag{1.13}$$

$$C_T/C_A = 0.0020 \pm 0.0022, \tag{1.14}$$

and the contours around the minimum correspond to 68%, 95%, and 99% confidence intervals, respectively.

The most stringent constraint on the scalar couplings is placed by $\mathcal{F}t$ values from $0^+ \rightarrow 0^+$ pure Fermi transitions. The constraint on the tensor coupling, on the other hand, is a factor of two weaker than that on the scalar coupling, as shown in Fig. 1-1. The weak constraint on the tensor coupling motivates a new generation of experiments aiming at stronger constraints.

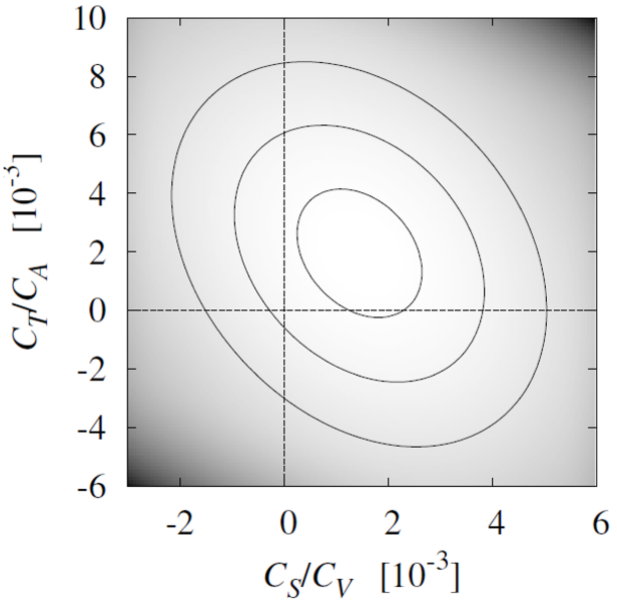

Figure 1-1: The current limits of scalar (horizontal) and tensor (vertical) couplings extracted from the fit to $\mathcal{F}t$ values, average neutron lifetime, average neutron β asymmetry $\tilde{A}_n$, and the λ_{AB} parameter. The contours around the minimum correspond to 68%, 95%, and 99% confidence intervals. Figure taken from Ref. [1].

1.2 Observables

1.2.1 Correlation Coefficients

The observables of these low-energy experiments searching for exotic couplings are the correlation coefficients, proposed by Jackson, Treiman and Wyld [26, 27] for allowed β decays. The correlation coefficients relate the effective couplings, C_i and C_i', to the angular and energy distributions of β particles. Using the effective Lagrangian (Eq. 1.2), and neglecting the recoil and electromagnetic corrections, the decay-rate distributions for allowed β decays are derived in Refs [26, 27]. For polarized nuclei, the distribution in electron energy (E_e), electron direction (Ω_e), and neutrino direction (Ω_ν) is

$$w(\langle \mathbf{J} \rangle | E_e, \Omega_e, \Omega_\nu) dE_e d\Omega_e d\Omega_\nu = \frac{F(\pm Z, E_e)}{(2\pi)^5} p_e E_e (E_0 - E_e)^2 dE_e d\Omega_e d\Omega_\nu$$
$$\times \xi \Bigg\{ 1 + a \frac{\mathbf{p}_e \cdot \mathbf{p}_\nu}{E_e E_\nu} + b \frac{m_e}{E_e}$$
$$+ c \left[\frac{\mathbf{p}_e \cdot \mathbf{p}_\nu}{3 E_e E_\nu} - \frac{(\mathbf{p}_e \cdot \mathbf{j})(\mathbf{p}_\nu \cdot \mathbf{j})}{E_e E_\nu} \right] \left[\frac{J(J+1) - 3\langle \mathbf{J} \cdot \mathbf{j} \rangle^2}{J(2J-1)} \right]$$
$$+ \frac{\langle \mathbf{J} \rangle}{J} \cdot \left[A \frac{\mathbf{p}_e}{E_e} + B \frac{\mathbf{p}_\nu}{E_\nu} + D \frac{\mathbf{p}_e \times \mathbf{p}_\nu}{E_e E_\nu} \right] \Bigg\}, \tag{1.15}$$

where $\mathbf{p}_e$ is the momentum of the β particle, $\mathbf{p}_\nu$ is the momentum of the electron neutrino, E_0 is the endpoint energy of the decay, $\langle \mathbf{J} \rangle$ is the expectation value of the spin of the initial nuclear state, J is the unit vector in the direction of $\langle \mathbf{J} \rangle$, and $F(\pm Z, E_e)$ is the Fermi function introduced in Sec. 2.1.

The correlation coefficients, ξ, a, b, c, A, B, and D, depend on different combinations of the sixteen Lee-Yang effective couplings, C and C', and are accessible experimentally. Specifically, a is the β-neutrino asymmetry, b is the Fierz interference term, A is the β asymmetry, B is the neutrino asymmetry, and D is a triple correlation coefficient. The c coefficient vanishes if the initial nucleus is nonoriented ($J(J+1) = 3\langle \mathbf{J} \cdot \mathbf{j} \rangle^2$).

In addition, for unpolarized nuclei, the distribution function in electron and neutrino directions, electron energy, and electron polarization for allowed β decay depend on correlation coefficients G, H, K, L. For polarized nuclei, the distribution function in electron energy, electron direction, and electron polarization depend on coefficients A, J, N, Q, R. Details of their origins and dependences on the effective couplings can be found in Refs. [26, 27]. The most common correlation coefficients are summarized with pictorial representation in Fig. 1-2.

It is important to identify the correlation coefficients that have linear dependences on the exotic couplings, which makes them most sensitive to new physics. Among them, the coefficients that have been accessed experimentally are: b, B, N, Q, R and D [28]. Both the scalar and tensor couplings contribute linearly to the Fierz interference term b and the neutrino asymmetry correlation coefficient B. The measurement of B is challenging because it involves the neutrino

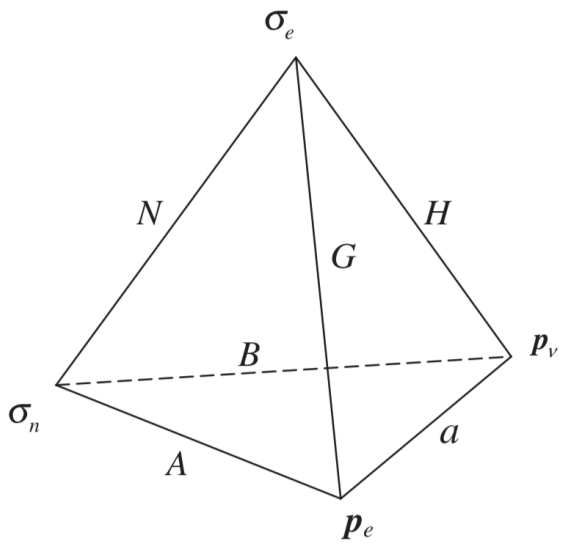

Figure 1-2: A pictorial representation of the most common correlation coefficients, the two-fold (edges) and the three-fold (faces) correlations between the kinematic vectors (vertices). Figure taken from Ref. [4].

momentum and the nuclear polarization [1]. It is also difficult to access the polarization-spin correlation N and the longitudinal polarization from polarized nuclei Q, as the analysis of the spin of β particles emitted from polarized neutrons or nuclei is required [28].

1.2.2 The Fierz Interference Term

The correlation coefficients that are most accessible in β decays of unpolarized nuclei are the β-neutrino asymmetry a and the Fierz interference term b. They are related to the Lee-Yang effective couplings in the following expressions [1]

$$a\xi = |M_F|^2 \left(|C_V|^2 + |C'_V|^2 - |C_S|^2 - |C'_S|^2\right) - \frac{|M_{GT}|^2}{3}\left(|C_A|^2 + |C'_A|^2 - |C_T|^2 - |C'_T|^2\right), \tag{1.16}$$

$$b\xi = \pm 2\gamma Re\left[|M_F|^2\left(C_V C_S^* + C'_V C'^*_S\right) + |M_{GT}|^2\left(C_A C_T^* + C'_A C'^*_T\right)\right], \tag{1.17}$$

$$\xi = |M_F|^2 \left(|C_V|^2 + |C'_V|^2 + |C_S|^2 + |C'_S|^2\right) + |M_{GT}|^2\left(|C_A|^2 + |C'_A|^2 + |C_T|^2 + |C'_T|^2\right), \tag{1.18}$$

where ξ is an overall factor, $\gamma = \sqrt{1-\alpha^2 Z^2}$ and α is the fine structure constant. As the SM predicts zero values of the scalar and tensor couplings, the Fierz interference term is predicted to be zero

by the SM. Any deviation of the measured Fierz interference term from zero would indicate the presence of new physics.

It is worth noticing that the β-neutrino asymmetry a depends quadratically on the scalar and tensor coupling constants, while the Fierz interference term b depends linearly on these couplings. Therefore, the measurement of a requires higher precision than b to have comparable constraints to the exotic couplings. The linear dependence of the Fierz interference term on the exotic couplings allows high sensitivity to new physics.

The Fierz interference term contributes to almost all other correlation coefficients. For most of the experiments determining the correlation coefficients, instead of directly measuring the correlation coefficient themselves, the actual measured quantity includes a contribution from the Fierz interference term [29]:

$$\tilde{X} = \frac{X}{1 + b\langle m/E_e \rangle}, \tag{1.19}$$

where $X = a, A, B, etc.$, which stands for a correlation coefficient, and $\langle m/E_e \rangle$ stands for the weighted average over the observed part of the β-energy spectrum. The sensitivities of these correlation coefficients are affected by the contribution of the Fierz interference term. The Fierz interference term, on the other hand, can be accessible experimentally through not only indirect measurements of the other correlation coefficients but also a direct measurement of b.

The expression of b can be simplified for pure Fermi and pure Gamow-Teller transition:

$$b_{\mathrm{F}} = \pm\gamma Re\left(\frac{C_S + C'_S}{C_V}\right), \tag{1.20}$$

$$b_{GT} = \pm\gamma Re\left(\frac{C_T + C'_T}{C_A}\right), \tag{1.21}$$

where b_{F} and b_{GT} stand for the Fierz interference terms in Fermi and Gamow-Teller transitions, respectively. In this case, b_{F} and b_{GT} are independent of the nuclear matrix elements, $|M_F|$ and $|M_{GT}|$. This is a great advantage because it circumvents a dedicated evaluation of $|M_F|$ or $|M_{GT}|$.

In summary, the discussion above shows that the Fierz interference term has unique advantages to place a stringent constraint on exotic couplings. In this work, the observable of choice is, therefore, the Fierz interference term in Gamow-Teller transitions, b_{GT}, which is sensitive to tensor

couplings. Remarkably, in most of the past experiments aiming at the exotic coupling searches, little attention had been paid to the Fierz interference term. There have been no direct measurements of the Fierz interference term in Gamow-Teller decays in literature. The long-term goal of this work is to provide the first direct measurement of the Fierz interference term in Gamow-Teller decay.

1.2.3 Current Status of the Fierz Interference Term

The Fierz interference term in Fermi transitions, b_{F}, has been extracted by Hardy and Towner through years of analysis of the $\mathcal{F}t$ values in superallowed $0^+ \rightarrow 0^+$ Fermi transitions. The latest value is [30]

$$b_{\mathrm{F}} = -0.0028 \pm 0.0026, \tag{1.22}$$

providing a strong constraint on the scalar couplings.

The first and only direct extracted Fierz interference term in neutron decay (b_n) has be obtained by the UCNA Collaboration, finding [31] $b_n = 0.067 \pm 0.005_{stat}{}^{+0.090}_{-0.061\,sys}$, which is consistent with zero, as predicted by the SM. While the statistical uncertainty is on the order of 10^{-3}, the systematic uncertainty, dominated by the energy calibration, is too high for a stringent constraint on the exotic couplings. Significant improvement in the characterization of the energy response of the detection system is required. One ongoing effort aiming to improve the precision of b_n in neutron decay is the Nab experiment [32]. Their precision goal is $\delta b_n \simeq 3 \times 10^{-3}$.

For the measurement of the Fierz interference term in nuclear Gamow-Teller decays (b_{GT}), several experiments are ongoing or planned. At the National Superconducting Cyclotron Laboratory, the β-energy spectra of ^{6}He and ^{20}F have been measured with scintillating detectors [33]. The ongoing data analyses aim at a $O(10^{-3})$ precision of b_{GT}. The β-energy spectrum in ^{45}Ca decay has been measured by the UCNA-Nab-Leuven collaboration with a 4π magnetic spectrometer. The ongoing data also aim at a $O(10^{-3})$ sensitivity to b_{GT}. Another experiment dedicated to the measurement of the β-energy spectrum uses the miniBETA spectrometer [34], which incorporates a low-pressure multiwire drift chamber and is currently being commissioned.

The current benchmark uncertainty on the Fierz interference term is provided in Ref. [1], where the uncertainty is derived from the exotic couplings extracted from a fit assuming no right-handed neutrinos. Twenty-eight experimental input data were incorporated in the fit, including the $\mathcal{F}t$ values from $0^+ \rightarrow 0^+$ transitions and all neutron and nuclear data. The resulting absolute uncertainties for neutron and Gamow-Teller decays are respectively

$$\delta b_n = 3.2 \times 10^{-3}, \tag{1.23}$$

$$\delta b_{GT} = 3.9 \times 10^{-3}. \tag{1.24}$$

These uncertainties provide a precision level any new measurement needs to reach to improve the current constraint on the tensor couplings. The above result for b_{GT} is extracted from indirect measurements.

The sensitivities to new physics in low-energy experiments can be compared with that in high-energy experiments with the EFT approach. The analysis of the data taken at the LHC in the SMEFT framework has provided a constraint on the quark-level tensor couplings. The 90% confidence level bound on ϵ_T is $|\epsilon_T| \lesssim 0.6 \times 10^{-3}$. The corresponding 1σ uncertainty is 0.37×10^{-3}. This uncertainty can be converted to the uncertainty of b_{GT}, according to Eq. 1.12:

$$b_{GT}^{LHC} \lesssim 2.9 \times 10^{-3}. \tag{1.25}$$

Equation 1.25 provides a precision level any new low-energy measurement has to reach to have a comparable level of constraint with the LHC searches.

1.3 The Shape of the β-energy Spectrum and the Test of the CVC Hypothesis

The Fierz interference term can be extracted by precision measurements of the energy spectrum of β particles in a neutron or nuclear β decay. A non-zero Fierz interference term would induce a distortion to the β-energy spectrum. For allowed decays, the shape of the β-energy spectrum is described by

$$N(W)dW = pW(W_0 - W)^2 \eta(W) dW \left(1 + \frac{b_{GT}}{W}\right) f_1\left(E, b_{WM}\right), \tag{1.26}$$

where p is the momentum of β particle, W is the electron total energy in the unit of the rest energy of the electron, mc^2 (natural unit), where m is the electron mass. W_0 is the maximum electron total energy allowed by kinematics and is referred to as the endpoint energy. $pW(W_0 - W)^2 dW$ is the dominating statistical factor that is referred to as the phase space factor. $\eta(W)$ is the product of several theoretical corrections that are discussed in details in Chapter 2. $(1 + b_{GT}/W)$ is the distortion to the β-energy spectrum by the possible presence of the Fierz interference term b_{GT}. Finally, $f_1(E, b_{WM})$ is the spectral function and it is associated with the weak magnetism form factor, b_{WM}, where E is the kinetic energy of β particle in the SI unit $\left(E = (W - 1)mc^2\right)$. In the Gamow-Teller decay of ^{6}He [35], with the inclusion of the recoil to first order, assuming the absence of the second class currents and the induced tensor produced by the second class currents [36][37], the spectral function has the expression:

$$f_1(E, b_{WM}) = 1 + C_0 + C_1 W + \frac{C_{-1}}{W}, \tag{1.27}$$

where

$$W = E + mc^2, \tag{1.28}$$

$$C_0 = -\frac{2W_0 mc^2}{3M}\left(1 + \frac{b_{WM}}{c}\right) = -1.234(14)\%, \tag{1.29}$$

$$C_1 = \frac{2}{3M}\left(5 + \frac{2b_{WM}}{c}\right) = 0.650(7)\%/\text{MeV}[5], \tag{1.30}$$

$$C_{-1} = -\frac{2mc^2}{3M}\left(1 + \frac{b_{WM}}{c}\right) = -0.0802(9)\%\text{MeV}[5], \tag{1.31}$$

$$b_{WM} = \sqrt{\frac{6\Gamma_{M1}M^2}{\alpha E_\gamma^3}} = 68.22(79). \tag{1.32}$$

Here, Γ_{M1} is the $M1$ γ decay width of an analog state within an isospin triplet [38], E_γ is the energy of the γ transition [39], M is the nuclear mass of the daughter nucleus ^{6}Li [40], and $c = g_A M_{GT} = 2.7491$ is the dominant Gamow-Teller strength [41].

The above expression of the weak magnetism form factor, b_{WM}, is predicted in terms of the M1 electromagnetic decay width of an analog state in an isospin triplet. This prediction is based on the CVC hypothesis, which stands for Conservation of the Vector Current that is analogous to the

conservation of electric charge, and it relates the matrix elements of the charged weak polar vector current with the corresponding electromagnetic amplitudes. The CVC hypothesis can be tested by measuring the β-energy spectrum and extracting the value of b_{WM}.

While b_{WM} is present in all C_0, C_1 and C_{-1} coefficients, its most significant impact on the shape of β-energy spectrum is through the C_1 coefficient, which mostly dominates the slope of the spectral function. Most of the existing tests of the CVC hypothesis [42, 43, 44, 12] were performed by measuring the slopes of the spectral functions and comparing them with the slopes predicted by the CVC hypothesis, rather than directly measuring the values of b_{WM}.

1.4 The Candidate: ^{6}He

The candidate selected for this study is the nuclear β decay of ^{6}He. The decay scheme is shown in the left panel of Fig. 1-3, where a ^{6}He decays into a ^{6}Li in an allowed pure Gamow-Teller transition. The right panel of Fig. 1-3 shows the simplified level scheme in the mass $A = 6$ isospin triplet, where the ^{6}He ground state forms an isospin triplet with the 0^+ state of ^{6}Li at 3563 keV and the unbound ground state of ^{6}Be. The CVC value of b_{WM} in ^{6}He decay can be calculated with the width and energy of the M1 transition in ^{6}Li.

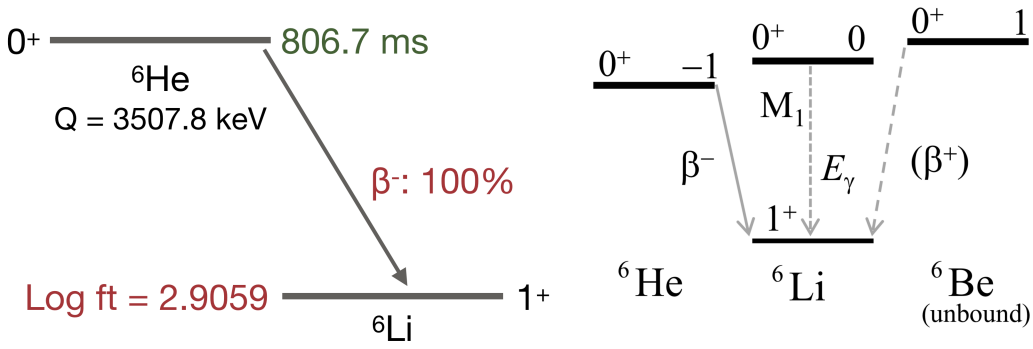

Figure 1-3: Left panel: the decay scheme of the ^{6}He nuclear β decay. Right panel: the simplified level scheme and transition in the mass $A = 6$ isospin triplet taken from Ref. [5].

The ^{6}He decay is an attractive candidate for several advantages listed below:

- This transition is sensitive to tensor couplings because the nuclear β decay of ^{6}He is a

100% Gamow-Teller decay. Since the Fierz interference term is proportional to tensor couplings in Gamow-Teller decays, this decay process is sensitive to tensor couplings through a measurement of the Fierz interference term.

- The endpoint of ^{6}He decay is about 3.5 MeV, which results in high kinematic sensitivity to the Fierz interference term. Reference [6] has studied with Monte Carlo the impact of the endpoint on the statistical uncertainty of b. The results are shown in Fig. 1-4, where the 1σ statistical uncertainties of b are extracted by fitting the β-energy spectrum corresponding to each endpoint. It is worth noticing that the β decays of neutron and ^{6}He have high statistical sensitivities, and they are comparable.

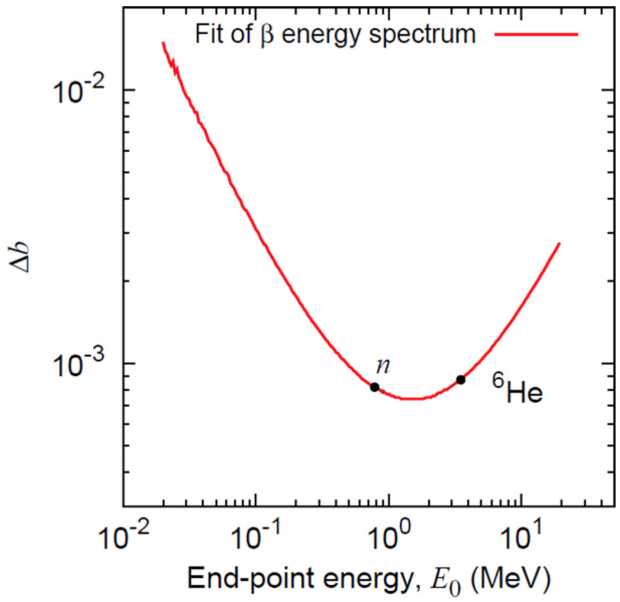

Figure 1-4: The 1σ statistical uncertainties of the Fierz interference term obtained by fitting the simulated β-energy spectra with different values of the endpoint energy. Figure taken from Ref. [6].

- There is no subsequent γ ray emitted in the decay of ^{6}He, which is a great advantage for a clean measurement of β-energy spectrum. In addition, Chap. 3 has shown that the measurements are performed in cycles, and each cycle consists of a beam implantation time window and a decay time window. The β decay of ^{6}He has a half-life of about 806 ms [45], which makes it convenient to manipulate the beam cycles and to perform decay measurements.

There have been no measurements of the weak magnetism form factor in ^{6}He decay reported in literature. The short-term goal of this work is to provide the first measurement of b_{WM} in ^{6}He decay as a test of CVC, before reaching the long-term goal of the first direct measurement of b_{GT} in Gamow-Teller decay.

1.5 Existing Measurements of β-energy Spectra

1.5.1 A Brief History of the Measurements of the β-energy Spectra in ^{6}He Decay

T. Bjerge *et al.* [7] have reported the earliest measurement of the β-energy spectrum in the decay of a helium isotope in the 1930s. The kinetic energy of β particles was measured with a cloud chamber. The obtained β-energy spectrum is shown in Fig. 1-5, from which the endpoint energy of this decay was determined to be 3.7 ± 0.5 MeV. The authors concluded that the most reasonable assumption of the isotope identity was ^{6}He.

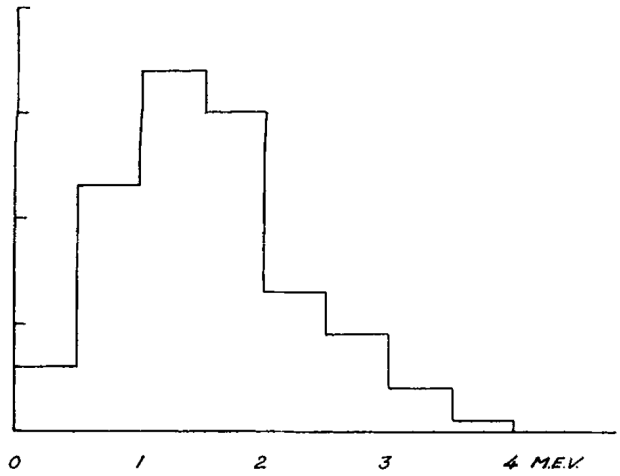

Figure 1-5: The β-energy spectrum in the decay of a helium isotope measured with a cloud chamber. The isotope identify was believed to be ^{6}He. Figure taken from Ref. [7].

V. Perez-Mendez *et al.* [8] have reported the first dedicated measurement of the β-energy spectrum in ^{6}He decay. The energy of β particles was measured with a semicircular focusing magnetic spectrometer. The obtained Kurie plot of the β-energy spectrum is shown in Fig. 1-6, where the tail near the endpoint is because the energy resolution is ~6%.

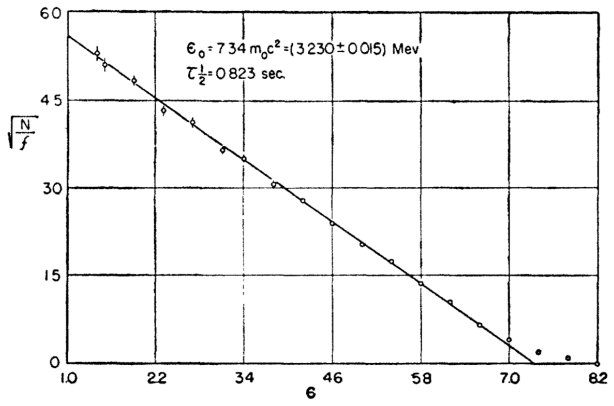

Figure 1-6: Kurie plot of the β-energy spectrum in ^{6}He decay. The horizontal axis is the kinetic energy of β particles in the natural unit (mc^2). Figure taken from Ref. [8].

C.S. Wu *et al.* [9] have remeasured the β-energy spectrum in ^{6}He decay with the Columbia magnetic solenoidal spectrometer. The Kurie plot shown in Fig. 1-7 is linear in the energy range of 0.6 MeV to the endpoint. The determined endpoint energy is 3.50 ± 0.05 MeV.

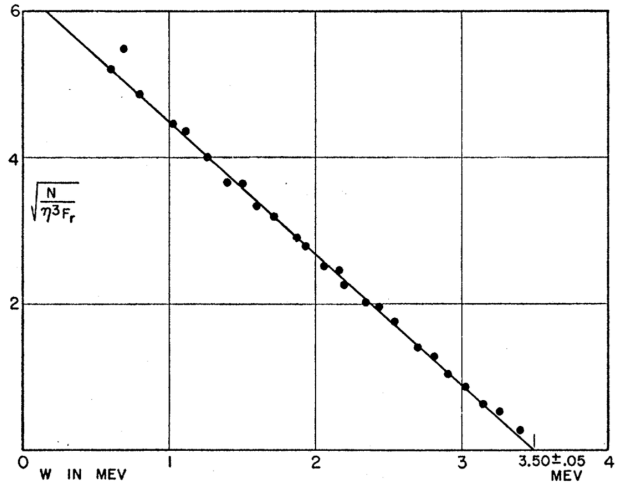

Figure 1-7: Kurie plot of the β-energy spectrum in ^{6}He decay. Figure taken from Ref. [9].

B.M. Rustad *et al.* [10] have performed a measurement of the β-neutrino angular correlation in ^{6}He decay in the 1950s. As a part of this experiment, a β-energy spectrum in ^{6}He was measured to determine whether an impurity with a half-life close to that of ^{6}He but of different endpoint energy was present. A schematic sketch of the experimental setup is shown in the left panel of Fig. 1-8, where the ^{6}He β-active volume and the scintillation spectrometer are located in a common vacuum

volume. The scintillation spectrometer measures the energy and direction of the β particles. The energy distribution of the β particles striking the stilbene plastic is shown in the right panel of Fig. 1-8. This experimental setup, with the decay source next to the detector, faced instrumental difficulties due to the backscattering of β particles from the stilbene plastic that greatly distorted the β-energy spectrum.

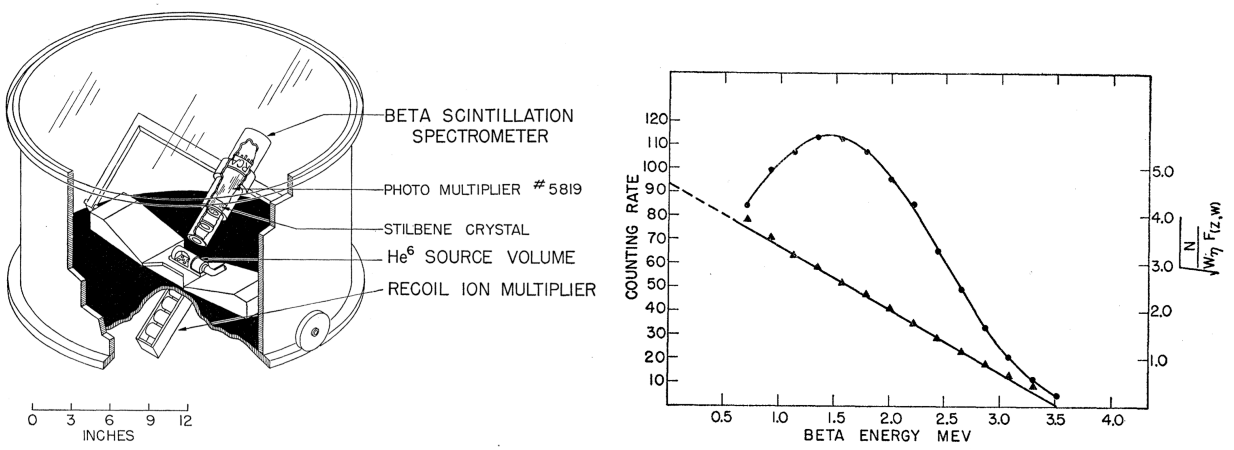

Figure 1-8: Left panel: a schematic sketch of the apparatus used to determine the electron-recoil ion correlation in the decay of ^{6}He. The beta-active source volume and the scintillation spectrometer are located in the common vacuum of the "bell-jar". Right panel: the ^{6}He β-energy spectrum measured with the stilbene scintillation spectrometer. Figures taken from Ref. [10].

It is interesting to notice that the motivation of this experiment was to determine the nature of weak interactions. The result had led the authors to believe that weak interaction was dominated by tensor couplings, which is different from what we know today: the contribution of tensor couplings is minimal if non-zero, and is precisely what this work is searching.

A. Schwarzschild [11] has reported in his Ph.D. thesis a dedicated precise measurement of the shape of β-energy spectrum in ^{6}He decay to provide limits on the axial vector and pseudoscalar couplings in β decay. The energy of β particles was measured with a magnetic spectrometer. Figure 1-9 shows a scale drawing of the spectrometer baffle system, the source volume, and the Geiger counter.

The greatest contributions to the systematics in this experiment came from the scattering of β particles. First of all, the scattering of the electrons in the source with a finite thickness caused

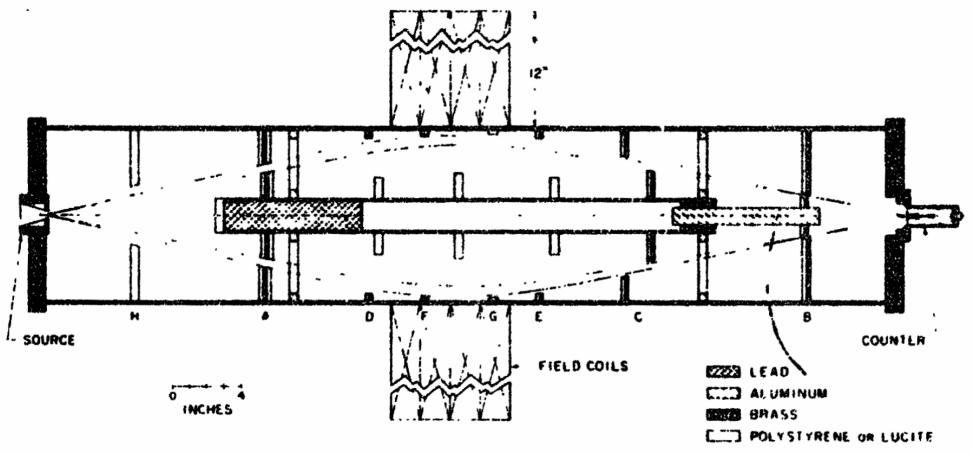

Figure 1-9: A scale drawing of the thin lens spectrometer baffle system, the source volume, and the Geiger counter. Figure taken from Ref. [11].

the energy loss of electrons, distorting the measured β-energy spectrum. Secondly, the scattering of the electrons in the counter window affects the shape of β-energy spectrum, as the thickness of the counter window also reduces the energy of β particles. Lastly, the most severe distortion to the β spectrum came from the scattering of electrons from the baffle system. This effect is far more difficult to investigate than the previous two, and the authors attempted to set an upper limit on the distortion to the β spectrum in the low energy region. Other effects taken into account in the analysis are the inconsistency of the activity of ^{6}He beam delivered to the spectrometer source volume, the background of the counter, the corrections for the energy resolution, and the corrections for the ^{23}Ne contaminant. Figure 1-10 shows the resulting Kurie plot of the ^{6}He beta spectrum, where the deviations in the low energy range are due to the scattering processes described above, dominated by the scattering of electrons from the baffle system.

1.5.2 More Recent Measurements of the β-energy Spectra

^{20}F

The most recent measurement of the β-energy spectrum in ^{20}F decay was performed by D. W. Hetherington *et al.*[12]. The extracted slope of the spectral function is in good agreement with

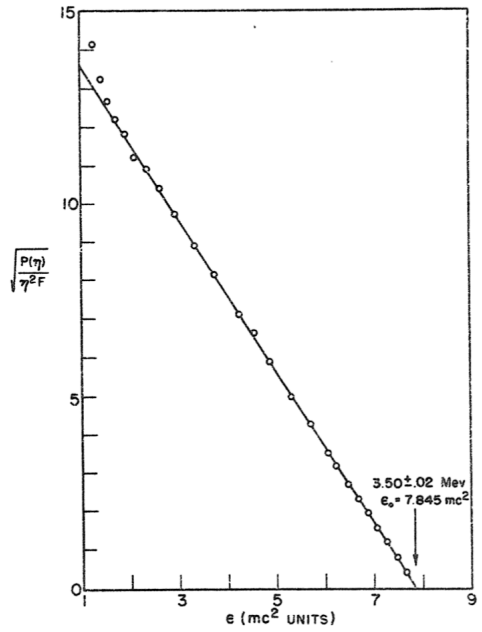

Figure 1-10: Kurie plot of the β-energy spectrum in ^{6}He decay. Figure taken from Ref. [11].

the prediction by CVC. In this measurement, the kinetic energy of β particles was measured with a high-purity germanium detector in a high-field superconducting solenoid. The layout of the spectrometer is shown in the left panel of Fig. 1-11, where the decay source is placed outside the active volume of the detector. Due to the backscattering and the bremsstrahlung production, the corresponding response from the detector (dashed line) shown in the right panel of Fig. 1-11 is greatly distorted relative to the theoretical spectrum (solid line).

^{66}Ga and ^{14}O

G. W. Severin *et al.*[13] have measured the β-energy spectrum in ^{66}Ga decay. The measurement was performed with a Wisconsin superconducting beta spectrometer [46], a Wu-type magnetic spectrometer similar to that described in Ref. [47]. The β particles passing through the annular slits are detected with a Si(Li) detector. The β-energy spectrum was obtained by recording the number of the detected β particles at several spectrometer currents in sequence. The left panel of Fig. 1-12 shows the energy spectrum deposited in the Si(Li) detector at a spectrometer current setting corresponding to a positron kinetic energy of 3.25 MeV. The long tail below 1.5 MeV

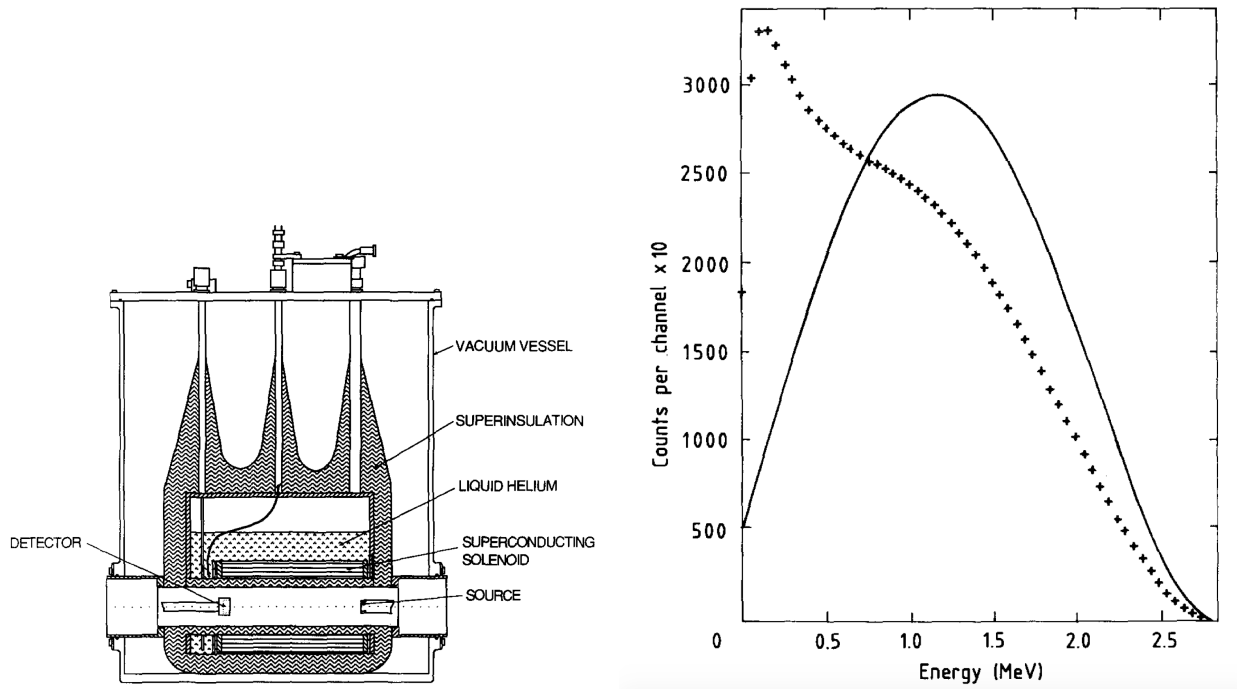

Figure 1-11: Left panel: the layout of the β spectrometer used to measure the kinetic energy of β particles. It consists of a high-purity germanium detector mounted on the axis in the bore of a superconducting solenoid. Right panel: the theoretical statistical distribution (solid line) and the corresponding response from the detector (dashed line). Figures taken from Ref. [12].

originates from the energy loss due to the backscattering of positrons and the bremsstrahlung process. The resulting Kurie plot of the β-energy spectrum is shown in the right panel of Fig. 1-12.

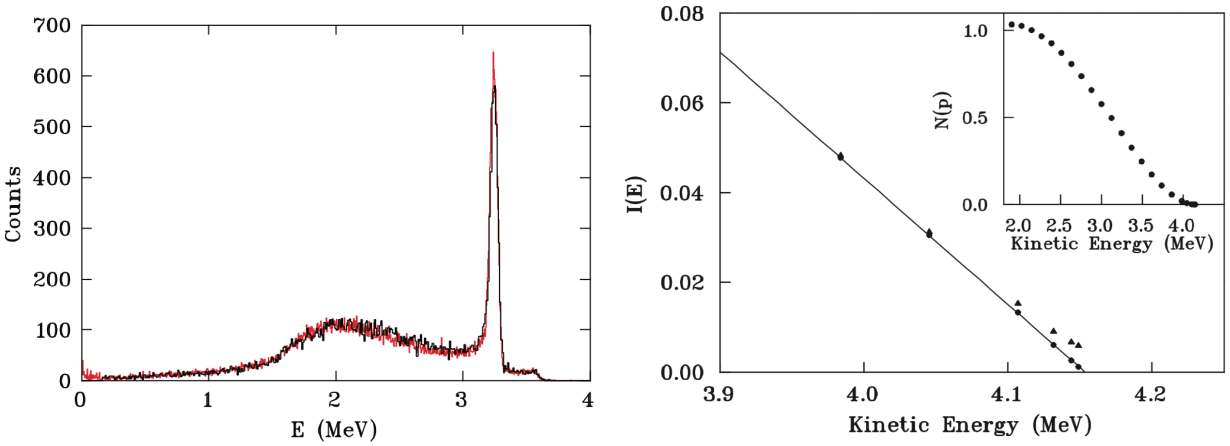

Figure 1-12: Left panel: measured (black) and simulated (red) energy spectra deposited in the Si(Li) detector with a spectrometer current corresponding to a positron kinetic energy of 3.25 MeV. Right panel: the β-energy spectrum in ^{66}Ga decay. Figures taken from Ref. [13].

With the same apparatus, E. A. George *et al.*[44] have measured the β-momentum spectrum in ^{14}O decay. The left panel of Fig. 1-13 shows the positron energy spectra deposited in the Si(Li) detector with two spectrometer current settings. Similar to the left panel of Fig. 1-12, the tails below the primary peak and above a channel number of 120 originates primarily from the energy loss due to the backscattering of positrons out of the detector. The resulting β-momentum spectrum is shown in the right panel of Fig. 1-13. In this experiment, the previously measured ^{66}Ga spectra [13] were used as model spectra in the analysis. It is shown in Refs. [44, 14] that the backscattering events in the ^{66}Ga spectra cannot be accurately described by Monte Carlo simulations. For all spectrometer currents, the simulations overpredict the backscattering events [44]; in the current range of 4-8 A, the simulations overpredict by 7% [14].

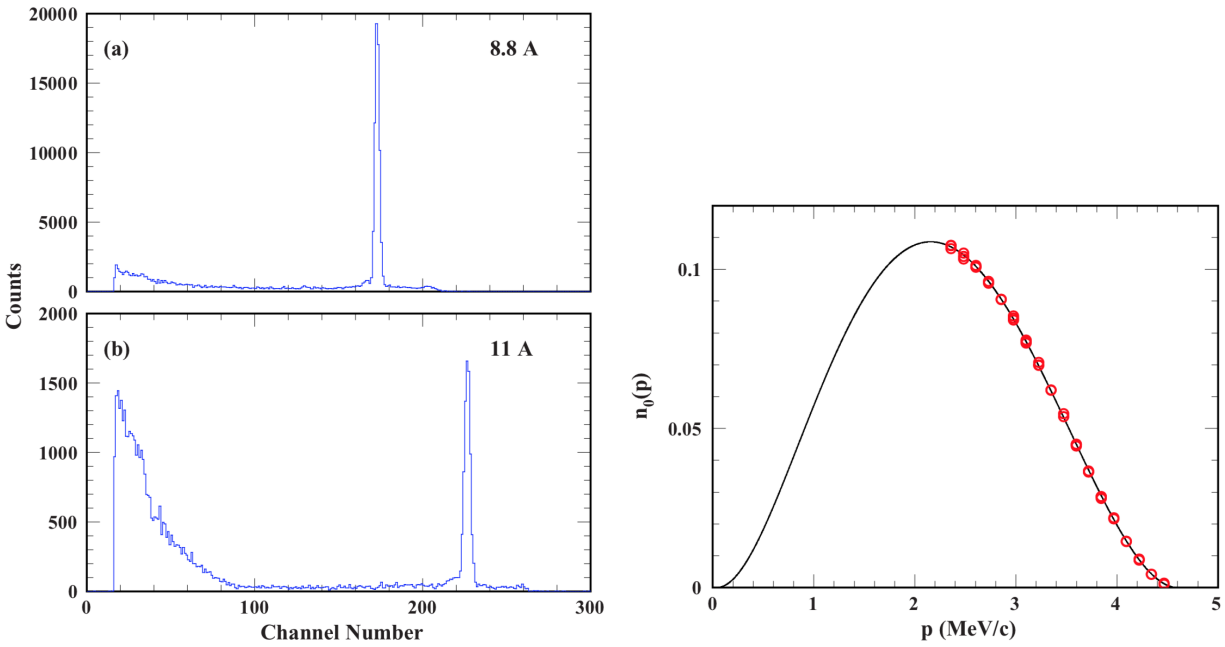

Figure 1-13: Left panel: Si(Li) spectra measured with the spectrometer current setting at 8.8 A and 11.0 A. Right panel: the β-momentum spectrum in ^{14}O decay including the measured spectrum (open circles) and the theoretical spectrum (solid line). Figures taken from Ref. [14].

1.5.3 What is Next?

It is clear now that among the experiments measuring the shapes of β-energy spectra, the most common and most severe instrumental effect is the backscattering of β particles from the active volume of the detector. For the new generation of experiments measuring the β-energy spectra, higher precisions are required to access any signatures of new physics. The new precision goals require a new experimental technique capable of eliminating the effect of backscattering.

CHAPTER 2

THEORETICAL CORRECTIONS TO THE β-ENERGY SPECTRUM

In Chap. 1, the full theoretical description of the allowed β-energy spectrum in ^{6}He decay was introduced in Eq. 1.26, where the factor $\eta(W)$, the product of several theoretical corrections, was not discussed. The corrections include: the Fermi function $F(Z, W)$, the screening correction $S(Z, W)$, the electrostatic finite size correction $L_0(Z, W)$, the convolution finite size correction $C^A(Z, W, W_0)$, the finite mass correction $R_N(W, W_0)$, and the radiative correction $\delta_R(Z, W, W_0)$ or $\delta(\mathcal{E})$. This chapter discusses the origin of each theoretical correction and calculates each correction for ^{6}He decay. Since the full theoretical description of the β spectrum has an uncertainty, the uncertainties of the observables associated with the theoretical description (theoretical uncertainties) are estimated.

Equation 1.26 is derived including the recoil to first order, assuming the absence of second class currents, and neglecting the induced tensor form factor in ^{6}He decay. To describe the transition to first order in recoil, it requires only three form factors [48, 36, 37], i.e., the dominant Gamow-Teller strength (c), the weak magnetism form factor (b_{WM}), and the induced tensor form factor (d), where d is the sum of a first class part (d^I) and a second class part (d^{II}). The first class part is neglected here, but its impact will be evaluated in the complete analysis. The second class part is absent in ^{6}He decay because a preliminary analysis in Ref. [48] found no evidence of a d^{II} term in ^{6}He $e\nu$ correlation measurements.

The theoretical evaluation is the first step towards an accurate description of the β spectrum, and it lays the foundation for the study of a series of instrumental effects discussed in later chapters. The study in this chapter applies for β^- and Gamow-Teller decays. Throughout the chapter, the variables are expressed in the natural unit (mc^2), with $\hbar = m = c = 1$.

2.1 Fermi Function

The Fermi function describes the electrostatic interaction between the emitted β particle and the Coulomb field of the daughter nucleus. It is derived from the solution to the Dirac equation for

the electron wave function at a distance R from an assumed infinitely heavy, point-like daughter nucleus. The Fermi function has the expression [49]

$$F(Z,W) = 2(\gamma+1)(2pR)^{2(\gamma-1)}e^{\pi y}\frac{|\Gamma(\gamma+iy)|^2}{[\Gamma(2\gamma+1)]^2}, \tag{2.1}$$

where Z is the atomic number of the daughter nucleus, $\gamma = \sqrt{1-(\alpha Z)^2}$, $y = \alpha ZW/p$, and Γ is the complex gamma function. For a point charge, the solution to the Dirac equation diverges at the origin. To circumvent the divergence, a cut-off radius R without physical significance is introduced [50]. The radius of the daughter nucleus is taken as the value of R and is determined in Sec. 2.7.

2.2 Screening Correction

For a departing electron, the presence of the other electrons in the atom of the daughter bound state produces a screening of the nuclear charge and effectively reduces the nuclear charge "seen" by the departing electron. This change of the electromagnetic field distorts the β-energy spectrum and can be taken into account by a screening correction. There are a few methods to calculate the screening correction in literature. In this work, four different formulas were considered: Rose's formula, Bühring's formula, simplified Bühring's formula, and weak-screening approximation of Bühring's formula. These formulas require a common input: the screening potential, which is derived here.

One of the simplest models describing a screened Coulomb potential is the Hulthén potential [51]:

$$V(r) = -\frac{\alpha Z\beta_s}{e^{\beta_s r}-1}. \tag{2.2}$$

Its behavior near the origin is [52]

$$V(r) = -\frac{\alpha Z}{r} + \frac{1}{2}\alpha Z\beta_s + O(r), \tag{2.3}$$

where the term $\frac{1}{2}\alpha Z\beta_s$ is a shift of the potential near the nucleus due to the screening. This shift of potential is sometimes also referred to as the screening potential, represented by V_S, and is negative for β^- decays [51]:

$$V_S = -\frac{1}{2}\alpha Z\beta_s,\ \beta_s = 2C(|\tilde{Z}|)\alpha|\tilde{Z}|^{1/3}. \tag{2.4}$$

Here, $\tilde{Z} = 2$ is the atomic number of the mother nucleus ^{6}He, $C(|\tilde{Z}|)$ is a slowly increasing function of $\tilde{Z}$. The value of $C(|\tilde{Z}|)$ is determined following the approach in Ref. [51]. Equating the Hartree potential in Ref. [53] with the three Yukawa potentials in Ref. [54] gives

$$C(|\tilde{Z}|) = 1.13 \sum\nolimits_j a_j b_j, \tag{2.5}$$

which is derived in Sec. A.1 in the Appendix. a_j and b_j are coefficients corresponding to the mother nucleus and their values for helium are adapted from Table I in Ref. [53]. This yields the value of $C(|\tilde{Z}|)$ for helium:

$$C(2) \simeq 1.386. \tag{2.6}$$

The screening potential is then determined by substituting the values of $C(2)$ and $|\tilde{Z}|$ into Eq. 2.4.

2.2.1 Rose's Formula

The earliest work on the screening correction was reported by Rose [49]. The correction is determined following a approximate WKB procedure [55] and has the form

$$S(Z, W) = \frac{\tilde{p}_R \tilde{W}}{pW} = \frac{F(Z, \tilde{W})}{F(Z, W)} = \frac{\tilde{W}}{W} \left(\frac{\tilde{p}_R}{p} \right)^{2\gamma - 1} e^{\pi(\tilde{y}_R - y)} \left| \frac{\Gamma(\gamma + i\tilde{y}_R)}{\Gamma(\gamma + iy)} \right|^2, \tag{2.7}$$

where

$$\tilde{W} = W + V_S, \tag{2.8}$$

$$\tilde{p}_R = \sqrt{\tilde{W}^2 - 1}, \tag{2.9}$$

$$\tilde{y_R} = \frac{\alpha Z \tilde{W}}{\tilde{p}_R}. \tag{2.10}$$

2.2.2 Bühring's Formula

The accurate calculation of the screening correction requires solving the Dirac equation in the superposition field of the nucleus and the extended electron shells or an acceptable surrogate for the two together [56]. Alternatively, one may solve the Klein-Gordon equation in the Hulthén potential, which is a useful surrogate for the superimposed fields [56]. Bühring has studied the Hulthén

potential and derived an approximate but close evaluation of the wave function normalization factor of the Dirac equation for a semi-realistic case [56]. The resulting expression for the screening correction is [3, 51]

$$S(Z,W) = X\frac{\tilde{W}}{W}e^{-\pi y}\left(\frac{2p}{\beta_s}\right)^{2(1-\gamma)}\left|\frac{\Gamma(\gamma+i\tilde{y})}{\Gamma(\gamma+iy)}\right|^2\left|\frac{\Gamma(\gamma+2i\tilde{p}/\beta_s)}{\Gamma(1+2ip/\beta_s)}\right|^2, \tag{2.11}$$

where

$$\begin{aligned} X =& \left[1+\frac{1}{4}\left(\frac{\beta_s}{p}\right)^2\right]^{-1}\times\left\{1+\frac{1}{8}\left(\frac{\tilde{W}+\gamma}{\tilde{W}}\right)\left(\frac{\beta_s}{p}\right)^2\right. \\ &\left.+\frac{1}{2}\gamma^2\left[1+\left(1-\frac{\alpha Z\beta_s}{W+1}\right)^{1/2}\right]^{-2}\frac{W-1}{\tilde{W}}\left(\frac{\beta_s}{p}\right)^2\left[1-\frac{1}{8}(1-\gamma)\frac{1}{\gamma}\left(\frac{\beta_s}{p}\right)^2\right]\right\}, \end{aligned} \tag{2.12}$$

$$\tilde{p} = \frac{1}{2}p+\frac{1}{2}\left[p^2-2\alpha Z\tilde{W}\beta_s\right]^{1/2}, \tag{2.13}$$

$$\tilde{y} = \frac{\alpha Z\tilde{W}}{\tilde{p}}. \tag{2.14}$$

Bühring's formula is a significant improvement compared with Rose's formula [51]. It can be shown that, in a certain limit, the latter can be derived from the former. Note that $\tilde{p}$ and $\tilde{p}_R$ differ only in higher-order terms:

$$\begin{aligned} \tilde{p} &= \frac{1}{2}p+\frac{1}{2}\left[p^2-2\alpha Z\tilde{W}\beta_s\right]^{1/2} \\ &= (\tilde{W}^2-1)^{1/2}+O(\beta_s^2) \\ &= \tilde{p}_R+O(\beta_s^2). \end{aligned} \tag{2.15}$$

As $\beta_S \to 0$, $\tilde{p} \to \tilde{p}_R$.

2.2.3 Simplified Bühring's Formula

In Eq. 2.12 of Bühring's formula, the factor X can be expressed as

$$X = 1+O(\beta_s^2). \tag{2.16}$$

As $\beta_S \to 0$, $X \to 1$. Therefore the Bühring's formula with $X = 1$ can be considered a good approximation to the Bühring's formula with the X calculated with Eq. 2.12. This gives the

simplified Bühring's formula:

$$S(Z,W) = \frac{\tilde{W}}{W} e^{-\pi y} \left(\frac{2p}{\beta_s}\right)^{2(1-\gamma)} \left|\frac{\Gamma(\gamma + i\tilde{y})}{\Gamma(\gamma + iy)}\right|^2 \left|\frac{\Gamma(\gamma + 2i\tilde{p}/\beta_s)}{\Gamma(1 + 2ip/\beta_s)}\right|^2. \tag{2.17}$$

2.2.4 Weak-Screening Approximation of Bühring's Formula

In Eq. 2.11 of Bühring's formula, if one performs an asymptotic expansion in power of β_s and omits the terms of order β_s^2, the weak-screening approximation of Bühring's formula can be obtained:

$$S(Z,W) = \frac{\tilde{W}}{W} \left(\frac{\tilde{p}}{p}\right)^{2\gamma-1} e^{\pi(\tilde{y}-y)} \left|\frac{\Gamma(\gamma + i\tilde{y})}{\Gamma(\gamma + iy)}\right|^2. \tag{2.18}$$

This is essentially the Rose's formula apart from the difference between $\tilde{p}$ and $\tilde{p}_R$, which is also responsible to the difference between $\tilde{y}$ and $\tilde{y}_R$. Once again, if $\beta \to 0$, $\tilde{p} \to \tilde{p}_R$ (Eq. 2.15), then Eq. 2.18 becomes Rose's formula. Therefore this result is also referred to as Rose† in Ref. [56].

Table 2-1 shows the calculated screening corrections in ^{6}He decay with the above four formulas. The Bühring's formula, the simplified Bühring's formula, and the weak-screening approximation of Bühring's formula give the same results at the level of 10^{-5}. The relative difference between the correction with Rose's formula and the rest is smaller than 2% for $p < 0.2$. For $p > 0.2$, the four formulas give identical results at the level of 10^{-5}. In the analysis in this work, the Bühring's formula is applied.

Table 2-1: The screening corrections for ^{6}He decay for $p \leq 0.3$. The values shown here are $[S(Z,W) - 1]$.

p	Bühring	Simplified Bühring	Weak-screening Approximation to Bühring	Rose
0.1	-0.01372	-0.01372	-0.01372	-0.01352
0.2	-0.00529	-0.00529	-0.00529	-0.00528
0.3	-0.00285	-0.00285	-0.00285	-0.00285

2.3 The Finite Size Corrections

2.3.1 Electrostatic Finite Size Correction

As mentioned in Sec. 2.1, the Fermi function assumes an infinitely massive, point-like daughter nucleus. In reality, the daughter nucleus has a finite charge distribution, and its deviation from the point charge distribution affects the solutions to the Dirac equation. Solving the Dirac equation in the field of the actual charge distribution of the daughter nucleus introduces an electrostatic finite size correction $L_0(Z, W)$ to the Fermi function.

The values of $L_0(Z, W)$ for $Z < 30$ were tabulated by H. Behrens and J. Jänecke [15] as a result of numerical computations assuming the daughter nucleus is an uniformly charged sphere of radius R. Based on these values, Wilkinson [57] performed an empirical fit and obtained an analytic expression of $L_0(Z, W)$ that applies to $Z < 40$:

$$L_0(Z, W) = 1 + 0.206(\alpha Z)^2 - 1.039WR\alpha Z - 0.0058(pR)^2 - 0.54\frac{R\alpha Z}{W}. \tag{2.19}$$

With the same tabulation as Ref. [15], Wilkinson improved the fit and extended the domain to $Z \leq 60$ [3]. The updated expression of $L_0(Z, W)$ for electron is

$$\begin{aligned} L_0(Z, W) = 1 + \frac{13}{60}(\alpha Z)^2 - WR\alpha Z\frac{41 - 26\gamma}{15(2\gamma - 1)} - \alpha ZR\gamma\frac{17 - 2\gamma}{30W(2\gamma - 1)} + a_{-1}\frac{R}{W} \\ + \sum_{n=0}^{5} a_n(WR)^n + 0.41(R - 0.0164)(\alpha Z)^{4.5}. \end{aligned} \tag{2.20}$$

In the above expression, the a-values are given by the parameterization

$$a = \sum_{x=1}^{6} b_x(\alpha Z)^x, \tag{2.21}$$

where the b_x-values are given in Table A-1 in Sec. A.2 of the Appendix and are different for each a_n.

Figure 2-1 shows the calculated $L_0(Z, W)$ applying the analytic expressions described above. The dashed blue line is obtained with Eq. 2.19, which has a small deviation from the numerical values of Ref. [15] (solid red line). The solid blue line is obtained with the improved analytic expression, Eq. 2.20, resulting in a better agreement with the values in Ref. [15].

In the above calculations with Eqs. 2.19 and 2.20, the same nuclear radius was applied as the radius used by H. Behrens and J. Jänecke in Ref. [15]: $R_1 = 0.42587A^{1/3}$. These calculations only serve the purpose of comparing the results with the values in Ref. [15]. It is shown in Sec. 2.7 that there are a few options for the nuclear radius in literature. In the actual analysis in this work, a different radius, R_3, described in Sec. 2.7, is used. With R_3, the calculated $L_0(Z, W)$ values are shown in Fig. 2-1, where the dashed black line is based on Eq. 2.19 and the solid black line is based on Eq. 2.20. The calculations with R_3 give lower values of $L_0(Z, W)$ than those with R_1.

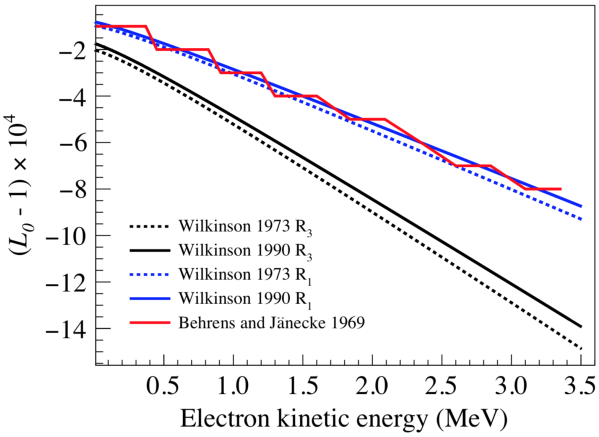

Figure 2-1: Electrostatic finite size corrections. The dashed lines and the solid line are calculated with Eq. 2.19 and Eq. 2.20, respectively. The colors indicate the radius used in the calculations: blue corresponds to R_1 and black corresponds to R_3. The results are compared with the numerical values (solid red) from Ref. [15].

2.3.2 Convolution Finite Size Correction

Another effect related to the finite nuclear size is the convolution of the leptonic and nucleonic wave functions through the nuclear volume. For Gamow-Teller decays it has the form [3]

$$C^A(Z, W, W_0) = 1 + C_0^A + C_1^A W + C_2^A W^2, \tag{2.22}$$

where

$$C_0^A = -\frac{233}{630}(\alpha Z)^2 - \frac{(W_0 R)^2}{5} + \frac{2}{35} W_0 R \alpha Z, \tag{2.23}$$

$$C_1^A = -\frac{21}{35} R\alpha Z + \frac{4}{9} W_0 R^2, \tag{2.24}$$

$$C_2^A = -\frac{4}{9} R^2. \tag{2.25}$$

Here the superscript A indicates the axial vector nature of the Gamow-Teller transition.

2.4 Finite Mass Correction

In the Fermi function, two assumptions about the mass are made: the neutrino is considered massless and the daughter nucleus is considered infinitely massive. The effect of the non-zero neutrino mass on the β spectrum can be safely neglected with a neutrino mass below 30 eV [3]. The effect related to the finite nuclear mass, however, requires a recoil correction. The correction for Gamow-Teller decays can be included by multiplying the phase space factor by a factor $R_N(W, W_0)$ provided in Ref. [3]:

$$R_N(W, W_0) = 1 + r_0^A + \frac{r_1^A}{W} + r_2^A W + r_3^A W^2, \tag{2.26}$$

where

$$r_0^A = -\frac{2W_0}{3M} - \frac{W_0^2}{6M^2} - \frac{77}{18M^2}, \tag{2.27}$$

$$r_1^A = -\frac{2}{3M} + \frac{7W_0}{9M^2}, \tag{2.28}$$

$$r_2^A = \frac{10}{3M} - \frac{28W_0}{9M^2}, \tag{2.29}$$

$$r_3^A = \frac{88}{9M^2}. \tag{2.30}$$

Here, M is the nuclear mass of ^{6}Li in the natural unit [40]. Once again, the superscript A corresponds to the axial vector nature of the Gamow-Teller transition.

2.5 Radiative Correction

During β decay, the virtual and real photons can be emitted and change the β-decay kinematics. The exchange of the virtual photons and the emission of the real photons can be taken into account

by multiplying the phase space factor by a radiative correction, $R(Z, W, W_0)$. It can be split into two parts [58]: the "inner radiative correction" which depends on the special form of the weak and strong interactions theory, and the "outer radiative correction" which is independent of the details of strong and weak interactions. The complete radiative correction has the form [16]

$$R(Z, W, W_0) = \left(1 + \Delta_R^{V/A}\right) [1 + \delta_R(Z, W, W_0)], \tag{2.31}$$

where $\left(1 + \Delta_R^{V/A}\right)$ and $[1 + \delta_R(Z, W, W_0)]$ represent the inner and outer radiative corrections, respectively.

The inner radiative correction is energy independent and nucleus independent. It affects the integrated form of the β-energy spectrum and is crucial for the analysis of the $\mathcal{F}t$ values. Because of the energy independence, the inner radiative correction manifests itself as a normalization constant in the differential form of the β-energy spectrum. Therefore it is irrelevant for the scope of this work.

The outer radiative correction depends on the energy of the outgoing β particles and distorts the shape of the β-energy spectrum. It includes processes involving virtual and real photons. Details about these processes are described below. Note that the real photon emitted during a decay is also referred to as the inner bremsstrahlung radiation, which is to be distinguished from both the inner radiative correction and the outer bremsstrahlung photon emitted as the β particle slows down in the detector.

This section focuses on the outer radiative correction. In the rest of the section, the term "radiative correction" refers to only the outer radiative correction. The radiative correction are discussed in two categories of experimental conditions: 1) the electrons and photons are completely distinguishable so that the energy measured in the detector is the energy of β particles only; 2) electrons and photons are completely indistinguishable so that the measured energy is the sum of electron and photon energy.

2.5.1 Distinguishable e^- and γ

The radiative correction δ_R includes the corrections of different orders of the fine-structure constant α. The first three orders are the most frequently discussed in literature:

$$\delta_R(Z, W, W_0) = \delta_1(W, W_0) + \delta_2(Z, W) + \delta_3(Z, W), \tag{2.32}$$

where $\delta_1(W, W_0)$, $\delta_2(Z, W)$, and $\delta_3(Z, W)$ are the radiative corrections of the orders α, $Z\alpha^2$, and $Z^2\alpha^3$, respectively.

The order α radiative correction is on the order of a few percent; it is one of the two dominant corrections (the other one is the Fermi function). The order $Z\alpha^2$ and $Z^2\alpha^3$ corrections have a remarkable influence on the $\mathcal{F}t$ value and are of small but non-negligible importance for the differential form of the spectrum.

Order α

The first order of the radiative correction is associated with the one-photon exchange processes, shown in Fig. 2-2. The pioneering work on the order α correction was published by Sirlin [59] in 1967 and it is still being applied in the precision electroweak studies as the default radiative correction:

$$\delta_1(W, W_0) = \frac{\alpha}{2\pi} g_\alpha(W, W_0), \tag{2.33}$$

where

$$\begin{aligned} g_\alpha(W, W_0) =& 3\ln m_p - \frac{3}{4} + \frac{4}{\beta_e} L\left(\frac{2\beta_e}{1+\beta_e}\right) + 4\left(\frac{\tanh^{-1}\beta_e}{\beta_e} - 1\right)\left[\frac{W_0 - W}{3W} - \frac{3}{2} + \ln[2(W_0 - W)]\right] \\ &+ \frac{\tanh^{-1}\beta_e}{\beta_e}\left[2(1+\beta_e^2) + \frac{(W_0 - W)^2}{6W^2} - 4\tanh^{-1}\beta_e\right], \end{aligned} \tag{2.34}$$

$$L(x) = \int_0^x \frac{\ln(1-t)}{t} dt. \tag{2.35}$$

Here, m_p is the proton mass, $\beta_e = p/W$, and $L(x)$ is the Spence function or Dilogarithm. The $\ln[2(W_0 - W)]$ term leads to a divergence of Eq. 2.34 as W approaches the endpoint energy W_0. This behavior can be eliminated [60] by replacing $t(\beta_e)\ln(W_0 - W)$ by $(W_0 - W)^{t(\beta_e)} - 1$, where

$t(\beta_e) = 2\alpha/\pi \left[(\tanh^{-1}\beta_e)/\beta_e - 1\right]$. Note that $t(\beta_e)\ln(W_0 - W)$ is just the leading term of the expansion of $(W_0 - W)^{t(\beta_e)} - 1$.

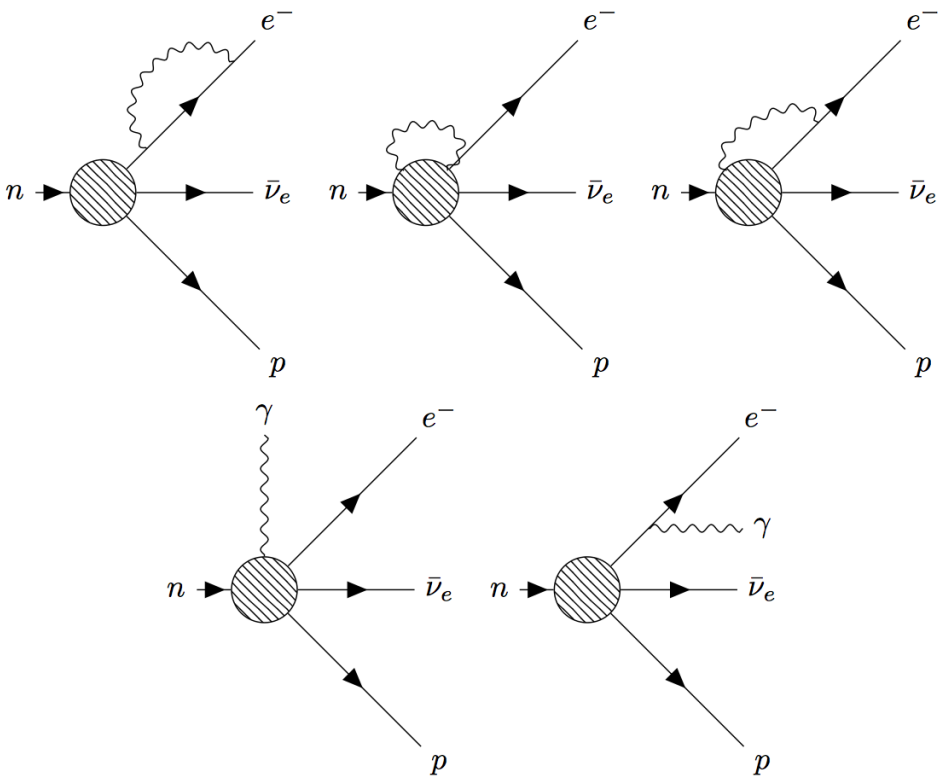

Figure 2-2: Feynman diagrams for the one-photon exchange processes associated with the order α outer radiative correction. The top row shows the processes involving virtual photon exchange, and the bottom row shows the processes involving real photon emission. Figure taken from Ref. [16].

Order $Z\alpha^2$

The order $Z\alpha^2$ of the radiative correction has the form [61]

$$\delta_2(Z, W) = \alpha Z^2 \sum_{i=1}^{4} \Delta_i(W). \tag{2.36}$$

It is convenient to split Δ_1 into two parts:

$$\Delta_1 = \Delta_1^0(W) + \Delta_1^F, \tag{2.37}$$

where Δ_1^0 corresponds to a point nucleus and is energy dependent, and Δ_1^F is energy independent but depends on the charge distribution of the daughter nucleus. In the extreme relativistic approximation, $\Delta_1^0(W) + \Delta_4(W)$ can be expressed analyticly:

$$\Delta_1^0(W) + \Delta_4(W) = \ln m_p - \frac{5}{3}\ln(2W) + \frac{43}{18}. \tag{2.38}$$

The terms Δ_1^F, Δ_2 and Δ_3 are finite nuclear size effects and depend on the charge distribution of the daughter nucleus. The analytic forms of the three terms are available in literature for three types of charge distributions: uniform distribution [61], modified Gaussian distribution [61], and Yukawa distribution [62]. For the first two charge distributions, the expressions of Δ_1^F, Δ_2 and Δ_3 are shown in Sec. A.3 of the Appendix. For the Yukawa charge distribution,

$$\Delta_1^F = \left(1 + \frac{2}{\pi}\frac{\Lambda}{m_p}\right)\ln\frac{\Lambda}{m_p} - \frac{2}{\pi}\frac{\Lambda}{m_p}, \tag{2.39}$$

$$\Delta_2 = \frac{1}{\pi}\frac{\Lambda}{M}\left(1 + \frac{\pi}{4}\frac{\Lambda}{m_p}\ln\frac{\Lambda}{m_p}\right), \tag{2.40}$$

$$\Delta_3 = \frac{1}{\pi}g_A(1+\kappa_V)\frac{\Lambda}{m_p}\left[-1 + \pi\frac{\Lambda}{m_p} - 2\left(1 + \frac{\pi}{8}\frac{\Lambda}{m_p}\right)\ln\frac{\Lambda}{m_p}\right]. \tag{2.41}$$

where $1 + \kappa_V = 4.7059$, Λ is related to the radius of the daughter nucleus: $\Lambda \equiv \sqrt{10}/R$.

Order $Z^2\alpha^3$

The order $Z^2\alpha^3$ radiative correction has the expression [61, 63, 64]:

$$\delta_3 = Z^2\alpha^3\left[a\ln\left(\frac{\Gamma}{m_p}\right) + bf(W) + dg(W) + h\ln(2W_0)\right] \tag{2.42}$$

where,

$$a = \left(\frac{\pi^2}{3} - \frac{3}{2}\right) \Big/ \pi, \tag{2.43}$$

$$b = \frac{4}{3\pi}\left(\frac{11}{4} - \gamma^E - \frac{\pi^2}{6}\right), \tag{2.44}$$

$$d = \frac{4}{3\pi}, \tag{2.45}$$

$$h = -0.649, \tag{2.46}$$

$$f(W) = \ln(2W) - \frac{5}{6}, \tag{2.47}$$

$$g(W) = \frac{1}{2}\left[\ln^2 R - \ln^2(2W)\right] + \frac{5}{3}\ln(2RW). \tag{2.48}$$

Here, γ^E is the Euler–Mascheroni constant.

The above radiative correction, $\delta_R(Z, W, W_0)$, is based on the assumption that the β spectrometer can separate photons from the β particles so that no energy of photons is detected. The validity of this assumption and its impact on the radiative correction need to be discussed for the experimental setup in this work shown in Chap. 3.

2.5.2 Indistinguishable e^- and γ

As the radiative correction involves the emission of real photons (i.e., the inner bremsstrahlung radiation), it is possible for the real photons to be detected along with the β particles in a measurement. The direct consequence will be that the measured energy spectrum would no longer be a clean β-energy spectrum, but rather a $(\beta + \gamma)$-energy spectrum. Whether the real photons can be detected and if so, the fraction of the detected photon energy, are decided by the experimental technique. Therefore the radiative correction for indistinguishable e^- and γ requires to be approached differently from the previous theoretical corrections, which are independent of the experimental setup.

The inner bremsstrahlung radiation is usually treated as a two-step process. First the β particle e' of energy W' is emitted in a virtual intermediate state, then it goes to its final state e^- of energy

W accompanied by a photon of energy k:

$$n \rightarrow p + \bar{\nu}_e + e' \rightarrow p + \bar{\nu}_e + e^- + \gamma. \tag{2.49}$$

For allowed β transitions, the theory of inner bremsstrahlung was suggested by Knipp and Uhlenbeck [65] and independently by Bloch [66], referred to as the KUB theory. According to the KUB theory, the probability for a β particle of initial energy W' to release a photon of energy k is given by

$$\Phi(W', k) = \frac{\alpha p}{\pi k p'} \left[\frac{W^2 + W'^2}{W' p} \ln (W + p) - 2 \right], \tag{2.50}$$

where $W' = W + k$ and $p' = \sqrt{W'^2 - 1}$. The inner bremsstrahlung spectrum is obtained by integrating the product of $\Phi(W', k)$ and the phase space factor over the energy range of $k + 1$ to W_0:

$$S(k) = \int_{k+1}^{W_0} pW'(W' - W_0)^2 dW' \Phi(W', k). \tag{2.51}$$

With Eqs. (2.50) and (2.51), the inner bremsstrahlung spectrum emitted in ^{6}He β decay is calculated and shown in Fig. 2-3. The majority of the photons are in the low energy part of the spectrum. These photons can in principle be detected in a calorimetric detector used in this work (see Chap. 3). For an efficient calorimeter, it is reasonable to assume that all bremsstrahlung photons fully deposit their energy in the detector. Therefore for this work, the radiative correction should take into account the indistinguishability of β particles and photons and the resulting energy summing effect.

For a decay event taking place in a calorimeter, the total energy recorded by the detector is represented by $\mathcal{E}$, and $\mathcal{E} = k + W$ if an inner bremsstrahlung photon is emitted. The maximum photon energy $k^{\max}$ is then equal to $k^{\max} = \mathcal{E} - 1$, where this 1 is the electron rest mass. To first order, the radiative correction can be written as

$$\delta(\mathcal{E}) = 1 + \frac{\alpha}{\pi} g(\mathcal{E}), \tag{2.52}$$

$$g(\mathcal{E}) = g_v(\mathcal{E}) + g_b(\mathcal{E}), \tag{2.53}$$

where $g_v(\mathcal{E})$ and $g_b(\mathcal{E})$ stand for the corrections associated with the virtual and real photon processes, respectively.

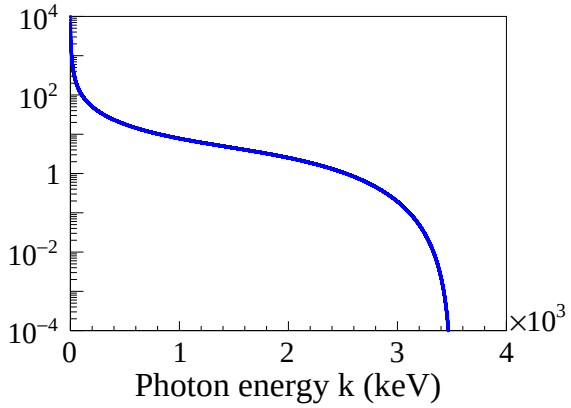

Figure 2-3: The energy spectrum of the inner bremsstrahlung photons emitted in ^{6}He β decay. The vertical axis has an arbitrary unit.

In the low photon-energy regime, i.e., $k \ll m_p$, the correction associated with the virtual photon is [67]

$$g_v(\epsilon) = \frac{3}{2}\ln\left(\frac{\mu}{m_p}\right) + 3\overline{Q}\ln\left(\frac{\mu}{M_A}\right) + \mathcal{A} - \frac{3}{8}, \tag{2.54}$$

$$\mathcal{A} = \frac{1}{2}\beta\ln\left(\frac{1+\beta}{1-\beta}\right) - 1 + 2\ln\lambda\left[\frac{1}{2\beta}\ln\left(\frac{1+\beta}{1-\beta}\right) - 1\right] + \frac{3}{2}\ln m_p - \frac{1}{\beta}\left[\frac{1}{2}\ln\left(\frac{1+\beta}{1-\beta}\right)\right]^2 + \frac{1}{\beta}L\left(\frac{2\beta}{1+\beta}\right), \tag{2.55}$$

where $\beta = \sqrt{\mathcal{E}^2 - 1}/\mathcal{E}$, λ is an artificial "photon mass". It will be shown that $\ln\lambda$ is canceled out when calculating the sum of $g_v(\mathcal{E})$ and $g_b(\mathcal{E})$. $\overline{Q}$ is the average charge of the quarks involved in the transition:

$$\overline{Q} = \frac{1}{2}(Q_u + Q_d) = \frac{1}{6}. \tag{2.56}$$

$M_A = 1260$ MeV [68], and $\mu \sim 1$ GeV is the energy scale under which the EFT is valid. As $\ln(\mu/m_p) \sim 0$ and $\overline{Q}\ln(\mu/M_A) \sim 0$, $g_v(\mathcal{E})$ is calculated to be

$$g_v(\mathcal{E}) = \mathcal{A} - \frac{3}{8}\,, \tag{2.57}$$

which is consistent with the expression of $g_v(\mathcal{E})$ in Ref. [69].

The correction associated with the real photons, $g_b(\mathcal{E})$, has been derived by Gardner et al. [69], who introduced a quantity ΔE that is referred to as "energy resolution", such that for $k \leqslant \Delta E$,

$\mathcal{E} = W + k$ is recorded. Under the previous assumption that all the bremsstrahlung photons deposit all the energy in the detector, $\Delta E = k^{\max} = \mathcal{E} - 1$, the real photon radiative correction $g_b(\mathcal{E})$ can be expressed as [69]

$$\begin{aligned} g_b(\mathcal{E}) =& 3 - 2\left(1 - \frac{\tanh^{-1}\beta}{\beta}\right)\ln\left(\frac{2k^{\max}}{\lambda}\right) + \frac{\tanh^{-1}\beta}{\beta} + \frac{1}{\beta}L\left(\frac{2\beta}{1+\beta}\right) \\ & - \frac{1}{\beta}(\tanh^{-1}\beta)^2 + \frac{1}{\beta}I_k^{-1} - \frac{1}{\mathcal{E}\beta}I_k^0 + \frac{1}{2\mathcal{E}^2\beta}I_k^1 \\ & - 2\frac{\sqrt{(\mathcal{E}-k^{\max})^2-1}}{\sqrt{\mathcal{E}^2-1}} + \frac{2}{\beta}\ln\left(\frac{\mathcal{E}-k^{\max}-\sqrt{(\mathcal{E}-k^{\max})^2-1}}{\mathcal{E}-\sqrt{\mathcal{E}^2-1}}\right) \\ & + 2\ln\left[\frac{\mathcal{E}^2-1-\mathcal{E}k^{\max}+\sqrt{\mathcal{E}^2-1}\cdot\sqrt{(\mathcal{E}-k^{\max})^2-1}}{2(\mathcal{E}^2-1)}\right] \end{aligned} \tag{2.58}$$

where

$$I_k^{-1} = \int_0^{k^{\max}} dk\frac{1}{k}\ln\left(\frac{1+\beta_e}{1-\beta_e}\cdot\frac{1-\beta}{1+\beta}\right), \tag{2.59}$$

$$I_k^n = \int_0^{k^{\max}} dk\,k^n\ln\left(\frac{1+\beta_e}{1-\beta_e}\right), n = 0, 1, \tag{2.60}$$

$$\beta_e = \frac{p}{W} = \frac{\sqrt{(\mathcal{E}-k)^2-1}}{\mathcal{E}-k}. \tag{2.61}$$

Summing up $g_v(\mathcal{E})$ and $g_b(\mathcal{E})$ above gives the total radiative correction $g(\mathcal{E})$:

$$\begin{aligned} g(\mathcal{E}) =& 2\ln[2(\mathcal{E}-1)]\left(\frac{1}{\beta}\tanh^{-1}\beta - 1\right) - 2\ln\left[2(\mathcal{E}+1)\right] + \frac{3}{2}\ln m_p + \frac{13}{8} - \frac{2}{\beta}(\tanh^{-1}\beta)^2 \\ & + \frac{2}{\beta}L\left(\frac{2\beta}{1+\beta}\right) + \beta\tanh^{-1}\beta + \frac{3}{\beta}\tanh^{-1}\beta + \frac{1}{\beta}\left(2I_{-1} + \frac{I_1}{\mathcal{E}^2} - \frac{2I_0}{\mathcal{E}}\right), \end{aligned} \tag{2.62}$$

where

$$I^{-1} = \int_1^{\mathcal{E}}\frac{dE}{(\mathcal{E}-E)}\ln\frac{E+p}{\mathcal{E}(1+\beta)}, \tag{2.63}$$

$$I^n = \int_1^{\mathcal{E}} dE(\mathcal{E}-E)^n\ln(E+p), n = 1, 0. \tag{2.64}$$

Equation 2.62 is equivalent to the Eq. (19) obtained by Vogel in Ref. [70]. The derivation of Eq. 2.62 from Eq. 2.58 is shown in Sec. A.4 of the Appendix.

The closed forms of the integrals I_0, I_1, I_{-1} are given in Ref. [71]:

$$\frac{I_0}{\mathcal{E}} = \frac{1}{2}\ln\frac{1+\beta}{1-\beta} - \beta, \tag{2.65}$$

$$\frac{I_1}{\mathcal{E}^2} = \left(\frac{3}{8} - \frac{\beta^2}{8}\right)\ln\frac{1+\beta}{1-\beta} - \frac{3}{4}\beta, \tag{2.66}$$

$$I_{-1} = \frac{1}{2}\ln\frac{1+\beta}{1-\beta}\ln\left[2\left(1+\frac{1}{\sqrt{1-\beta^2}}\right)\right] - \frac{1}{4}\ln^2\frac{1+\beta}{1-\beta} - \mathrm{Li}_2\left(\frac{2\beta}{1+\beta}\right), \tag{2.67}$$

where

$$\mathrm{Li}_2(x) = \sum_{k=1}^{\infty}\frac{x^4}{k^2} \tag{2.68}$$

is the polylogarithm of the second order. $\mathrm{Li}_2(x)$ can be substituted by the Spence function $-L(x)$ as $\mathrm{Li}_2(x)$ is the approximate form of $-L(x)$ when $|x| \leqslant 1$. In addition, one can substitute Eqs. 2.65-2.67 into Eq. 2.62. This results in

$$g(\mathcal{E}) = \ln\frac{1+\beta}{1-\beta}\left\{\frac{2}{\beta}\ln\left[\frac{2\beta}{1+\beta}\right] + \frac{3}{8}\beta + \frac{7}{8\beta}\right\} - 2\ln\left(\frac{4\beta^2}{1-\beta^2}\right) + \frac{4}{\beta}\mathrm{L}\left(\frac{2\beta}{1+\beta}\right) + \frac{23}{8} + \frac{3}{2}\ln m_p, \tag{2.69}$$

which is equivalent to Eq. (25) in Ref. [71]. The derivation of Eq. 2.69 from Eq. 2.62 is shown in Sec. A.5 of the Appendix.

Equation (2.69) is the final expression of the radiative correction for measurements in which the β particles and photons are completely indistinguishable. It is equivalent to Eq. 2.62 which is identical to Eq. (19) in Ref. [70] as well as Eq. 2.58 which is derived from Eq. (9 - 13) in Ref. [69] with $\Delta E = k^{\max} = \mathcal{E} - 1$. With Eq. 2.69, the radiative correction for indistinguishable β particles and photons in ^{6}He decay is calculated and shown in Fig. 2-4. The size of the correction is on the order of 10^{-2}.

For comparison, Fig. 2-4 also includes the radiative correction for distinguishable β particles and photons calculated with Eq. 2.34, which is of the same order as the indistinguishable correction for the most relevant part of the spectrum. However, the slopes of the two corrections differ by a factor of 10. This difference is because in the distinguishable case, the real photons emitted during the decays reduce the measured energy of β particles in the detector, distorting the β-energy

spectrum by introducing a negative slope; while in the indistinguishable case, the emitted inner bremsstrahlung photons are collected back in the detector volume, which essentially cancels the effect of the possible energy loss due to the real photon emission. The remaining slope is mostly due to the change of β decay kinematics by the virtual photon exchange.

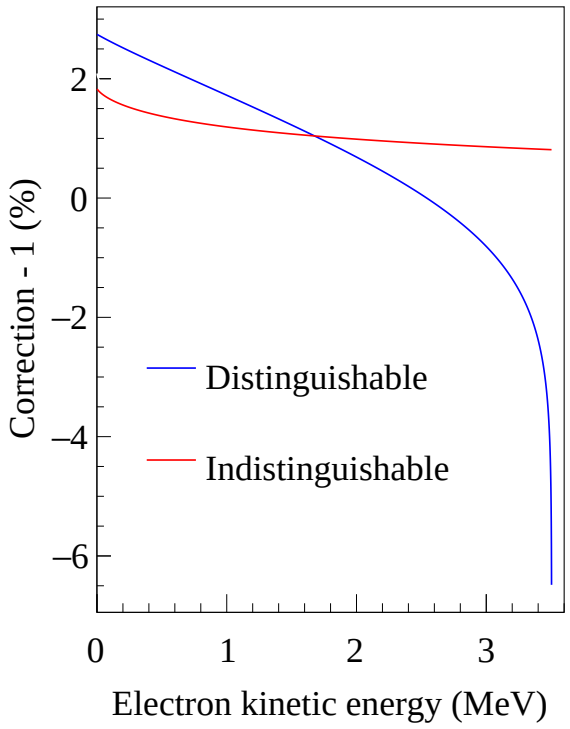

Figure 2-4: Radiative corrections for ^{6}He decay when the β particles and photons are distinguishable (blue) calculated with Eq. 2.34 and distinguishable (red) calculated with Eq. 2.69.

The calculation of the radiative correction for indistinguishable β particles and photons with Eq. 2.69 is based on the assumption that all the inner bremsstrahlung photons would fully stop in the detector. In reality, it is possible for the photons populating the high energy part of Fig. 2-3 to escape from the detector. Therefore the exact radiative correction for this work is Eq. 2.69 with an additional correction taking into account the escape of the inner bremsstrahlung photons from the detector. As the probability for a photon to escape depends on the photon energy and the geometry and material of the detector, the size of the correction needs to be determined with a detector simulation, which is part of the undergoing effort. The exact radiative correction is expected to be

between the two extreme cases represented by the two corrections in Fig. 2-4.

2.6 Summary of the Corrections to the β-energy Spectrum in ^{6}He Decay

Equipped with the studies in the previous sections, the size of each correction is calculated for ^{6}He decay. The results are shown in Fig. 2-5. The dominating correction is the Fermi function and the sizes of the rest of the corrections are all below 2%. The complete theoretical β-energy spectrum described by Eq. 1.26 is now determined.

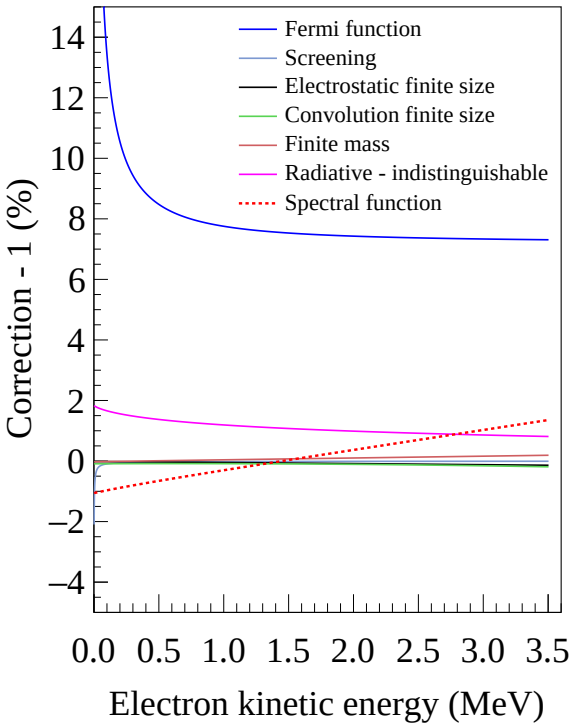

Figure 2-5: Calculated theoretical corrections to the β-energy spectrum in ^{6}He decay. The dashed line shows the expected spectral function.

2.7 Theoretical Uncertainty

The theoretical β-energy spectrum described by Eq. 1.26 depends on a few inputs determined from experiments. The experimental uncertainties of these inputs introduce an uncertainty to the theoretical spectrum. The dominant contributions to the theoretical β-energy spectrum are from the

^{6}Li radius R and the endpoint energy W_0. Specifically, R enters the Fermi function, the screening correction, the electrostatic finite size correction, the convolution finite size correction, and the $Z\alpha^2$ and $Z^3\alpha^3$ order radiative corrections; W_0 enters the α order radiative correction, the finite mass correction, the convolution finite size correction, and most importantly, the phase space factor.

2.7.1 Calculations of the Endpoint Energy and the Nuclear Radius

The calculation of the endpoint energy is performed following the procedure described in Ref. [72], which includes the recoil effect of the daughter nucleus:

$$W_0 = \frac{\Delta\left(1 + \frac{1}{2M\Delta}\right)}{1 + \frac{\Delta}{2M}}, \tag{2.70}$$

$$M = \frac{1}{2}(M' + M), \tag{2.71}$$

$$\Delta = M' - M, \tag{2.72}$$

where M' is the nuclear mass of the parent nucleus. The atomic masses used to calculate M' and M are taken from Ref. [73] for ^{6}He and Ref. [40] for ^{6}Li. The calculated W_0 for ^{6}He decay has the value of

$$W_0 = 7.8568 \pm 0.0001 \tag{2.73}$$

in the natural unit, where the uncertainty is from the uncertainties of the atomic masses of ^{6}He and ^{6}Li.

Among the different expressions of the nuclear radius available in literature, the most commonly used is

$$R_1 = r_0 A^{1/3}, \tag{2.74}$$

where $r_0 = 0.42587$ is a constant fitted from electron scattering experimental data [15]. For ^{6}Li, R_1 has the value of

$$R_1 = 5.7 \times 10^{-3} \tag{2.75}$$

in natural unit. Another widely used description of the radius is the Elton formula [74]:

$$R_2 = 0.0029A^{1/3} + 0.0063A^{-1/3} - 0.017A^{-1}. \tag{2.76}$$

For ^{6}Li, R_2 has the value of

$$R_2 = 5.9 \times 10^{-3} \tag{2.77}$$

in natural unit. Note that both Eq. 2.74 and Eq. 2.76 give general descriptions of the nuclear radius as a function of the mass number A, covering a wide range of isotopes. The calculated radius with Eq. 2.74 and Eq. 2.76 increases as a function of A. However, G. Ewald et al. [75] have measured the nuclear charge radius of Li isotopes and found that the rms charge radius of ^{6,7,8,9}Li decreases as the neutron number increases. Such details are not taken into account by Eq. 2.74 or Eq. 2.76. In this work, the description of the nuclear radius as a function of A is not relevant, rather, this work only needs one accurate radius of ^{6}Li. The measured rms nuclear charge radius of ^{6}Li is [76]

$$\left\langle r^2 \right\rangle^{1/2} = 2.589 \pm 0.039 \ \text{fm}. \tag{2.78}$$

The corresponding radius of the uniformly charged sphere converted to natural unit is [3]

$$R_3 = \sqrt{\frac{5}{3}} \left\langle r^2 \right\rangle^{1/2} \times 2.5896 \times 10^{-3}. \tag{2.79}$$

In the following text, R is used to represent R_3 and it has the value of

$$R = (8.66 \pm 0.13) \times 10^{-3} \tag{2.80}$$

in natural unit, where the uncertainty is from $\left\langle r^2 \right\rangle^{1/2}$.

2.7.2 Estimation of the Theoretical Uncertainty

The theoretical uncertainties, i.e., the impacts of the uncertainties of the theoretical β-energy spectrum on the observables, are estimated here. This was done by estimating the sensitivities of b_{WM} and b_{GT} to the uncertainties of the ^{6}Li radius and the endpoint energy. For illustration, the sensitivity of b_{WM} to the radius is determined with the following procedure:

1. Calculate the theoretical β-energy spectrum with the radius and endpoint energy equal to the central values of R in Eq. 2.80 and W_0 in Eq. 2.73; and with $b_{WM} = 68.22$, $b_{GT} = 0$. Two parameters associated with the calibration of the detector are introduced in the spectrum: an offset and a gain. Details of the offset and the gain are discussed in Chapter 6.

2. Construct a fit function with the radius equal to $R + \delta R$ and the endpoint energy equal to W_0, and with b_{WM} and b_{GT} being parameters in the fit function. The offset is fixed at the initial value and the gain is a free parameter.

3. The spectrum calculated in Step 1 is fitted by the function constructed in Step 2 using the χ^2 method with the "SM" fit, i.e., b_{GT} was fixed to 0 and b_{WM} was left as a free parameter along with the overall normalization and the gain. The offset is fixed at the initial value. The fitted b_{WM} is labeled as $b_{WM}(R + \delta R, W_0)$.

4. Set the radius in Step 2 at $R - \delta R$ and repeat Step 3. The fitted b_{WM} is labeled as $b_{WM}(R - \delta R, W_0)$.

5. The uncertainty of b_{WM} arising from δR can be estimated by

$$\delta b_{WM} = \frac{|b_{WM}(R + \delta R, W_0) - b_{WM}(R - \delta R, W_0)|}{2}. \tag{2.81}$$

Similar to the sensitivity of b_{WM} to the radius, the sensitivity of b_{WM} to the endpoint energy is determined with the endpoint energy in Step 2 and Step 4 fixed at $W_0 + \delta W_0$ and $W_0 - \delta W_0$, respectively, and with the radius fixed at the central value. In addition, similar to the sensitivities of b_{WM}, the sensitivities of b_{GT} can be determined by performing "BSM" fits, i.e., fix b_{WM} to 68.22 and leave b_{GT} as a free parameter along with the normalization and the gain.

The results from the above procedure are summarized in the first two rows of Table 2-2, where δW_0 and δR have comparable impacts on b_{WM}, whereas for b_{GT}, δW_0 has a larger impact than δR. The total uncertainties of b_{WM} and b_{GT} are shown in the third row of the table. The theoretical uncertainty of b_{WM} is a factor of 10 smaller than the uncertainty of the CVC value of b_{WM} (0.79, see Eq. 1.32). The theoretical uncertainty of b_{GT} is a factor of 100 smaller than the precision goal ($\mathcal{O}(10^{-3})$).

In the actual analysis, the theoretical β-energy spectrum is convolved with the detector response, including the detector simulations with Geant4 and the subsequent convolution with the energy resolution, and then fitted to the experimental data. The actual theoretical uncertainties will be

Table 2-2: Sensitivities of b_{WM} and b_{GT} to the uncertainties of the ^{6}Li radius and the endpoint energy.

	δb_{WM} (10^{-2})	δb_{GT} (10^{-5})
δR	5.9	-1.8
δW_0	-5.7	2.4
total	8.2	3.0

determined by the full analysis. Therefore the values estimated in Table 2-2 are the upper limits of the theoretical uncertainties of b_{WM} and b_{GT}.

CHAPTER 3

DESCRIPTION OF THE EXPERIMENT

Precision measurement of the β-energy spectrum requires the minimum distortion to the measured spectrum from the true spectrum. The measured spectrum could be distorted by any instrumental effect that prevents the β particles from depositing all the energy in the detector. Several instrumental challenges are discussed at the beginning of this chapter, followed by a new instrumental technique proposed to avoiding these instrumental effects. An experiment performed using this new technique is described. Sample data from a typical experimental run are provided.

3.1 General Instrumental Challenges

Two of the common instruments to study the β-energy spectrum are a magnetic spectrometer [77] and a detecting system with the β emitter located outside the active volume of the detector [12]. In such measurements, some instrumental effects have great impacts on the detector response and distort the measured β-energy spectrum [12]. These effects are described below.

- **The backscattering** occurs when a β particle enters the surface of a material and undergoes sufficient deflections so that it reemerges from the surface through which it entered [78]. It is most pronounced for electrons with low incident energy and absorbers with high atomic number. The backscattered electrons do not deposit all the energy in the medium and therefore can have a significant effect on the detector response, resulting in a big distortion to the measured spectrum [12]. Such a distortion makes the backscattering one of the most severe instrumental effects in the detection of β particles.

- **The outscattering** occurs when an electron leaves the edge of the detector after multiple Coulomb scatterings. The electron carries away energy when it leaves the detector volume, resulting in partial energy deposition.

- **The dead layer** is a surface layer on the active volume that the incident electrons must pass

before reaching the active volume. This is a disadvantage because a portion of the electron energy is lost before reaching the active volume.

3.2 Calorimetric Technique

The instrumental effects discussed above can be eliminated by confining the β decay source inside the active volume of the detector. The ^{6}He decays inside of the detector, emitting β particles. The detector encloses the whole 4π solid angle of the decay products and absorbs the energy of β particles. The ^{6}He decay source can be sent into the detector by implanting a ^{6}He ion beam into the detector. If the beam is implanted deep enough so that the decay source is fully enclosed in the detector volume, no β particles would be able to escape.

3.3 Beam Conditions

3.3.1 Beam Facility

The ^{6}He beam was produced at the Coupled Cyclotron Facility shown in Fig. 3-1 located at National Superconducting Cyclotron Laboratory (NSCL) at Michigan State University (MSU). A beam of $^{18}O^+$ stable ions from the electron cyclotron resonance ion source was injected into the K500 cyclotron and accelerated to an energy sufficient to strip most of the remaining electrons in a foil positioned near the center of the K1200 cyclotron [79]. The highly stripped ions were then accelerated to an energy of 120 MeV per nucleon. The primary beam impinged on a 2.54 g/cm^2 thick Be target, where ^{6}He was produced from fragmentation reactions. The fragments were separated by the A1900 projectile fragment separator [80][79], extracting a ^{6}He secondary beam at the energy of 76 MeV per nucleon, which was directed to the experimental area. In the experimental area, the ^{6}He ions exited from the beam pipe through a 75 μm thick Zr vacuum window and were implanted into a CsI(Na) or a NaI(Tl) detector. Details of the detectors are discussed in Sec. 3.4.

It is important to control the implantation of the ^{6}He beam into the detector such that the detector volume fully encloses the range of the β particles from the decays (6 mm in CsI). We have placed an Al degrader 1 m upstream from the detector, as shown in Fig. 3-2. The degrader can be

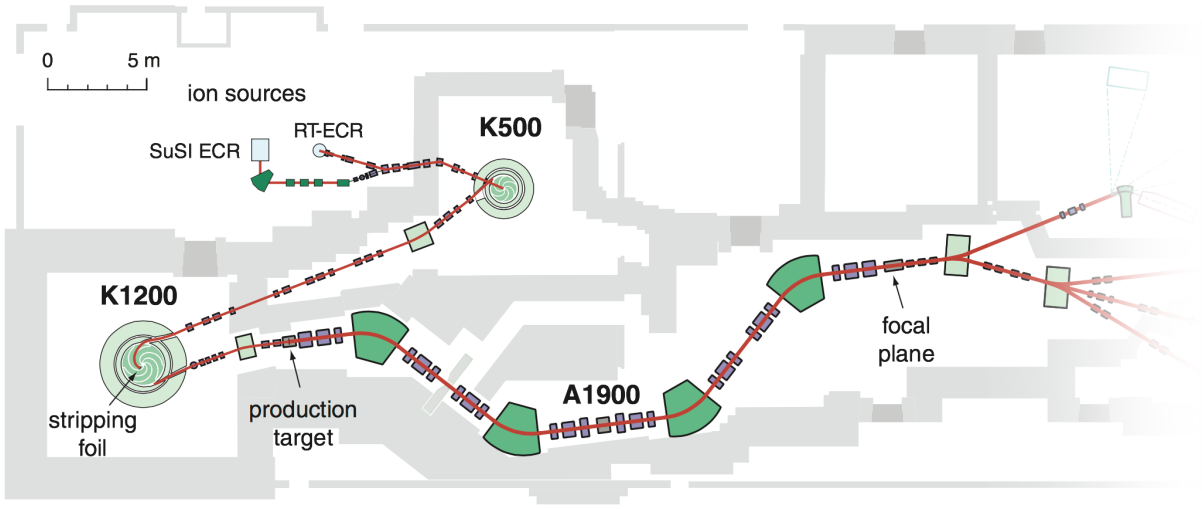

Figure 3-1: A schematic layout of the beam facility at National Superconducting Cyclotron Laboratory.

rotated along the vertical axis. The angle of the rotation determines the effective thickness passed through by the beam to control the beam energy. During regular measurements, the energy of the implanted beam was 46 MeV per nucleon corresponding to a degrader angle of 0°, i.e., when the effective thickness of the degrader was the lowest and the implantation depth was the highest.

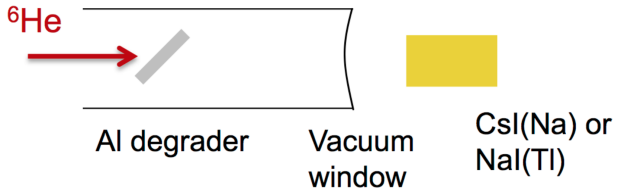

Figure 3-2: A cartoon of the top view of the setup. The secondary ^{6}He beam (red) of 76 MeV per nucleon passes through a degrader (gray). The beam was decelerated by the degrader down to 46 MeV per nucleon and was implanted into a CsI(Na) or NaI(Tl) detector (yellow).

3.3.2 The Beam Geometry and the Calculated Range

The transverse profile of the implanted beam in the detector was measured from an image taken by a digital night vision camera which has high photosensitivity in low-light environments. The beam

was cut by the A1900 focal plane slits that were set to 2×1.5 mm^2. The beam is magnified during the transport and produced a rectangular image of 4.5×4.6 mm^2 recorded by the camera.

The longitudinal profile of the implanted beam in the detector was determined with beam transport calculations using the LISE++ code [81]. Figure 3-3 shows the range distributions of the implanted beam in the CsI and the NaI detectors while the angle of the degrader with respect to the beamline is 0°. The range, defined as the distance from the surface where the beam enters, has a mean value of 1.23 cm for CsI and 1.48 cm for NaI. Figure 3-4 shows the range distributions in CsI while the angle of the degrader with respect to the beamline is at 0°and 42°. The smaller angle of the degrader gives a lower effective thickness along the beamline, thus a higher energy of the implantation beam, resulting in a larger range. The widths of the distributions resulting from the range straggling are discussed in the next subsection. For any case shown in Figs. 3-3 and 3-4, the deposited ^{6}He ions are fully enclosed by the detector.

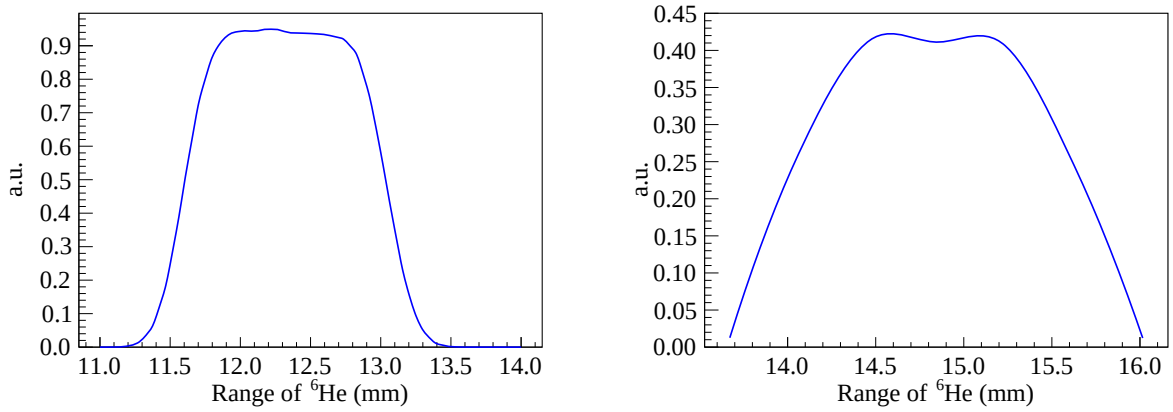

Figure 3-3: Range distributions of the implanted ^{6}He in CsI (left) and NaI (right) calculated with the LISE++ code. The angle of the degrader with respect to the beamline is 0°.

3.3.3 Measurement of the Beam Range

A measurement of the beam range was performed during the experiment. The range distribution of the ^{6}He ions can be determined by passing the beam through different thicknesses of the degrader and measuring the ratio of the transmitted to the incident ions. We measured the counts in the

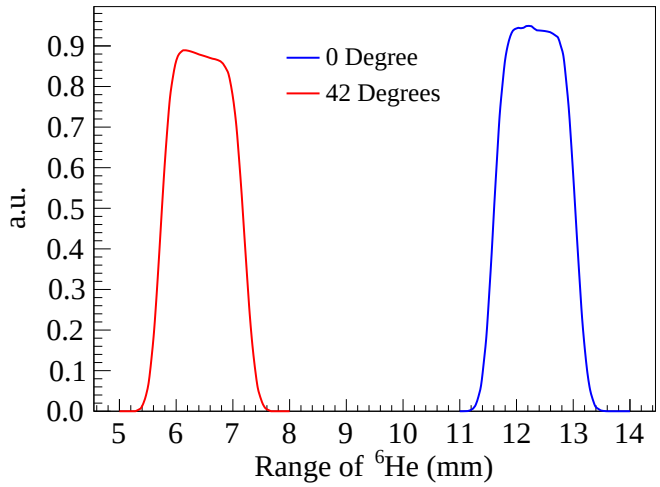

Figure 3-4: Range distributions of the implanted ^{6}He in CsI while the angle of the degrader with respect to the beamline is at 0°(blue) and 42°(red).

CsI(Na) detector while the degrader was at fourteen different angles with respect to the beamline and divided each count by the count measured without the degrader. This ratio, or transmission, is shown as the range number-distance curve [82] in Fig. 3-5. From 0 mm to 30 mm, the ratio decreases slowly because of the increasing nuclear reactions between the beam and the degrader. In the thickness range of 30-35 mm, the ratio suddenly drops to zero over a spread of thickness rather than a single value of thickness because when the implantation beam enters the detector, the energy loss is not continuous but statistical in nature. The absolute value of the derivative of the ratio, known as the range straggling curve, is shown in Fig. 3-5, where the range of the ^{6}He ions is then a statistical distribution centered about a mean value rather than being a constant [82].

The measured range straggling curve can be compared with the beam transport calculations by LISE++. The results are shown in Fig. 3-6, where the red curve is from measurements and the blue curve is from LISE ++ calculations. The spread of the range distribution is higher from the calculations than from the experiments. Similar overestimates have been seen in Ref. [83], where the range straggling has been determined from experiments and TRIM95 [84] calculations. The Table 1 in Ref. [83] provided the range straggling values for helium isotopes in three scintillators: GsO(Ce), CsI(Tl), and BGO. The TRIM95 code systematically gives larger range straggling values

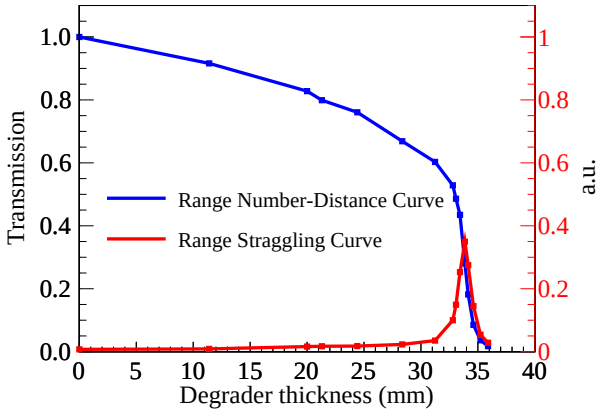

Figure 3-5: Blue: the ratio of the transmitted to the incident ^{6}He ions versus the effective thickness of the degrader. Red: the corresponding range distribution of the ^{6}He ions.

than the experiments. Specifically, the range straggling of ^{6}He in CsI(Tl) at 258 MeV determined from experiments and TRIM95 are 2.2% and 4.0%, respectively.

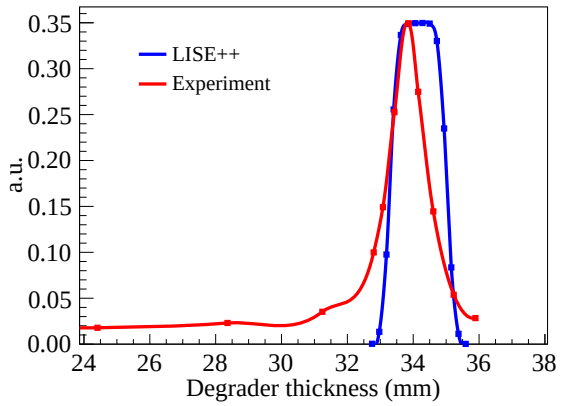

Figure 3-6: The range straggling curve of the ^{6}He beam from calculations using LISE++ (blue) and measurements (red).

3.3.4 Beam Purity

The beam purity is determined by measuring beam energy without a degrader shown in Fig. 3-7. The left panel is the beam energy measured in the CsI (Na) detector in channel (chan), which is an energy unit related to the data acquisition (DAQ) system. The HV of the detector was at +300 V.

The dominant feature is the main peak with a narrow width. Details of the energy distribution are shown in the right panel in the log scale. Specifically, the tail in the energy range between 0-2000 chan is due to the beam-induced reactions in the detector; the short peak at 4000 chan and the data in the energy range of 2400-4000 chan are due to the pile-up in the DAQ system. One possible contaminant could be ^{8}Li with a half-life of (838.4 ± 0.36) ms [85], which is very close to the half-life of ^{6}He [45]. If ^{8}Li was present, its energy is expected to be the energy of ^{6}He times 8/6, corresponding to a channel number roughly 4/3 of the channel number of ^{6}He. A dashed line in the plot marks the expected channel number of ^{8}Li if it was present, where no visible traces of ^{8}Li are seen. From this spectrum, the level of contaminants was deduced to be lower than 2×10^{-5}.

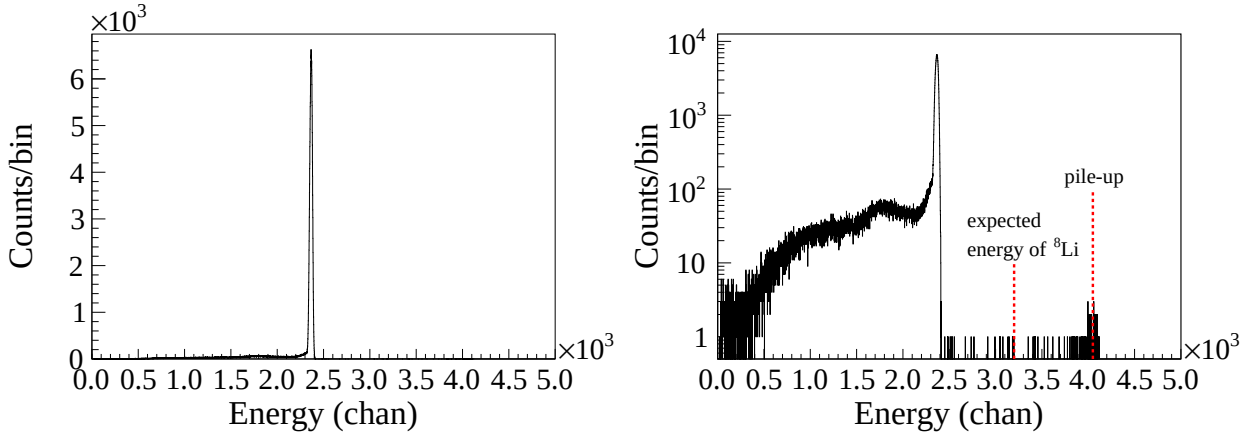

Figure 3-7: Energy of the ^{6}He beam measured in the CsI (Na) detector without a degrader in linear (left panel) and log (right panel) scales. The first dashed line in the right panel indicates the expected energy of the ^{8}Li contaminant if it was present; the short peak at 4000 chan marked by the second dashed line and the data in the energy range of 2400-4000 chan are due to the pile-up in the DAQ system.

3.3.5 Beam Cycles

During the measurement, the beam was chopped periodically by dephasing the radio-frequency signal of one of the cyclotrons. This forms implantation and decay cycles. Each cycle consists of a 2.5 s implantation interval with the beam on, referred to as the beam-on interval, and a subsequent decay/measurement period with the beam off, referred to as the beam-off interval. The beam-off

period is 10 s for the CsI(Na) detector and 15 s for the NaI(Tl) detector. The long beam-off intervals were chosen for background estimations discussed in Chap. 9.

3.4 Detectors

As mentioned earlier, the ^{6}He beam was implanted into two types of scintillating detectors, a CsI(Na) detector, and a NaI(Tl) detector. The CsI(Na) detector is a $9.8 \times 5 \times 5$ cm^3 rectangular cuboid scintillator from the CAESAR array [86] manufactured by ScintiTech. The NaI(Tl) detector is a $\varnothing 7.6 \times 7.6$ cm^2 cylindrical scintillator, where the scintillation crystal is manufactured by Saint-Gobain (Bicron). Figure 3-8 shows the setup of the NaI(Tl) detector on the beamline. The setup for the CsI(Na) detector is shown in Fig. 3-9, where the CsI(Na) detector was surrounded by a shield constructed with lead bricks to reduce the ambient background during the regular measurement runs. In addition, an OR120 Ge semiconductor detector shown in Fig. 3-10 was placed next to the beamline to measure the γ rays induced by the beam in the detectors.

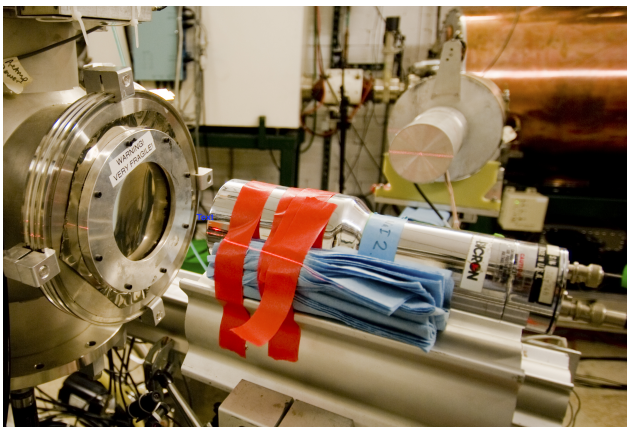

Figure 3-8: The setup of the NaI(Tl) detector on the beamline. The ^{6}He ions exiting from a beam pipe through the 75 μm thick Zr vacuum window (left) were implanted into the NaI(Tl) detector (right) aligned along the beamline.

3.5 Data Acquisition System

The DAQ system of this experiment was based on the implementation of the Digital Data Acquisition System (DDAS) developed at the NSCL [87]. Two Pixie-16 digitizing modules manufactured

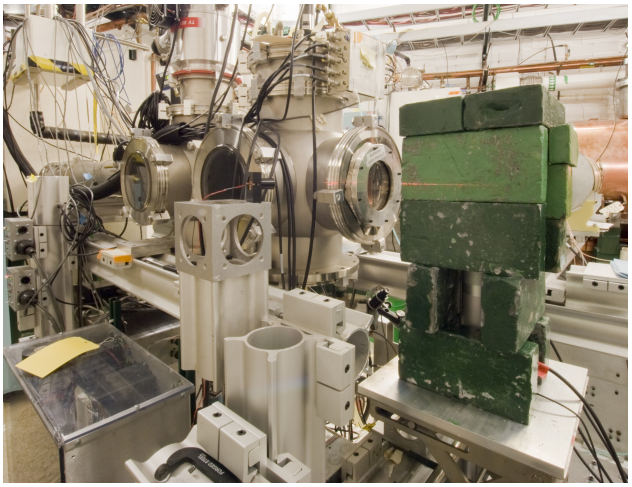

Figure 3-9: The setup of the CsI(Na) detector on the beamline. The ^{6}He ions exiting from the beam pipe through the 75 μm thick Zr vacuum window (left) were implanted into the CsI(Na) detector (right) aligned perpendicular to the beamline. The CsI(Na) detector is surrounded by lead bricks (green).

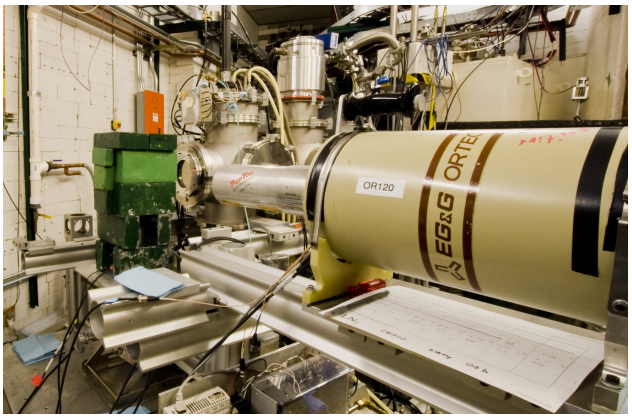

Figure 3-10: The setup of the OR120 Ge semiconductor detector mounted next to the beamline.

by XIA LLC were used. Each Pixie-16 module is capable of digitizing signals at a rate of 100 MHz. The signals from both the CsI(Na) and the NaI(Tl) detectors were sent to the first module, and the signal from the Ge detector was sent to the second module. Both modules received three additional signals associated with the beam-on start, the beam-off start, and a 100 Hz pulser. The digitizers provided the information of the time stamp and the energy of each signal sent to each channel in the two modules, where the energy was converted using a trapezoidal filter [87].

For each incoming signal, the waveform was digitized by a Pixie-16 module. Once the waveform

was above a certain threshold, it was processed by the Field-Programmable Gate Arrays (FPGAs) in the Pixie-16 system, and the information was recorded. The FPGAs provide an estimate of the energy of each signal, during which no other triggers were accepted. If multiple signals took place too close in time to each other, their waveforms would overlap, and the overlapping signals would be reported as one signal. The energy of the first signal would, therefore, be overestimated, and the reported value would be between the energy of the first signal and the sum of the overlapping signals. This is the origin of the pile-up in the DAQ system mentioned in Fig. 3-7. The contribution of the pile-up has a great impact on the measured β-energy spectrum and is discussed in the data analysis in Chaps. 4 and 8.

3.6 Data Collections

3.6.1 Regular Measurements

The regular measurements consisted of 22 runs with the CsI(Na) detector and 30 runs with the NaI(Tl) detector. Most of the runs were about one hour long. The experimental conditions for the two detectors are summarized in Table 3-1, including the high voltage, the primary beam intensity, the lengths of beam-on and beam-off time intervals, and the number of collected implantation-and-decay cycles.

Table 3-1: Experimental conditions for the CsI(Na) and the NaI(Tl) detectors during the regular measurements.

Detector	HV (V)	Beam intensity (μA)	Implantation time (s)	Decay time (s)	Collected cycles
CsI(Na)	+860	1.6±0.1	2.5	10	5760
NaI(Tl)	+1000	1.2±0.1	2.5	15	4114

3.6.2 Calibration Runs

Detector calibration measurements with the ^{60}Co and the ^{137}Cs γ sources were performed before, during, and after the experiment. Most of the measurements lasted for a few minutes. The voltage settings were the same as in Table 3-1.

3.6.3 Background Measurements

This experiment involves two types of background: the ambient background and the beam-induced background. The ambient background was measured before and after the beam time, with and without the lead shield around the CsI(Na) detector. It was observed that the ambient background event rate is reduced by 13% with the presence of the lead shield. Therefore for all regular runs collecting β decay events with the CsI(Na) detector, the detector was placed in the lead shield. The beam-induced background was measured in four runs between the regular runs with the CsI(Na) detector. The obtained energy spectra have both the signal (β decay) events and the background events. These measurements provide valuable inputs to the background analysis in Chap. 9.

3.6.4 Gain Drift Test

To test the drifts of the system gain, a dedicated experimental run was performed with a ^{137}Cs γ source placed next to the CsI(Na) detector during the beam implantation. The energy spectrum of this run is then a superposition of the β-energy spectrum from ^{6}He and the γ-energy spectrum from the ^{137}Cs source. The shift of the full-energy peak in the γ spectrum would indicate a possible gain drift during the ^{6}He decay. The results are discussed in Chap. 7.

3.7 Sample Data

The sample data collected in a typical run with the CsI(Na) detector is shown in Fig. 3-11. The left panel shows a two-dimensional histogram of the registered time versus deposited energy during the beam-off time intervals (2.5-12.5 s in each beam cycle) collected in an one-hour run. The projection of the two-dimensional histogram on the energy axis is a β-energy spectrum, which is shown in the right panel of Fig. 3-11 after subtracting events in the 9.43-9.61 s interval from events in the 3.43-3.61 s interval, see discussions about the background subtraction in Chap. 9. The structure above 5200 chan are due to the pile-up in the DAQ system. The analysis of the measured β-energy spectrum is the focus of the rest of the thesis.

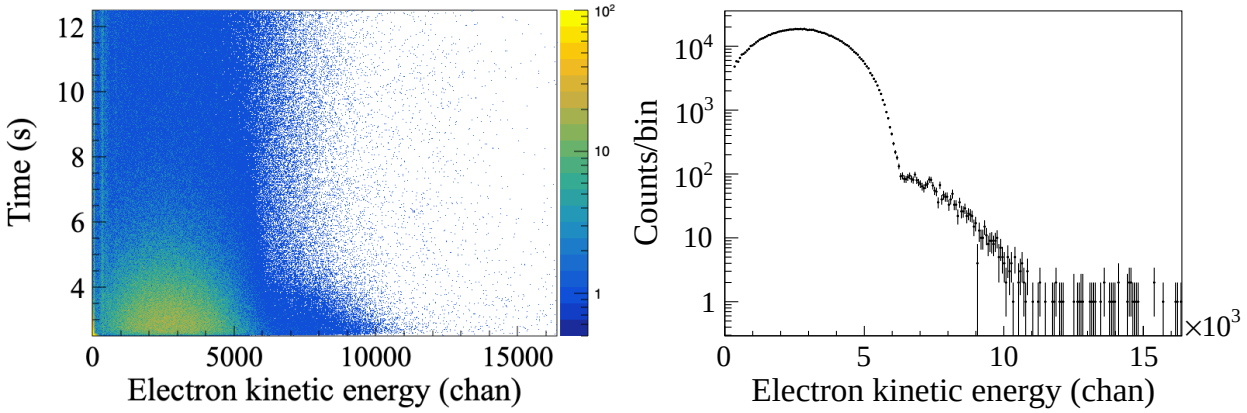

Figure 3-11: Left panel: a two-dimensional histogram of the registered time versus deposited energy during the beam-off time intervals collected in an one-hour run with the CsI(Na) detector. Right panel: a background-subtracted β-energy spectrum measured in the CsI(Na) detector during the beam off period.

CHAPTER 4

BIG PICTURE OF THE ANALYSIS

The rest of the thesis focuses on analyzing the shape of the measured β-energy spectrum in ^{6}He decay. As the effect of the CVC value of b_{WM} on the spectrum is small, and the effect of the SM value of b_{GT} on the spectrum is zero, dedicated study of each systematic effect is performed focusing on its impact on the shape of the spectrum. An overview of the data analysis is illustrated in Fig. 4-1, where the top row focuses on building an accurate and precise function describing the measured β-energy spectrum, and the bottom row focuses on the experimental data; the function is then fitted to the data to extract the observables.

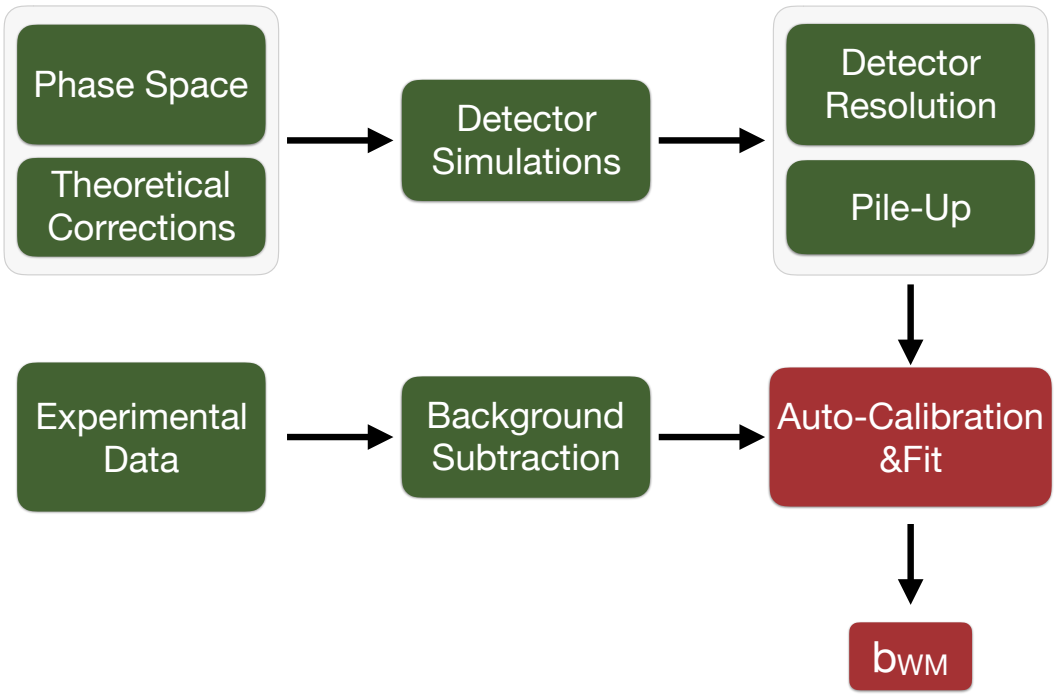

Figure 4-1: Overview of the data analysis steps in this experiment.

To analyze the measured β-energy spectra (Chap. 3), an accurate theoretical description of the β-energy spectrum, which is a product of the phase space factor (Chap. 1) and the theoretical

corrections (Chap 2), is calculated and taken as the input for the detector simulations with the Geant4 Monte Carlo toolkit (Chap. 5) to take into account part of the detector response [17]. The output of the detector simulation, the absorbed spectrum shown in Fig. 4-2 in red, is convolved with a Gaussian to take into account the detector energy resolution, resulting in the convolved spectrum in green, which is used to calculate a pile-up spectrum in black. A superposition of the convolved spectrum and the pile-up spectrum expressed in channel (chan) after the energy calibration (Chaps. 6 and 7), multiplied by the spectral function and $(1 + b_{GT}/W)$ in Eq. 1.26, was used as a fit function that describes the shape of the measured β-energy spectrum. The fit function has four free parameters: an observable (b_{WM} or b_{GT}), a calibration parameter (gain), a normalization factor for the convolved spectrum, and a normalization factor for the pile-up spectrum.

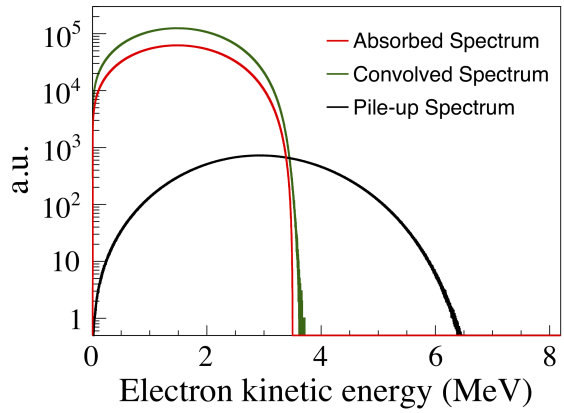

Figure 4-2: The shapes of the energy spectra used in the fit function.

The measured spectra include both the β-decay events and the background events. The spectra after background subtractions (Chap. 9) are fitted by the fit function to extract the observables with a single-step auto-calibration and fit method [88] (Chap. 6). The observables can be extracted without bias in the fits (Chap. 8).

The analysis is currently entering the final stage and is expected to provide the first measurement of the weak magnetism form factor in ^{6}He decay, the first direct measurement of the Fierz interference term in Gamow-Teller decay, and a new constraint on the tensor interactions beyond the SM.

CHAPTER 5

DETECTOR SIMULATIONS

This chapter simulates the responses of the CsI(Na) and NaI(Tl) detectors to the β-energy spectrum. Two approaches were taken: 1) simulating the detector responses to monoenergetic electrons and parameterizing the response functions as a function of energy; 2) directly simulating the energy spectra absorbed in the detectors using the theoretical spectrum as a continuous input source. For both approaches, the photon production and the energy absorption fraction were studied. In addition, the systematic uncertainties associated with the detector simulations were estimated.

The response function of the detector is defined as the energy spectrum observed in the detector as a response to a given monoenergetic radiation. After eliminating the backscattering effect in Chap. 3, there is another instrumental effect that prevents the electrons from fully depositing the energy in the detectors. Some electrons in the detectors may emit bremsstrahlung photons as they decelerate, and these photons may escape from the detector and carry away energy. This effect produces a low energy tail in a response function, distorting the observed β energy spectrum in the detectors. As the probability for a photon to escape depends on the photon energy and the geometry and material of the detector, this effect needs to be studied with detector simulations. The simulations were performed using the Geant4 toolkit [89].

In practice, because of the statistical nature of the interaction between the electrons and the detector, the energy deposited by a monoenergetic source is dominated by a Gaussian distribution instead of a Delta function. The standard deviation of the Gaussian is associated with the energy resolution of the detector. The finite detector resolution is taken into account by convolving the absorbed energy spectrum simulated with Geant4 with the Gaussian distribution. A parametrization of the response function consisting of a Gaussian peak and a low energy tail is provided, but will not be used in the analysis. The second approach mentioned above was chosen when analyzing the β-energy spectrum.

5.1 Simulation Conditions

Electrons lose energy in the detectors by atomic collisions and bremsstrahlung radiation. Collisions include the ionization and excitation processes which can produce Auger electrons and X-rays. These processes are incorporated in the Geant4 toolkit. In this work, the simulations were performed with the version 10.3.0 of Geant4. The majority of the work in this chapter has been published in Ref. [17].

5.1.1 Particle Source and Detector Configurations

The geometries of the electron sources and the detectors used in the simulations are shown in Fig. 5-1. They correspond to the actual experimental conditions described in Chapter 3. Specifically,

- The geometries of the detectors are a $9.8 \times 5 \times 5$ cm^3 rectangular cuboid for the CsI(Na) detector and a $\text{Ø}7.6 \times 7.6$ cm^2 cylinder for the NaI(Tl) detector.
- The geometry of the electron sources are described by a rectangular cuboid with the dimensions of $4.6 \times 4.5 \times 1.5$ mm^3 in the CsI(Na) detector and $4.6 \times 4.5 \times 1.7$ mm^3 in the NaI(Tl) detector.
- In the CsI(Na) detector, the center of the electron source is located 2.44 cm from the top and 1.23 cm from the front face. In the NaI(Tl) detector, the center of the source is on the cylindrical axis and is 1.48 cm from the front face.

The absorber materials implemented in the simulations are CsI for the CsI(Na) detector and NaI for the NaI(Tl) detector. The CsI and NaI materials were constructed with the predefined materials in the Geant4 NIST database: `G4_CESIUM_IODIDE` and `G4_SODIUM_IODIDE`.

The primary particle source was defined with the `G4GeneralParticleSource` (GPS) class in Geant4 toolkit. GPS allows the specifications of the spectral, spatial, and angular distribution of the primary particles. In this work, electrons with an isotropic angular distribution were generated and uniformly distributed within the volumes of the sources inside the detectors shown in Fig. 5-1.

Two types of energy distributions were implemented in this study: a list of monoenergetic primary electron sources in the energy range of 0-4 MeV and a continuous theoretical β-energy spectrum in ^{6}He decay including the phase space factor and the theoretical corrections.

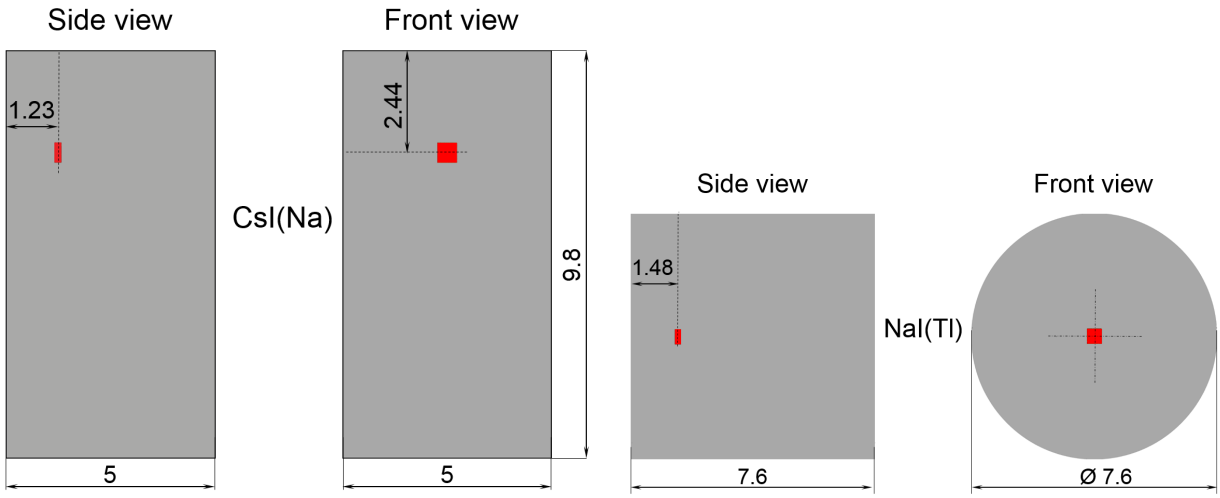

Figure 5-1: Left panel: geometry of the CsI(Na) detector (gray) and position of the electron source (red) used in the simulations. Dimensions are in cm. Right panel: geometry of the NaI(Tl) detector (gray) and position of the electron source (red) used in the simulations. (Published in Ref. [17].)

5.1.2 Geant4 Physics Constructors

The physical processes of interest are electromagnetic and are taken into account by the electromagnetic physics constructors in Geant4, where the electromagnetic physics lists are implemented. The constructors can provide different CPU performances, and some constructors are adapted to low-energy processes. In addition, these physics constructors may differ in the production and absorption of photons, resulting in different response functions. To study the possible differences among the simulations, this work has included the constructors in Table 5-1.

The Livermore (liv), Penelope (pen) and Option4 (opt4) constructors are optimized for low-energy processes, among which the Option4 constructor is considered "using the most accurate standard and low-energy models" according to an on-line documentation [90]. The Standard

Table 5-1: Physics constructors in Geant4 applied in the simulations.

Physics constructors	Denomination
`PhysListEmStandard`	Standard
`G4EmLivermorePhysics`	Livermore
`G4EmPenelopePhysics`	Penelope
`G4EmStandardPhysics_option4`	Option4

constructor is not specially optimized for low-energy processes and is included here to compare its results with the other constructors'. In this work, the Standard constructor is taken from Ref. [91].

For each physics constructor, the models describing the electromagnetic processes are discussed in the Geant4 Physics Reference Manual [92]. In particular, the bremsstrahlung process in the Standard, Livermore and Penelope constructors is described by `G4SeltzerBergerModel`, `G4LivermoreBremsstrahlungModel` and `G4PenelopeBremsstrahlungModel`, respectively. An inspection of the source code indicates that Option4 uses `G4SeltzerBergerModel` for the electron energy range considered in this work. Note that these constructors are not mutually independent, as the Option4 constructor is using the same bremsstrahlung model as Standard in this work. In addition, Livermore and Penelope use common data libraries such as the Evaluated Electron Data Library [93], according to the Physics Reference Manual [92].

5.1.3 Geant4 Parameters

Some parameters control the physical processes in each physics constructor. The default parameters in each physics constructor have been adapted in this work. Specifically, the range factor parameter, F_R, and the geometry factor parameter, F_G, affect the multiple scattering process [94]. Their default values in each physics constructor are summarized in Table 5-2.

Table 5-2: Default values of the range factor parameter and the geometry factor parameter in each physics constructor.

	F_R	F_G
Standard	0.04	2.5
Livermore	0.02	2.5
Penelope	0.02	2.5
Option4	0.02	2.5

The event tracking is controlled by a parameter referred to as the range cut, or "cut for secondaries". It is worth clarifying that the only kind of primary particle in the simulation is the primary electron source. All the photons and electrons produced by the primary electrons are considered secondary particles. The range cut controls the creation of secondary particles in the following way: if a primary particle has enough energy to produce a secondary particle offspring that can travel over a distance greater or equal to the range cut in a given material, the secondary particle is created. Otherwise, the energy of the primary particle is absorbed locally. In this work, unless stated otherwise, the range cut values in the CsI and NaI detectors are 5.0 μm and 5.7 μm, respectively. These values correspond to an energy of 20 keV for the primary electrons.

5.1.4 Visualization

The simulation process can be visualized with the OpenGL event display. Figure 5-2 illustrates a simulation with the CsI detector, where 10^3 monoenergetic electrons of 1 MeV were generated. The trajectories of the particles are color-coded with red representing electrons and green representing photons. All the electrons stop inside the detector while a small fraction of photons escapes. This simulation was performed applying the Standard physics constructor.

5.2 Discrete Monoenergetic Electrons

In this section, the production and the absorption of photons for the monoenergetic primary electron sources are studied. For illustration, Fig. 5-3 shows the photon spectrum produced by 2×10^7 electrons of 3.5 MeV in the CsI detector. The dominant contributions are from bremsstrahlung photons, a majority of which populate the low energy range of the spectrum. The peak at 0.511 MeV is due to positron annihilations following pair productions by the bremsstrahlung photons above 1.022 MeV. In addition, characteristic X-ray lines are produced under 50 keV, with details shown in the insert to Fig. 5-3. The X-ray lines correspond to the Kα1, Kα2, Kβ1, and K-edge lines for I and Cs and the L-lines at lower energy. This simulation was performed with the Standard constructor, and similar simulations with the other three constructors were also performed. The

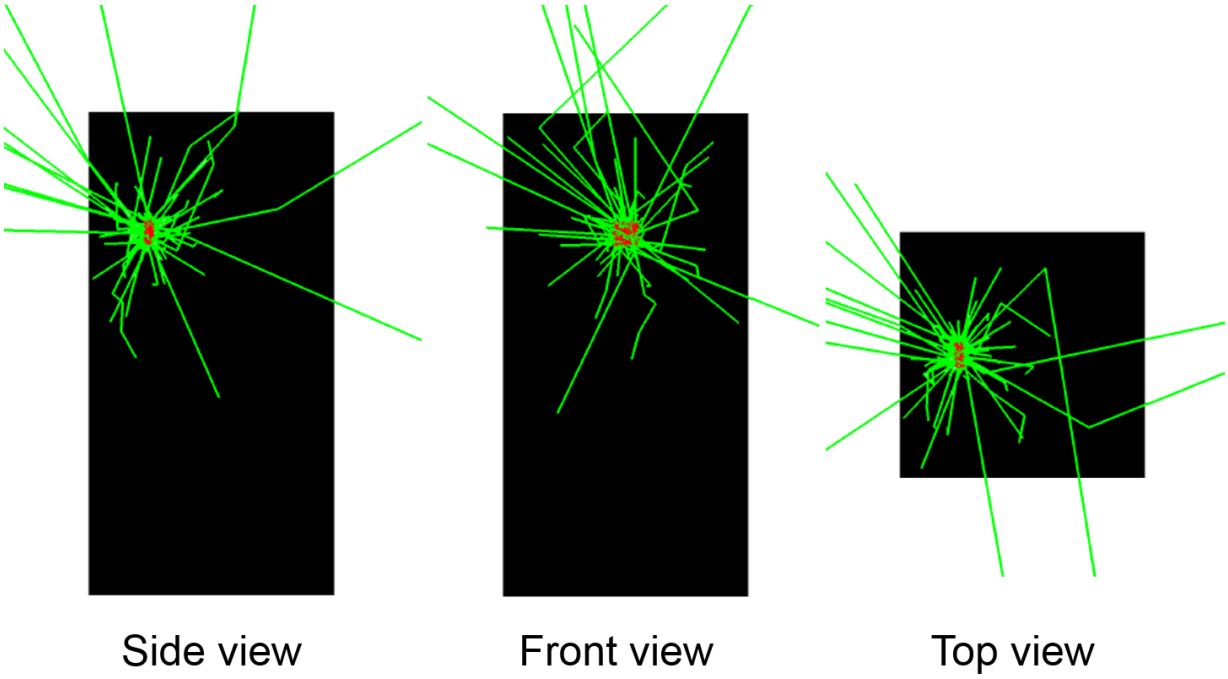

Figure 5-2: Visualization of a Geant4 simulation with the CsI detector. 10^3 monoenergetic electrons of 1 MeV were generated. Left: side view of the detector; Middle: front view; Right: top view. The green lines indicates that a fraction of the photons escape from the detector. (Published in Ref. [17].)

intensity (I) of the X-ray peaks produced by the constructors show a relative difference of up to 20%, with $I_{\text{pen}} > I_{\text{std}} > I_{\text{liv}} > I_{\text{opt4}}$.

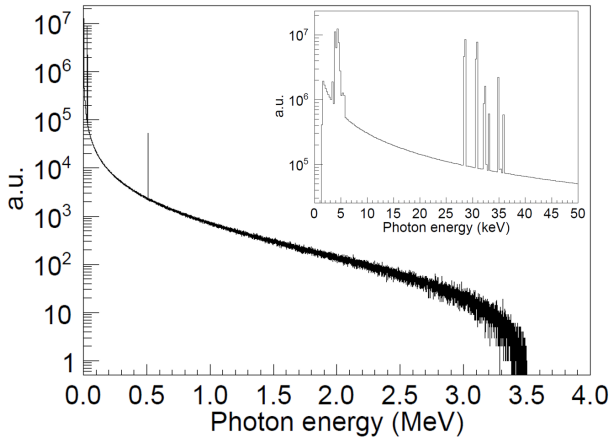

Figure 5-3: The photon energy spectrum produced by 2×10^7 monoenergetic primary electrons of 3.5 MeV. The physics constructor is Standard. (Published in Ref. [17].)

The above results show that at least the photons produced by the atomic processes vary when applying different physics constructors. As a result, the energy absorption may also be different. The differences in the photon production and the energy absorption associated with different physics constructors were studied with detector simulations with the monoenergetic electrons. For both the CsI and the NaI detectors, simulations with each physics constructor were performed by varying the energy of the primary electron source in the range of 0.5-4 MeV in steps of 0.5 MeV. In each simulation, 2×10^7 primary events were generated, and the information about the photon production and the energy absorption was recorded. The rest of this section discusses the simulation results focusing on the photon production and the energy absorption characterized by the photon yield and the absorption fraction, respectively.

5.2.1 Photon Yield

The photon yield, Y, is defined as the fraction of the initial kinetic energy of the primary electrons converted into photons. Figure 5-4 shows the photon yields in the CsI and the NaI detectors obtained with the Standard constructor as a function of the initial energy of the primary electron source. As the photon can come from different production mechanisms, the sources of photon production were studied quantitatively with three simulation conditions:

1. All photon production processes are switched on, corresponding to the open markers (squares and circles) in Fig. 5-4.

2. The atomic deexcitations, including the fluorescence photons, the Auger electrons, and the Particle Induced X-ray Emission, are switched off. The results are represented by the light gray markers in Fig. 5-4.

3. Only the bremsstrahlung photons from the primary electrons are collected. This requires that, on the one hand, the photon threshold should be reasonably low to include most of the photons produced by the primary electrons; on the other hand, besides the photon production by the primary electrons, all other photon production processes should be switched off.

The former can be done by setting the range cuts for photons at 3.5 μm in the CsI and 5 μm in the NaI, respectively. The latter requires that in addition to disabling the atomic deexcitation processes, the interactions of the photons and the secondary electrons with the detectors should be switched off. The interaction of photons with the detectors is disabled by switching off the photoelectric effect, the Compton scattering, and the pair production. The interaction of the secondary electrons with the detectors is disabled by switching off multiple scattering. In addition, by setting the range cut for electrons at 1 km which is considered "infinity" in Geant4, any photon production process by the secondary electrons is disabled.

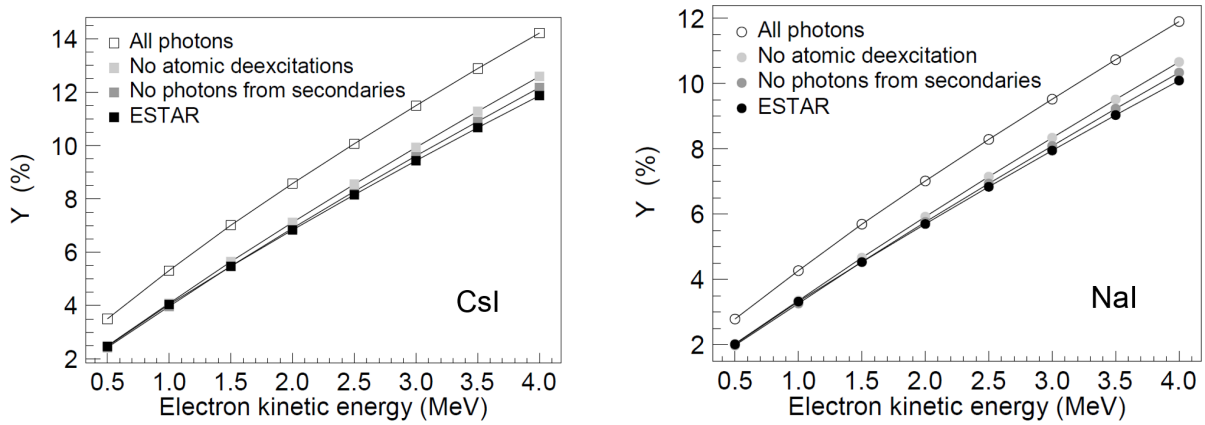

Figure 5-4: Photon yields obtained from simulations with the CsI (left panel) and the NaI (right panel) detectors as a function of the initial kinetic energy of the primary electron. The simulations were performed with the Standard constructor. The open, light gray, and dark gray markers correspond to Geant4 simulations; the black marker corresponds to the values from the NIST ESTAR program. Details are explained in the text. (Published in Ref. [17].)

The conditions above allow one to deduce the relative contributions of the main photon production mechanisms. It is shown by the dark gray markers in Fig. 5-4 that the dominant contribution is from the bremsstrahlung photons produced by the primary electrons. The second greatest contribution is from the atomic deexcitations. The smallest contribution is from the photons produced by the secondary electrons and photons. The above simulation results are compared with the radiation yield (black markers) from the NIST ESTAR program, which is defined as the average fraction of the initial kinetic energy of an electron that is converted to bremsstrahlung energy as the particle

slows down to rest calculated in the continuous-slowing-down approximation. Between the ESTAR values and the dark gray marker values, there is a small but visible difference. The origin of this difference is unclear but can be attributed to the details in the calculations of the radiation yield, including the cutoff in energy integration, or the difference between the continuous-slowing-down approximation used in ESTAR and the discrete steps used in Geant4. In practice, and in the rest of the chapter, all photon contributions are included because once a photon is produced, it has a chance to escape from the detector.

Similarly, the photon yields can be obtained from simulations with the three other constructors. The results are indistinguishable from those obtained with the Standard constructor on the scale of Fig. 5-4. The differences can be made visible by normalizing the results obtained with the Standard, Penelope, and Livermore constructors to those with the Option4 constructor. The normalized yields are defined as

$$r_X = Y_{\mathrm{X}}/Y_{\mathrm{opt4}} - 1, \tag{5.1}$$

where X = std, pen, liv. The results are shown in Fig. 5-5, where it is observed that the normalized yields obtained with the Standard and Penelope constructors show a larger energy dependence than that obtained with Livermore. The Livermore and Option4 constructors produce the closest results in the photon yield and the energy dependence of the normalized yield.

From the above result, one can estimate the uncertainty of the photon yield of the β-energy spectrum in ^{6}He decay shown in Fig. 5-9, which has a mean energy of 1.6 MeV. From Fig. 5-5, the normalized yields at 1.6 MeV calculated with the four constructors show maximum spreads of about 5% for the CsI detector and 4% for the NaI detector. These spreads are taken as an estimate of the relative uncertainties applying to the photon yields of 8% for the CsI and 6% for the NaI (Fig. 5-4). Therefore one can expect the absolute uncertainty of the photon yield from the β-energy spectrum in ^{6}He decay to be on the order of 10^{-3}.

The differences in the photon production obtained with different physics constructors do not imply that the difference in the energy absorption will have the same magnitude. The former is uniquely determined by the energy of the primary electron source and the detector material. The

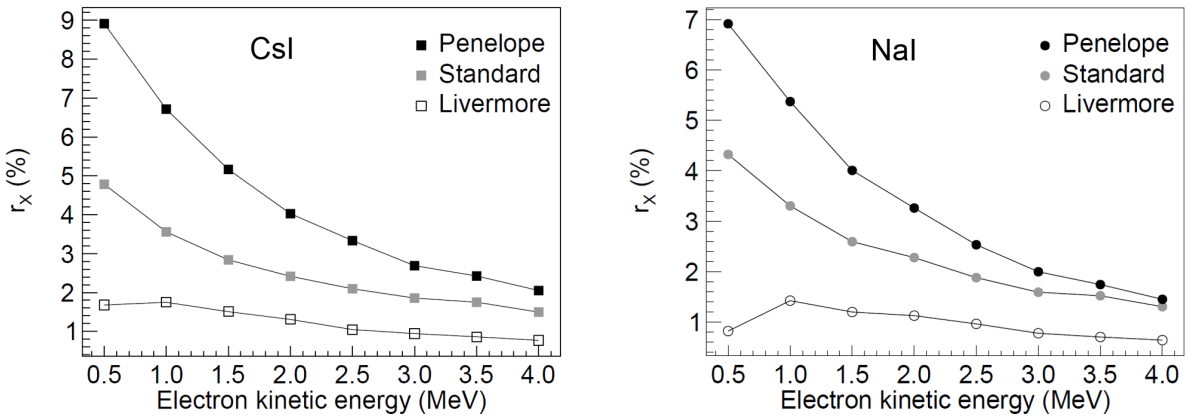

Figure 5-5: Normalized photon yields obtained from simulations with the CsI (left) and the NaI (right) detectors as a function of the initial kinetic energy of the primary electron source. The results are extracted from the simulations with the Penelope (black markers), the Standard (gray markers), and the Livermore (open markers) physics constructors by normalizing the photon yields relative to that obtained with Option4. (Published in Ref. [17].)

latter is also affected by the detector geometry. If the detectors were infinitely large, regardless of the differences in the photon production, all photons and thus all the energy would be absorbed.

5.2.2 Absorption Fraction

From the simulations described at the beginning of Sec. 5.2, one can extract the absorption fraction, f, defined as the fraction of the initial kinetic energy of the primary electrons absorbed in the detector. Figure 5-6 shows the absorption fractions in the CsI and the NaI detectors obtained with the Standard constructor as a function of the initial energy of the primary electron source. It is worth emphasizing that the geometries of the two detectors are different and would affect the results.

With the results in Fig. 5-6, one can estimate the average size of the correction to the β-energy spectrum in ^{6}He decay due to the photons escaping from the detector. Taking again a mean energy of 1.6 MeV shown in Figure 5-9, the average correction is the average fraction of energy lost by the detector, which is about 1%-2% according to Fig. 5-6. Since the absorption fraction is energy-dependent, the correction to the β-energy spectrum is energy-dependent as well. As the electron energy increases, the absorption fraction decreases, and the size of the correction increases.

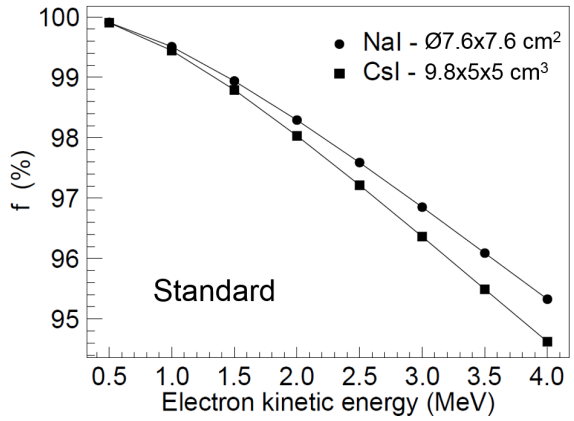

Figure 5-6: Absorption fractions obtained from simulations with the CsI (squares) and the NaI (circles) detectors as a function of the initial kinetic energy of the primary electron source. The simulations were performed with the Standard constructor. (Published in Ref. [17].)

The absorption fractions from simulations with the three other constructors can be obtained similarly. The results are indistinguishable from those obtained with the Standard constructor on the scale of Fig. 5-6. Once again, the differences can be made visible by normalizing the results obtained with the Standard, Penelope, and Livermore to those obtained with the Option4 constructor. The normalized absorption fraction is defined as

$$s_X = f_X / f_{\text{opt4}} - 1. \tag{5.2}$$

The results are shown in Fig. 5-7, where the error bars are derived from the statistical uncertainties of the mean absorbed energy per event. Unlike the normalized photon yields shown in Fig. 5-5, the normalized absorption fractions do not show a common trend as a function of the electron energy. As the electron energy increases, the normalized absorption fraction obtained with the Penelope constructor increases, whereas the result obtained with the Livermore constructor decreases. These two trends result in a spread that increases as a function of electron energy. In addition, the difference in the results obtained with the Livermore and the Option4 constructors is larger than that obtained with the Penelope and the Option4 constrictors, which is possibly because the pair production model in Option4 (`G4PenelopeGammaConversionModel`) is taken from the Penelope constructor.

With the above result, one can estimate the uncertainty of the absorption fraction for the β-

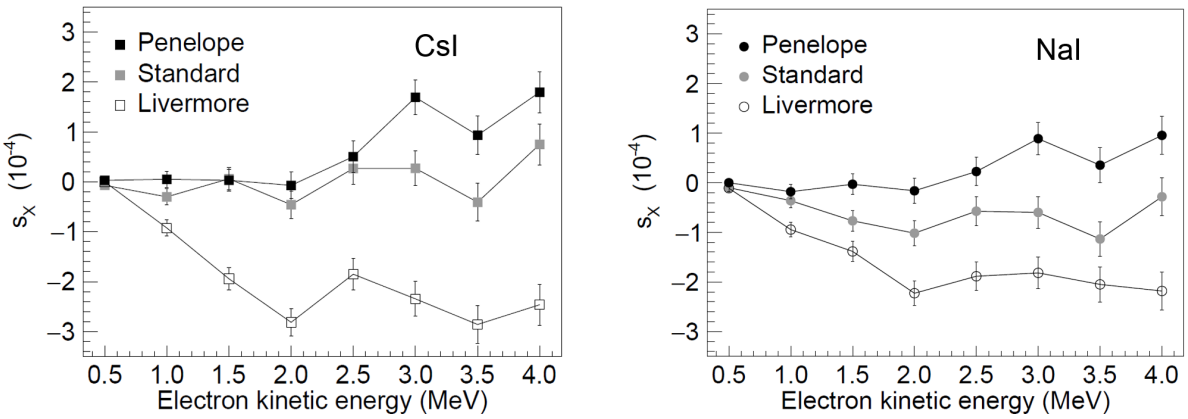

Figure 5-7: Normalized absorption fraction obtained from simulations with the CsI (left) and the NaI (right) detectors as a function of the initial kinetic energy of the primary electron source. The results are extracted from the simulations with the Penelope (black markers), the Standard (gray markers), and the Livermore (open markers) physics constructors by normalizing the absorption fractions relative to that obtained with Option4. (Published in Ref. [17].)

energy spectrum in ^{6}He decay shown in Fig. 5-9. Taking again a mean energy of 1.6 MeV, the normalized absorption fractions calculated with the four constructors show maximum spreads of about 2×10^{-4} for the CsI detector and 1.5×10^{-4} for the NaI detector. These spreads are considered the relative uncertainties that apply to the absorption fractions that are close to 1. Therefore one can expect the absolute uncertainties of the absorption fraction from the β-energy spectrum in ^{6}He decay to be on the order of 10^{-4} for both detectors. These uncertainties are an order of magnitude lower than those of the photon yields. Such small differences in the absorption fractions obtained with different constructors are difficult to benchmark experimentally.

5.3 Detector Response

The absorbed energy spectra produced by the monoenergetic electron sources are obtained from the simulations. For a 3.5 MeV electron source, the spectrum is shown in the upper panel of Fig. 5-8. The number of primary events is 2×10^7, and the physics constructor is Standard. The spectrum is dominated by a full-energy peak at 3500 keV followed by a continuous electron-energy spectrum below 3500 keV due to the escape of bremsstrahlung photons. The two peaks of energy 0.511 MeV and 1.022 MeV below the full energy peak are the "single escape peak" and the "double

escape peak" originated from the annihilations following the pair productions of the bremsstrahlung photons above 1.022 MeV.

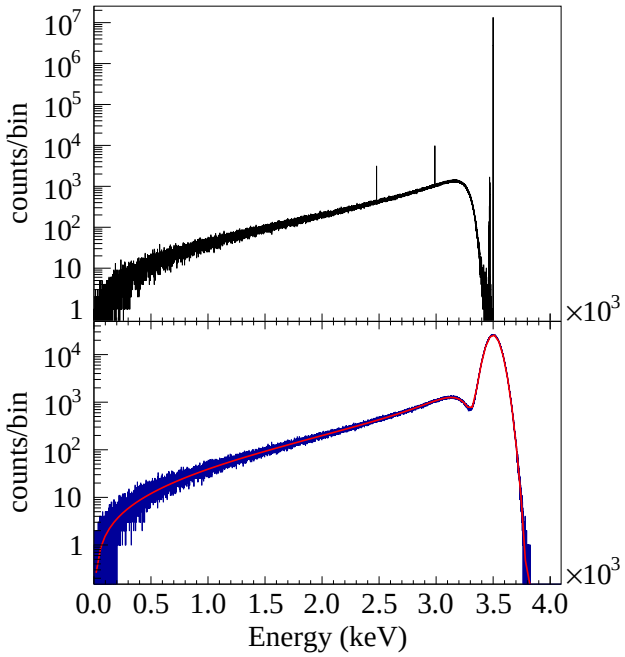

Figure 5-8: Upper panel: the absorbed energy spectrum produced by a monoenergetic primary electron source of 3.5 MeV in the CsI detector. The number of primary events is 2×10^7 and the physics constructor is Standard. Lower panel: the response function at 3.5 MeV obtained by convolving the upper panel with a Gaussian.

To take into account the energy resolution, the above absorbed spectrum is convolved with a Gaussian, resulting in a convolved spectrum describing the response function. Considering that the energy resolution is energy-dependent, the convolution is performed in a bin-by-bin case. The events in each bin are redistributed following a Gaussian distribution with the following mean (μ) and standard deviation (σ^E)

$$\mu = E, \tag{5.3}$$

$$\sigma^E = \sigma_0 \sqrt{E}, \tag{5.4}$$

where E is the kinetic energy in keV at the center of a bin, and the coefficient σ_0 is determined with γ sources (Chaps. 6 and 7). In this example, $\sigma_0 = 1.044$ keV$^{1/2}$. For each bin, the redistributed

events are filled in a new histogram, resulting in the convolved spectrum shown in the lower panel of Fig. 5-8.

The response function described by the shape of the convolved spectrum can be expressed as

$$f_r(E; E_0, P_0, ..., P_7) = t_r(E; P_0, ..., P_7) + P_8 e^{-\frac{1}{2}\left(\frac{E-E_0}{P_9}\right)^2}. \tag{5.5}$$

Here, E_0 is fixed at the initial energy of the monoenergetic electron in keV. The second term in Eq. 5.5 corresponds to the main Gaussian peak and $t_r(E; P_0, ..., P_7)$ describes the shape of the asymmetric tail and has the form

$$t_r(E; P_0, ..., P_7) = P_7 \tilde{\mathcal{L}}(E; P_0, ..., P_6) + (1 - P_7)\tilde{\mathcal{G}}(E; P_0, ..., P_6), \tag{5.6}$$

where, $\tilde{\mathcal{L}}$ and $\tilde{\mathcal{G}}$ are the modified Lorentzian distribution and the modified Gaussian distribution, respectively:

$$\tilde{\mathcal{L}}(E; P_0, ..., P_6) = \frac{P_0}{1 + \left[\frac{E-P_1}{\tilde{\gamma}(E;P_1,...,P_6)}\right]^2}, \tag{5.7}$$

$$\tilde{\mathcal{G}}(E; P_0, ..., P_6) = P_0 e^{-\frac{1}{2}\left[\frac{E-P_1}{\tilde{\gamma}(E;P_1,...,P_6)}\right]^2}, \tag{5.8}$$

$$\tilde{\gamma}(E; P_1, ..., P_6) = \frac{P_2}{1 + P_3 e^{P_4(E-P_1)} + P_5 e^{P_6(E-P_1)}}. \tag{5.9}$$

With the ten free parameters, $P_0, ..., P_9$, and one fixed parameter, E_0, one can use Eq. 5.5 to describe a spectral shape shown in the lower panel of Fig. 5-8, where the red curve shows a best fit that determines a set of values for the ten free parameters. Similarly, new sets of values for the ten parameters can be obtained by fitting the convolved spectra produced by other monoenergetic electron sources. Each parameter as a function of the electron source energy is fitted by a linear function. In this way, the response function of a monoenergetic electron source with any energy in the range of 0-4 MeV can be determined.

For the β-energy spectrum, the detector response can be expressed as a linear combination of a list of response functions

$$F_r(E) = \sum_{E=E_{\min}}^{E_{\max}} f_r(E; E_0, P_0, ..., P_7) w_E, \tag{5.10}$$

where w_E is the statistical weight at the energy E. The number of functions in the sum is determined by the energy step size.

This seemingly direct approach to determine the response of the detector to a β-energy spectrum is long and tedious. Also, the expression of the response function, Eq. 5.5, has no physical significance: it only serves the purpose of describing the shape of the convolved spectra. Instead of simulating the absorbed energy spectra of monoenergetic electrons, the β-energy spectrum can be directly used as a continuous primary particle source in Geant4. The GPS class in Geant4 is capable of defining a primary particle source with continuous energy distribution. The simulation with the continuous source provides the absorbed β-energy spectrum, which is convolved with the Gaussian, producing a convolved β-energy spectrum that represents the response of the detector to a β-energy spectrum. This approach includes only two steps: the simulation with Geant4 and the convolution with Gaussian.

5.4 Continuous β-energy Spectrum

A β-energy spectrum with 10^9 events was generated following Eq. 5.11, which is Eq. 1.26 without the $(1 + b_{GT}/W)$ and the $f_1\,(E, b_{WM})$ factors associated with the observables. These two factors will be included in the spectrum when fitting the measured β-energy spectrum, with b_{WM} and b_{GT} being free parameters in the fits, which is discussed in Chap. 8. This generated spectrum was used as a primary electron source for the simulation, shown in Fig. 5-9 in blue. From a simulation with the CsI detector, the absorbed β-energy spectrum obtained, as shown in Fig. 5-9 in red, where a clear distortion of the spectrum is observed. The difference between the generated and the absorbed spectra originates from the energy loss due to the escapes of the bremsstrahlung photons from the detector. Such a distortion is smaller in the NaI detector.

$$N(W)dW = pW(W_0 - W)^2\eta(W)dW. \tag{5.11}$$

The size of the distortion can be characterized by a spectral slope. The absorbed spectrum (red) is divided by the generated spectrum (blue), the derivate of the resulting ratio is the slope introduced by the distortion. Figure 5-10 shows the slope calculated from the simulations with the

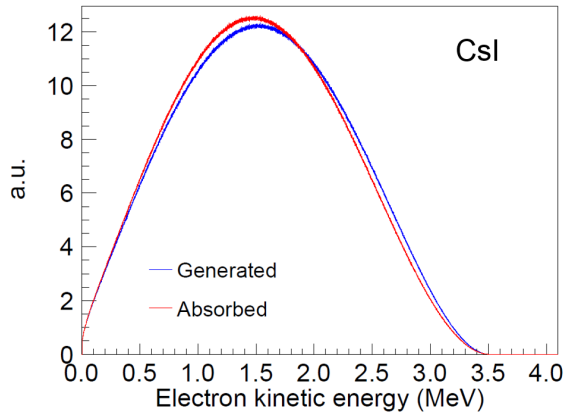

Figure 5-9: The β-energy spectrum in ^{6}He decay. Blue: energy spectrum of the primary electron source with 10^{9} events; Red: absorbed energy spectrum in the CsI detector. The simulation was performed with the Standard constructor. (Published in Ref. [17].)

CsI (squares) and the NaI (circles) detectors as a function of the β particles energy. The slopes vary by a factor of 4 and change the sign at 0.9 MeV. Near the endpoint energy, the slopes are the largest, but the weights are much smaller than the weight at the mean energy of the β-energy spectrum. The mean values of the slopes derived from Fig. 5-10 taking into account the weights are -5.4%/MeV for the CsI detector and -4.8%/MeV for the NaI detector. These two slopes provide estimates of the corrections for the effect of the photon escape applied to the generated spectrum.

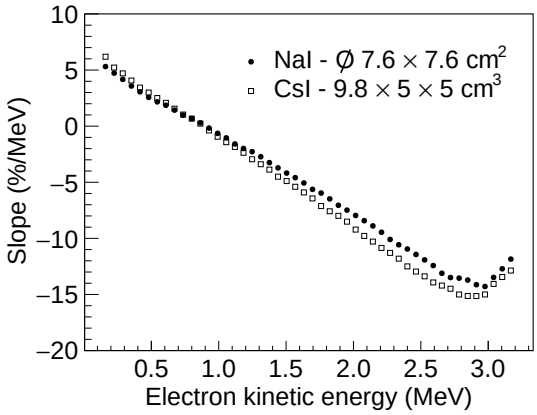

Figure 5-10: Numerical derivatives of the ratio between the absorbed and the generated β-energy spectra for the NaI (circles) and CsI (squares) detectors. (Published in Ref. [17].)

Section 5.2 has shown the differences in the photon production and the energy absorption

among the physics constructors for monoenergetic electrons and estimated the mean effects on the β-energy spectrum in ^{6}He decay. This effect can be more accurately calculated by performing Geant4 with the continuous β-energy spectrum as the primary electron source. For both the CsI and the NaI detectors, a simulation with each physics constructor was performed. In each simulation, 2×10^7 primary events were generated following Eq. 5.11, and the information about the photon production and the energy absorption was recorded.

5.4.1 Photon Yield

The photon yield of the continuous β-energy spectrum can be calculated from the simulated photon energy spectrum. For illustration, Fig. 5-11 shows the photon energy spectrum obtained from a simulation with 2×10^7 primary electrons with the Standard constructor. It shows similar features to the photon spectrum produced by the monoenergetic electrons shown in Fig. 5-3. Both spectra have a dominant continuous bremsstrahlung distribution, a 511 keV peak, and some characteristic X-ray lines. The photon yield can be calculated by dividing the total energy of photons in Fig. 5-11 by the total energy of the primary electrons.

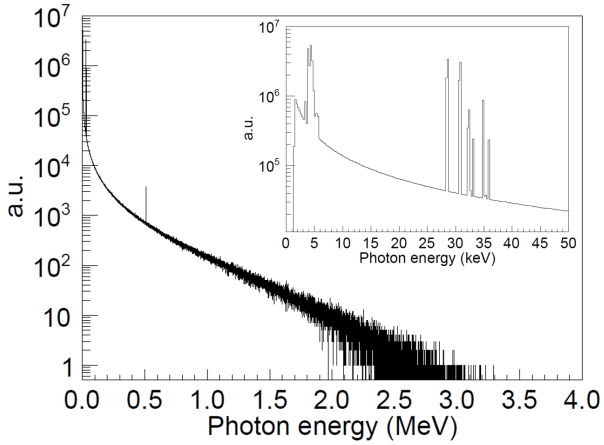

Figure 5-11: The photon energy spectrum produced by a β-energy spectrum generated following Eq. 5.11. The number of primary events is 2×10^7 and the physics constructor is Standard.

The photon yields calculated from the simulations with the four physics constructors are summarized in Table 5-3. The largest value of the photon yield is produced by the Penelope constructor,

followed by the Standard, the Livermore and the Option4 constructors, showing a similar trend to the simulations with the monoenergetic source (Figs. 5-4 and 5-5). The largest differences in the photon yields calculated with the four constructors are 3.4×10^{-3} for the CsI and 2.2×10^{-3} for the NaI, as expected from the estimates at 1.6 MeV in Sec. 5.2.1.

Table 5-3: Photon yields (in %) produced by a β-energy spectrum generated following Eq. 5.11. In each simulation, the number of primary events is 2×10^{7}. The results are obtained with four physics constructors.

	pen	std	liv	opt4
CsI	8.30	8.16	8.07	7.96
NaI	6.75	6.68	6.60	6.53

5.4.2 Absorption Fraction

The absorption fraction of the continuous β-energy spectrum can be calculated from the simulated β-energy spectrum. The total energy in the absorbed spectrum divided by the total energy of the primary electrons gives the absorption fraction. The results calculated from the simulations with the four physics constructors are summarized in Table 5-4. The largest value of the absorption fraction is produced by the Penelope constructor, followed by the Option4, the Standard, and the Livermore constructors, showing a similar trend to the simulations with the monoenergetic source (Figs. 5-6 and 5-7). The largest differences in the absorption fractions calculated with the four constructors are 3×10^{-4} for the CsI and 2×10^{-4} for the NaI, as expected from the estimate at 1.6 MeV in Sec. 5.2.2. As previously indicated, these differences are an order of magnitude smaller than the differences among the photon yields.

Table 5-4: Absorption fractions (in %) produced by a β-energy spectrum generated following Eq. 5.11. In each simulation, the number of primary events is 2×10^{7}. The results are obtained with four physics constructors.

	pen	std	liv	opt4
CsI	98.15	98.14	98.12	98.14
NaI	98.39	98.39	98.37	98.39

5.4.3 Comparison of the Simulated Spectra

The absorbed energy spectra obtained from the above simulations are similar to the red spectrum shown in Fig. 5-9 but with 2×10^7 events each. The spectra obtained with different physics constructors are indistinguishable from each other at those scales. As indicated by the absorption fractions in Table 5-4, the differences are expected to be small. Therefore simulations with high statistics are required to quantify the differences. In addition to the red spectrum in Fig. 5-9 simulated with the Standard constructor, the absorbed β-energy spectra were simulated with the three other physics constructors for both the CsI and the NaI detectors. In each simulation, 10^9 primary events were generated. The outcomes of these simulations are four spectra with high statistics for each detector.

If one takes the spectrum obtained with Option4 as a reference, and divide the spectra simulated with the other three constructors by the one simulated with Option4, the slopes of the resulting ratio spectra are taken as estimates of the uncertainties of the absorbed spectra related to the differences among the constructors. The slopes are extracted by fitting the ratio spectra by a linear function.

For illustration, the upper panel of Fig. 5-12 shows the ratio between the absorbed spectra simulated with the Standard and the Option4 constructors. The ratio spectrum was fitted by a linear function with the χ^2 minimization method in the energy range of 100-3000 keV. The lower panel of the figure shows the residuals of the fit defined as

$$\text{Residual} = \frac{y_{\text{bin}} - y_{\text{fit}}}{\sigma_{\text{bin}}}, \tag{5.12}$$

where, y_{bin} and σ_{bin} are the content and error of a bin, respectively, y_{fit} is the value of the fitted function at the bin. Table 5-5 summarizes the slopes extracted from the fits to the ratio spectra[1], where the uncertainties are statistical uncertainties calculated with the minimization algorithm.

[1] In Ref. [17], other values of the slopes were provided. This is because the generated spectra in Ref. [17] and in this work are different. The former includes a radiative correction assuming the electrons and the photons are distinguishable in the detector, whereas the latter includes a radiative correction for electrons and the photons that are indistinguishable in the detector. Details of this distinction are discussed in Sec. 2.5.

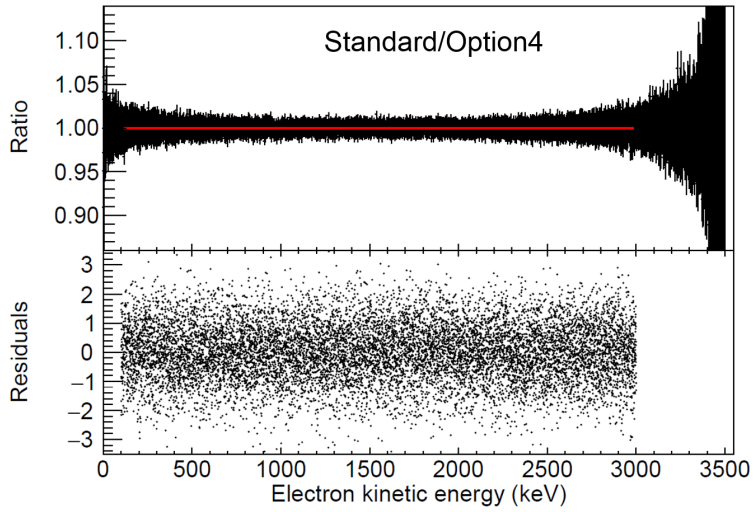

Figure 5-12: Upper panel: the ratio between the absorbed energy spectra simulated with the Standard and the Option4 constructors. The red line is a linear fit to the ratio spectrum. Lower panel: the residuals of the fit.

Table 5-5: Slopes (in 10^{-8}/keV) extracted from the fits to the ratio spectra

	pen	std	liv
CsI	20.0 ± 6.7	-7.1±6.7	-65.1±6.7
NaI	6.8 ±6.7	-5.3±6.7	-44.2±6.7

In Table 5-5, both the signs and the absolute values of the slopes are consistent with the trend and amplitude of the absorption fractions for monoenergetic electrons shown in Fig. 5-7. Among the slopes calculated with the four constructors, the largest spreads are $\pm 4.2(1) \times 10^{-7}$/keV for the CsI and $\pm 2.6(1) \times 10^{-7}$/keV for the NaI. These values are used to calculate the upper limits of the uncertainties of the absorbed spectra. As the mean corrections to the spectra due to the effect of photon escape were estimated to be -5.4%/MeV for CsI and -4.8%/MeV for NaI, the slopes introduced by the difference among physics constructors represent relative uncertainties of 0.78% and 0.54% for the CsI and the NaI detectors, respectively.

The largest spreads of the slopes for the two detectors are also used to derive the uncertainties of the observables based on the spectral function (Eq. 1.27). This results in

$$\delta b_{WM} = 4.41, \qquad \delta b_{GT} = 1.76 \times 10^{-3} \tag{5.13}$$

for the CsI detector, and

$$\delta b_{WM} = 2.73, \qquad \delta b_{GT} = 1.09 \times 10^{-3} \tag{5.14}$$

for the NaI detector. These are the uncertainties of b_{WM} and b_{GT} associated with the Geant4 simulations.

CHAPTER 6

ENERGY CALIBRATION

6.1 Introduction

A crucial part of the analysis of the β-energy spectrum is the energy calibration. Its significance can be seen in a measurement of the Fierz interference term in free-neutron β decay [31], where the systematic uncertainty of b_n, dominated by the absolute energy calibration and the linearity of the β spectroscopy energy response, is 6.1%. The measured b_n with such a high systematic uncertainty provides no sensitivity to the exotic couplings.

In this work, a β particle of energy E in a detector produces a signal, which undergoes the digitizing process, resulting in a measured kinetic energy expressed in channels (chan), which is also referred to as the "ADC units" or the "digitizer units". Assuming the detector chain has a linear energy response, the relation between the kinetic energy and the channel value is

$$CH(E) = A \cdot E + B \ \text{ chan}, \tag{6.1}$$

where A is the system gain in chan/keV, B is the pedestal or offset in chan.

In practice, the energy response of the detector chain could have a small deviation from the perfect linear response described in Eq. 6.1. This deviation is described by introducing an additional quadratic term:

$$CH(E) = P \cdot E^2 + A \cdot E + B \ \text{ chan}, \tag{6.2}$$

where the coefficient P describes the nonlinearity of the detector chain and its unit is chan/keV^2.

Another important contribution to the energy calibration is a Gaussian standard deviation (σ^E) associated with the detector energy resolution. As mentioned in Chap. 5, the energy resolution is taken into account by convolving the absorbed energy spectrum simulated using Geant4 with a Gaussian distribution that has an energy-dependent standard deviation:

$$\sigma^E = \sigma_0 \sqrt{E}, \tag{6.3}$$

where σ_0, referred to here as the "width parameter", is determined by fitting the full-energy peaks of several of γ sources.

In summary, the energy calibration in this work requires to determine four parameters: gain (A), offset (B), nonlinearity (P), and the width parameter (σ_0). The determinations of the energy-calibration parameters have significant impacts on the observables. The sensitivities of the observables to the energy-calibration parameters are studied, which is followed by initial determinations of the calibration parameters. For the gain, an auto-calibration method is described. For the offset, the nonlinearity and the width parameter, initial estimates are provided in this chapter, which are updated in Chap. 7 after taking into account an additional systematic effect related to the event rate.

6.2 Sensitivity to the Energy Calibration

The two observables, b_{WM} and b_{GT}, manifest themselves in the shape of the β-energy spectrum through a positive and a negative slope, respectively. Any inaccuracy of the energy-calibration parameters would cause a wrong description of the measured β-energy spectrum, introducing systematic uncertainties of b_{WM} and b_{GT}.

Figure 6-1 illustrates how an incorrect gain produces such a systematic effect and how similar arguments hold for other energy-calibration parameters. The left panel shows a hypothetical experimental spectrum (blue) and a theoretical spectrum (red) to be adjusted to the experimental spectrum. The experimental spectrum is the phase space factor. To make the effect visible, the theoretical spectrum is obtained by stretching the experimental spectrum (blue) along the horizontal axis by a factor of 1.1. If we consider the gain of the experimental spectrum to be 1, then the theoretical spectrum has a gain of 1.1, overestimating the gain by 10%. The middle panel shows the ratio between a similar theoretical spectrum with a gain of 1.001 and the experimental spectrum with a gain of 1. The systematically wrong description of the experimental spectrum by the theoretical function produced a slope which increases towards the endpoint energy. The right panel shows the derivative of the ratio shown in the middle panel weighted with the square root of

the phase space factor. The average slope in the energy range of 1-2 MeV is about 0.25%/MeV, which is about 40% of the value of C_1, the dominant slope of the spectral function. Therefore a 0.1% systematic uncertainty of the gain produces a large spectral slope that has significantly effects on the correct extractions of the observables.

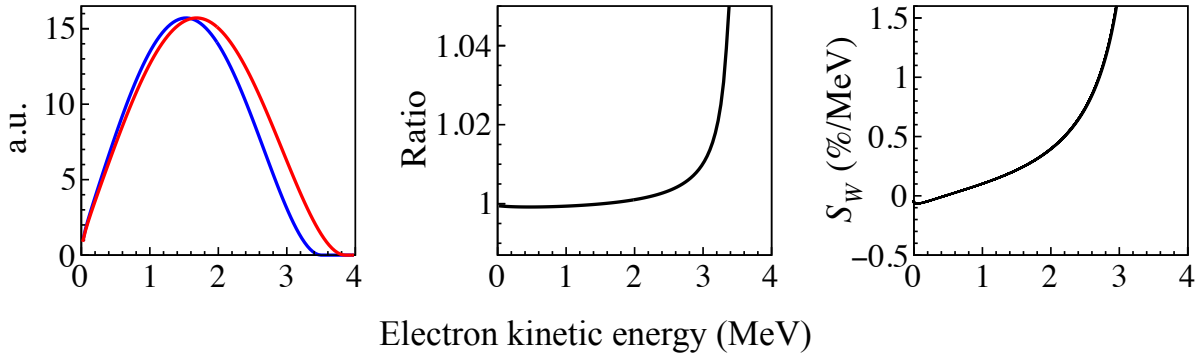

Figure 6-1: Left panel: analytic β-energy spectrum obtained only from the phase space factor. The theoretical spectrum (red) is obtained by stretching the experimental spectrum (blue) along the horizontal axis by a factor of 1.1. Middle panel: the ratio between a theoretical spectrum (red) with a stretch factor of 1.001 and the experimental spectrum (blue). Right panel: the slope of the ratio shown in the middle panel weighted with the square root of the phase space factor.

6.2.1 General Procedure

The sensitivities of b_{WM} and b_{GT} to the energy-calibration parameters can be studied with Monte Carlo simulations. As the shape of β-energy spectrum is dominated by the phase space factor, one can neglect the theoretical corrections and the detector response for the moment, and estimate the impacts of the energy-calibration parameters on the observables with the following function as an approximation to the β-energy spectrum:

$$f(CH; N_0, A, b) = pW(W_0 - W)^2 \times f_1(E, b_{WM}) \times \left(1 + \frac{b_{GT}}{E}\right), \tag{6.4}$$

$$E = \frac{CH - B}{A}, \tag{6.5}$$

where the spectrum is expressed in chan.

A Monte Carlo sample consisting of 200 β-energy spectra were generated with the SM values of the observables, i.e., $b_{WM} = b_{WM}^{SM} = 68.22$ and $b_{GT} = b_{GT}^{SM} = 0$. Each spectrum contains 10^6 events distributed among 256 bins. The spectra were fitted by Eq. 6.4 in a channel range corresponding to the energy range of 300-3200 keV. Depending on the observable of interest, the fit can be either a "SM" fit with b_{WM} as a free parameter and b_{GT} fixed at b_{GT}^{SM}, or a "BSM" fit with b_{GT} as a free parameter and b_{WM} fixed at b_{WM}^{SM}. In both fits, there are two additional free parameters: the gain and an overall normalization factor.

The above is the general procedure to study the impacts of each energy-calibration parameter on the physics observables. Depending on the effect of interest, the procedure differs when generating or fitting the spectra.

6.2.2 Sensitivity to the Gain

The sensitivity to the gain was studied by generating β-energy spectra following Eq. 6.4 with $A = A_{\mathrm{MC}} = 1.5$ chan/keV and $B = B_{\mathrm{MC}} = 20$ chan. The sample was fitted by Eq. 6.4 with the gain fixed in the range of 1.495-1.505 chan/keV in steps of 0.001 chan/keV and the offset fixed at $B = B_{\mathrm{MC}}$ chan. For each fixed gain, an average b_{WM} was extracted from the 200 SM fits, and an average b_{GT} was extracted from the 200 BSM fits. Figure 6-2 shows the results as a function of the relative gain variation defined as

$$A_r = \frac{A}{A_{\mathrm{MC}}} - 1, \tag{6.6}$$

where A is the gain in the fit function. The extracted sensitivities of b_{WM} and b_{GT} to a 0.1% variation of A_r are -32 and 1.4×10^{-2}, respectively. This variation of b_{WM} produces a slope of -0.29%/MeV for C_1, which is comparable to the estimates made in Sec. 6.2 with the analytic spectra.

It is worth pointing out that it is the relative gain variation rather than the absolute gain variation that is relevant to characterize the sensitivities of b_{WM} and b_{GT}. The Monte Carlo simulations with a different A_{MC} but the same range of values of A_r result in the same sensitivities of b_{WM} and b_{GT} to A_r.

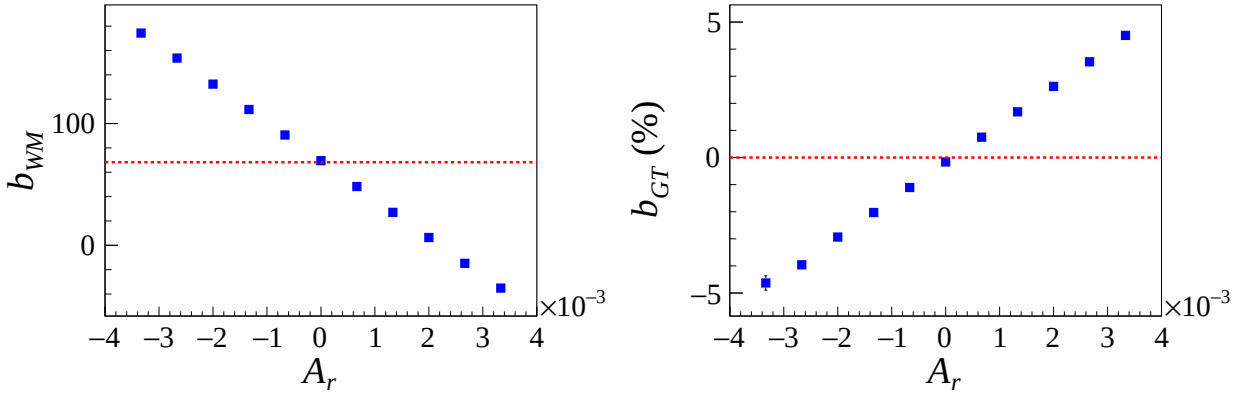

Figure 6-2: Left panel: the average b_{WM} extracted from 200 Monte Carlo simulations and fits as a function of the relative gain variation. The dashed line indicates the input value of b_{WM} in the simulations. Right panel: The average b_{GT} extracted from 200 Monte Carlo simulations and fits as a function of the relative gain variation. The dashed line indicates the input value of b_{GT} in the simulations.

6.2.3 Sensitivity to the Offset

The same Monte Carlo sample as above was used to study the sensitivity to the offset. These spectra were fitted by Eq. 6.4 with the gain fixed at $A_{\rm MC}$ and the offset fixed in the range of 15-25 chan and in steps of 1 chan. For each fixed offset, an average b_{WM} was extracted from the 200 SM fits, and an average b_{GT} was extracted from the 200 BSM fits. Figure 6-3 shows the results as a function of the offset used in the fits. The extracted sensitivities of b_{WM} and b_{GT} to a 1-chan variation of B are -12 and 5.7×10^{-2}, respectively. It is worth pointing out that it is the absolute offset variation that is relevant to characterize the sensitivities of $b_{\rm WM}$ and $b_{\rm GT}$.

6.2.4 Sensitivity to the Nonlinearity

The sensitivity to the nonlinearity was also studied by generating β-energy spectra following Eq. 6.4 but with a quadratic response shown in Eq. 6.2, with $A = A_{\rm MC} = 1.5$ chan/keV, $B = B_{\rm MC} = 20$ chan, and P fixed in the range of $2 \times 10^{-7} - 1 \times 10^{-6}$chan/keV^2 in steps of 1×10^{-7}chan/keV^2. For each value of P, a sample of 200 spectra was generated. Each sample was fitted assuming a linear response shown in Eq. 6.1 with the gain and the offset fixed at $A = A_{\rm MC}$ and $B = B_{\rm MC}$,

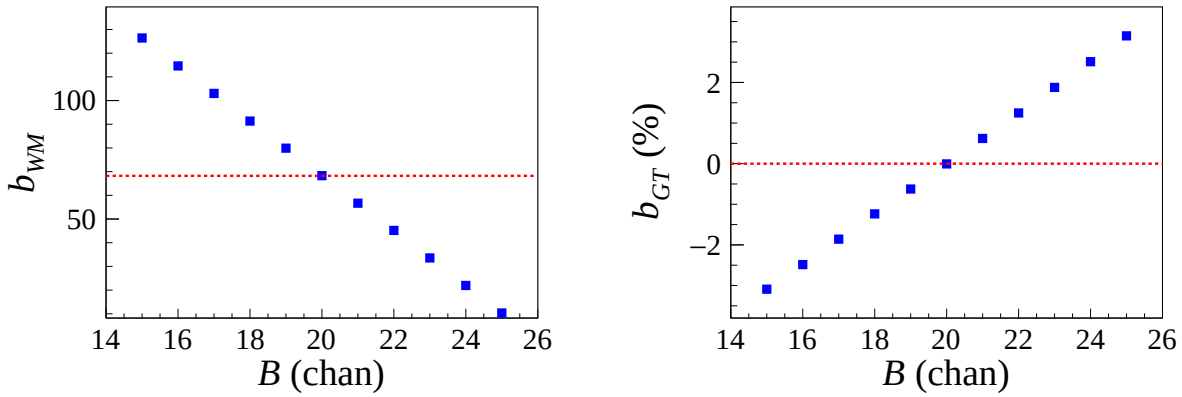

Figure 6-3: Left panel: the average b_{WM} extracted from 200 Monte Carlo simulations and fits as a function of the offset used in the fit. The dashed line indicates the input value of b_{WM} in the simulations. Right panel: the average b_{GT} extracted from 200 Monte Carlo simulations and fits as a function of the offset used in the fit. The dashed line indicates the input value of b_{GT} in the simulations.

respectively, and an average b_{WM} was extracted from the 200 SM fits and an average b_{GT} was extracted from the 200 BSM fits. Figure 6-4 shows the results as a function of P. The extracted sensitivities of b_{WM} and b_{GT} to a 1×10^{-7}chan/keV^2 variation of P are 3.5 and -1.3×10^{-3}, respectively.

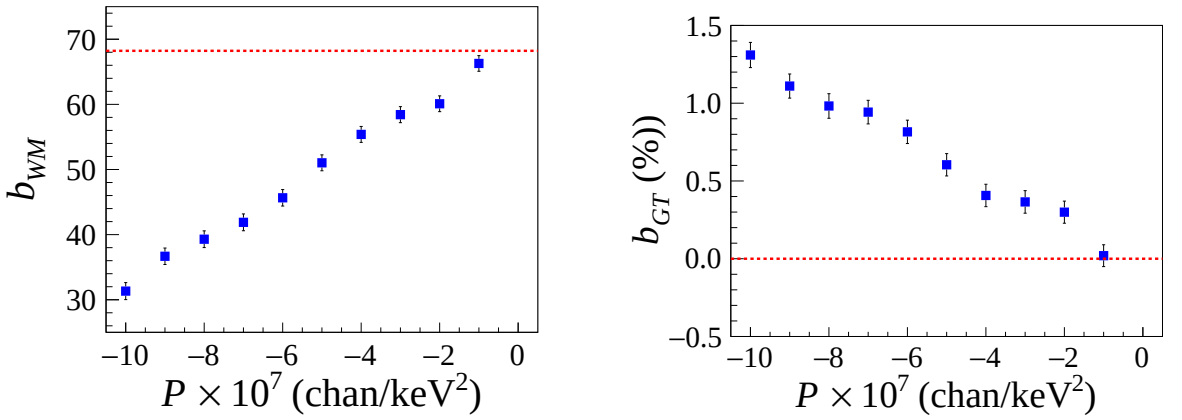

Figure 6-4: Left panel: the average b_{WM} extracted from 200 Monte Carlo simulations and fits as a function of the input nonlinearity in the simulations. Right panel: the average b_{GT} extracted from 200 Monte Carlo simulations and fits as a function of the input nonlinearity in the simulations.

6.2.5 Sensitivity to the Energy Resolution

The sensitivity to the width parameter σ_0 which is associated with the energy resolution was studied with Monte Carlo simulations. A β-energy spectrum following the phase space factor was generated with Monte Carlo. The spectrum is convolved with a Gaussian distribution with a varying width parameter in the range of 1-1.25 in steps of 0.025, producing ten convolved spectra. For each value of σ_0, a sample of 200 spectra was generated following the distribution that is a product of the corresponding convolved spectrum and $f_1(E, b_{WM}) \times \left(1 + \frac{b_{GT}}{E}\right)$, with $A = A_{\mathrm{MC}} = 1.5$ chan/keV and $B = B_{\mathrm{MC}} = 20$ chan. Each sample was fitted by Eq. 6.4 with the gain and the offset fixed at $A = A_{\mathrm{MC}}$ and $B = B_{\mathrm{MC}}$, respectively, and an average b_{WM} was extracted from the 200 SM fits and an average b_{GT} was extracted from the 200 BSM fits. Figure 6-5 shows the results as a function of σ_0. The extracted sensitivities of b_{WM} and b_{GT} to a 1% variation of σ_0 are -0.24 and 2.0×10^{-4}, respectively.

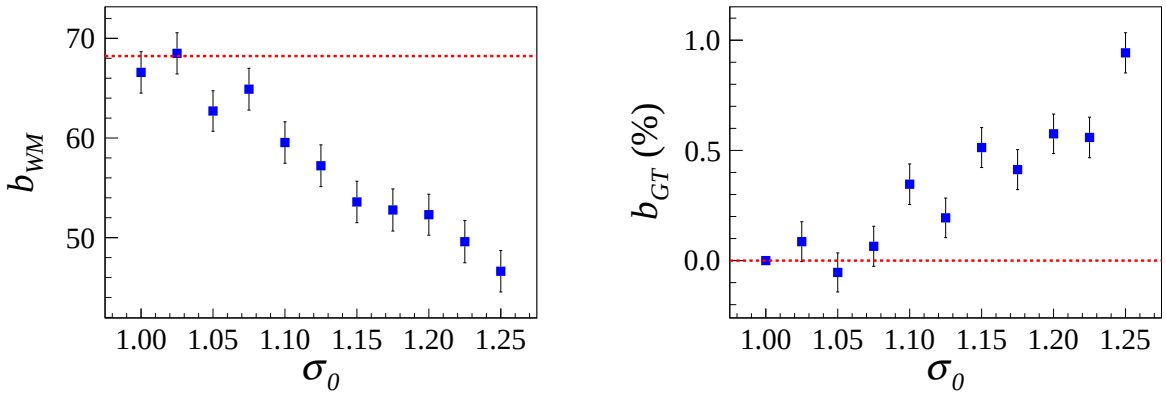

Figure 6-5: Left panel: the average b_{WM} extracted from 200 Monte Carlo simulations and fits as a function of the width parameter in the simulations. Right panel: the average b_{GT} extracted from 200 Monte Carlo simulations and fits as a function of the width parameter in the simulations.

6.2.6 Summary

The sensitivities of b_{WM} and b_{GT} to the energy-calibration parameters are summarized in Table 6-1, which is used to evaluate the systematic uncertainties of the observables associated with the

energy calibration.

Table 6-1: Sensitivities of b_{WM} and b_{GT} to the energy-calibration parameters

	Δb_{WM}	$\Delta b_{GT} \times 10^3$
10^{-3} variation of A_r	-32	14
1-chan variation of B	-12	5.7
10^{-7}chan/keV^2 variation of P	3.88	-1.4
10^{-2} variation of σ_0	-0.8	0.4

6.3 Determination of the Gain with Auto-Calibration

From the sensitivity studies, it is clear that the energy calibration has a significant impact on the systematic uncertainties of b_{WM} and b_{GT}. To meet the precision goal of $O(10^{-3})$ for b_{GT}, the systematic uncertainty of the gain needs to be at the level of 10^{-4} chan/keV or lower, which is extremely challenging to reach. Even if the gain could be determined with this accuracy, it is still crucial to be able to monitor the gain during the measurement of the β-energy spectrum with the same level of accuracy. A common way to calibrate scintillating detectors such as CsI(Na) and NaI(Tl) is to use external γ sources. Such a procedure can be problematic to determine the gain in this experiment. First of all, the CsI(Na) and the NaI(Tl) detector crystals respond differently to γ and electrons; the former produces more photons than the latter, resulting in a higher gain. Secondly, the gain determined from an external calibration source depends on the location of the source relative to the detector, and it is impossible to place the γ source at the identical place with the β particles emitting inside the calorimeter. Thirdly, a rate-dependent gain drift has been observed, as discussed in Chap. 7.

All the above effects producing gain shifts can be eliminated by an auto-calibration technique, which determines the gain and an observable (here either b_{WM} or b_{GT}) simultaneously by fitting the β-energy spectrum. It is, however, possible that this procedure would induce a correlation between the gain and the observable. The potential correlation effect, as well as the performance of the auto-calibration technique, are studied in this section.

6.3.1 Fitting the Spectrum with the Gain as a Free Parameter

A similar general procedure to that in Sec. 6.2.1 was followed. A Monte Carlo sample consisting of 200 β-energy spectra was generated following Eq. 6.4, with $b_{WM} = b_{WM}^{SM} = 68.22$, $b_{GT} = b_{GT}^{SM} = 0$, and $B = B_{\mathrm{MC}} = 20$. Each spectrum contains 10^6 events distributed among 256 bins. Here instead of having a fixed value of A_{MC} when generating the spectra, a randomly generated A_{MC} in the range of 1.5-1.8 chan/keV is applied to each spectrum. This range of gain covers a 20% relative variation of the gain. The spectra were fitted by a Eq. 6.1 but with an additional normalization parameter. These fits were performed in a channel range corresponding to an energy range of 300-3200 keV and with the offset fixed at 20 chan. Three free parameters are included in each fit: a normalization factor, the gain (A), and an observable (b_{WM} or b_{GT}).

Figure 6-6 shows the values of the gain extracted from the SM fits. The results from the BSM fits are similar, but the statistical uncertainties of the gain are about 30% smaller than those from the SMs fit. The upper panel shows the gain extracted from the fits as a function of the random input gain in the Monte Carlo. The lower panel shows the relative gain variation defined in Eq. 6.6. It is worth pointing out that the fluctuations of the values of A_r are not purely statistical, as discussed in Sec. 6.3.3.

From the same fits, the values of the observables are extracted, as shown in Fig. 6-7, where the dotted lines indicate the input values in the Monte Carlo. Remarkably, the fitted values of the observables fluctuate around the input values without showing any correlation with the gain. The absence of such a correlation is because the dominant contribution of the fit function is the phase space factor, which is the decisive factor that determines the gain in the fit.

6.3.2 Statistical Uncertainties

As the auto-calibration technique extracts the observables and the gain from the same data, it is interesting to study the statistical impacts of the technique. This study requires simulations with a larger sample size. Following the same procedure as that in Sec. 6.3.1, the simulations and fits were performed with 10^4 spectra in a sample. The distributions of the statistical uncertainties of

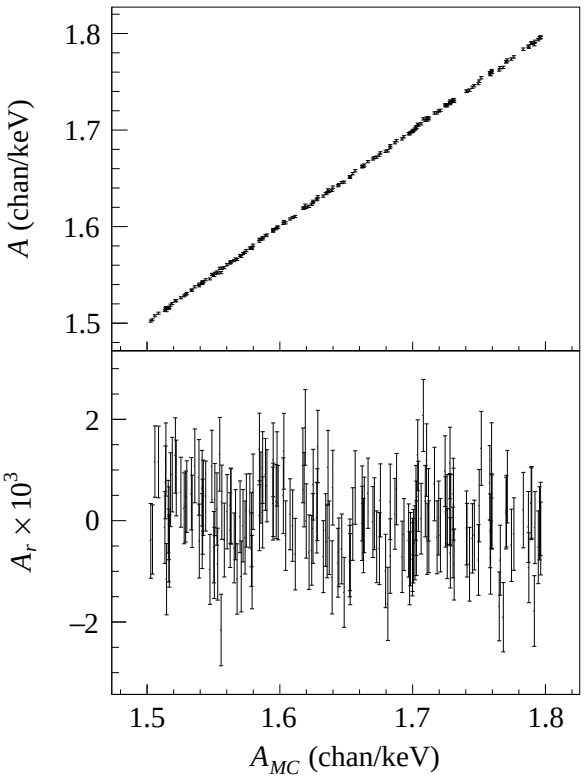

Figure 6-6: The gain extracted from fits (upper panel) and the relative gain variation multiplied by 1000 (lower panel) obtained from the SM fits as a function of input values of the gain used in the simulations.

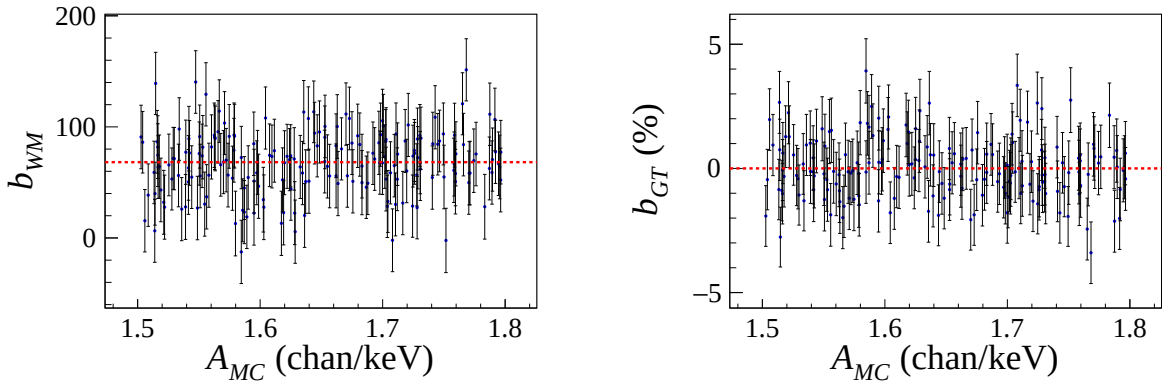

Figure 6-7: Left panel: values of b_{WM} extracted from the SM fits with the gain as a free parameter. The dotted line indicate the input value used in the Monte Carlo. Right panel: values of b_{GT} extracted from the BSM fits with the gain as a free parameter. The dotted line indicate the input values used in the Monte Carlo.

the gain are shown in Fig. 6-8, where the mean statistical uncertainties are 1.2×10^{-3} chan/keV for the SM fits and 0.9×10^{-3} for the BSM fits.

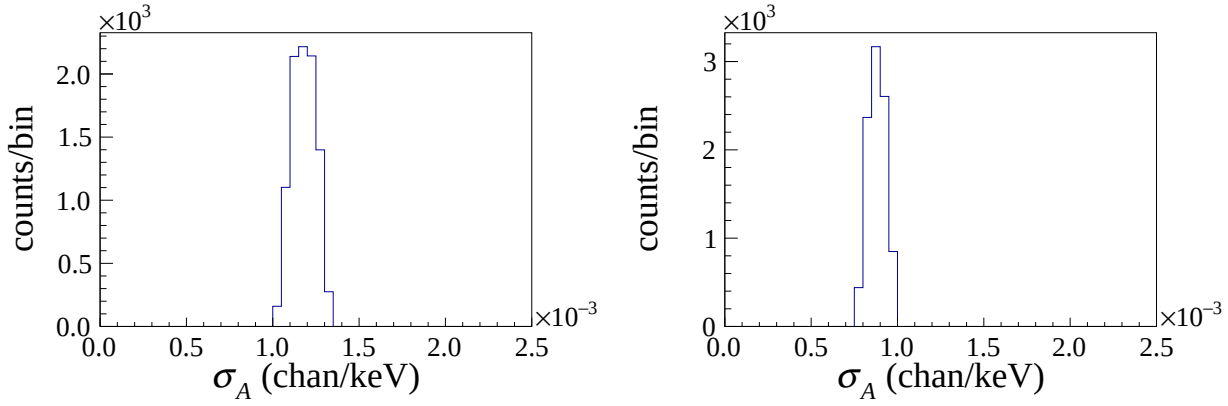

Figure 6-8: The distributions of the statistical uncertainties of the gain extracted from the SM fits (left panel) and the BSM fits (right panel) to a sample of 10^4 simulated spectra.

The left panel of Fig. 6-9 shows the distribution of the b_{WM} values extracted from the SM fits to the sample. The blue histogram shows the distribution of b_{WM} extracted from the fits with the gain as a free parameter and has a standard deviation of 28.51. If we assume that the gain is exactly known and is equal to the input values in the simulations, the gain can be fixed at A_{MC} during the fit. The resulting distribution of b_{WM} extracted fits with fixed values of gain is shown by the red histogram with a standard deviation of 16.74. Therefore leaving the gain as a free parameter increases the statistical uncertainty of the mean b_{WM} by a factor 1.7. The right panel of Fig. 6-9 shows the similar results extracted from the BSM fits to the sample. The standard deviations of b_{GT} with the free and the fixed gains are 1.25% and 0.98%, respectively. Leaving the gain as a free parameter increases the statistical uncertainty of b_{GT} by a factor 1.28.

6.3.3 Correlations

It is worth noticing from the lower panel of Fig. 6-6 and the left panel of Fig. 6-7, where the results were extracted from the same fits, that the values of b_{WM} have shown an anti-correlation with the relative gain variation, despite the absence of the correlation between b_{WM} and the gain

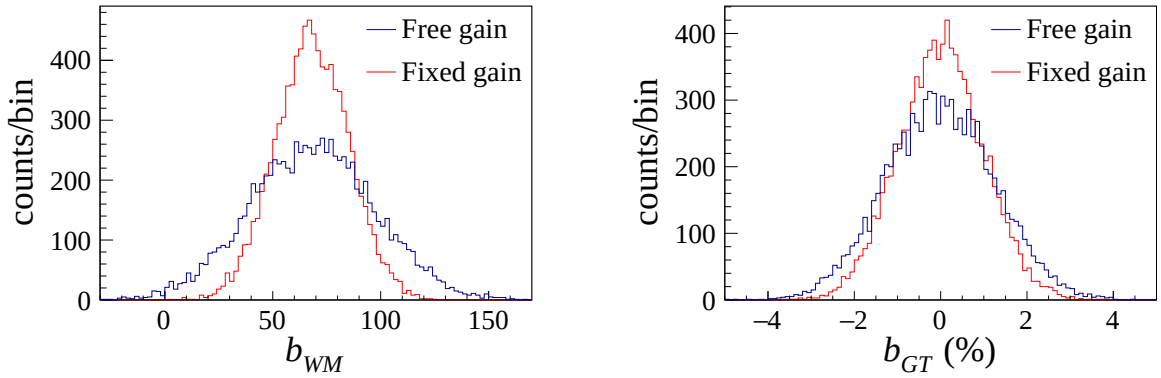

Figure 6-9: The distributions of the values of b_{WM} (left panel) and b_{GT} (right panel) extracted from fits to a sample of 10^4 spectra, with the gain in the fits as a free parameter (blue) and fixed to the input value (red).

value. Similar to A_r, we define a relative variation of b_{WM} :

$$b_r = \frac{b_{\mathrm{WM}}}{b_{WM}^{SM}} - 1, \tag{6.7}$$

where b_{WM} is the extracted value from the fits. The scatter plot of b_r relative to A_r is shown in the left panel of Fig. 6-10, where the results are extracted from fits to the sample of 10^4 spectra and show an anti-correlation. The scatter plot of b_{GT} relative to A_r is shown in the right panel, where a correlation is observed.

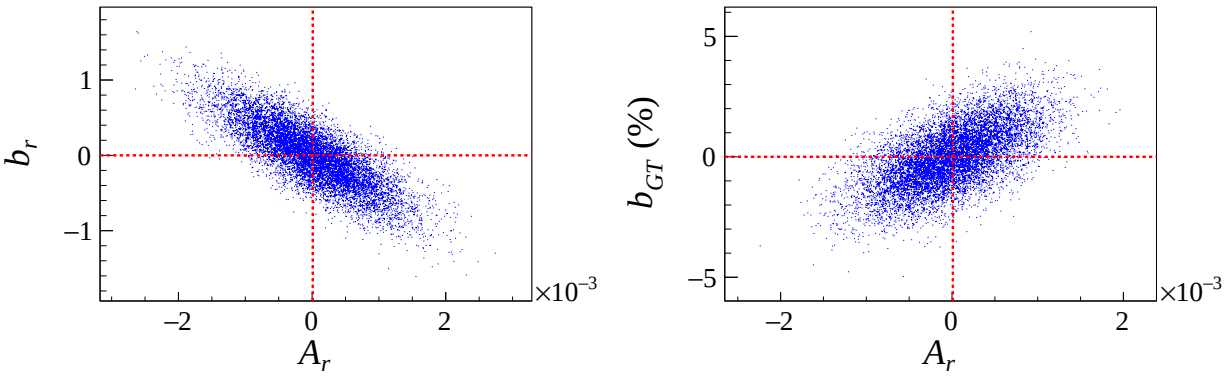

Figure 6-10: The scatter plots of the values of b_r (left panel) and b_{GT} (right panel) relative to A_r. The results are extracted from fits to a sample of 10^4 spectra.

6.4 Determination of the Offset

The offset was estimated with external γ sources. Here we include two γ-energy spectra of a ^{137}Cs source measured with the CsI(Na) detector at a rate of 8170.8 ± 5.1 (cps), shown in the left panel of Fig. 6-11, and a ^{60}Co source measured with the same detector at 14153.4 ± 6.3 (cps), shown in the right panel of Fig. 6-11. The salient features are a full-energy peak in the ^{137}Cs spectrum and two full-energy peaks in the ^{60}Co spectrum. Since the full-energy peaks have known values of energy, if the peak centroids in chan can be determined, the offset can then be extracted from a fit, assuming a linear energy response. Therefore to extract an accurate offset, it is crucial to determine the peak centroids accurately.

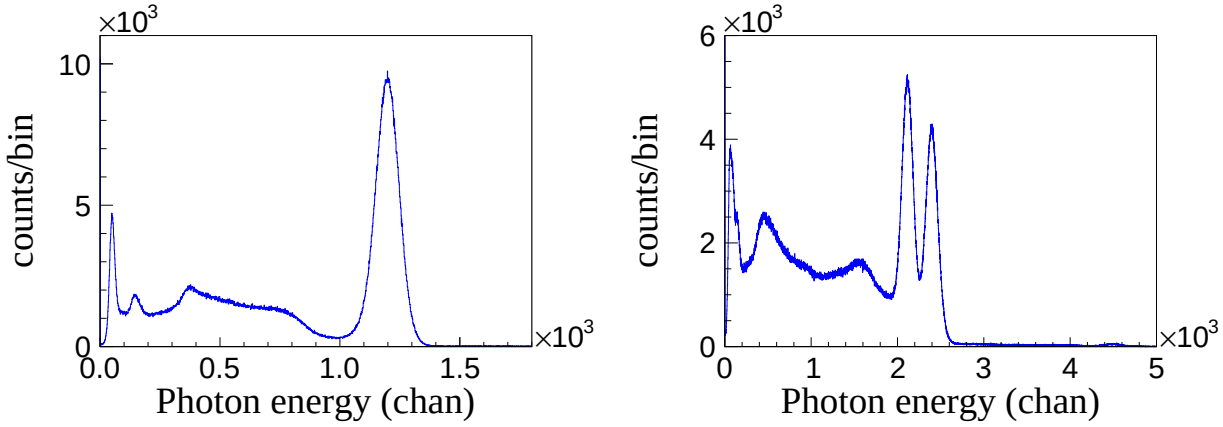

Figure 6-11: Left panel: the γ-energy spectrum of the ^{137}Cs source measured with the CsI(Na) detector at a rate of 8170.9 ± 5.1 (cps). Right panel: the γ-energy spectrum of the ^{60}Co source measured with the CsI(Na) detector at a rate of 14153.4 ± 6.3 (cps).

The shape of each full-energy peak in Fig. 6-11 can be described with a Gaussian function, where the Gaussian mean (μ) and standard deviation (σ^E) represent the centroid and width of the peak and can be extracted from a best fit. However, the presence of the Compton events under the Gaussian peaks affects the fitted value of the centroid. This effect is the smallest when the ratio between the number of Gaussian events and the number of Compton events is the highest. This ratio can be varied by changing the energy range in the fit, as shown in Fig. 6-12 for the ^{137}Cs peak in the left panel of Fig. 6-11, where the light and dark bands represent two energy ranges. Each

band has a width of N chan, covering the same number of channels ($N/2$) above and below the Gaussian centroid determined from a crude estimate. An increase of the band width would reflect the decrease of the Gaussian to Compton ratio.

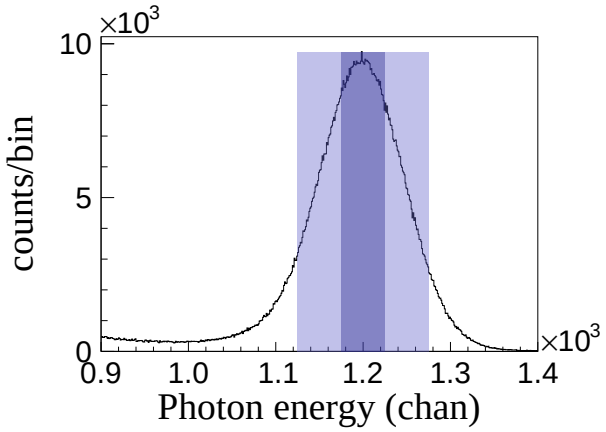

Figure 6-12: The γ-energy spectrum of the ^{137}Cs source measured with the CsI(Na) detector (left panel of Fig. 6-11) zoomed in near the peak. The light and blue bands are examples of two different energy ranges for the fit.

The ^{137}Cs γ peak shown in the left panel of Fig. 6-11 or 6-12 is fitted by a Gaussian function over the ranges of different band widths. The band width varied from 0 to two Gaussian standard deviations determined from a crude estimate. The extracted mean and standard deviation of the peak as a function of the band width are shown in Figs. 6-13. For both the centroid and the width of the peak, the fitted values show clear trends of either increasing or decreasing as the band width increases. As the band width decreases, the fitted results converge to stable values with higher accuracies because of the higher Gaussian to Compton ratio but lower precisions because of the fewer number of events included in the fits.

As the band width decreases from two standard deviations to zero, both the centroid and the width start to converge at a certain band width. This is the optimal band width as a result of a compromise between the accuracy and the precision. For the ^{137}Cs peak, the optimal band width is 72 chan. Similar studies have been done for the two peaks in the ^{60}Cs γ spectrum; the results are shown in Fig. 6-14 and Fig. 6-15 for the left and the right peaks. The optimal band width is 98 chan for the left peak and 168 chan for the right peak.

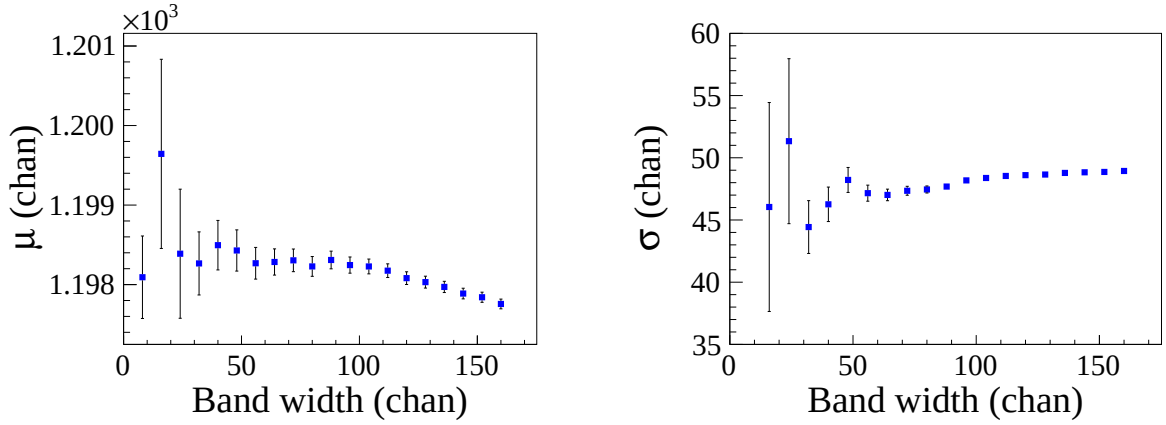

Figure 6-13: The centroid (left panel) and width (right panel) of the peak in the ^{137}Cs γ spectrum (Fig. 6-12 or the left panel of Fig. 6-11) extracted from Gaussian fits as a function of the band width.

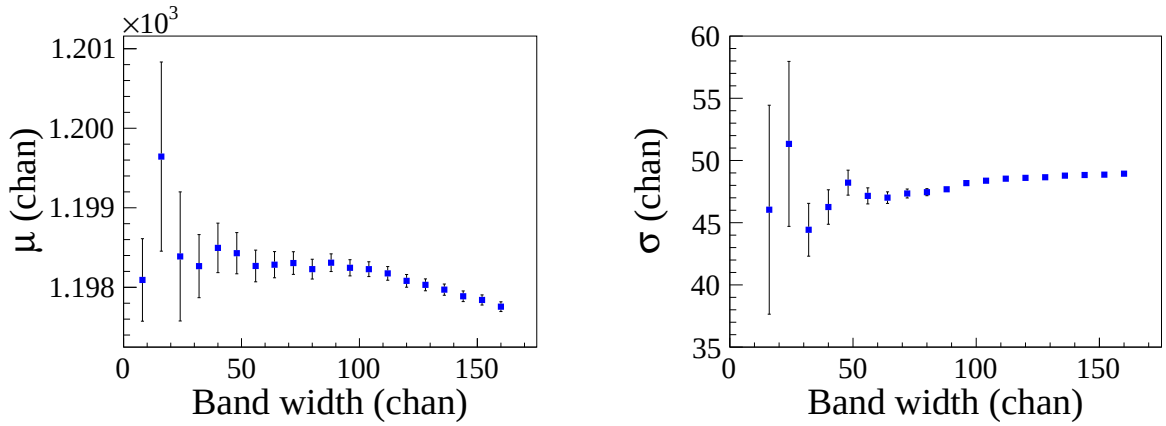

Figure 6-14: The centroid (left panel) and width (right panel) of the left peak in the ^{60}Co γ spectrum (the right panel of Fig. 6-11) extracted from Gaussian fits as a function of the band width.

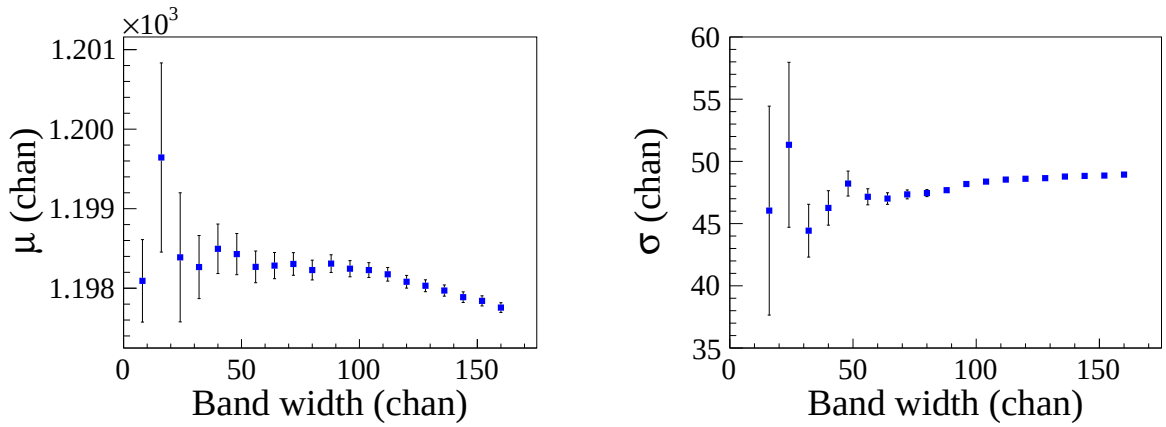

Figure 6-15: The centroid (left panel) and width (right panel) of the right peak in the ^{60}Co γ spectrum (the right panel of Fig. 6-11) extracted from Gaussian fits as a function of the band width.

Table 6-2 summarizes the fit results of the three peaks in ^{137}Cs and the ^{60}Co γ spectra. For each peak, the fits were performed at the optimal band width determined above. The upper panel of Fig. 6-16 shows the centroid as a function of the peak energy. A linear fit gives the following values of gain and offset

$$A = 1.7860 \pm 0.0003 \text{ chan/keV}, \; B = 16.67 \pm 0.32 \text{ chan} \tag{6.8}$$

Table 6-2: The fit results of the ^{137}Cs and ^{60}Co γ peaks. The energy values in the first column are adapted from the NuDat2.7 database [2].

E (keV)	μ (chan)	σ^E (chan)	Band width (chan)	Rate (cps)
661.657(3)	1198.31 ± 0.14	47.35 ± 0.36	72	8170.8 ± 5.1
1173.228(3)	2115.44 ± 0.25	68.28 ± 0.67	98	14153.4 ± 6.3
1332.492(4)	2395.58 ± 0.15	71.90 ± 0.25	168	14153.4 ± 6.3

It is worth emphasizing that the above calibration result is extracted from the ^{137}Cs and ^{60}Co γ spectra measured at high rates of 8170.78 ± 5.14 (cps) and 14153.4 ± 6.3 (cps). It will be shown in Chap. 7 that both the fitted centroid and the width of the peak are affected by the event rate. Therefore rate corrections have to be made to the centroid before determining a final value of the offset. More details about the rate effect are discussed in Chap. 7, where the γ calibration is updated after the rate correction.

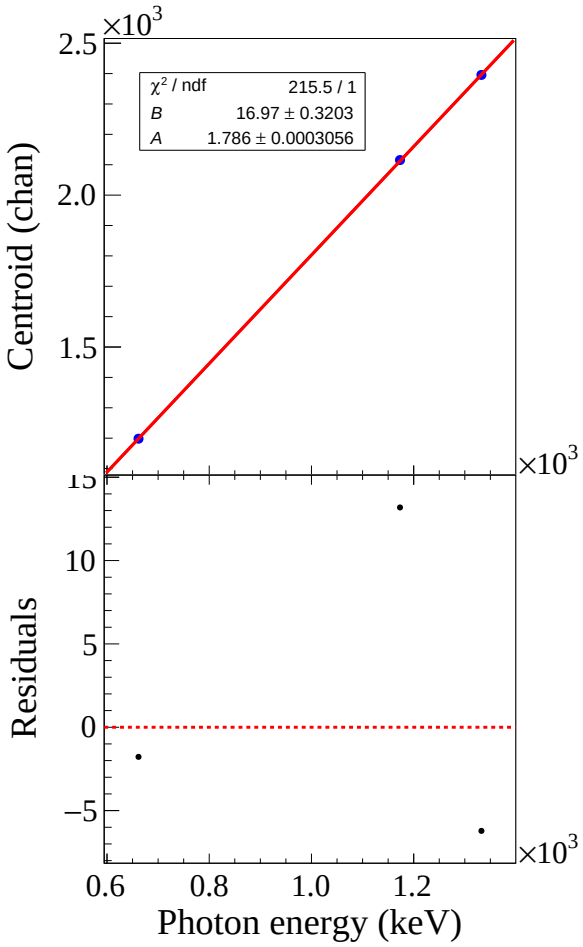

Figure 6-16: Upper panel: the centroid of the γ peaks from ^{137}Cs and ^{60}Co as a function of the peak energy. The red line is a linear fit to the graph. Lower panel: the residuals of the fit.

6.5 Determination of the Nonlinearity

The same data with those in Fig. 6.8 are fitted by a quadratic function shown in Eq. 6.2, where A, B, and P are all free parameters in the fit. The result of the fit is shown in Fig. 6-17, where the extracted value of the non-linearity is

$$P = (-5.04 \pm 0.34) \times 10^{-5} \frac{\text{chan}}{\text{keV}^2}. \tag{6.9}$$

Similar to the offset, since P is determined based on the values of the peak centroid, the rate corrections to the centroid have to be included before determining a final value of P. An updated value of P is provided in Chap. 7.

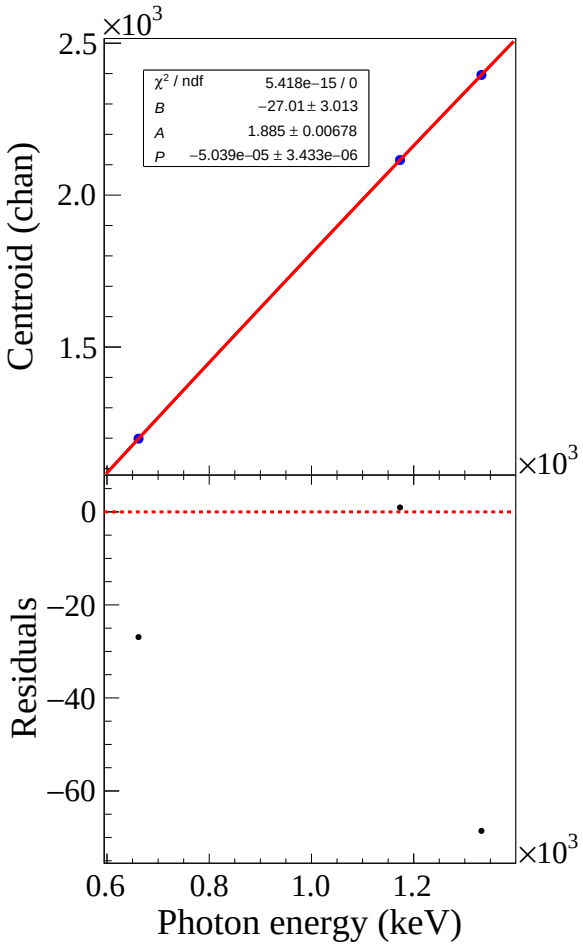

Figure 6-17: Upper panel: the centroid of the γ peaks from ^{137}Cs and ^{60}Co as a function of the peak energy. The red line is a quadratic fit to the graph. Lower panel: the residuals of the fit.

6.6 Determination of the Energy Resolution

The fitted peak widths shown in Table 6-2 can be converted to keV using Eq. 6.8. The resulting width in keV as a function of the peak energy is shown in Fig. 6-18. The graph is fitted by Eq. 6.3, where σ_0 is a free parameter. The extracted value of σ_0 is

$$\sigma_0 = 1.086 \pm 0.003\,(\text{keV})^{1/2}\,. \tag{6.10}$$

An updated value of σ_0 is provided in Chap. 7 after both the fitted peak width and the γ calibration are updated after the rate correction.

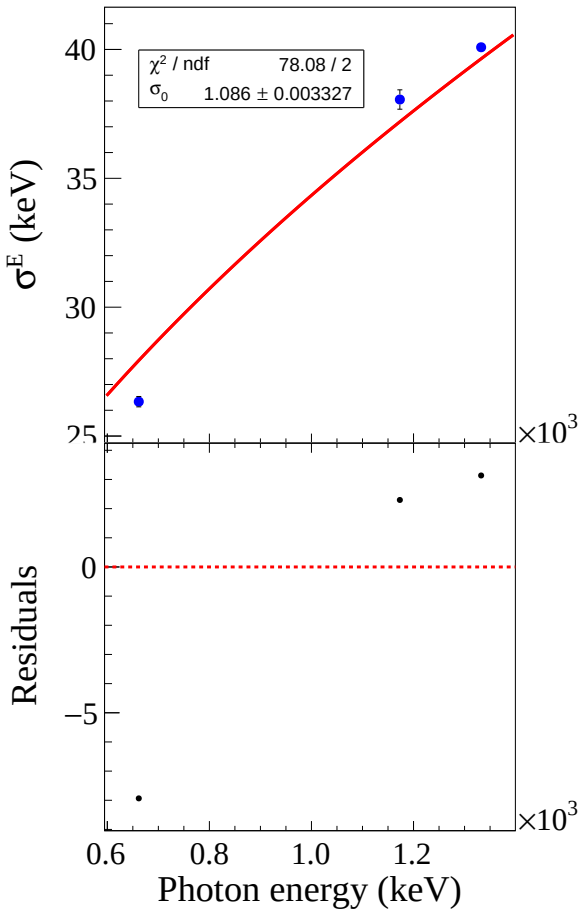

Figure 6-18: Upper panel: the width of the γ peaks from ^{137}Cs and ^{60}Co as a function of the peak energy. The red line is the result of a fit by Eq. 6.3. Lower panel: the residuals of the fit.

CHAPTER 7

RATE EFFECT

The previous chapter has described the energy-calibration parameters without considering the effect of the event rate. However, it was found that the event rate has a significant impact on the recorded spectra. This chapter introduces the size and origin of the rate effect and applies corrections to the energy-calibration parameters accordingly. The updated values of the parameters as well as their uncertainties are provided.

7.1 Introduction

The potential rate effect in the energy calibration was monitored with a ^{137}Cs γ source, whose full-energy peak is described with a Gaussian distribution. The centroid and the width of the peak were measured as a function of the rate with the same CsI(Na) detector described in Chapter 3. The measurements were performed in two conditions: 1) with the ^{6}He beam implanting into the detector at the same time (on-line measurement), and 2) without the implanting ^{6}He beam (off-line measurement). Since the energy of the γ peak is a constant, any changes in the measured peak centroid and peak width are due to the changes in the energy calibration.

7.1.1 On-Line Measurement

In one of the runs during the experiment, a ^{137}Cs source was placed next to the CsI(Na) detector while the detector was being implanted by the ^{6}He beam. The recorded events include both the β particles from ^{6}He decay and the γ rays emitted by the ^{137}Cs source. Figure 7-1 shows a two-dimensional histogram of the time versus the deposited energy recorded during the beam-off intervals. The main features of this two-dimensional histogram are similar to the one shown in the left panel of Fig. 3-11 . In both cases, the number of events decreases as a function of time due to the decay of ^{6}He. A noticeable difference between these two two-dimensional histograms is the presence of a line at about 1000 chan in Fig. 7-1, which is produced by the γ ray from the ^{137}Cs

source.

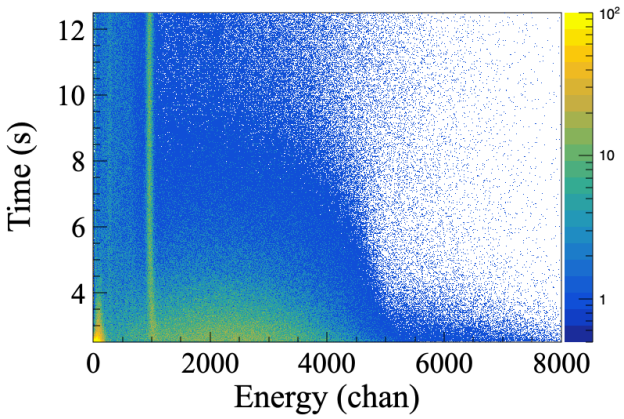

Figure 7-1: Two-dimensional histogram of the time versus the deposited energy of ^{6}He β particles and ^{137}Cs γ rays measured with the CsI(Na) detector recorded during the beam-off intervals

The effect of the rate on the centroid and the width of the γ peak can be studied with the energy spectra projected from different time windows in the two-dimensional spectrum. Figure 7-2 shows the energy spectra projected from four time widows in this run. Each time window contains approximately half a million events.

The energy spectrum corresponding to each time window was fitted by a function consisting of a Gaussian and a β-energy spectrum. The Gaussian centroid extracted from the fits and the average event rate in the time window are shown in each panel of Fig. 7-2. It is clear that as the event rate decreases, both the centroid and the width of the peak decrease as well, indicating the apparent changes to the gain related to the rate.

To quantify the effect of the rate on the peak centroid and width, the data in Fig.7-1 were divided into 49 time windows, and from each, a projected energy spectrum was obtained. Similar fits to the spectra have been performed and the extracted centroid as a function of the average rate in the time window is shown in the left panel of Fig. 7-3. The peak centroid appears to increase linearly as a function of the rate. The data were fitted by the function

$$\mu(r) = a_\mu \times r + b_\mu, \tag{7.1}$$

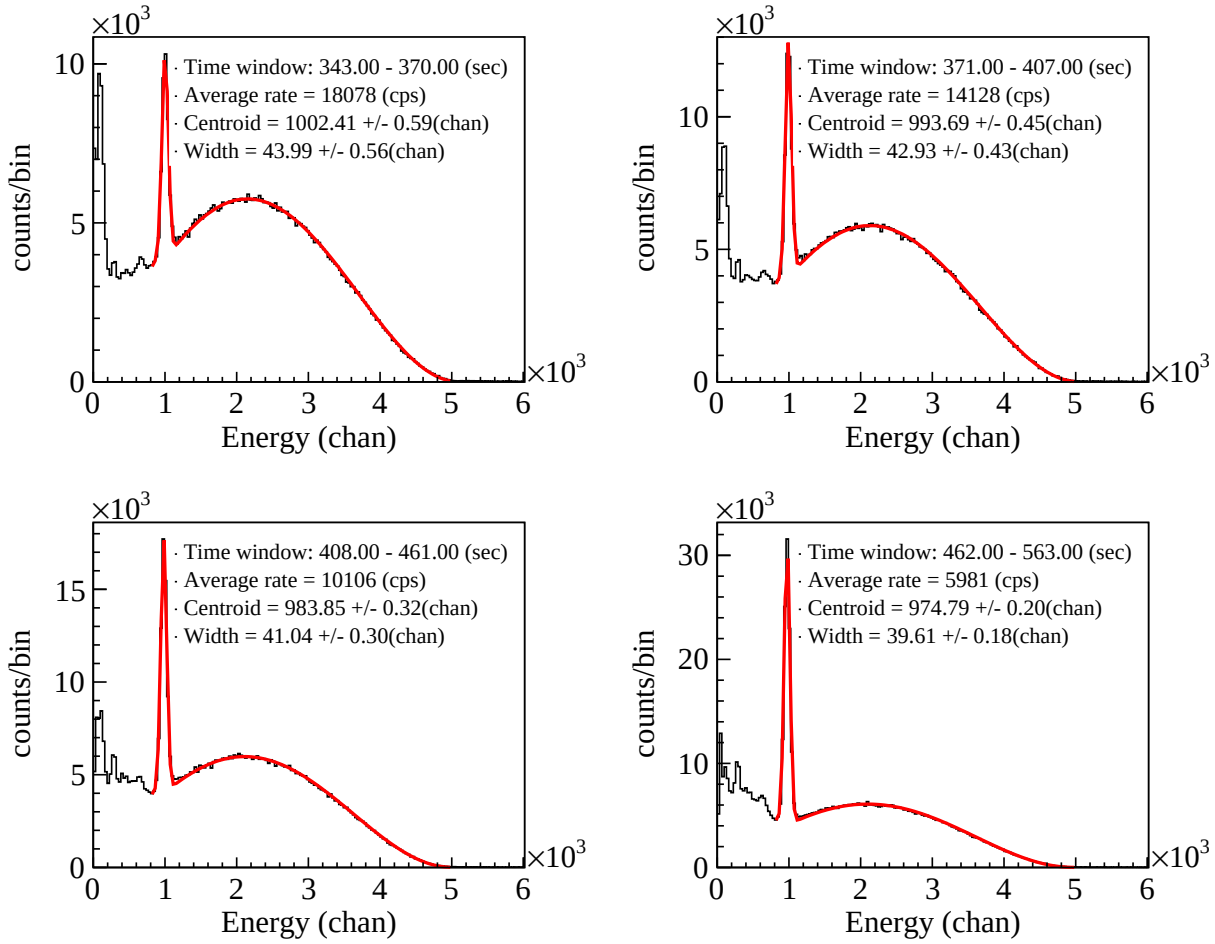

Figure 7-2: The measured energy spectrum of β particles in ^{6}He decay and γ rays emitted by ^{137}Cs projected from four time windows in Fig. 7-1 . The uncertainties associated with the fitted centroid and width are statistical.

where r represents the average rate in a time window, $\mu(r)$ represents the centroid of the peak in chan at rate r, and b_μ is the centroid at zero rate. The fitted slope a_μ is 2.3×10^{-3} chan/cps. Similarly, the peak width appears to increase linearly as a function of the rate, as shown in the right panel of Fig. 7-3. The data were fitted by the function

$$\sigma(r) = a_\sigma \times r + b_\sigma, \tag{7.2}$$

where $\sigma(r)$ represents the width of the peak in chan at rate r, and b_σ is the width at zero rate. The fitted slope a_σ is 4.2×10^{-4} chan/cps.

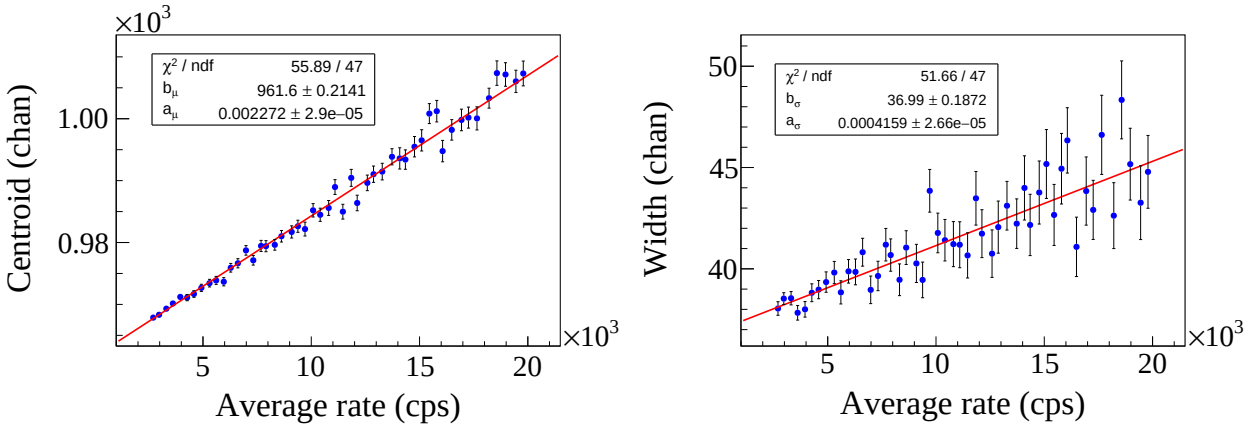

Figure 7-3: The centroid (left panel) and the width (right panel) of the ^{137}Cs γ peak as a function of the average rate in a time window from the on-line measurement.

7.1.2 Off-Line Measurements

The energy of the ^{137}Cs γ peak was also measured at different rates without the ^{6}He beam implanting the CsI(Na) detector. The rate was varied by changing the distance of the ^{137}Cs source from the CsI(Na) crystal. Five measurements were performed with rates at approximately 2, 5, 10, 20, and 40 kcps. The γ peak in each spectrum was fitted with a Gaussian function. The extracted centroid and width of the peak as functions of the event rate are plotted in Fig. 7-4. Similar to the on-line measurement, both the centroid and the width increase linearly with the rate, where the fitted slopes are a_μ is $1.458(2) \times 10^{-3}$ chan/cps and a_σ is $1.27(4) \times 10^{-4}$ chan/cps, respectively.

7.1.3 Origin of the Rate Effect

A possible explanation of the origin of the observed rate effect is the after-glow or phosphorescence in the crystal. The remaining scintillation yield as a fraction of the initial primary scintillation was measured at different times after the deposition of a γ source of 1.5(±0.2) MeV in a CsI(Na) and a CsI(Tl) detector, as shown in Fig. 7-5 [18]. It is clear that the scintillation is still present 10^{-2} seconds after the interaction. In the measurement of the β-energy spectrum, the remaining after-glow scintillation introduces a pile-up effect. As the event rate increases, more scintillation photons corresponding to the previous events pile up to those corresponding to the current event, causing

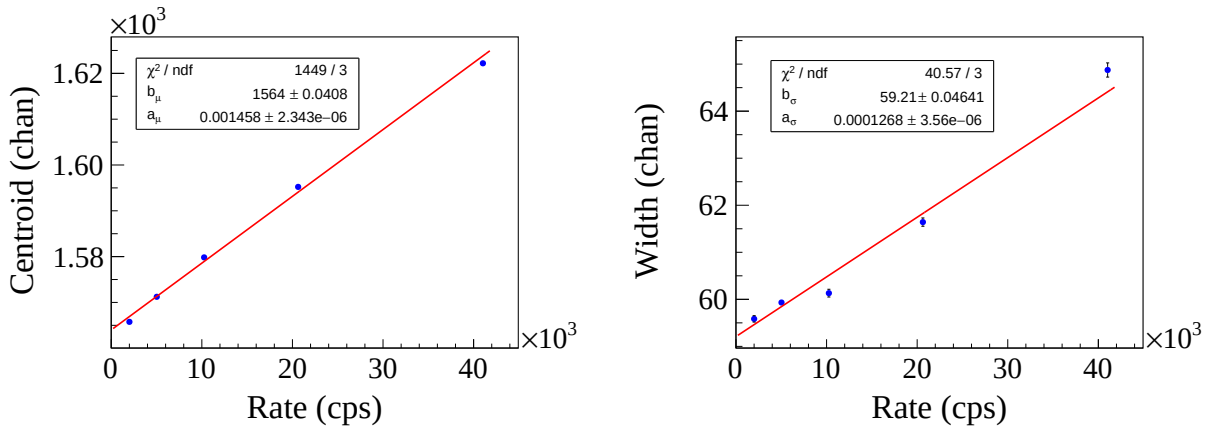

Figure 7-4: The centroid (left panel) and the width (right panel) of the ^{137}Cs γ peak as a function of the average rate in a time window from the off-line measurement

an apparent increase of the observed gain, which explains the increase of the γ peak centroid as a function of rate.

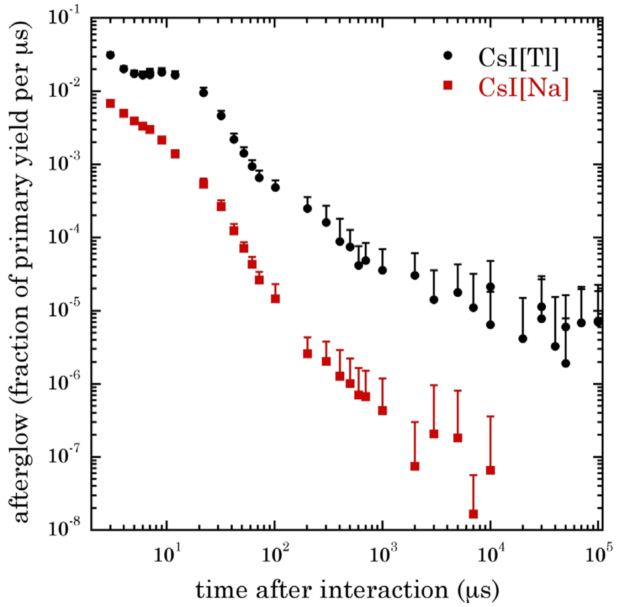

Figure 7-5: The remaining scintillation yield as a fraction of the initial primary scintillation measured at different times after the deposition of a 1.5(±0.2) MeV γ source in the CsI(Na) and the CsI(Tl) detectors. Figure taken from Ref. [18].

7.2 The Impact of the Rate on the Gain

Section 6.3 has discussed the disadvantages of the common calibration method using external γ sources. One of the disadvantages is the rate-dependent gain drift, which would introduce a serious consequence in this experiment. In the on-line measurement shown in Fig. 7-3, the centroid of the γ peak increased by a factor of 3.6% from the lowest rate to the highest, indicating a 3.6% uncertainty of the gain if the γ source were used to determine the gain. According to Table 6-1, this variation of the gain introduces a -1152 variation of b_{WM} and a 0.504 variation of b_{GT}. Such huge systematic uncertainties would make it impossible to extract any useful information of the observables. Therefore the calibration using external γ sources cannot be applied in this analysis.

In the actual analysis, it is shown in Chap. 9 that each one-hour run is divided into six time windows to separate events in different rate ranges. For a given time window, the correct gain corresponds to this particular set of data with the unique amount of after-glow pile-up determined by the history of the crystal. With the auto-calibration method described in Sec. 6.3, the gain corresponding to each time window is extracted from the data themselves, eliminating a potential rate effect on the gain similar to that observed in γ source calibrations.

7.3 The Impact of the Rate on the Offset

7.3.1 Rate Correction to the Offset

The offset was previously estimated in Chap. 6 with the ^{137}Cs and ^{60}Co γ sources. That estimate did not take into account the rate effect on the peak centroid used in the calibration fit shown in Fig. 6.8. Assuming the offset is independent of the event rate, the correct offset is extracted by extrapolating the centroid to zero rate and redoing the fit.

The dependence of the centroid of the ^{137}Cs peak on the rate shown in Eq. 7.1 is generalized for a peak with any energy E:

$$\mu^E(r) = a_\mu^E \times r + \mu^E(0), \tag{7.3}$$

where $\mu^E(r)$ is the centroid of a γ peak of energy E measured at a rate r, $\mu^E(0)$ is the expected

centroid of the same peak at zero rate, and a_μ^E is related to the fitted slope in the left panel Fig. 7-4:

$$a_\mu^E = \frac{E}{E_0} a_\mu, \tag{7.4}$$

where E_0 is the energy of the ^{137}Cs γ peak. Substituting Eq. 7.4 into Eq. 7.3, the expected centroid of a γ peak of energy E at zero rate has the expression

$$\mu^E(0) = \mu^E(r) - \frac{E}{E_0} a_\mu \times r. \tag{7.5}$$

Using the values of $\mu^E(r)$ and the rate in Table 6-2, and the value of a_μ from off-line measurements, the extrapolated centroid at zero rate as a function of energy is shown in Fig. 7-6. A linear fit gives a new calibration:

$$A = 1.7410 \pm 0.0003 \text{ chan/keV}, \; B = 34.52 \pm 0.32 \text{ chan}. \tag{7.6}$$

By comparison, with the peak centroids at non-zero rates shown in Fig. 6-16, the extracted offset is 16.97 ± 0.32 chan. Compared with the new offset after the rate corrections to the centroid, the offset without rate corrections is underestimated by 18 chan. According to Table 6-1, this variation of the offset introduces a -216 variation of b_{WM} and a 0.103 variation of b_{GT}. Such high systematic uncertainties would make it impossible to extract any useful information of the observables. Therefore it is crucial to perform rate corrections to the γ centroid when determining the offset.

7.3.2 Uncertainty of the Offset

The uncertainty of the offset originates from three sources.

- $\delta B_1 = 0.32$ is the uncertainty in the calibration fit shown in Fig. 7-6, which is related to the error of the peak centroid at the non-zero rate shown in Table 6-2.
- δB_2 is the uncertainty related to the error of the fitted a_μ in Fig. 7-4. By replacing the a_μ in Eq. 7.5 by $a_\mu - \delta a_\mu$ and $a_\mu + \delta a_\mu$, two sets of corrected centroids are calculated and are used to determine B. The resulting two offsets are considered the upper and lower limits of

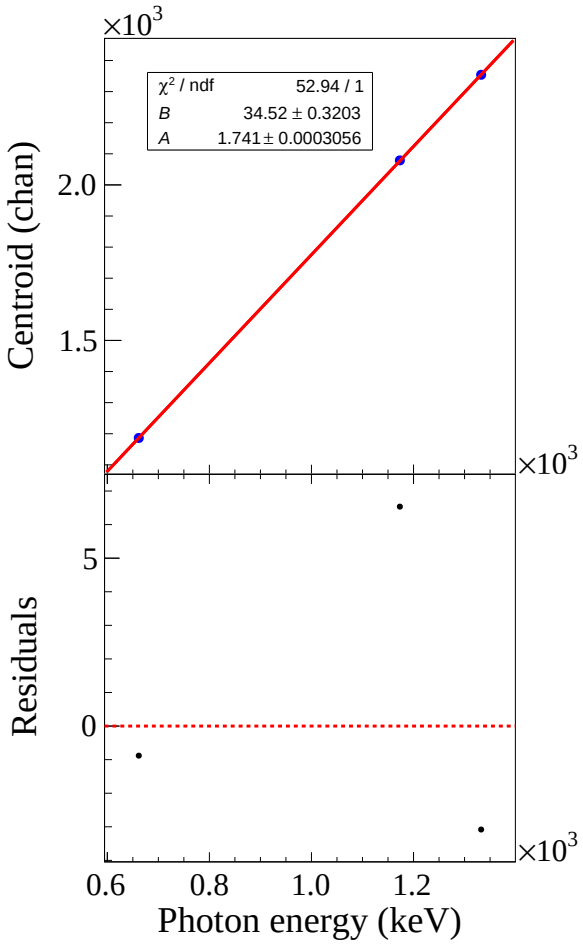

Figure 7-6: Upper panel: the corrected centroid of the γ peaks from ^{137}Cs and ^{60}Co as a function of the peak energy. The red line is a linear fit to the graph. Lower panel: the residuals of the fit.

the offset related to the error of a_μ. Their difference divided by two is an estimate of δB_2 of 0.03 chan.

- δB_3 is the uncertainty related to the rate of the online measurement, which is extracted from the same time windows with those produced Fig. 7-3. The β and γ energy spectra projected from each time window is fitted with an offset shown in Eq. 7.6, producing a reconstructed energy of the ^{137}Cs γ peak. The distribution of the reconstructed γ energy from these time windows is shown in Fig. 7-7. A Gaussian fit to the distribution gives a mean γ energy of 674.9 ± 0.4 keV, where $\delta E_0 = 0.4$ is considered the uncertainty of the γ energy associated with the rate. Similarly, a different mean γ energy is obtained with a different offset (*e.g.* ,

from Eq. 6.8). These results are used to calculate dB/dE_0, which, multiplied with $\delta E_0 = 0.4$, gives the an estimate of δB_3 of 0.7 chan.

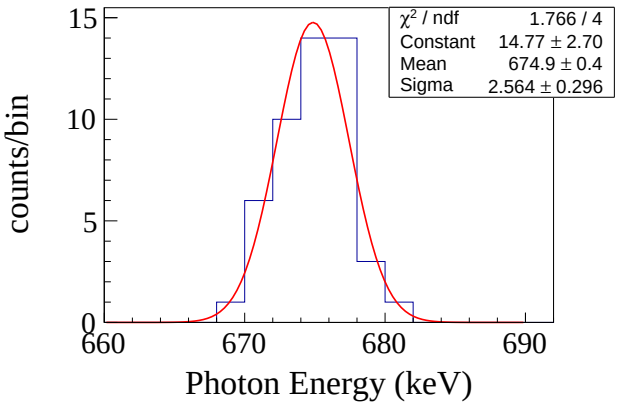

Figure 7-7: The distribution of the reconstructed energy of the ^{137}Cs γ peak extracted from the on-line measurement with the offset value taken from Eq. 7.6.

To summarize, the uncertainty of the offset is

$$\delta B = \sqrt{(\delta B_1)^2 + (\delta B_2)^2 + (\delta B_3)^2} = 0.77 \text{ chan}. \tag{7.7}$$

According to Table 6-1, the projected systematic uncertainties of b_{WM} and b_{GT} are 9.24 and 4×10^{-3}, respectively.

7.4 The Impact of the Rate on the Nonlinearity

The non-linearity was previously estimated in Chapter 6 by fitting the centroid of the ^{137}Cs and the ^{60}Coγ peaks with a quadratic function, which did not take into account the rate effect on the peak centroid. With the corrected centroid calculated in Sec. 7.3.1, a new fit with the quadratic function can be performed. The result of the fit is shown in Fig. 7-8, where the extracted value of the non-linearity is

$$P = (-2.5 \pm 0.3) \times 10^{-5} \frac{\text{chan}}{\text{keV}^2}. \tag{7.8}$$

Compared with the P extracted without the rate corrections shown in Eq. 6.9, the updated P has reduced by a factor of two.

The result in Fig. 7-8 can also be compared with Fig. 7-6, where the same data were fitted by a linear function instead. It is worth noticing that the residuals in Fig. 7-8 are significantly larger than those in Fig. 7-6, which indicates that a linear function describes these data better than a quadratic function. Therefore it is safe to assume a linear response between channel and energy in the analysis and consider P to be zero.

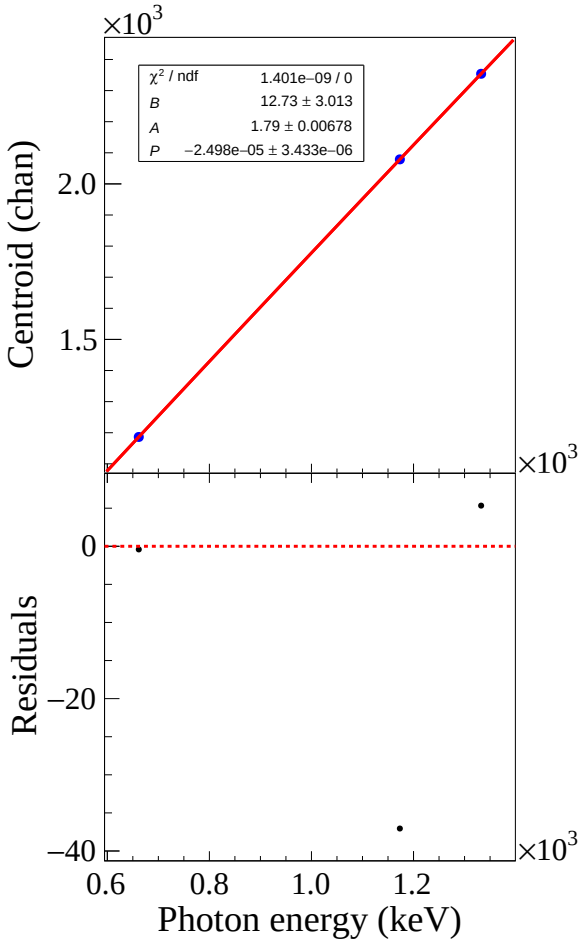

Figure 7-8: Upper panel: the corrected centroid of the γ peaks from ^{137}Cs and ^{60}Co as a function of the peak energy. The red line is a quadratic fit to the graph. Lower panel: the residuals of the fit.

7.5 The Impact of the Rate on σ_0

7.5.1 Rate Correction to the Width

In Chaps. 5 and 6, the width of the peak as a function of energy is described:

$$\sigma^E = \sigma_0\sqrt{E}, \tag{7.9}$$

where σ_0 is estimated in Chapter 6 with the ^{137}Cs and the ^{60}Co γ sources, which did not take into account the rate effect on the peak width.

The dependence of the width of the ^{137}Cs peak on the rate shown in Eq. 7.2 is generalized for a peak with any energy E:

$$\sigma^E(r) = a_\sigma^E \times r + \sigma^E(0), \tag{7.10}$$

where $\sigma^E(r)$ is the width of a γ peak of energy E measured at a rate r, $\sigma^E(0)$ is the expected width of the same peak at zero rate, and a_σ^E is related to the fitted slope in the right panel Fig. 7-4:

$$a_\sigma^E = \sqrt{\frac{E}{E_0}}a_\sigma, \tag{7.11}$$

where E_0 is the energy of the ^{137}Cs γ peak. Substituting Eq. 7.11 into Eq. 7.10, the expected width of a γ peak of energy E at zero rate has the expression

$$\sigma^E(0) = \sigma^E(r) - \sqrt{\frac{E}{E_0}}a_\sigma \times r. \tag{7.12}$$

Using the values of $\sigma^E(r)$ and the rate in Table 6-2, and the value of a_σ extracted from the off-line measurements, the extrapolated width at zero rate as a function of the γ energy is calculated and converted to keV according to the calibration relation shown in Eq. 7.6. The new width in keV at zero rate as a function of energy in keV is shown in Fig. 7-9. A fit by Eq. 6.3 gives the new value of σ_0:

$$\sigma_0 = 1.077 \pm 0.003\,(\text{keV})^{1/2}\,. \tag{7.13}$$

By comparison, with the peak width at non-zero rates shown in Fig. 6-18, the extracted σ_0 is 1.086 ± 0.003 keV$^{1/2}$. Compared with the new value of σ_0 after the rate corrections to the width

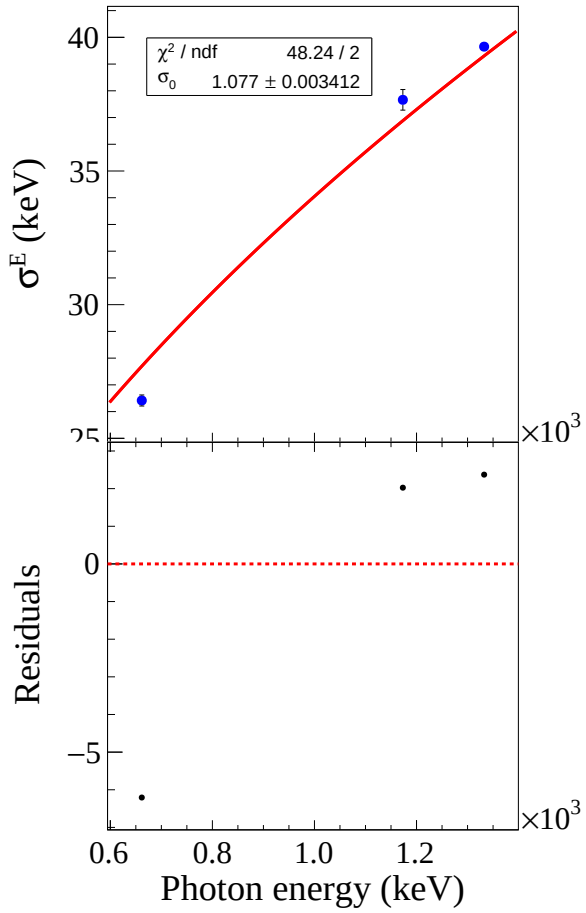

Figure 7-9: Upper panel: the corrected Gaussian width (keV) of the peaks in the ^{137}Cs and the ^{60}Co γ spectra as a function of peak energy. The red line is the result of a fit by Eq. 6.3. Lower panel: the residuals of the fit.

shown in Eq. 7-9, the σ_0 without rate corrections is overestimated by 0.01 keV$^{1/2}$. According to Table 6-1, this variation of σ_0 introduces a -0.74 variation for b_{WM} and a 3×10^{-5} variation for b_{GT}. The rate effect on σ_0 has significantly smaller impacts on the physics observables than the rate effect on the offset does.

The σ_0 can also be extracted from a different set of calibration measurements, including a ^{40}K peak at 1461 keV, a ^{214}Pb peak at 1764 keV, a ^{208}Tl peak at 2615 keV, and the two ^{60}Co peaks. The peak width in keV as a function of the γ energy is shown in Fig. 7-9, where the widths are not corrected based on the event rate since the rates in these measurement are low. A fit by Eq. 6.3

gives a value of σ_0:

$$\sigma_0 = 1.063 \pm 0.003\,(\text{keV})^{1/2}\,. \tag{7.14}$$

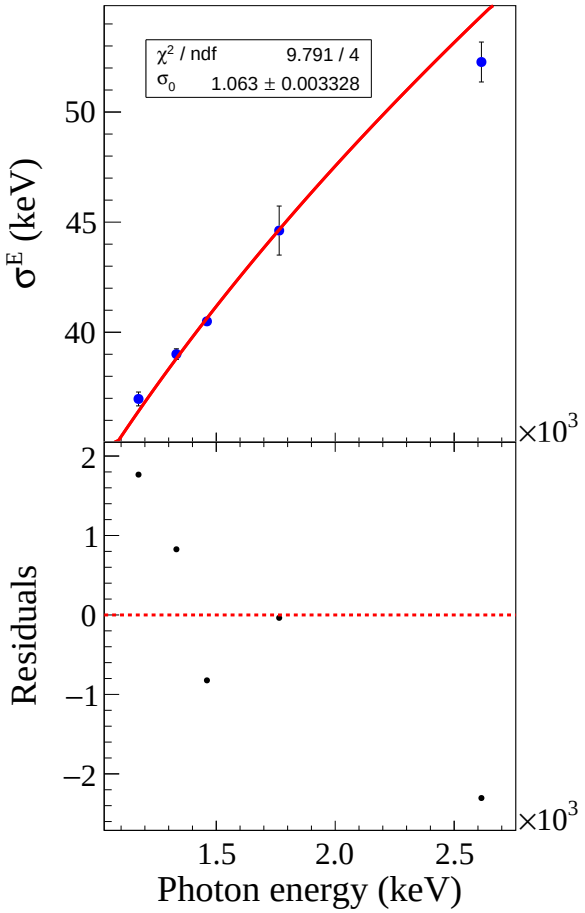

Figure 7-10: Upper panel: the uncorrected Gaussian width (keV) of the peaks in ^{40}K, ^{214}Pb, ^{208}Tl and ^{60}Co γ spectra as a function of the peak energy. The red line is the result of a fit by Eq. 6.3. Lower panel: the residuals of the fit.

Compared with the new value of σ_0 after the rate corrections shown in Eq. 7.13, this σ_0 without rate corrections is underestimated by 0.01 keV$^{1/2}$. Combing the results in Eqs. 6.10, 7.13, and 7.14, for the γ peaks in the rate range of 0-14 kcps, the upper limit of the rate effect on σ_0 is 0.01 keV$^{1/2}$.

7.5.2 σ_0 in the Analysis

In the analysis of the β-energy spectrum in ^{6}He decay, the event rate varies in a wider range of 0-20 kcps. As mentioned in Sec. 7.2, each one-hour run is divided into six time windows to analyze data in different rate ranges separately. The average rate of r for each time window is used to calculate a new σ_0 corresponding to rate r. Specifically, the values of $\sigma^E(r)$ for the three γ peaks at rate r are calculated with Eq. 7.10 and converted to keV according to the auto-calibration to the β-energy spectrum. The new width in keV at rate r as a function of energy in keV is fitted by Eq. 6.3 to extract the σ_0 at rate r. For each time window, the absorbed spectrum from Geant4 is convolved with a σ_0 corresponding to the average rate of the time window.

7.5.3 Uncertainty of the σ_0

The uncertainty of σ_0 originates from three sources.

- $\delta\sigma_{01} = 3 \times 10^{-3}$ keV$^{1/2}$ is the uncertainty in the fit shown in Fig. 7-9, which is related to the error of the width in chan at the non-zero rate shown in Table 6-2.

- $\delta\sigma_{02}$ is the uncertainty related to the error of the fitted a_σ in Fig. 7-4. By replacing the a_σ in Eq. 7.12 by $a_\sigma - \delta a_\sigma$ and $a_\sigma + \delta a_\sigma$, two sets of corrected widths are calculated and are used to determine σ_0. The resulting two values of σ_0 are considered the upper and lower limits of the σ_0 related to the error of a_σ. Their difference divided by two is an estimate of $\delta\sigma_{02}$ of 5×10^{-5} keV$^{1/2}$.

- $\delta\sigma_{03}$ is the uncertainty related to the rate variation within a time window since an average rate of r is used to describe a range of rate in the time window. The average rate variation within a time window can be calculated theoretically assuming an exponential decay. For each bin of the time window in the exponential decay spectrum, the deviation of the rate in this bin from r is calculated. The average rate variation within the time window is the weighted average of these deviations, where the weight is the square root of the number of events in each bin. The calculated average rate variation is $0.0023r$.

A typical r in the first time window (beginning of the decay) is 18.5 kcps (Fig. 9-15), resulting in an average rate variation of 0.04 kcps. Since a much wider rate variation of 0-14 kcps for the γ peaks produced a 0.01 $\text{keV}^{1/2}$ variation of σ_0, the effect of a 0.04 kcps rate variation on σ_0 is much smaller than 0.01 $\text{keV}^{1/2}$. The effect is even smaller in subsequent time windows because of their narrower rate ranges. We use 0.01 $\text{keV}^{1/2}$ as a very conservative estimate of $\delta\sigma_{03}$.

To summarize, the upper limit of uncertainty of σ_r is

$$\delta\sigma_0 = \sqrt{(\delta\sigma_{01})^2 + (\delta\sigma_{02})^2 + (\delta\sigma_{03})^2} = 0.01 \text{ keV}^{1/2}. \tag{7.15}$$

According to Table 6-1, the projected systematic uncertainties of b_{WM} and b_{GT} are 0.8 and 4×10^{-4}, respectively.

CHAPTER 8

FITTING THE β-ENERGY SPECTRUM

The previous chapters have determined an accurate description of the measured β-energy spectrum in ^{6}He decay, from which a function is constructed to fit the measured spectrum, where the observables, b_{WM} and b_{GT}, are extracted. This chapter determines an acceptable fit procedure including three parts: constructing the fit function, finding a robust minimization tool, and determining a fit condition that introduces no bias to the observables. The software tool used in this chapter is ROOT [95], which is an object-oriented data analysis framework for data storage, statistical analysis, and visualization developed at CERN.

8.1 Fit Function

8.1.1 The Expression of the Fit Function

The fit function includes the convolved spectrum in keV described in Chaps. 5, 6, and 7, an energy calibration that transforms the spectrum in keV to a spectrum in chan described in Chaps. 6 and 7, the contributions from the observables described in Eq. 1.26: a spectral function associated with the b_{WM}, and a factor associated with b_{GT}. The expression of the fit function is

$$f(CH; N_0, A, b) = N_0 \times f_c^0(E) \times f_1(E, b_{WM}) \times \left(1 + \frac{b_{GT}}{E}\right), \tag{8.1}$$

$$E = \frac{CH - B}{A}, \tag{8.2}$$

where $f_c^0(E)$ is a function representing the shape of the convolved spectrum. The expression of the spectral function is shown in Eq. 1.27. Equation 8.2 takes into account the energy calibration, where E is the kinetic energy of a β particle in keV, B is the offset determined in Chap. 7, and A is the gain determined during the fit with the auto-calibration described in Chap. 6.

Similar to the Monte Carlo studies and fits in Chapter 6, the fit function $f(CH; N_0, A, b)$ has one variable, CH, which represents the channel number in the β-energy spectrum, and three free

parameters, N_0 for the overall normalization, A for the gain, and b representing either b_{WM} in the SM fit or b_{GT} in the BSM fit.

8.1.2 Constructing a Function from a Histogram

The construction of the fit function requires constructing the function $f_c^0(E)$ that represents the shape of the convolved spectrum. As the convolved spectrum is described by a histogram, $f_c^0(E)$ is not an analytic function. Three methods have been explored to construct a non-analytic fit function from a histogram. The quality of each method is evaluated based on the consistency among the statistical uncertainties of the fitted gain.

For each method, a Monte Carlo sample consisting of 100 β-energy spectra were generated following Eq. 8.1, with $N_0 = 1$, $b_{WM} = b_{WM}^{SM} = 68.22$, $b_{GT} = b_{GT}^{SM} = 0$, $B = 20$ chan, and A=A_{MC}, which a random number in the range of 1.5-1.8 chan/keV. Each spectrum (referred as the Monte Carlo histogram) contains 10^6 events distributed among 256 bins. The spectra were then fitted by Eq. 8.1, where $f_c^0(E)$ was constructed from a histogram using this method. N_0, A, and an observable (b_{WM} for SM fit or b_{GT} for BSM fit) are the free parameters in the fit and B is fixed at 20 chan.

For the simplicity of the study, the $f_c^0(E)$ in Eq. 8.1 was replaced by the phase space spectrum of ^{6}He decay as an approximation. When generating the spectra, the analytic expression of the phase space spectrum was used; whereas when fitting the spectra, a histogram (refereed as the function histogram) generated by Monte Carlo following the phase space factor with 10^9 events distributed among 16384 bins was used. This makes the sample identical for the three methods, leaving the fit function to the sample, specifically, $f_c^0(E)$ constructed with each method, the only difference in this study. The above approximation is valid because a robust fit method determined with one fit function remains robust after introducing a small variation to the fit function. The implementation of each method and the results from the fits are described below. The robustness of the fits is evaluated based on the fraction of the converged fits (f_c), the fraction of fits with p-values above 0.05 (f_p), and the consistency among the statistical uncertainties of the fitted gain.

8.1.2.1 GetBinContent

The most direct estimate to $f_c^0(E)$ is the number of events in the bin corresponding to energy E, which can be acquired with the `GetBinContent` method in the `TH1` class in ROOT. From the 100 SM fits with this method, $f_c = 28\%$ and $f_p = 10\%$. The fit results with p-values above 0.05 as a function of the input gain in the Monte Carlo is shown in Fig. 8-1, where both b_{WM} (left panel) and the relative gain variation A_r (right panel) from the fits show inconsistent statistical errors among the fits. From the BSM fits, $f_c = 13\%$ and $f_p = 5\%$. The fit results with p-values above 0.05 are shown in Fig. 8-2, where similar inconsistencies among the statistical errors are observed.

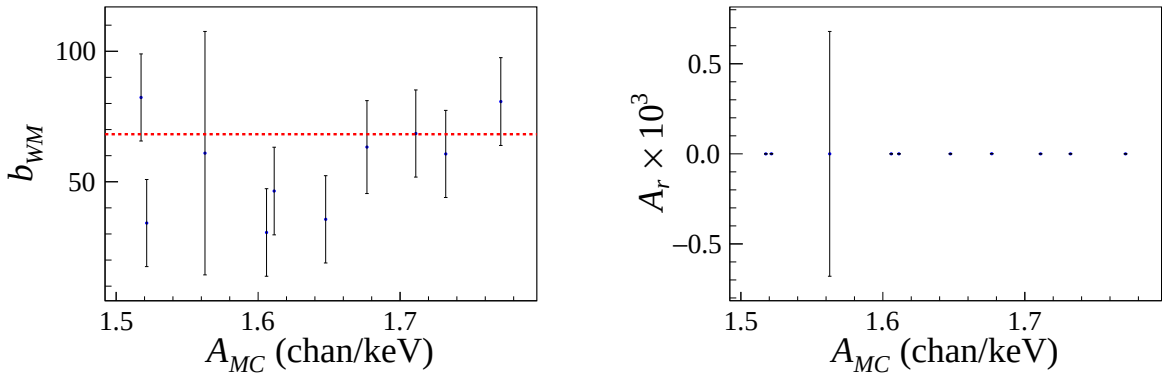

Figure 8-1: Left panel: values of b_{WM} extracted from SM fits using `GetBinContent`. The dotted line indicates the input value used in the Monte Carlo. Right panel: values of A_r calculated with A extracted from the same fits.

The above discrepancy among the statistical errors originates from the statistical nature of a histogram. As the number of events in a bin and in its neighbor bins is subject to statistical fluctuations, the constructed fit function is not smooth. Figure 8-3 shows a typical SM fit to a β-energy spectrum generated by Monte Carlo zoomed in near the top of the spectrum. The fit function shows a zig-zag structure, causing inconsistent statistical errors among fits.

8.1.2.2 Linear Interpolation

To improve the smoothness of the fit function, when estimating the value of $f_c^0(E)$ using the bin content, one should take into account not only the exact bin corresponding to energy E, but

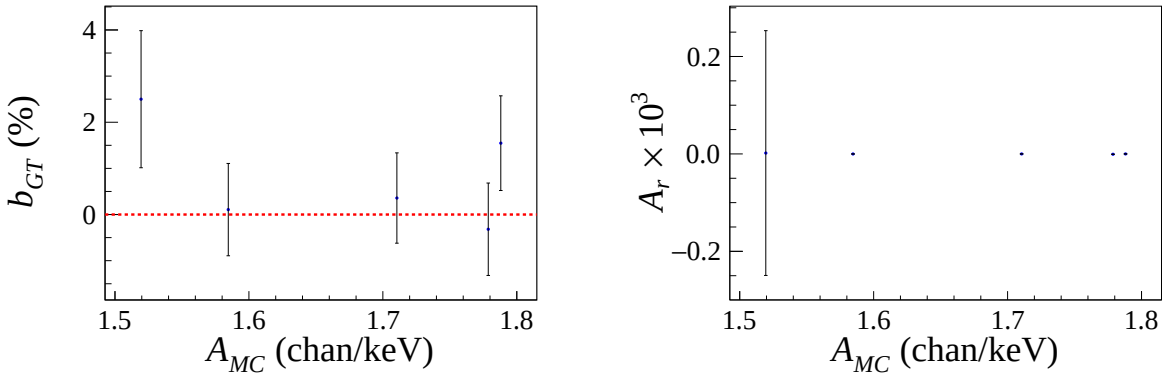

Figure 8-2: Left panel: values of b_{GT} extracted from BSM fits using `GetBinContent`. The dotted line indicates the input value used in the Monte Carlo. Right panel: values of A_r calculated with A extracted from the same fits.

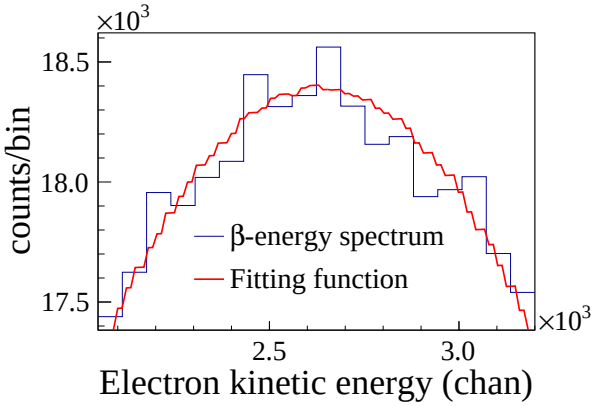

Figure 8-3: A typical SM fit to a β-energy spectrum generated by Monte Carlo. The fit uses the number of events in the bin corresponding to E to estimate $f_c^0(E)$. The spectrum is zoomed in near the top to show the details of the structure.

also the neighbor bins. One approach is to perform a linear interpolation with the `Interpolate` method in the `TH1` class in ROOT. Given an energy E, `Interpolate` looks for the bin number (i) corresponding to E, and estimates $f_c^0(E)$ by an interpolation based on the content of the two nearest bins ($i-1$ and $i+1$).

With $f_c^0(E)$ constructed using `Interpolate`, the new fit function results in $f_c = 99\%$ and $f_p = 96\%$ from the 100 SM fits. The extracted b_{WM} from fits with p-values above 0.05 is shown in the left panel Fig. 8-4 with mostly consistent statistical errors among the fits. The distribution of these statistical errors is plotted in the right panel, where the majority of the statistical errors are

consistent while there are a few fits that produced significantly lower statistical errors. From the same fits, the calculated A_r from the fitted A has a similar behavior, as shown in Fig. 8-5, where the left panel shows the values of A_r and the right panel shows the statistical errors of A. From the BSM fits, f_c = 100% and f_p = 92%. The results from fits with p-values above 0.05 are shown in Figs. 8-6 and 8-7, where both b_{GT} and A have mostly consistent statistical errors among the fits but with a few fits resulting in lower statistical errors.

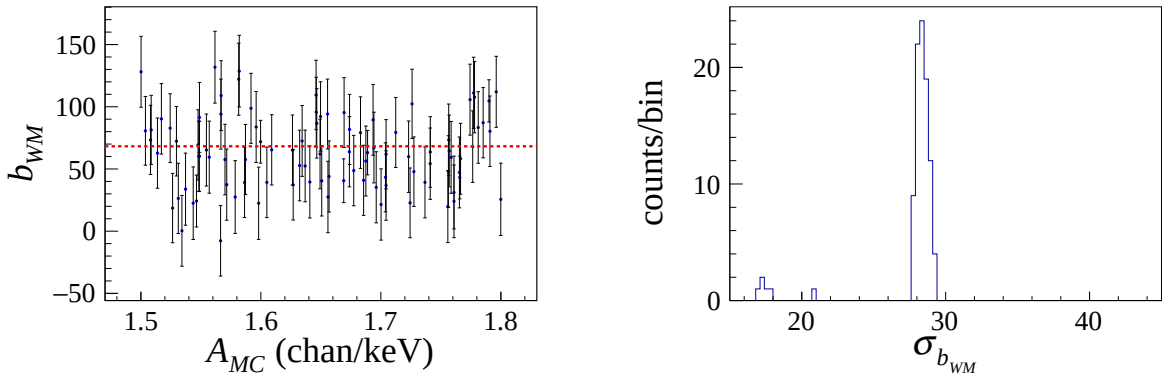

Figure 8-4: Left panel: values of b_{WM} extracted from SM fits using `Interpolate`. The dotted line indicates the input value used in the Monte Carlo. Right panel: distribution of the statistical errors of b_{WM} from the same fits.

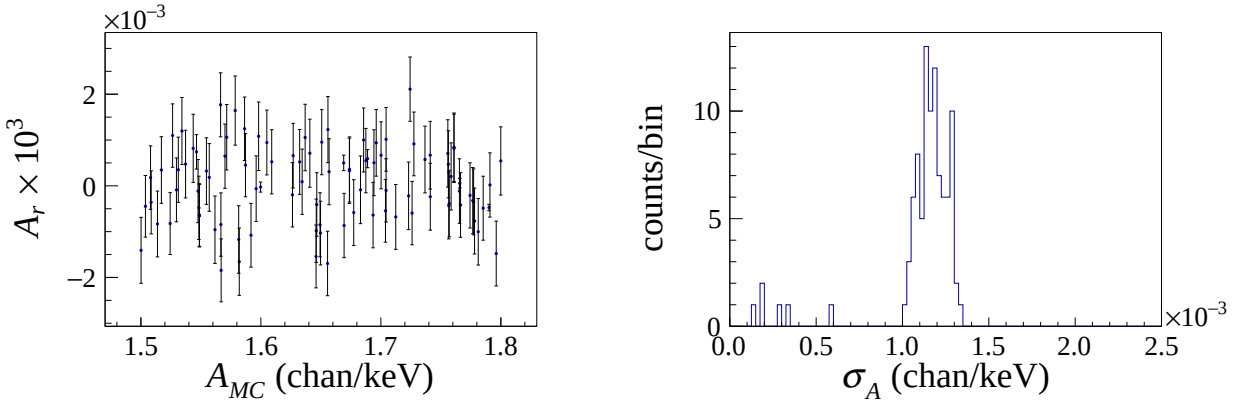

Figure 8-5: Left panel: values of A_r extracted from SM fits using `Interpolate`. Right panel: distribution of the statistical errors of A from the same fits.

The above results indicate that the `Interpolate` method is robust with close to 100% converged fits, but the statistical errors of the parameters extracted from the fits are not completely consistent.

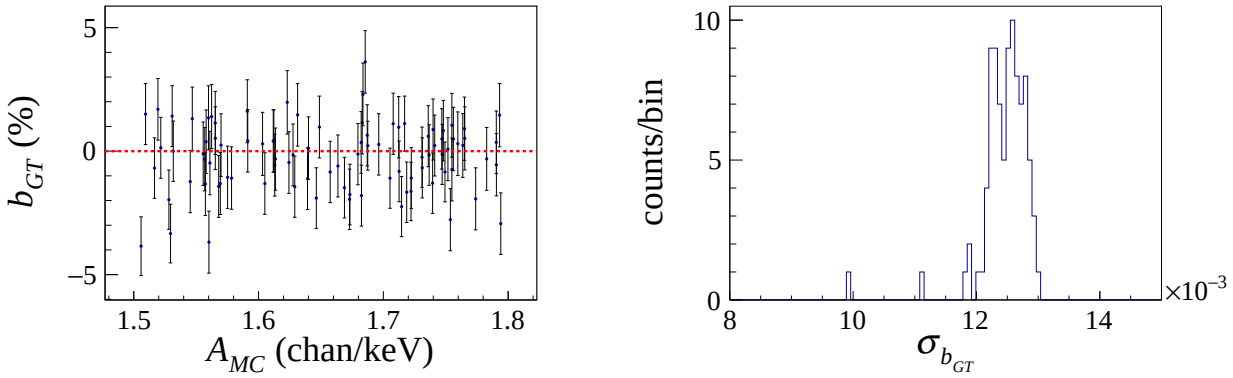

Figure 8-6: Left panel: values of b_{GT} extracted from BSM fits using `Interpolate`. The dotted line indicates the input value used in the Monte Carlo. Right panel: distribution of the statistical errors of b_{GT} from the same fits.

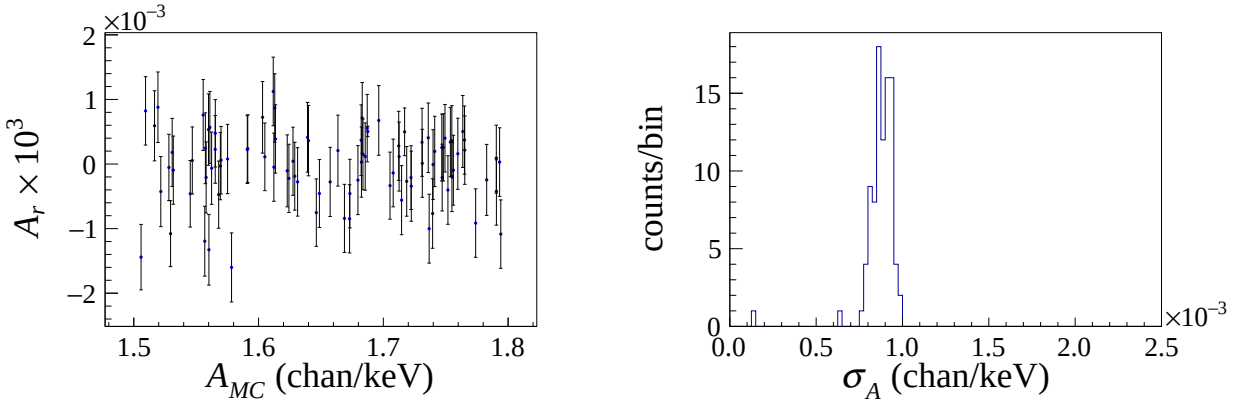

Figure 8-7: Left panel: values of A_r extracted from BSM fits using `Interpolate`. Right panel: distribution of the statistical errors of A from the same fits.

The possible reason is that the linear interpolation is not sufficient to make the fit function smooth enough, and a higher-order interpolation is required.

8.1.2.3 Spline Interpolation

To further improve the smoothness of the fit function, spline interpolations have been explored to estimate $f_c^0(E)$. The `TSpline` class in ROOT is capable of performing third (`TSpline3`) and fifth (`TSpline5`) spline interpolations. For a given a histogram, a spline object can be created that describes the shape of the histogram, and it acts as a smooth function. The value of the spline

object at E, acquired with an `Eval` method, provides a smooth estimate of $f_c^0(E)$.

With $f_c^0(E)$ constructed using `Tspline3`, the new fit function results in f_c = 100% and f_p = 98% from the 100 SM fits. The results extracted from fits with p-values above 0.05 are shown in Fig. 8-8 for b_{WM} and Fig. 8-9 for A_r, where the statistical errors of both b_{WM} and A are consistent. From the BSM fits, f_c = 100% and f_p = 89%. The result extracted from fits with p-values above 0.05 are shown in Fig. 8-10 for b_{GT} and Fig. 8-11 for A_r, where both b_{GT} and A show consistent statistical errors among the fits.

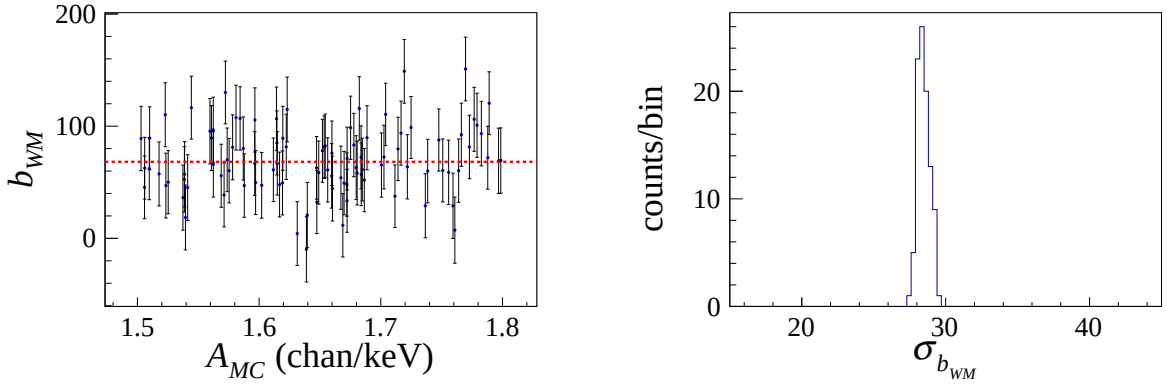

Figure 8-8: Left panel: values of b_{WM} extracted from SM fits using `Tspline3`. The dotted line indicates the input value used in the Monte Carlo. Right panel: distribution of the statistical errors of b_{WM} from the same fits.

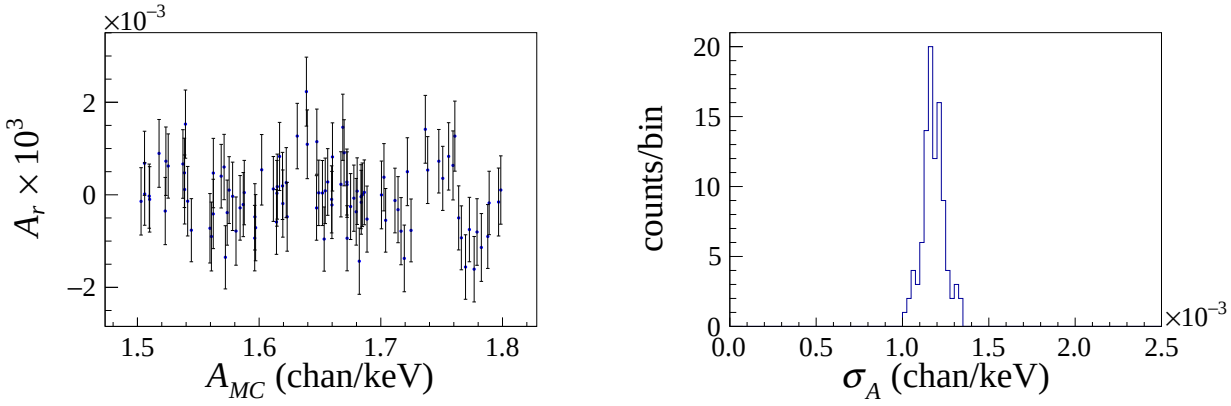

Figure 8-9: Left panel: values of A_r extracted from SM fits using `Tspline3`. Right panel: distribution of the statistical errors of A from the same fits.

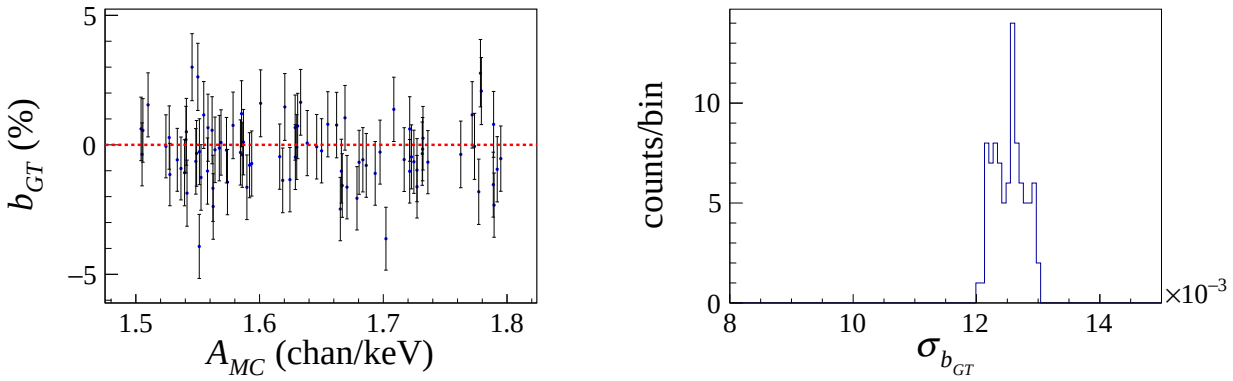

Figure 8-10: Left panel: values of b_{GT} extracted from BSM fits using `Tspline3`. The dotted line indicates the input value used in the Monte Carlo. Right panel: distribution of the statistical errors of b_{GT} from the same fits.

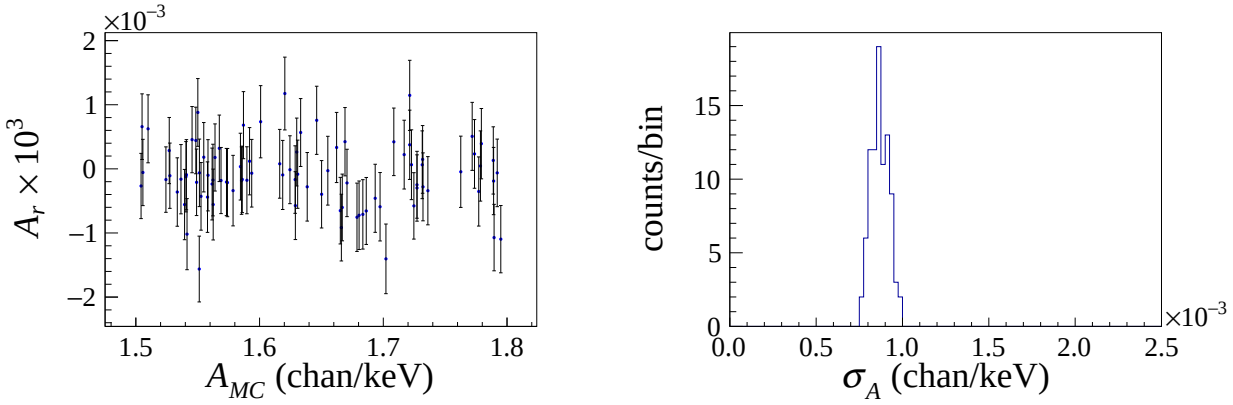

Figure 8-11: Left panel: values of A_r extracted from BSM fits using `Tspline3`. Right panel: distribution of the statistical errors of A from the same fits.

To compare the shape of the fit function in Fig. 8-3 where `GetBinContent` was used, Fig. 8-12 shows a SM fit to the same β-energy spectrum as that shown in Fig. 8-3 but with a spline interpolation. The spectrum zoomed in near the top, a much smoother fit function is seen.

It is clear that among the three methods studied above, the spline interpolation, which gives consistent statistical errors of the fitted parameters and a f_c of 100%, is a correct approach to construct $f_c^0(E)$ from a histogram. For all three methods, f_p is higher for the SM fits than for BSM fits. The methods and conditions used in the fit with the spline interpolation are taken as a reference in the rest of the chapter. Each of the rest of the studies was performed with one method

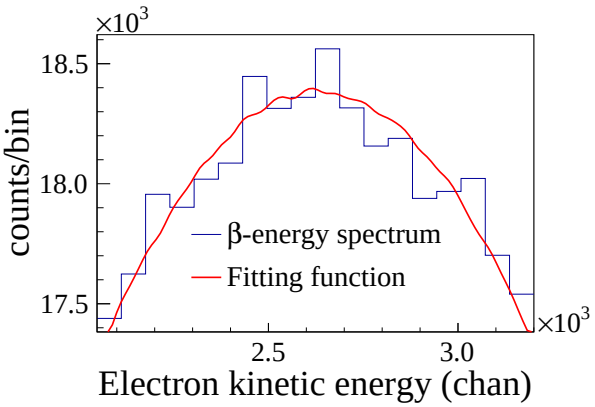

Figure 8-12: A typical SM fit to a β-energy spectrum generated by Monte Carlo. The fit uses a spline interpolation at E to estimate $f_c^0(E)$. The spectrum is zoomed in near the top to show the details of the structure.

or condition different from this reference.

8.2 Fit Procedure

With a correct fit function constructed, one can use the `TH1:Fit` method to fit the data. It is important to determine a robust fit procedure, i.e., the fit method and the minimization tool.

8.2.1 χ^2 and Log-Likelihood

The available fit methods in the `ROOT::Fit::Fitter` class include: least-square fit, binned likelihood fit, un-binned likelihood fit, and linear fit, which all require a minimization process. This chapter has studied the least-square (χ^2) and the binned likelihood (refereed as log-likelihood below) fits. The results shown previously in Figs. 8-8, 8-9, 8-10, and 8-11 are from the χ^2 fits. Similar fits are performed but with the log-likelihood method. The results for SM fits are similar to Figs. 8-8 and 8-9, with $f_c = 100\%$ and $f_p = 93\%$, and the results for BSM fits are similar to Figs. 8-10 and 8-11, with $f_c = 100\%$ and $f_p = 92\%$. In both SM and BSM fits, consistent statistical errors of both the observables and the fitted gain are observed. Therefore under this fit condition, the χ^2 and the log-likelihood methods have similar performance in terms of the robustness.

8.2.2 Minimizer

For the minimization process required by the χ^2 and the log-likelihood fits, a few minimizer libraries are available in ROOT. The ROOT website [96] recommends the use of `Minuit` (`TMinuit` or `Minuit2`) for multi-dimensional minimizations. Since the fit function in Eq. 8.1 has three free parameters, `Minuit` is used for minimizations in this study.

Here we have studied the `TMinuit` and the `Minuit2` fits. The results shown in Figs. 8-8, 8-9, 8-10, and 8-11 are from `Minuit2` fits. Similar fits can be performed but with the `TMinuit` method. The results for SM fits are similar to Figs. 8-8 and 8-9 and the results for BSM fits are similar to Figs. 8-10 and 8-11. Both SM and BSM fits resulted in $f_c = 100\%$ and $f_p = 91\%$ and consistent statistical errors of both the observables and the fitted gain were observed. Therefore in this study, `TMinuit` and the `Minuit2` minimization methods have similar performances in terms of the robustness.

8.3 Fit Condition

The fit results depend on the properties of the histograms, such as the statistics and binning. In the previous fits, 10^6 events were generated for each Monte Carlo spectrum. Both the Monte Carlo histogram and the function histogram had 16384 initial bins and were rebinned by a factor of 64 before the fit. This section studies the impacts of the statistics and the binning on the fit results, from which we have determined acceptable fit conditions, i.e., the conditions that result in a high f_c, a high f_p, and a bias smaller than one standard deviation. The bias of a variable X is defined as

$$\text{Bias} = \frac{\overline{X} - X_i}{\sigma_{\overline{X}}}, \tag{8.3}$$

where $\overline{X}$ is the mean value of X extracted from the fits, X_i is the input value of X in the Monte Carlo, and $\sigma_{\overline{X}}$ is the standard deviation of the fitted values.

8.3.1 Number of Events

To study the impact of the number of events (N_e) in each Monte Carlo spectrum on the results, similar simulations and fits to those in Sec. 8.1.2.3 were performed but with the different number of events generated in each spectrum. The results fitted with the χ^2 method and `Minuit2` minimizer are shown as a function of N_e in Figs. 8-13 and 8-14 for the SM and the BSM fits, respectively. The left panels of both figures show the results for f_c, where most fits to the spectra with more than 10^4 events have acceptable convergence performances. However, f_p highly depends on N_e, as shown in the middle panels, where 10^5 and 10^6 number of events produce the highest f_p. The absolute value of the bias decreases as a function of N_e in both SM and BSM fits, as shown in the right panels. The values of N_e that result in both high f_p and bias under one standard deviation in the SM and the BSM fits are 10^5 and 10^6.

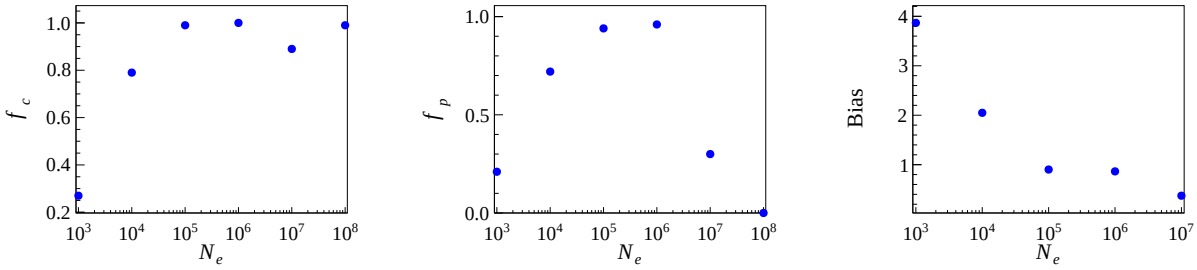

Figure 8-13: Results from SM fits with the χ^2 method. Left panel: the fraction of the converged fits as a function of the number of events in each Monte Carlo histogram. Middle panel: the fraction of fits with p-values above 0.05 as a function of the number of events. Right panel: the bias as a function of the number of events.

Similar results fitted with the log-likelihood method are shown in Figs. 8-15 and 8-16 for the SM fits and the BSM fits, respectively. The left panels of both figures show that the fits to spectra with more than 10^5 events have acceptable convergence performances. Similar to the results with the χ^2 method, f_p highly depends on N_e, as shown in the middle panels, with 10^5 and 10^6 number of events producing the highest f_p. The absolute value of the bias decreases as a function of N_e in the BSM fits but shows no trend in the SM fits. The value of N_e resulting in both high f_p and values of bias under one standard deviation in the SM and the BSM fits is 10^6.

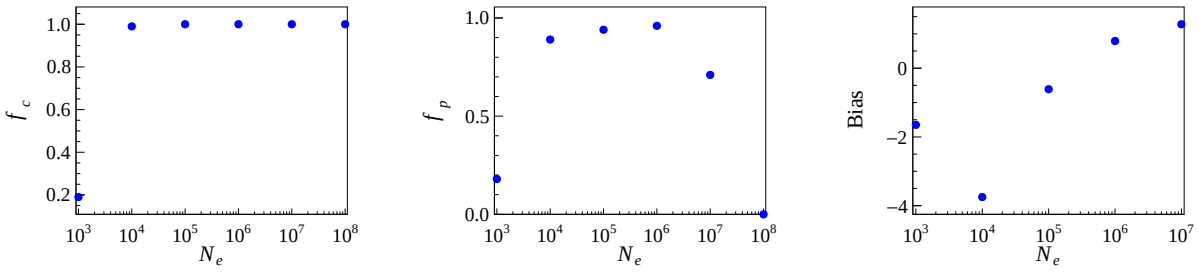

Figure 8-14: Results from BSM fits with χ^2 method. Left panel: the fraction of the converged fits as a function of the number of events in each Monte Carlo histogram. Middle panel: the fraction of fits with p-values above 0.05 as a function of the number of events. Right panel: the bias as a function of the number of events.

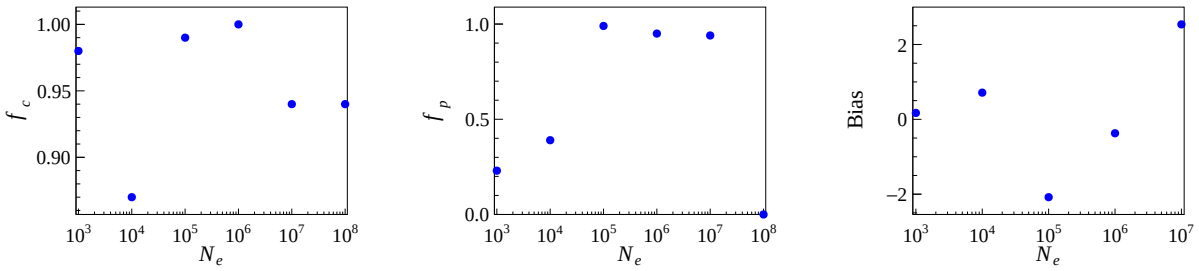

Figure 8-15: Results from SM fits with the log-likelihood method. Left panel: the fraction of the converged fits as a function of the number of events in each Monte Carlo histogram. Middle panel: the fraction of fits with p-values above 0.05 as a function of the number of events. Right panel: the bias as a function of the number of events.

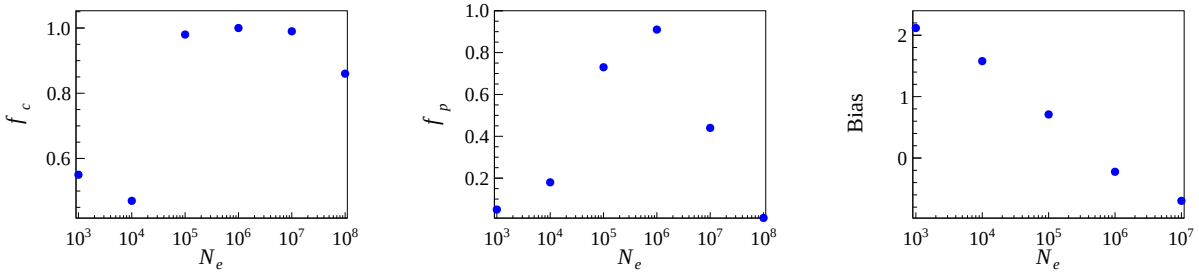

Figure 8-16: Results from BSM fits with log-likelihood method. Left panel: the fraction of the converged fits as a function of the number of events in each Monte Carlo histogram. Middle panel: the fraction of fits with p-values above 0.05 as a function of the number of events. Right panel: the bias as a function of the number of events.

From the above results of the χ^2 and the log-likelihood fits, the optimal number of events for the fitted histogram is 10^6 when the function histogram has a statistics of 10^9 events.

8.3.2 Number of Bins

The numbers of bins for both the Monte Carlo histogram and the function histogram have impacts on the quality of the fit. These impacts are studied with similar simulations and fits to those in Sec. 8.1.2.3 but with different combinations of the rebin factor of the function spectrum (R_{F}) and the rebin factor of the Monte Carlo histogram (R_{MC}) . Here both histograms have an initial number of bins equal to 16384.

For the SM fits with χ^2, the f_c and f_p results are show as a function of the $\log_2 R_{\mathrm{MC}}$ and $\log_2 R_{\mathrm{F}}$ in Fig. 8-17. he result of f_p suggests that the (R_{F}, R_{MC}) pairs that satisfy $R_{\mathbf{F}} \geq R_{\mathbf{MC}}$ are preferred. Therefore for the bias results shown in Fig. 8-18, only binning combinations satisfying $R_{\mathbf{F}} \geq R_{\mathbf{MC}}$ are of interest. The left panel of Fig. 8-18 shows the bias from the SM fits with χ^2, and the right panel is a zoomed-in view of the left graph. Most of the ($R_{\mathbf{F}}$, $R_{\mathbf{MC}}$) pairs on the diagonal have biases lower than one standard deviation. For the BSM, similar results to the SM fits were observed. The combinations of R_{F} and R_{MC} that satisfy $R_{\mathbf{F}} \geq R_{\mathbf{MC}}$ are preferred based on the f_c and f_p results, and most of the (R_{F}, R_{MC}) pairs on the diagonal have biases lower than one standard deviation.

For the log-likelihood fits, similar results to the χ^2 fits were observed. The results for the SM fits with log-likelihood are shown in Figs. 8-19 and 8-20, where combinations of R_{F} and R_{MC} that satisfy $R_{\mathbf{F}} \geq R_{\mathbf{MC}}$ are preferred based on the f_c and f_p results, and most of the (R_{F}, R_{MC}) pairs on the diagonal have biases lower than one standard deviation. Similar results were observed in the BSM fits with log-likelihood.

8.4 Determined Fit Condition

To summarize, in this study, both χ^2 and log-likelihood fits are acceptable fit methods, and both `TMinuit` and `Minuit2` are acceptable minimizers. For high f_c and f_p, 10^5 and 10^6 events

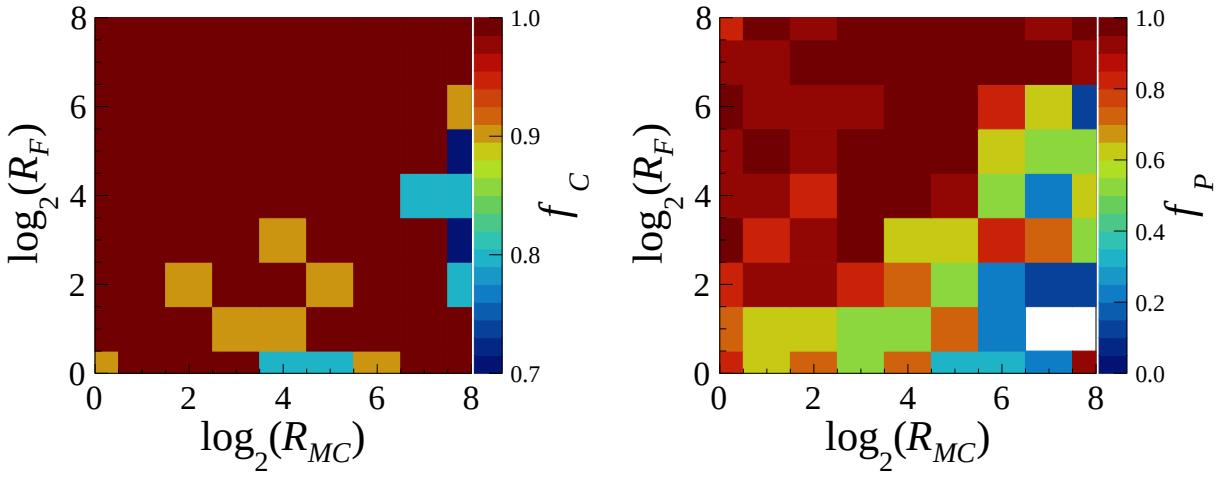

Figure 8-17: Left panel: the fraction of convergent SM fits with χ^2 as a function of the function spectrum rebin factor (R_{F}) and the Monte Carlo histogram rebin factor (R_{MC}). Right panel: the fraction of the fits with p-values over 0.05 as a function of the function spectrum rebin factor (R_{F}) and the Monte Carlo histogram rebin factor (R_{MC}).

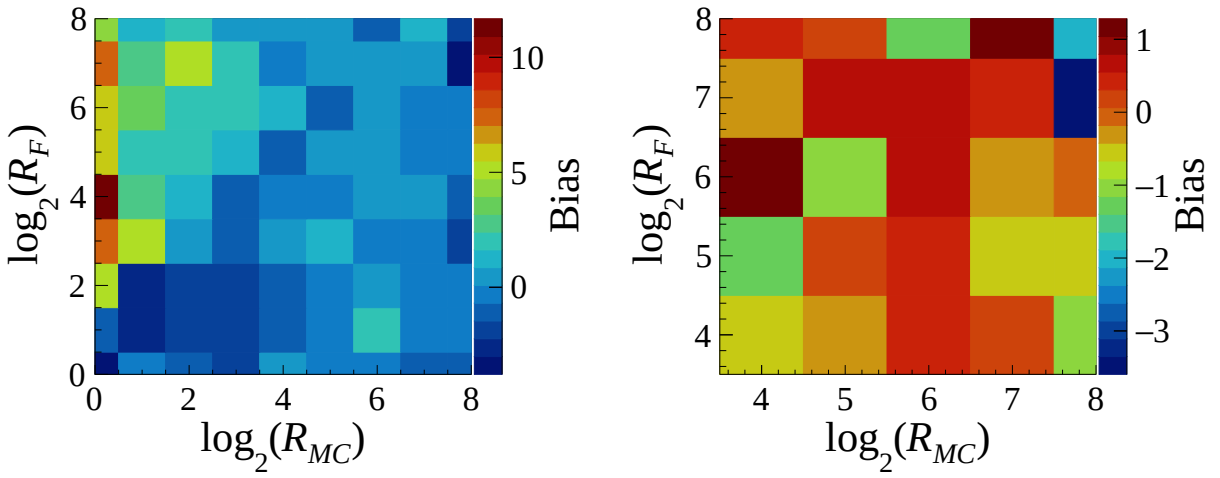

Figure 8-18: Left panel: the bias of b_{WM} extracted from SM fits with χ^2 as a function of the function spectrum rebin factor (R_{F}) and the Monte Carlo histogram rebin factor (R_{MC}). Right panel: zoomed view of the left panel.

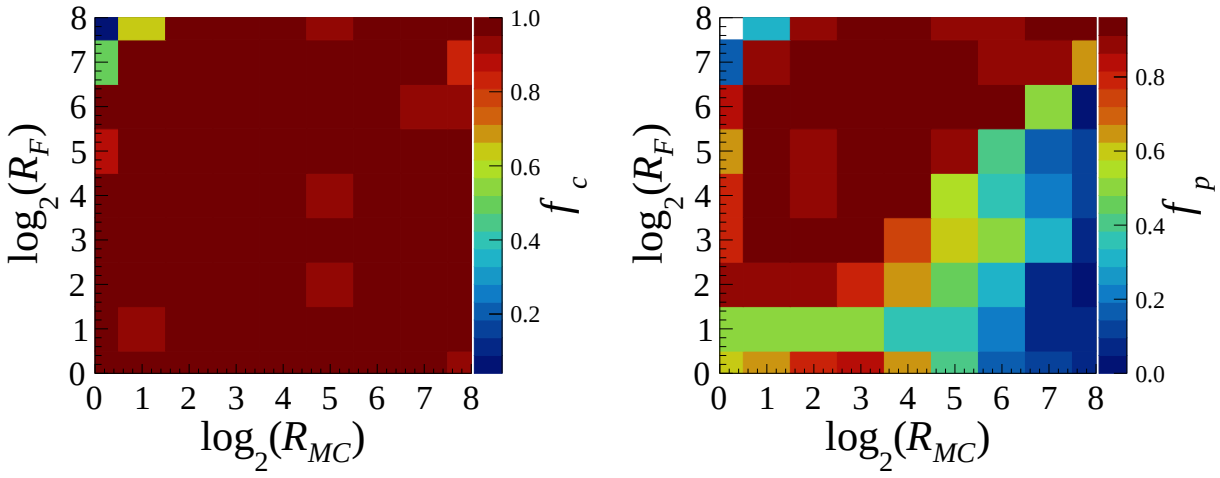

Figure 8-19: Left panel: the fraction of convergent SM fits with log-likelihood as a function of the function spectrum rebin factor (R_{F}) and the Monte Carlo histogram rebin factor (R_{MC}). Right panel: the fraction of the fits with p-values over 0.05 as a function of the function spectrum rebin factor (R_{F}) and the Monte Carlo histogram rebin factor (R_{MC}).

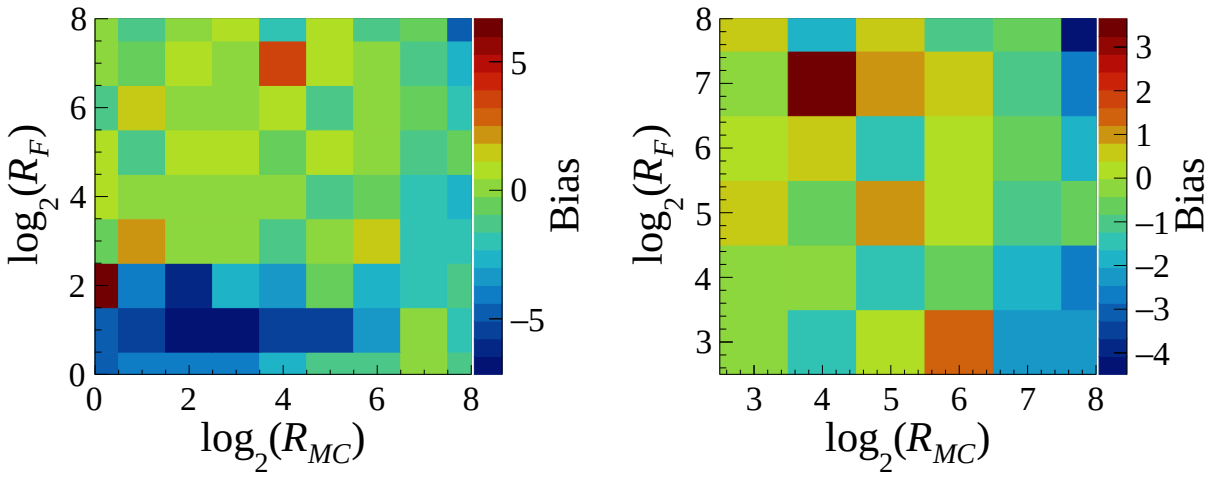

Figure 8-20: Left panel: the bias of b_{WM} extracted from SM fits with log-likelihood as a function of the function spectrum rebin factor (R_{F}) and the Monte Carlo histogram rebin factor (R_{MC}). Right panel: zoomed view of the left panel.

in the Monte Carlo histogram are preferred. Under the same condition with that in Sec. 8.1.2.3, histograms with 10^6 events can consistently be fitted with less than one standard deviation. Finally, the same rebin factor for the function histogram and the Monte Carlo histogram is recommended, and the most reliable choices of (R_{F}, R_{MC}) pairs are (32, 32) and (64,64), assuming both the function histogram and the Monte Carlo histogram have 16384 initial bins before rebinning.

8.5 Pile-Up Contribution to the Fit Function

In the experimental spectrum, in addition to the expected β-decay events, a pile-up spectrum is introduced by the digital DAQ system. As seen in the right panel of Fig. 3-11, the events above the endpoint energy are pile-up events. Therefore the pile-up spectrum is also included when fitting the experimental data. The function used to fit the experimental data including the pile-up spectrum has the expression

$$f(CH; N_0, A, b)_{PL} = N_0 \times f_c^0(E) \times f_1(E, b_{WM}) \times \left(1 + \frac{b_{GT}}{E}\right) + N_1 \times f_{pl}(E), \tag{8.4}$$

$$E = \frac{CH - B}{A}, \tag{8.5}$$

where $f_{pl}(E)$ is a function corresponding to the shape of the pile-up spectrum. The shape of a pile-up spectrum was calculated according to the shape of $f_c^0(E)$ using the parameters and algorithms in the digital DAQ system. Figure 4-2 shows the shape of the pile-up spectrum (black) calculated based on the shape of the convolved spectrum (green). The event rate has no impact on the shape of $f_{pl}^0(E)$ but affects the normalization factor N_1, or the weight of the pile-up spectrum. With the above four-parameter function the experimental spectrum shown in the right panel of Fig. 3-11 is fitted and shown in Fig. 8-21, where the χ^2 to the number of degree of freedom ratio from the fit equal to 0.98. The measured β-energy spectrum in ^{6}He decay can now be understood over than range of four orders of magnitude.

8.6 Complete Fit Function

Equation 8.4 is the fit function used in the current analysis and is, in fact, an approximation form of a complete fit function since it ignored the effects of the detector simulation response and

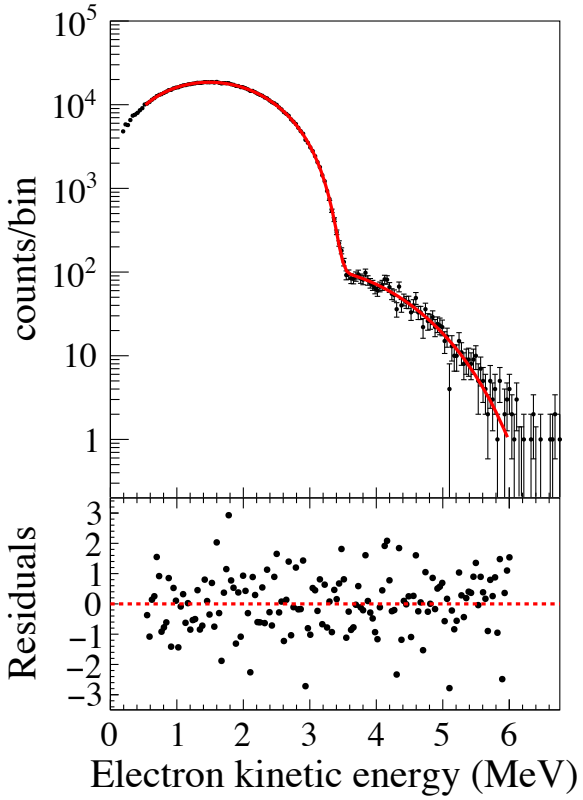

Figure 8-21: A β-energy spectrum in ^{6}He decay measured in the CsI(Na) detector (the right panel of Fig. 3-11) fitted by Eq. 8.4.

the energy-resolution convolution on the two factors associated with the observables shown in Eq. 1.26: the spectral function and the $\left(1 + \frac{b_{GT}}{W}\right)$ factor. A complete fit function will be used in future analysis, which has the expression

$$f(CH; N_0, A, b) = N_0 \times pW(W_0 - W)^2\eta(W)dW \times f_1(E, b_{WM}) \times \left(1 + \frac{b_{GT}}{W}\right) \circledast \mathcal{F}_c(E) + N_1 \times f_{pl}(E), \tag{8.6}$$

$$E = \frac{CH - B}{A}, \tag{8.7}$$

where $\mathcal{F}_c(E)$ is the detector response function including the correction based on the detector simulations and the convolution with the Gaussian width. The above expression can be rewritten

by substituting $f_1(E, b_{WM})$ with Eq. 1.27.

$$
\begin{aligned}
f(CH; N_0, A, b) =& N_0\big[(1 + C_0 + b_{GT}C_1)f_c^0(E) + C_1 f_c^1(E) \\
&+ (C_{-1} + b_{GT} + b_{GT}C_0)f_c^{-1}(E) + b_{GT}C_{-1}f_c^{-2}(E)\big] + N_1 f_{pl}(E), && (8.8)\\
\approx& N_0\big[(1 + C_0)f_c^0(E) + C_1 f_c^1(E) + (C_{-1} + b_{GT})f_c^{-1}(E)\big] + N_1 f_{pl}(E), && (8.9)\\
f_c^0(E) =& pW(W_0 - W)^2\eta(W)dW \circledast \mathcal{F}_c(E), && (8.10)\\
f_c^1(E) =& pW(W_0 - W)^2\eta(W)WdW \circledast \mathcal{F}_c(E), && (8.11)\\
f_c^{-1}(E) =& \frac{pW(W_0 - W)^2\eta(W)dW}{W} \circledast \mathcal{F}_c(E), && (8.12)\\
f_c^{-2}(E) =& \frac{pW(W_0 - W)^2\eta(W)dW}{W^2} \circledast \mathcal{F}_c(E), && (8.13)
\end{aligned}
$$

where $f_c^0(E)$, $f_c^1(E)$, $f_c^{-1}(E)$, and $f_c^{-2}(E)$ are the convolved spectra, i.e., the absorbed spectra simulated with Geant4 with $pW(W_0-W)^2\eta(W)dW$, $pW(W_0-W)^2\eta(W)WdW$, $\frac{pW(W_0-W)^2\eta(W)dW}{W}$, and $\frac{pW(W_0-W)^2\eta(W)dW}{W^2}$ as the source spectra that are convolved with the Gaussian width. The complete function also has four free parameters but is based on four convolved spectra and a pile-up spectrum. Therefore more Geant4 simulations will be performed to complete the analysis.

CHAPTER 9

BACKGROUND STUDY

In addition to the β-decay events, the experimental data also include background events. This chapter focuses on eliminating the impact of the background on the shape of the measured β-energy spectrum. The first half of this chapter studies the origin of the background, estimates the size of the background contribution, and provides a solution to include the background in the analysis. The second half of the chapter studies the corrections to the background through both Monte Carlo simulations and the analysis of the experimental data, based on which the impacts of the background corrections on the physics observables are estimated. The systematic uncertainties of the observables associated with the background are provided.

9.1 Background in the Analysis

9.1.1 Background Component

The background originates from both the beam-induced background and the ambient background. Figure 9-1 shows the decay spectrum from the run shown in Fig. 3-11, where the events in the left panel of Fig. 3-11 are projected to the time axis. The dominant feature of the decay spectrum is an exponential decay of the number of events as a function of time. Towards the end of the cycle (12.5 s), the number of events converges to a constant with the events dominated by the background. The red and blue dashed lines indicate the levels of the beam-induced background and the ambient background measured in dedicated background runs.

The ambient background was measured with the CsI(Na) detector for twelve hours. The resulting energy spectrum is shown in Fig. 9-2, where the γ peaks of ^{40}K, ^{214}Bi, ^{214}Bi, and ^{208}Tl are observed. The beam-induced background originates from the nuclear reactions between the beam and the detector. Immediately after stopping the beam, the beam-induced background was measured for eighteen minutes. The energy spectrum measured with the CsI(Na) detector is shown

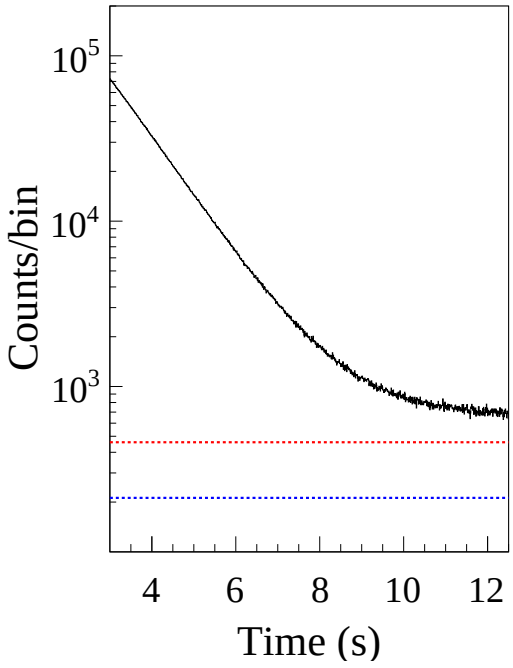

Figure 9-1: The ^{6}He decay spectrum recorded during the beam-off interval. The data is collected during a single one-hour run. The red and blue dashed lines indicate the levels of the beam-induced background and the ambient background.

in Fig. 9-3, where the peaks are from the decays of the reaction products. Theoretical calculations have predicted that the reaction products are dominated by ^{124}Cs, ^{126}Cs, ^{122}I, and ^{128}Cs.

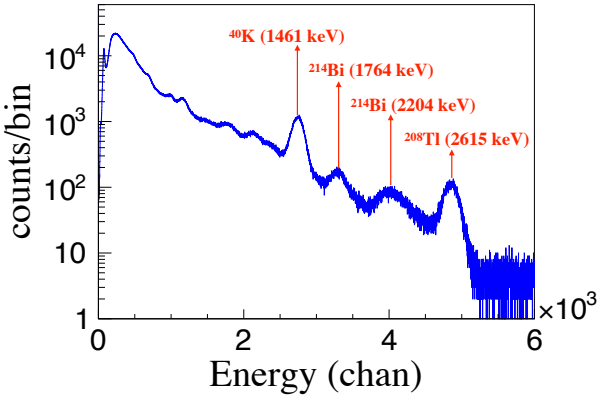

Figure 9-2: The energy spectrum of the ambient background measured with the CsI(Na) detector with peak identifications.

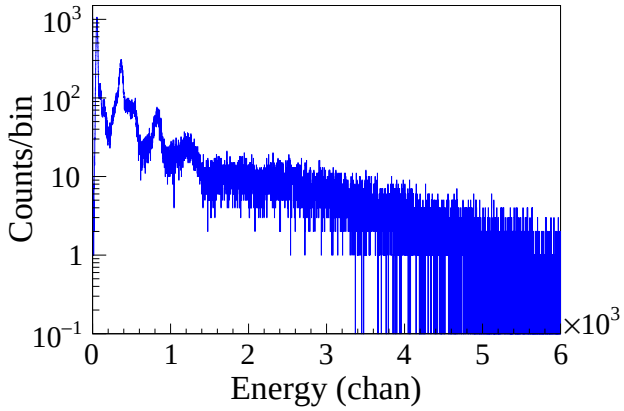

Figure 9-3: The energy spectrum of the beam-induced background measured with the CsI(Na) detector

9.1.2 Background Subtraction

The contribution of the background is eliminated by subtracting the background spectrum from the measured signal+background (S+B) spectrum that includes both the β-decay events and the background events. As the true background contribution to the S+B spectrum is unknown, the energy spectrum near the end of the decay cycle, dominated by background events, is taken as an estimate to the true background spectrum. As shown in the left panel of Fig. 9-4, the time interval of 3.43-3.61 s is selected as the S+B window, during which the measured spectrum is shown in the upper right panel of Fig. 9-4 in black; and the time interval of 9.43-9.61 s is selected as the background window, during which the measured spectrum is shown in the upper right panel of Fig. 9-4 in blue. The background spectrum is subtracted from the S+B spectrum, resulting in the spectrum shown in the lower right panel of Fig. 9-4.

For each one-hour run like Fig. 9-1, six pairs of S+B and background windows are defined. When defining the time windows, we require the event rate to be below a maximum acceptable rate $r_{\max}$, and the number of events after the background subtraction to be about 10^6 to satisfy the fit condition determined in Chap. 8. For each pair of time windows, the background window starts six seconds after the S+B window starts, and the two windows have the same width. The first S+B time window in a run starts at the first bin with an event rate below $r_{\max}$, and stops at the

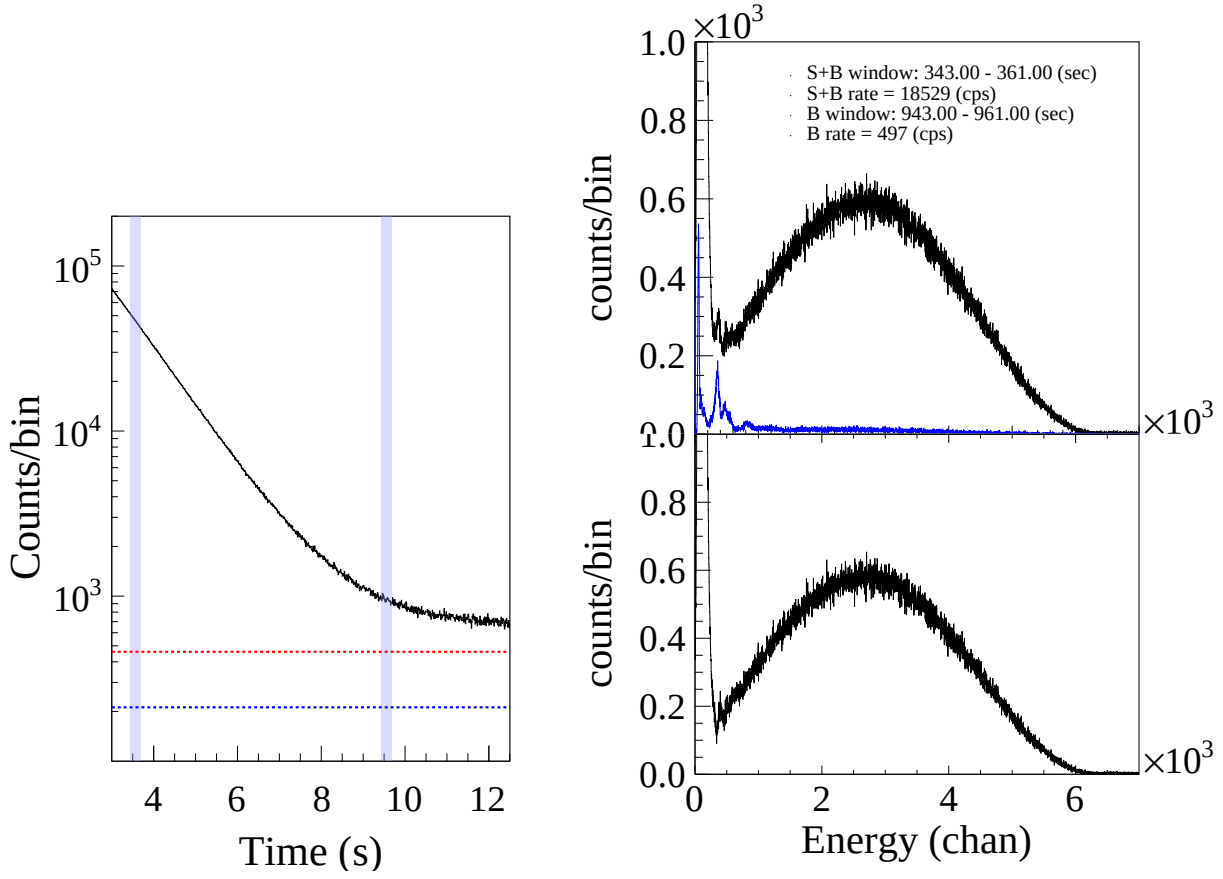

Figure 9-4: Left panel: an example of selected S+B and background time windows. The time interval of 3.43-3.61 s (left vertical band) is selected as the S+B window, and time interval of 9.43-9.61 s (right vertical band) is selected as the background window. Right panel: the energy spectra measured with the CsI(Na) detector during 3.43-3.61 s (black) and 9.43-9.61 s (blue) corresponding to the two time windows marked in the left panel.

first bin where the background-subtracted spectrum has over 10^6 events. Each subsequent signal window starts at the next bin after the end of its previous window and stops at the bin where the background-subtracted spectrum has over 10^6 events.

The deviation of the estimated background spectrum from the true background spectrum introduces a distortion to the background-subtracted spectrum and has a potential impact on the extracted observables. This deviation originates from the differences in the gain and the sigma (the Gaussian width) between the true and the estimated background spectra. Due to the after-glow pile up discussed in Chap. 7, the estimated background at low rate has a lower gain and a lower sigma than the true background at a high rate does.

Figure 9-5 shows the background-subtracted spectra from the run shown in Fig. 7-2, with the S+B spectra from a high-rate time window and the background spectra from a low-rate time window. The structure near 1000 chan shows that the events in the background γ peak are populated at lower channels than the events in the S+B γ peak, indicating lower gains in the background spectra than in the S+B spectra. The presence of this structure indicates that the background has not been successfully subtracted. In order to successfully subtract the background, gain-and-sigma corrections were applied to the estimated background spectra, producing corrected background spectra with the same gain and sigma with the S+B spectra. The methods of these background corrections are first demonstrated with Monte Carlo simulations.

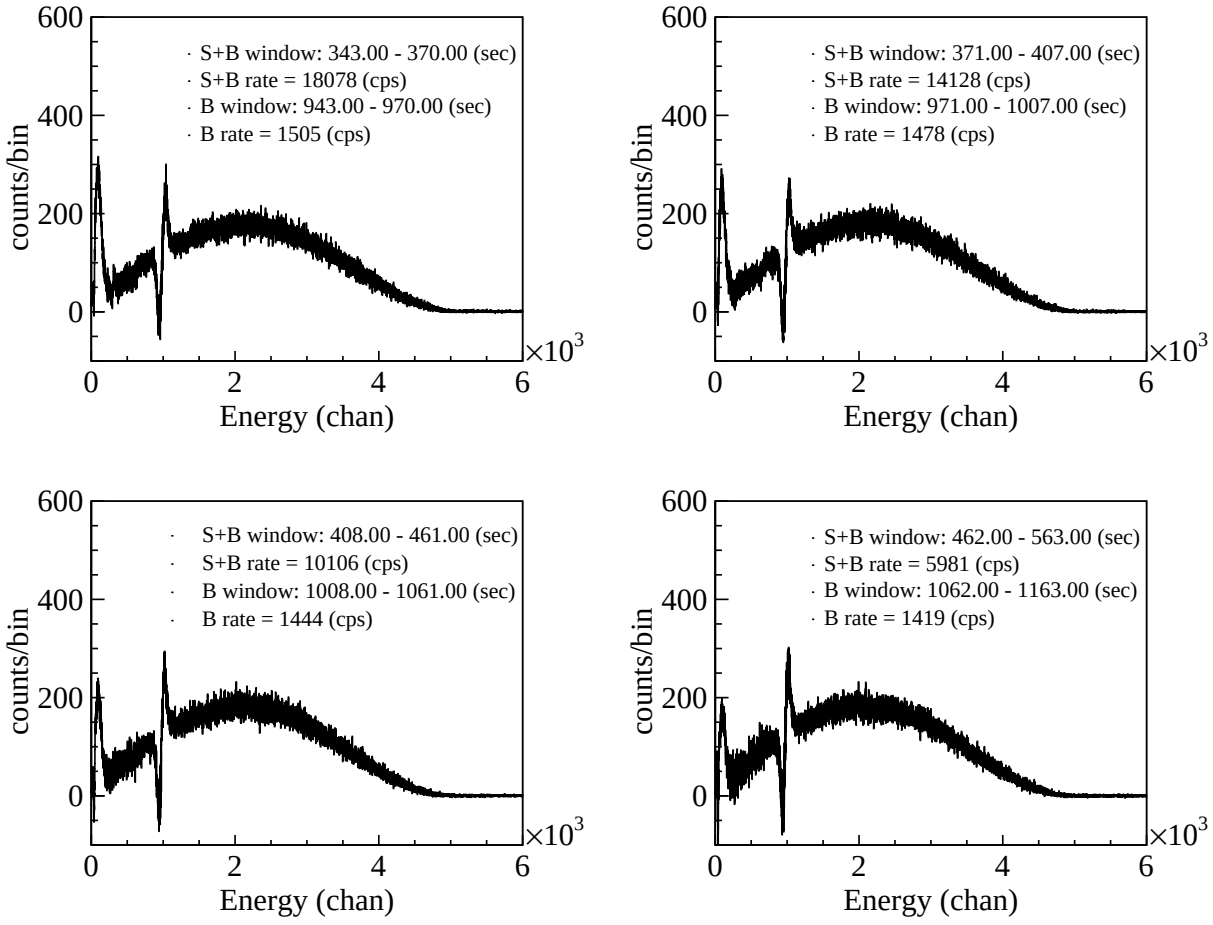

Figure 9-5: The background-subtracted spectrum for the β spectra with an extra ^{137}Cs γ peak, where the S+B spectra were projected from four time windows.

9.2 Corrections to the Background: Monte Carlo

In the Monte Carlo study, instead of generating β-energy spectra only, energy spectra similar to Fig. 7-2 were generated in order to use the Gaussian peak to evaluate the quality of the background subtraction. The S+B spectrum, shown in the upper panel of Fig. 9-6 in black, was generated with a higher gain and a higher sigma than the background spectrum (blue) shown underneath the S+B spectrum.

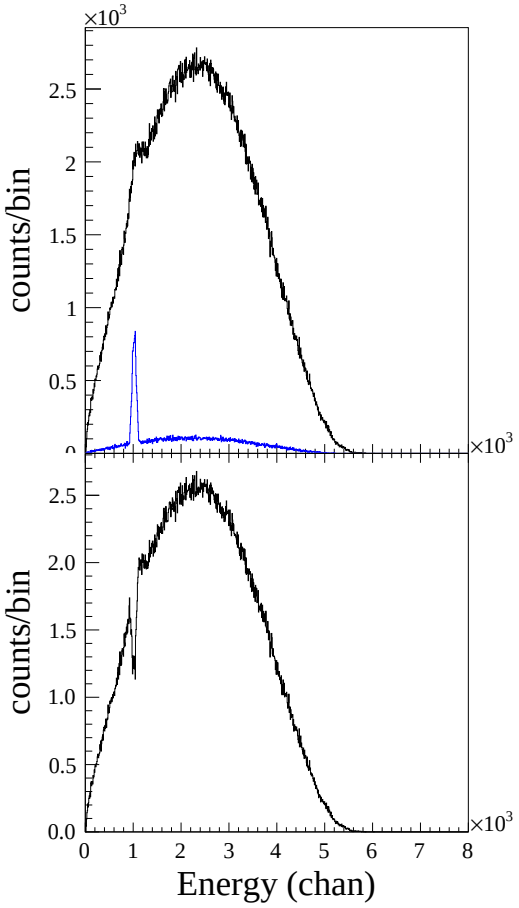

Figure 9-6: Upper panel: the S+B (black) and background (blue) spectra generated with Monte Carlo. The S+B spectrum has a higher gain and a higher sigma than the background spectrum. Lower panel: the spectrum after background subtraction.

The S+B spectrum is a sum of a β-energy spectrum with 1.05×10^6 events and a Gaussian peak with 10^4 events. The β-energy spectrum was generated following the distribution of a convolved

spectrum. The convolved spectrum is from the convolution of the absorbed spectrum from Geant4 with a Gaussian whose centroid is E and width is $\eta\sigma_0\sqrt{E}$, where E is the energy in keV, and η is a factor larger than 1. The Gaussian peak was generated following the distribution of a Gaussian whose centroid is the energy of the ^{137}Cs peak in keV and width is $\eta\sigma_0$. The S+B spectrum was generated in chan with a gain of A_H.

The background spectrum is a sum of a β-energy spectrum with 4×10^4 events and a Gaussian peak with 10^4 events. The β-energy spectrum was generated following the distribution of a convolved spectrum. The convolved spectrum is from the convolution of the absorbed spectrum from Geant4 with a Gaussian whose centroid is E and width is $\sigma_0\sqrt{E}$. The Gaussian peak was generated following the distribution of a Gaussian whose centroid is the energy of the ^{137}Cs peak in keV and width is σ_0. The background spectrum was generated in chan with a gain of A_L that is smaller than A_H and was subtracted from the S+B spectrum, producing the spectrum shown in the lower panel of Fig. 9-6. The structure near 1000 chan indicates that the background is not correctly subtracted.

9.2.1 Background Gain Correction

Since the background gain is underestimated, we have performed corrections to the background to match its gain to that of the S+B spectrum. A gain-corrected background spectrum is generated following the distribution of the uncorrected background shown in the upper panel of Fig. 9-6 with an additional gain factor of A_H/A_L, resulting in the same gain with the S+B spectrum.

The left panel of Fig. 9-7 shows the S+B spectrum (black), the uncorrected background spectrum (blue), and the gain-corrected background spectrum (red) zoomed in near the Gaussian peak. The Gaussian peak is shifted to higher channels after the gain correction. The right panel of Fig. 9-7 shows the full view of the S+B spectrum and the gain-corrected background spectrum in the upper panel, and the new background-subtracted spectrum in the lower panel. The structure near 1000 chan is still present because the S+B and background spectra have different sigmas, but is reduced compared with Fig. 9-6 because the S+B and background spectra have the same gain.

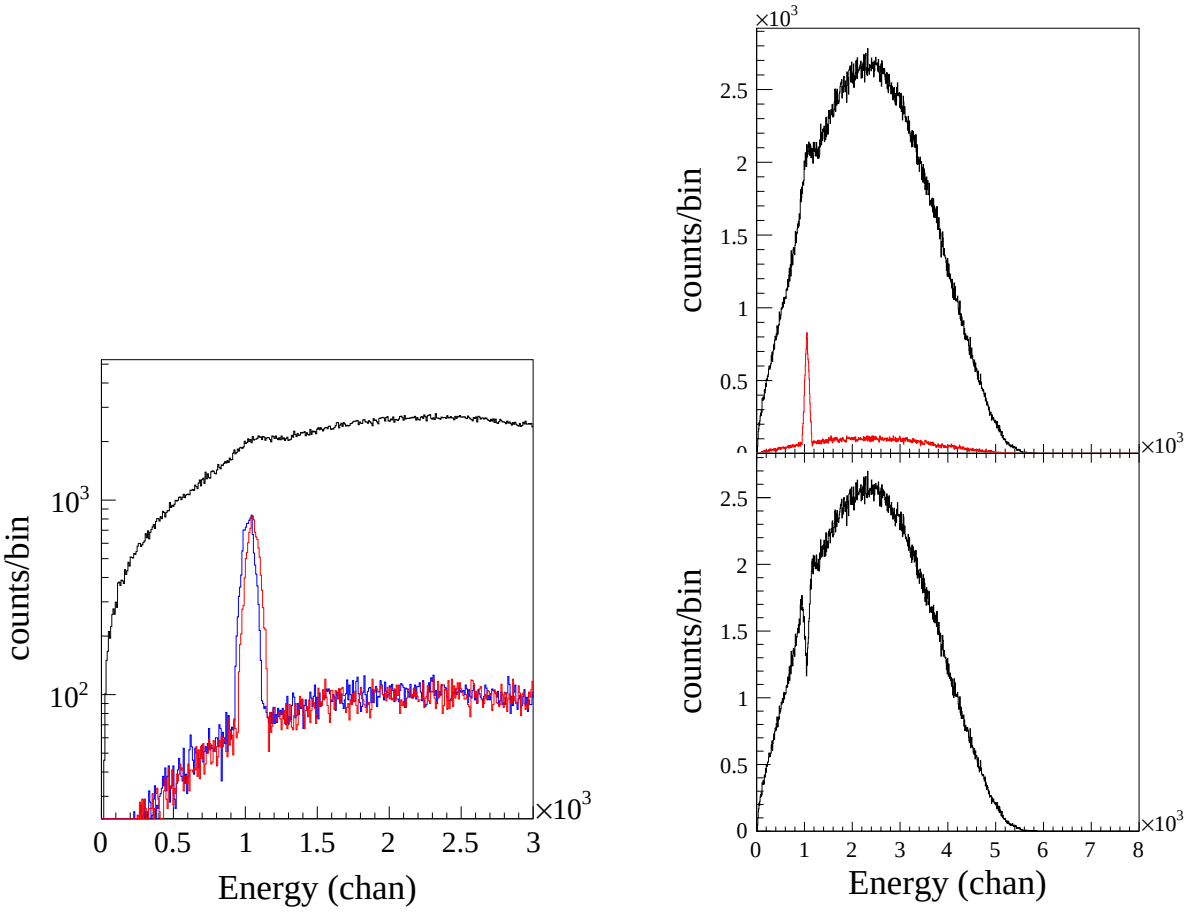

Figure 9-7: Left panel: zoomed-in view of the S+B (black), uncorrected background (blue), and gain-corrected background (red) spectra generated with Monte Carlo. Right panel: the full view of S+B (black) and gain-corrected background (red) spectra in the upper panel, and the new background-subtracted spectrum in the lower panel.

9.2.2 Background Gain-and-Sigma Correction

Since the background sigma is underestimated, we have performed corrections to the background to match its sigma to that of the S+B spectrum. A gain-and-sigma corrected background spectrum is generated following the distribution of the gain-corrected background shown in the upper panel of Fig. 9-7, with an additional convolution with a Gaussian whose centroid is energy in chan and width is $\sqrt{\eta^2 - 1} A_H \sigma_0 \sqrt{E}$, resulting in the same sigma with the S+B spectrum.

The left panel of Fig. 9-8 shows the S+B spectrum (black), the uncorrected background spectrum (blue), and the gain-and-sigma corrected background spectrum (red) zoomed in near the

Gaussian peak. The Gaussian peak is stretched wider after the sigma correction. The right panel of Fig. 9-8 shows the full view of the S+B and the gain-and-sigma corrected background spectra in the upper panel, and the new background-subtracted spectrum in the lower panel. The structure near 1000 chan has disappeared because the S+B and background spectra have the same gain and sigma, and the background is fully subtracted.

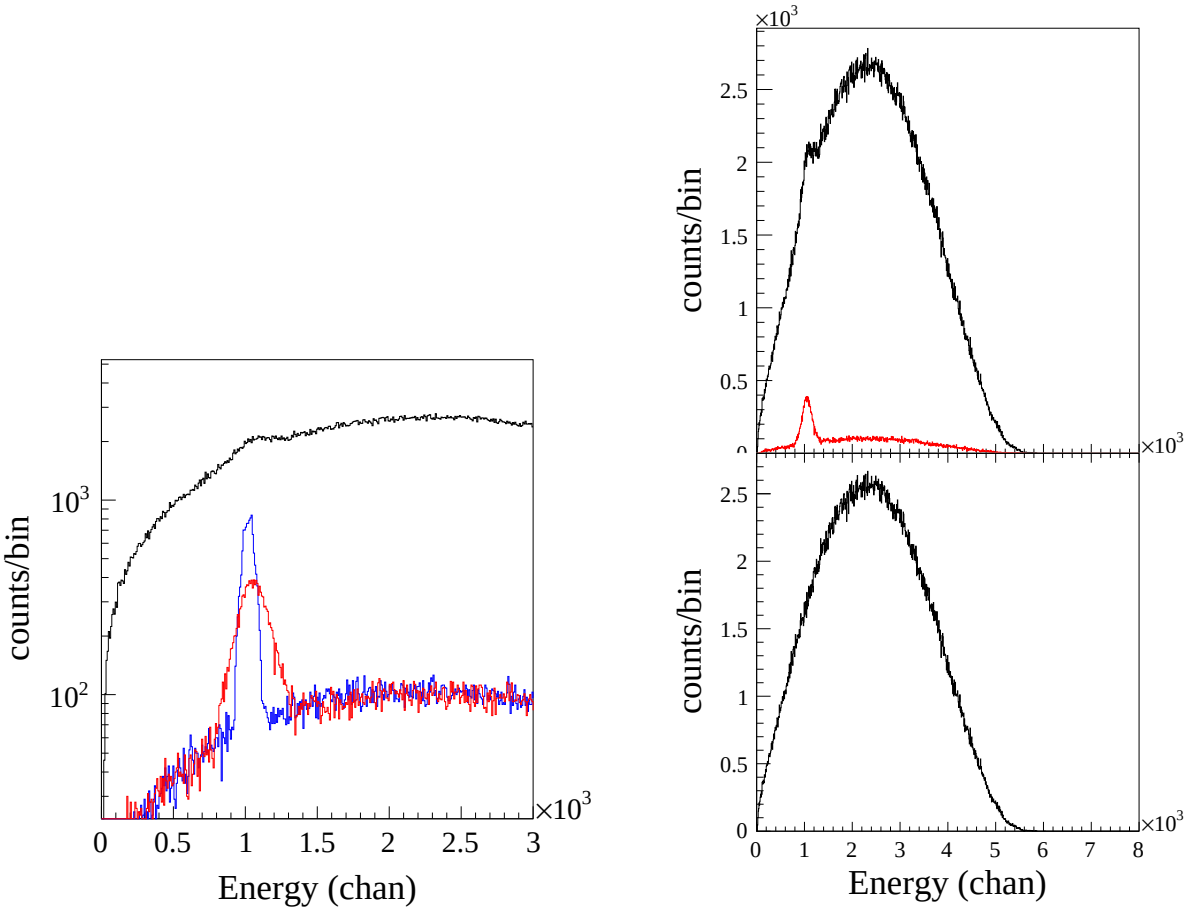

Figure 9-8: Left panel: zoomed-in view of the S+B (black), uncorrected background (blue), and gain-and-sigma corrected background (red) spectra generated with Monte Carlo. Right panel: the full view of S+B (black) and gain-and-sigma corrected background (red) spectra in the upper panel, and the new background-subtracted spectrum in the lower panel.

9.3 Corrections to the Background: Experiment

The gain+sigma background correction procedure successfully demonstrated with Monte Carlo simulations are applied to the experimental data. We have first performed background corrections to the same experimental data shown in Figs. 9-5 and 7-2 in order to use the Gaussian peak to evaluate the quality of background subtraction. These corrections were then applied to the measured β-energy spectra from the run shown in Fig. 3-11.

9.3.1 Corrections to the $\beta + \gamma$ Spectrum

The background-subtracted spectra shown in Fig. 9-5 were calculated with the S+B (black) and background (blue) spectra shown in Fig. 9-9 below. gain-and-sigma corrections to these background spectra have been performed. For the convenience of future comparisons, a zoomed-in view of Figs. 9-5 is provided in Figs. 9-10.

9.3.1.1 Gain Correction

Similar gain correction method to that in Sec. 9.2.1 has been applied to the background spectra shown in Fig. 9-9. The four S+B spectra in Fig. 9-9 were first fitted to extract the S+B gain (A_H) of each time window. A_H as a function of the rate is then used to extrapolate the background gain (A_L) in each time window. A gain-corrected background spectrum is generated following the distribution of the uncorrected background shown in Fig. 9-9 with an additional gain factor of A_H/A_L, resulting in the same gain with the S+B spectrum.

Figure 9-11 shows the S+B spectrum (black), the uncorrected background spectrum (blue), and the gain-corrected background spectrum (red) zoomed in near the Gaussian peaks. The Gaussian peaks were shifted to higher channels after the gain corrections. Figure 9-12 shows the new background-subtracted spectra. The structure near 1000 chan is still present because the S+B and background spectra have different sigmas, but are significantly reduced compared with Fig. 9-10 because the S+B and background spectra have the same gain.

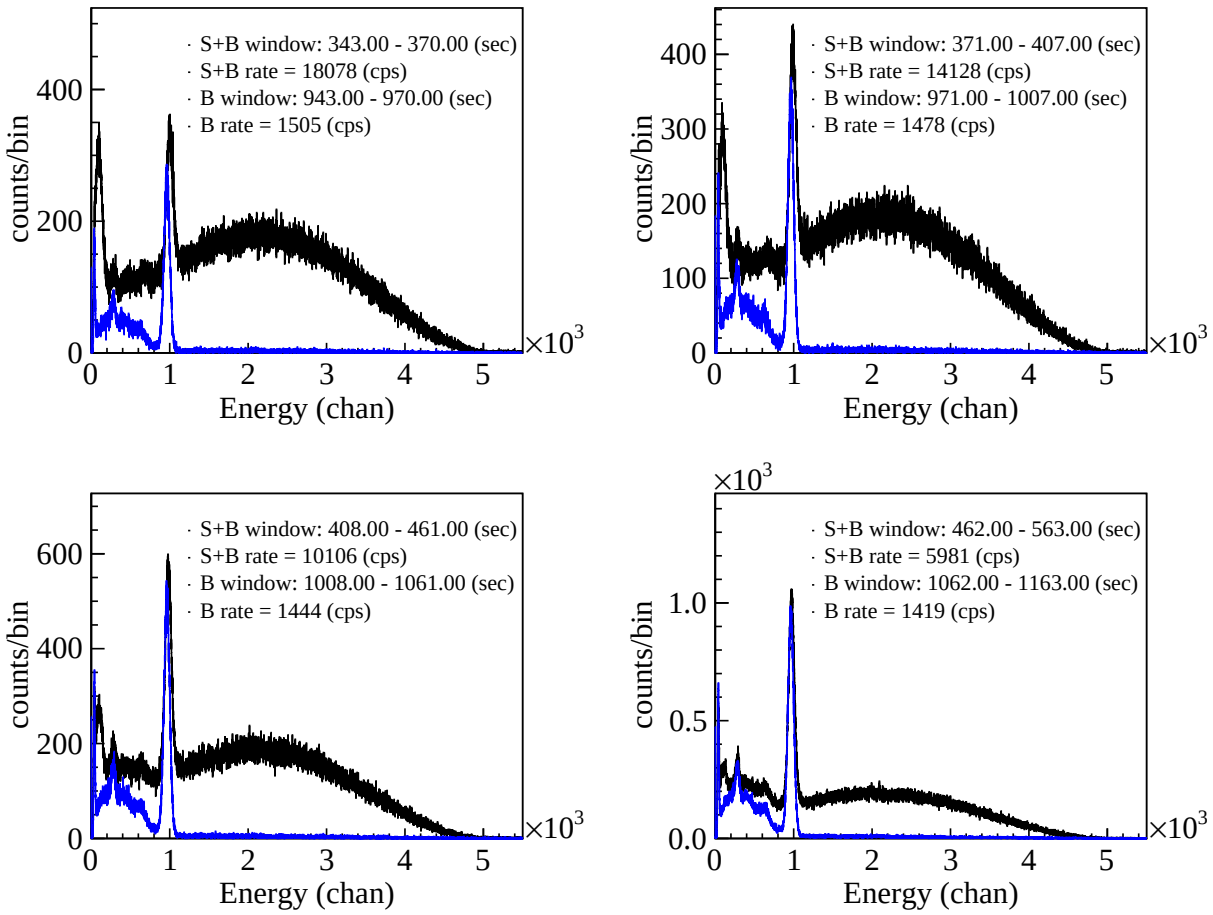

Figure 9-9: The S+B (black) and background (blue) spectra for the β spectra with an extra ^{137}Cs γ peak.

9.3.1.2 Gain-and-Sigma Correction

Similar sigma correction method to that in Sec. 9.2.2 has been applied to the gain-corrected background spectra shown in Fig. 9-11. The four S+B spectra shown in Fig. 9-9 were first fitted to extract the S+B sigma for the 611 keV peak (σ_H) in each time window. σ_H as a function of the rate is used to extrapolate the background sigma for the 611 keV peak (σ_L) in each time window. The gain-and-sigma corrected background spectra were then generated following the distributions of the gain-corrected background spectra shown in Fig. 9-11, with an additional convolution with a Gaussian whose centroid is energy in chan and width is $\sqrt{\left(\sigma_H^E\right)^2 - \left(\sigma_H^E\right)^2} A_H$, where $\sigma_H^E = \sigma_H \sqrt{E/661}$, and $\sigma_L^E = \sigma_L \sqrt{E/661}$.

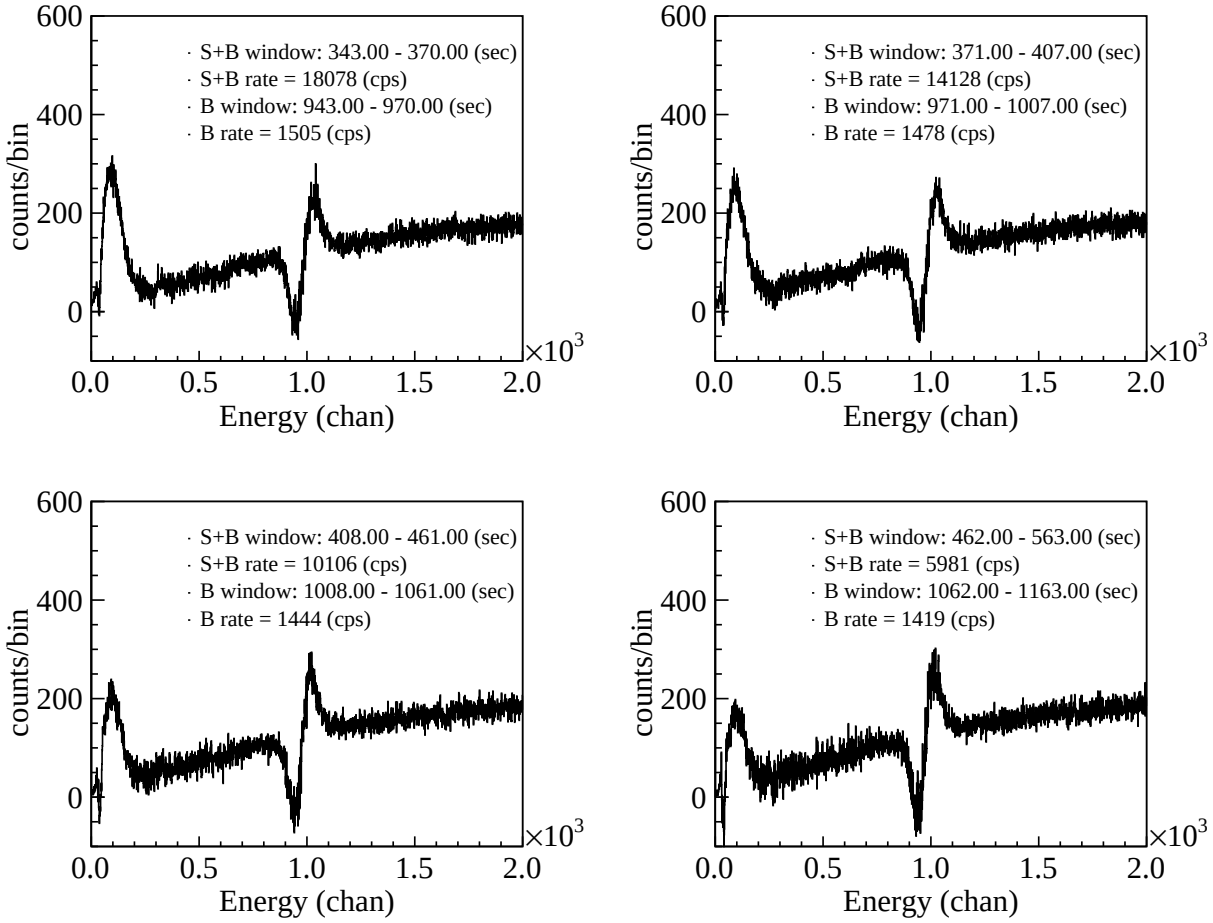

Figure 9-10: Zoomed-in view of the background-subtracted spectra for the β spectra with an extra ^{137}Cs γ peak (Fig. 9-5).

Figure 9-13 shows the S+B spectrum (black), the uncorrected background spectrum (blue), and the gain-and-sigma corrected background spectrum (red) zoomed in near the Gaussian peaks. The Gaussian peaks are stretched wider after the sigma corrections. Figure 9-14 shows the new background-subtracted spectra. The structure near 1000 chan is still present and has not significantly reduced compared with Fig. 9-12, which indicates that the sigma correction has a much lower impact on the background shape than the gain correction. The background spectra are not fully corrected because the gain and the sigma extracted by fitting the S+B spectra are not accurate due to the presence of background in the S+B spectra.

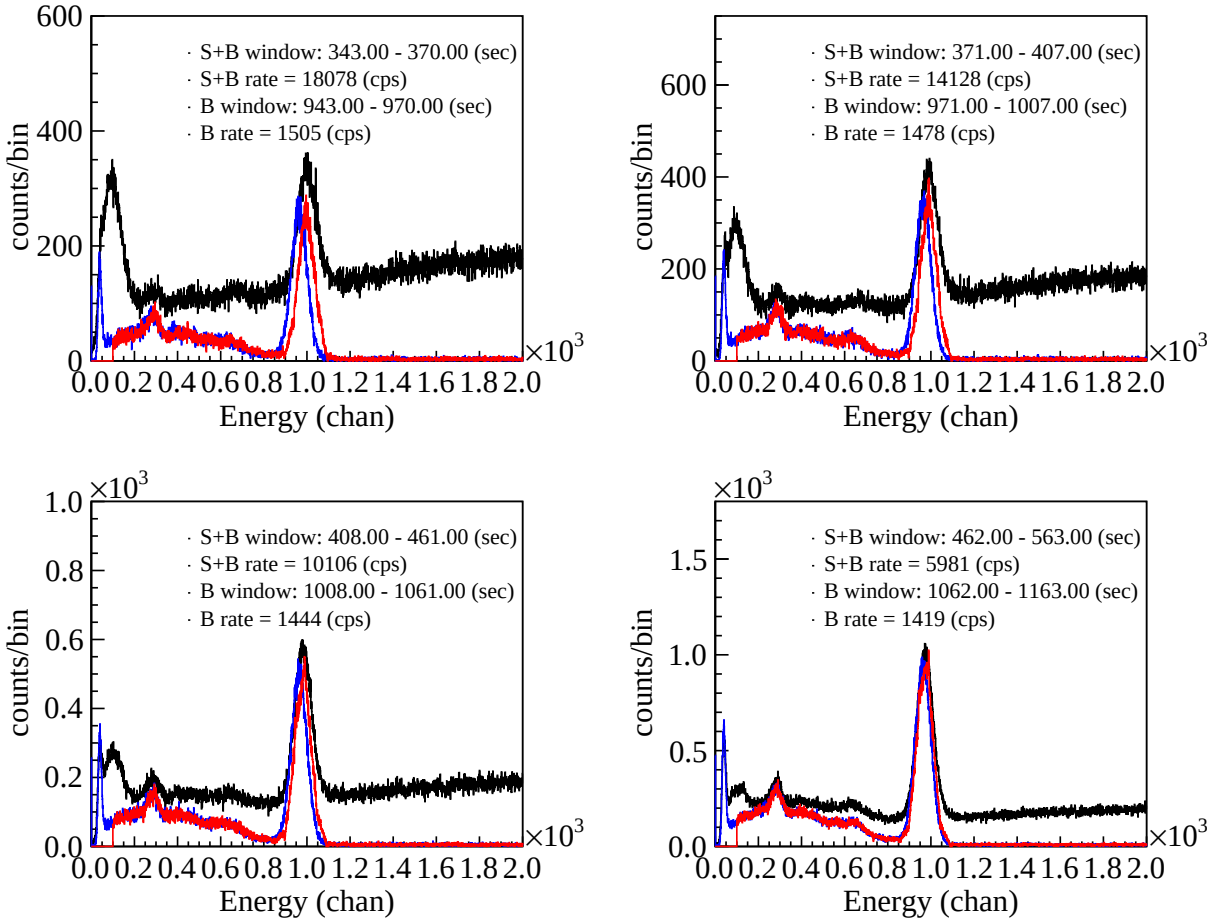

Figure 9-11: The S+B (black), background (blue), and gain-corrected background (red) spectra for the β spectrum with an extra ^{137}Cs γ peak.

9.3.2 Corrections to the β Spectrum

For the β-energy spectra from Fig. 3-11, the S+B (black) and background (blue) spectra are shown in Fig. 9-15. The resulting background-subtracted spectra are shown in Fig. 9-16, where a structure near 400 chan is observed. We have performed corrections to these background spectra. Since the gain in the β-energy spectra can be determined with high accuracy, the background spectra here are expected to be better corrected than the β+γ background spectra.

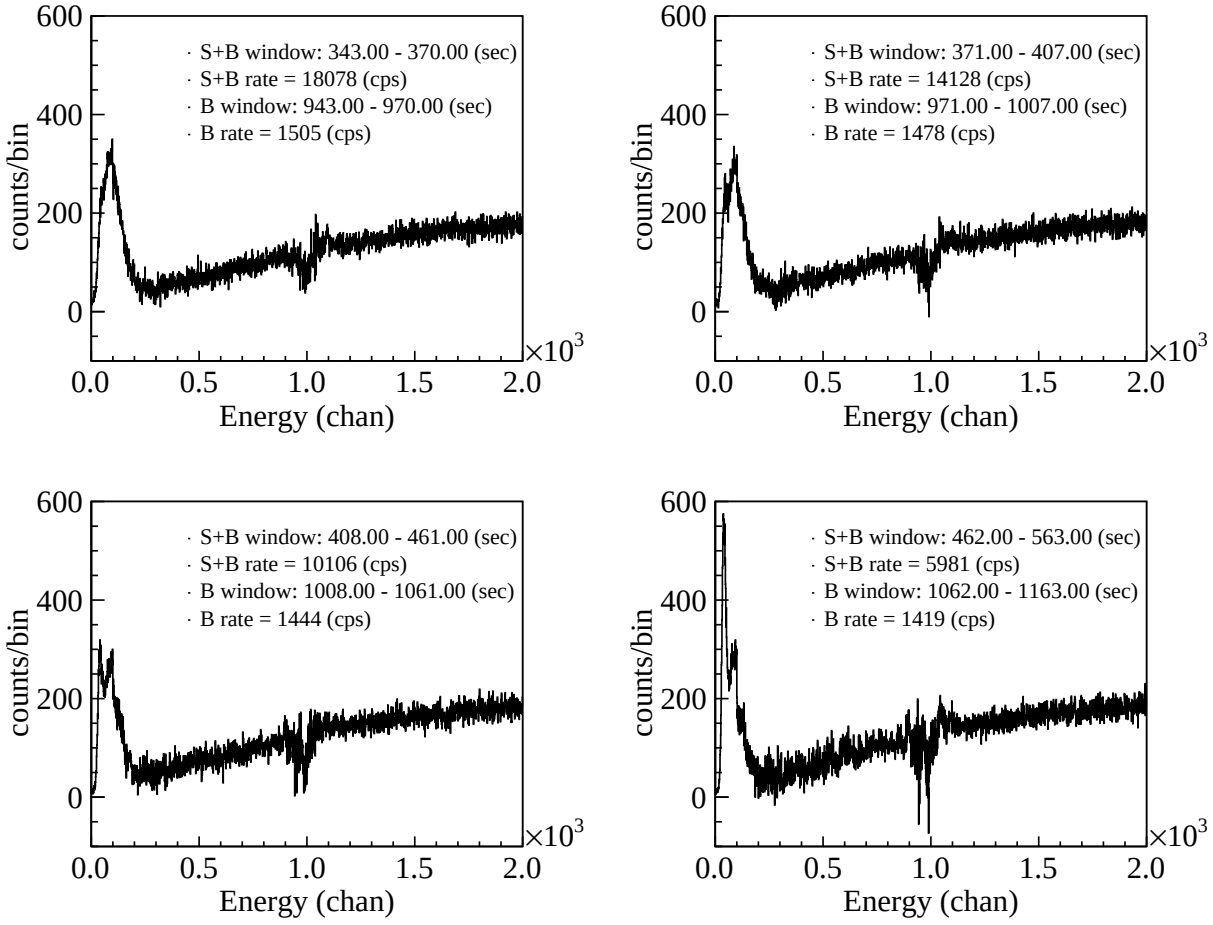

Figure 9-12: Zoomed-in view of the new background-subtracted spectra for the β spectra with an extra ^{137}Cs γ peak after gain corrections to the background spectra.

9.3.2.1 Gain Correction

A similar gain correction method to that in Sec. 9.3.1.1 has been applied to the background spectra shown in Fig. 9-15. The only difference is that the values of the S+B gain (A_H) in each time window were extracted from the background-subtracted spectra shown in Fig. 9-16 instead of the S+B spectra.

Figure 9-17 shows the S+B spectra (black), the uncorrected background spectra (blue), and the gain-corrected background spectra (red) zoomed in near the structure near 400 chan. The background peaks in the structure were shifted to higher channels after the gain corrections. Figure 9-18 shows the new background-subtracted spectra. The structure near 400 chan is significantly

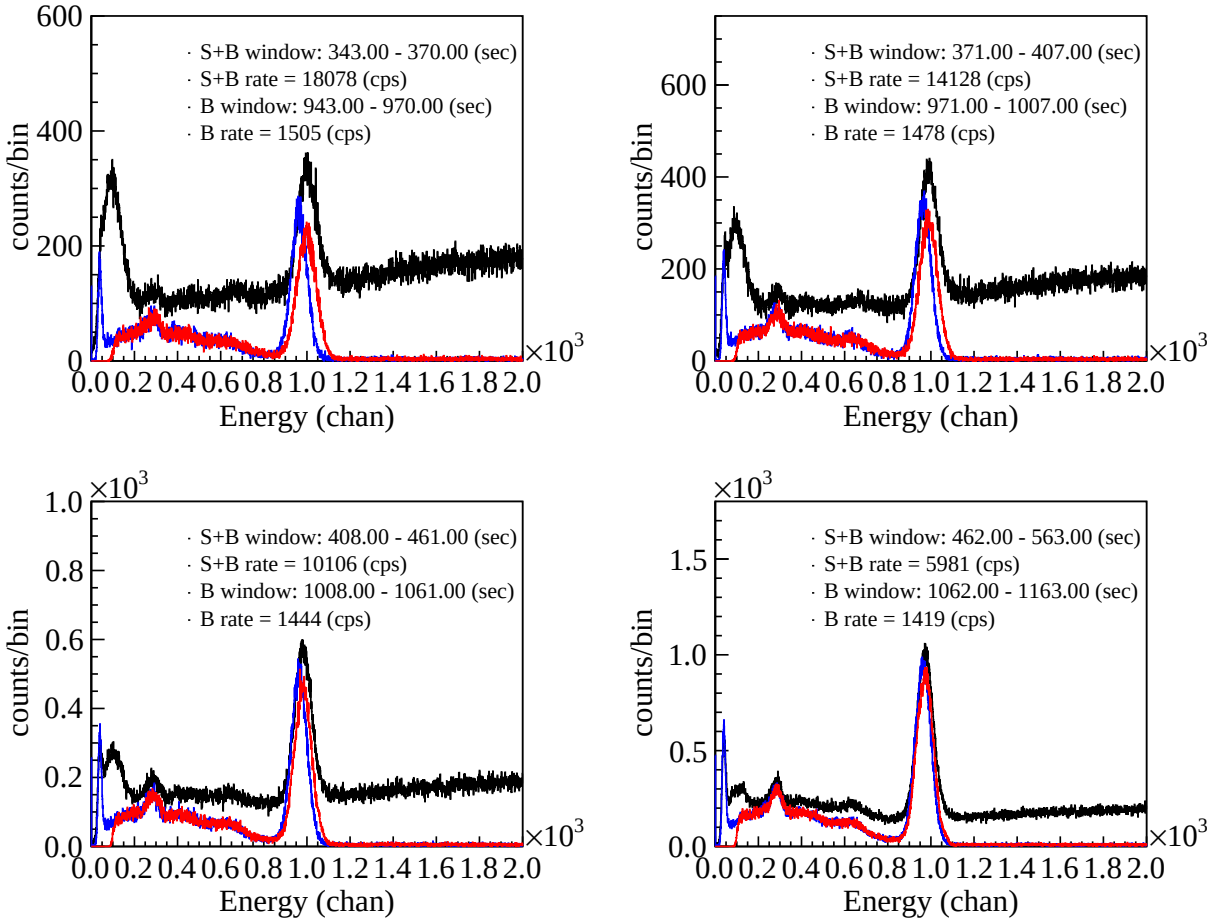

Figure 9-13: The S+B (black), background (blue), and gain-and-sigma corrected background (red) spectra for the β spectra with an extra ^{137}Cs γ peak.

reduced after the gain correction to the background. The background appears to be fully subtracted.

9.3.2.2 Gain-and-Sigma Correction

The same sigma correction method with that in Sec. 9.2.2 has been applied to the gain-corrected background spectra shown in Fig. 9-17 using the same σ_H versus rate relation with that in Sec. 9.2.2. Figure 9-19 shows the S+B spectra (black), the uncorrected background spectra (blue), and the gain-and-sigma corrected background spectra (red) zoomed in near the background peaks. The background peaks are stretched wider after the sigma corrections. Figure 9-20 shows the new background-subtracted spectra. The background again seems fully subtracted. The structure near

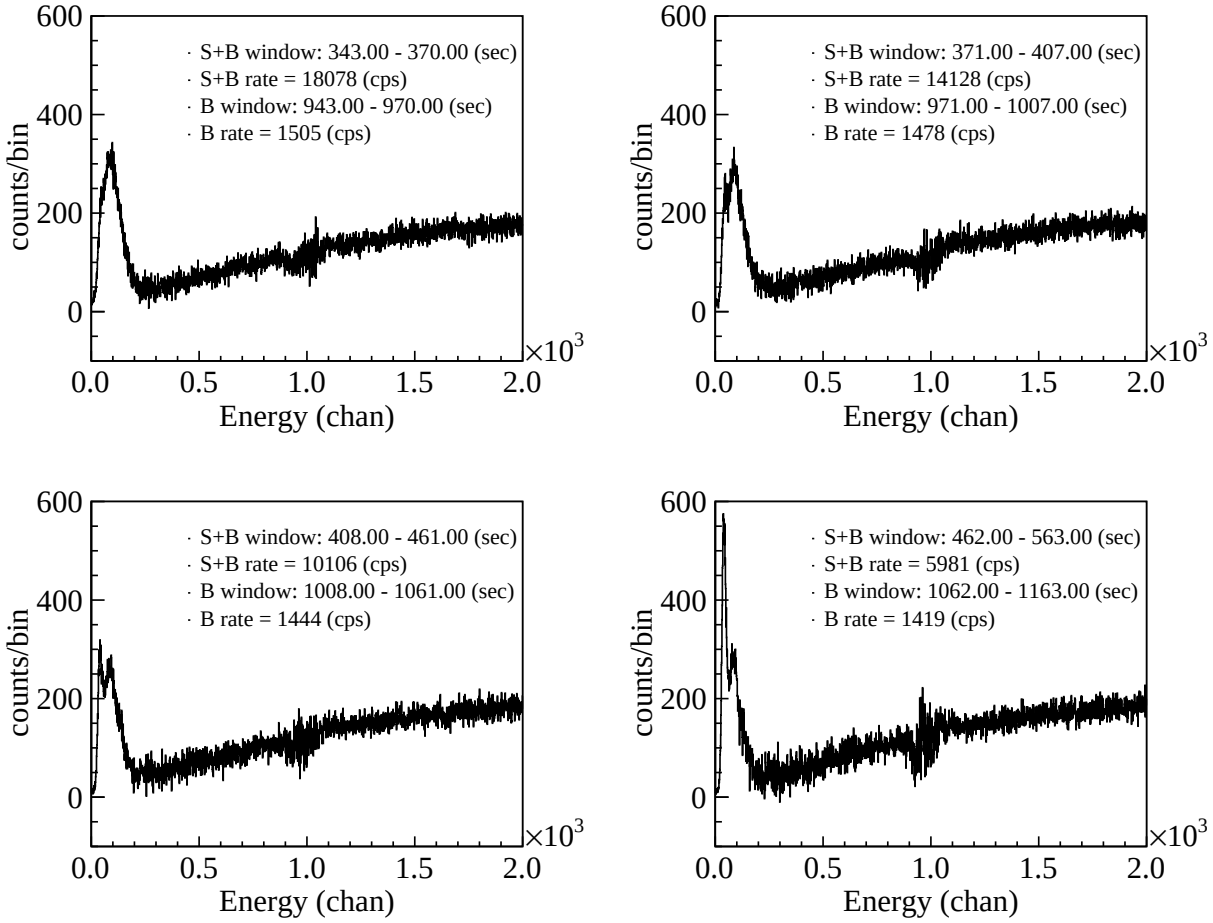

Figure 9-14: Zoomed-in view of the new background-subtracted spectra for the β spectra with an extra ^{137}Cs γ peak after gain-and-sigma corrections to the background spectra.

400 chan has no significant change compared with Fig. 9-18, indicating a much lower impact of the sigma correction on the background shape than the gain correction, which agrees with the observation in Sec. 9.2.2.

9.4 The Impact of the Background

The impact of the background corrections on the observables have been estimated. The CsI(Na) dataset in Table 3-1 were fitted to extract b_{WM} and b_{GT} under the three background conditions shown in Table 9-1.

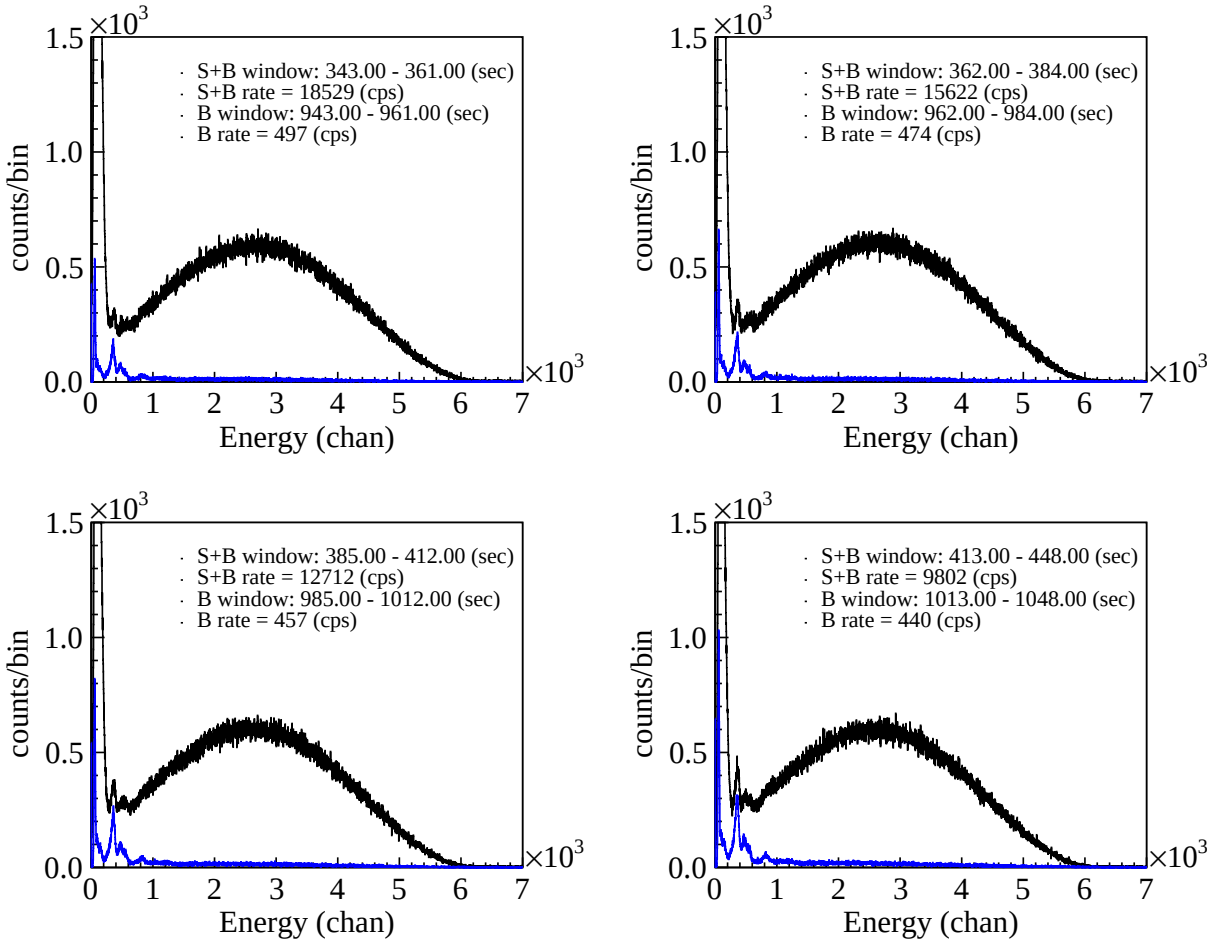

Figure 9-15: The S+B (black) and background (blue) spectra for ^{6}He β decay.

Table 9-1: List of background conditions applied when fitting the observables.

Condition	b_{WM}	b_{GT}
no background correction	${}^{0}b_{WM}$	${}^{0}b_{GT}$
gain background correction	${}^{1}b_{WM}$	${}^{1}b_{GT}$
gain-and-sigma corrections	${}^{2}b_{WM}$	${}^{2}b_{GT}$

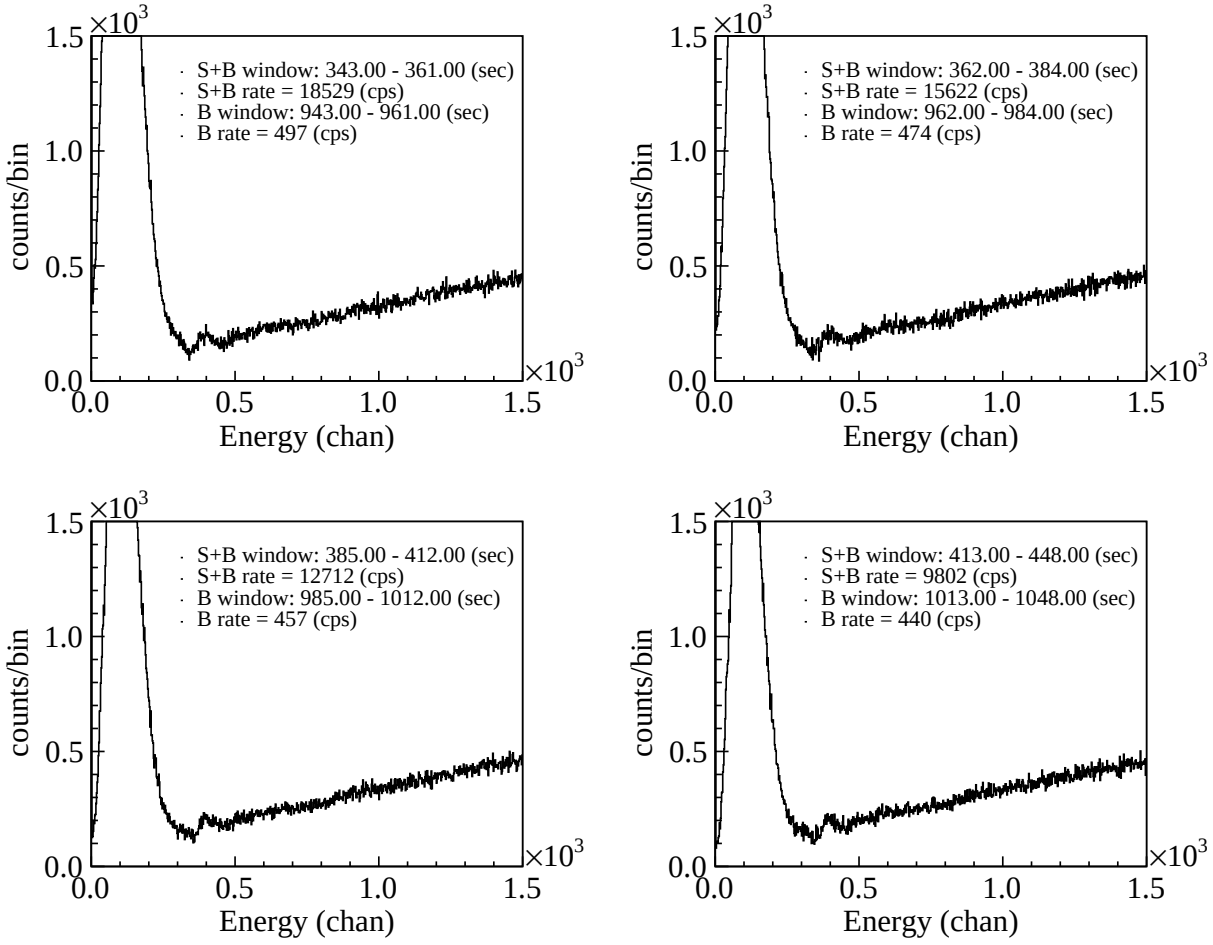

Figure 9-16: Zoomed-in view of the background-subtracted β-energy spectra in ^{6}He decay.

The corrections to b_{WM} and b_{GT} resulting from gain background correction are

$$^1b_{WM} - ^0 b_{WM} = -7.2 \pm 1.0, \tag{9.1}$$

$$^1b_{GT} - ^0 b_{GT} = 0.0031 \pm 0.0005, \tag{9.2}$$

where the uncertainties are from the uncertainties of A_H and A_L. The corrections to b_{WM} and b_{GT} resulting from background gain-and-sigma corrections are

$$^2b_{WM} - ^0 b_{WM} = -8.6 \pm 2.3, \tag{9.3}$$

$$^2b_{GT} - ^0 b_{GT} = 0.0046 \pm 0.0016, \tag{9.4}$$

where the uncertainties are from the uncertainties of A_H, A_L, σ_H, and σ_L. As shown in Eqs. 10.1 and 10.2, the statistical uncertainties of b_{WM} and b_{GT} from the CsI(Na) dataset are 4.9 and 0.0031,

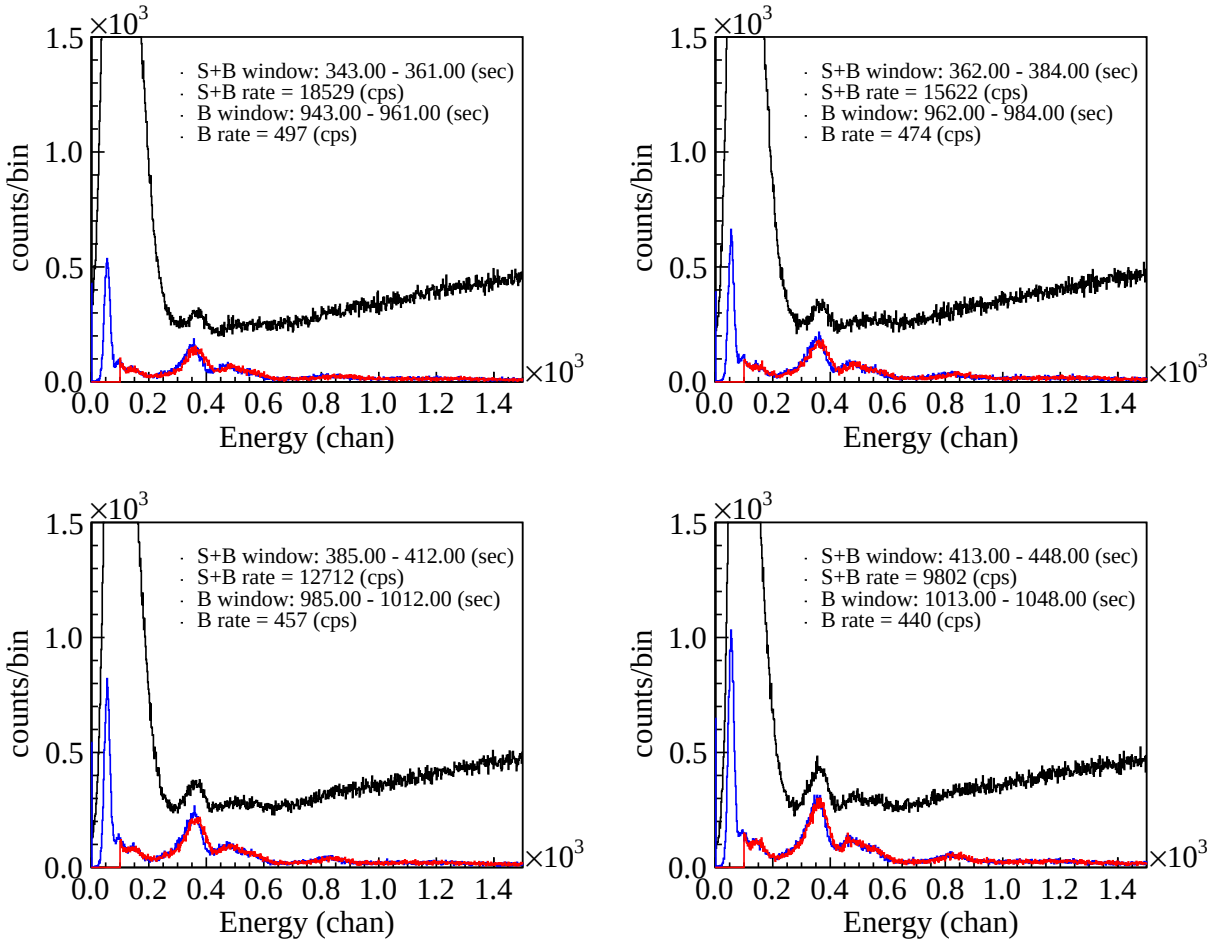

Figure 9-17: The S+B (black), background (blue), and gain-corrected background (red) spectra for ^{6}He β decay.

respectively. Therefore these corrections are non-negligible. In summary, the results in Eq. 9.3 and 9.4 are considered corrections to the observables resulting from the background corrections, and the uncertainties are the systematic uncertainties related to the background.

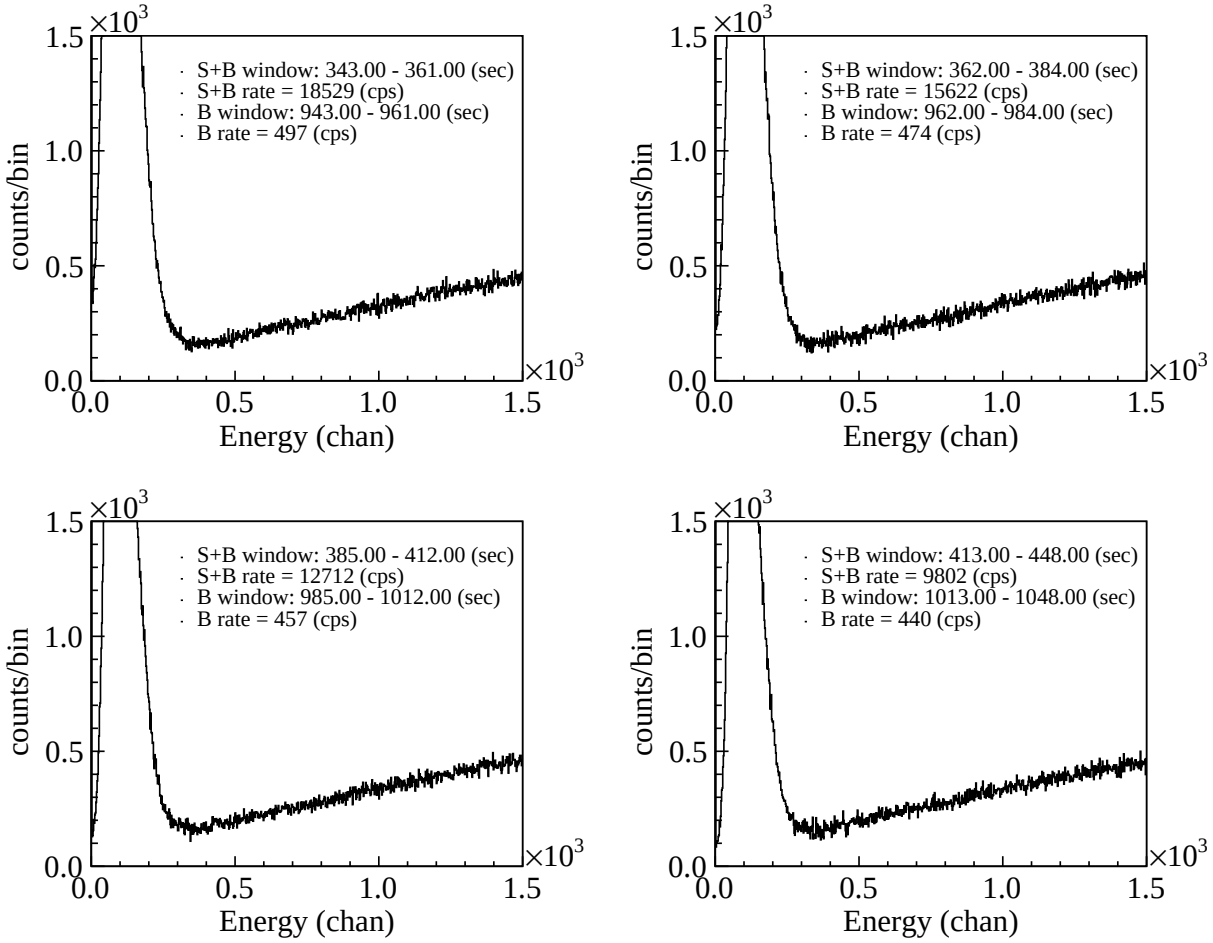

Figure 9-18: Zoomed-in view of the new background-subtracted β-energy spectra in ^{6}He decay after gain corrections to the background.

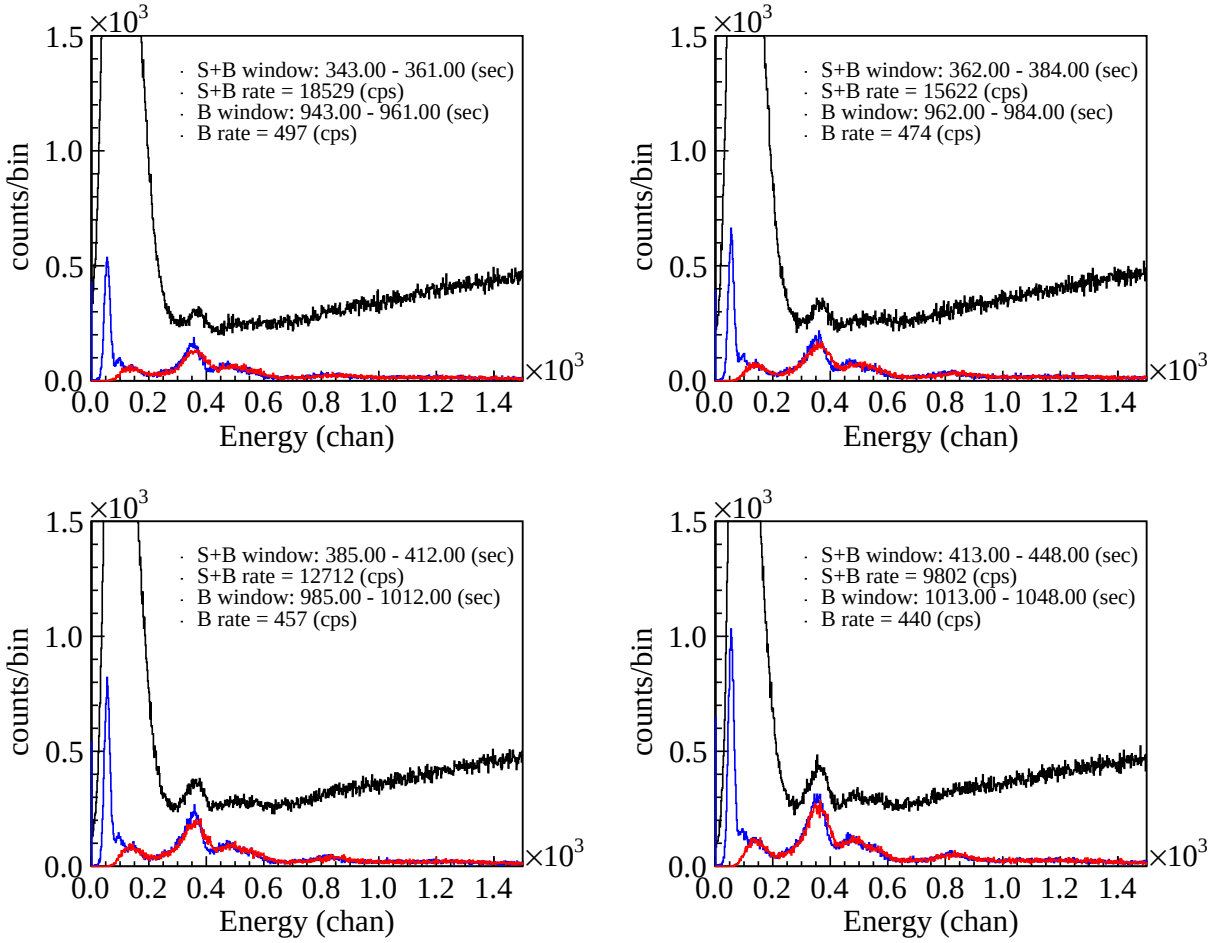

Figure 9-19: The S+B (black), background (blue), and gain-and-sigma corrected background (red) spectra for ^{6}He β decay.

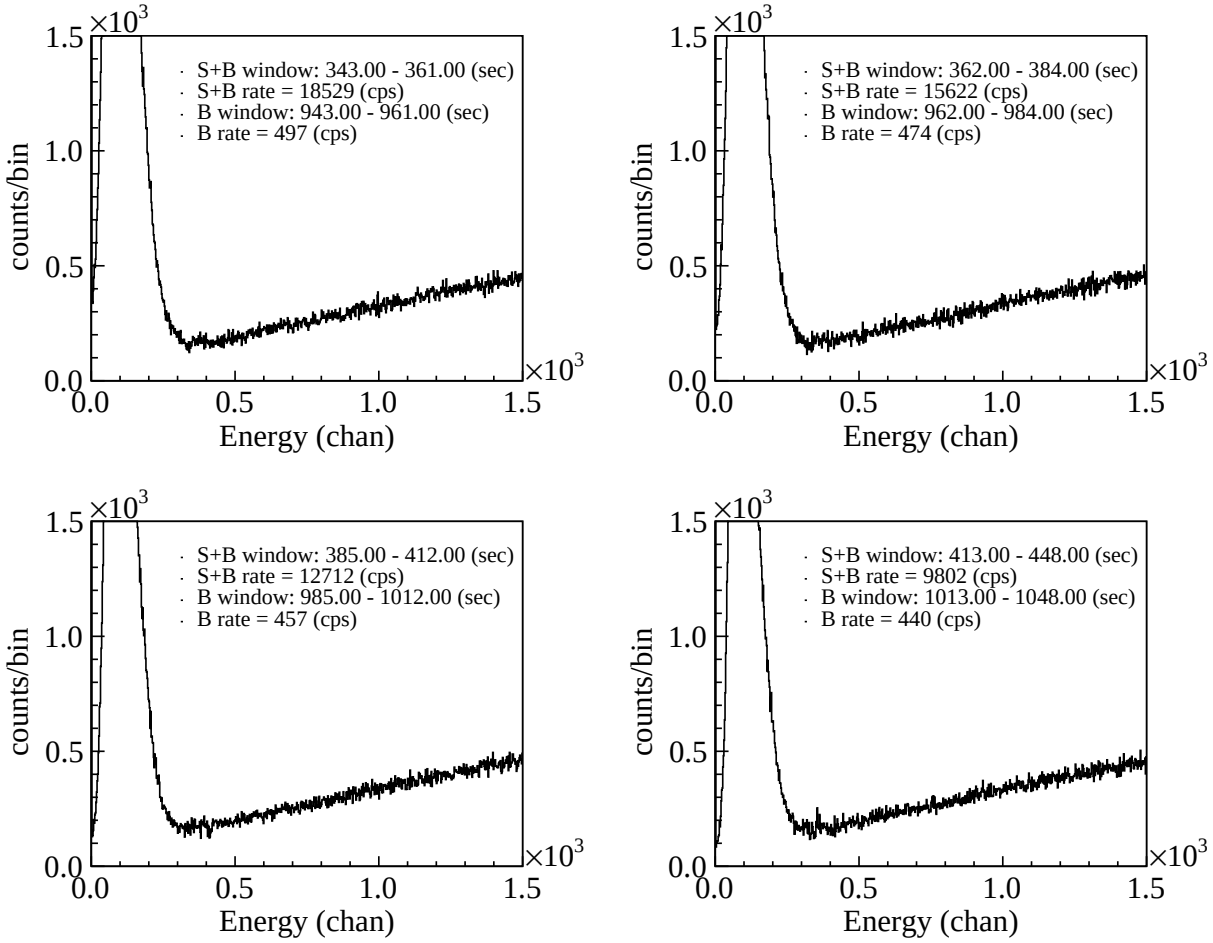

Figure 9-20: Zoomed-in view of the new background-subtracted β-energy spectra in ^{6}He decay after gain-and-sigma corrections to the background.

CHAPTER 10

SENSITIVITIES TO PHYSICS AND BEYOND

10.1 Sensitivities

The systematic effects of b_{WM} and b_{GT} estimated in previous chapters are summarized in Table 10-1.

Table 10-1: Systematic effects considered and the corresponding uncertainties in the error budget.

Source	Uncertainty on b_{WM}	Uncertainty on b_{GT} (10^{-3})
Theory	0.08	0.03
δb_{WM} (CVC)	N/A	0.29
Detector simulation	4.4	1.8
Gain	included	included
Offset	9.2	4.0
Energy resolution	0.80	0.40
Non-Linearity	negligible	negligible
Fit method	negligible	negligible
Background	2.3	1.6
Total	11	4.7

The statistical uncertainties extracted from fits to the CsI(Na) dataset in Table 3-1 are 4.93 for b_{WM} and 3.1×10^{-3} for b_{GT}. Therefore the estimates of b_{WM} and b_{GT} are

$$b_{WM} = \ ? \pm 4.9_{\text{stat}} \pm 11_{\text{sys}}, \tag{10.1}$$

$$b_{GT} = \left[? \pm 3.1_{\text{stat}} \pm 4.7_{\text{sys}}\right] \times 10^{-3}, \tag{10.2}$$

where the central values of b_{WM} and b_{GT} will be determined after completing the Monte Carlo study mentioned at the end of Chap. 2 as well as applying the complete fit function given in Eq. 8.13. The final result will provide the first measurement of the weak magnetism form factor in ^{6}He decay and a new constraint on the Fierz term in the Gamow-Teller transition. The predicted uncertainty of b_{GT} satisfies the precision goal of $O(10^{-3})$, a level which allows new constraints on tensor couplings beyond the SM.

10.2 Summary and Outlook

This work has explored a new calorimetric technique for the measurement β-energy spectrum and provides the current most precise and accurate measurement of the β-energy spectrum in ^{6}He decay. The next steps of this work include the Monte Carlo study of the detector's response to inner bremsstrahlung photons, the application of a more complete fit function, and the analysis of the NaI(Tl) dataset mentioned in Table 3-1. The final results of b_{WM} and b_{GT} will include data collected with both detectors.

The studies of the systematic effects associated with the new technique provide a solid foundation for next-generation β-decay experiments with this technique. Future experiments will focus on reducing the systematic uncertainties, including developing new approaches to determine the offset, improving the control of the rate effects, and exploring new experimental techniques. These high-sensitivity fundamental tests at the low energy scale open a unique window to physics beyond the SM. It is possible that new physics would first appear in the low-energy and high-precision nuclear-physics experiments before being discovered in high energy physics experiments.

APPENDIX

APPENDIX

DERIVATIONS IN CHAPTER 2

A.1 Derivation of Eq. 2.5

The screening component β_s has the following form for the Hartree potential [54]:

$$\beta_s = 2\sum_{j=1}^{3} a_j \beta_j, \tag{.1}$$

where β_j is given in Ref. [54]:

$$\beta_j = 1.13 b_j \alpha Z^{1/3}. \tag{.2}$$

In addition, β_s can be written in the usual form [51]:

$$\beta_s = 2C(|\tilde{Z}|)\alpha|\tilde{Z}|^{1/3}. \tag{.3}$$

Therefore,

$$C(|\tilde{Z}|) = 1.13\sum_{j=1}^{3} a_j b_j, \tag{.4}$$

where the a_j and b_j are parameters determined in Ref. [53] as a result of fitting 19 Hartree curves.

To benchmark this result, let us calculate the $C(|\tilde{Z}|)$ value for Hg ($Z = 80$). Following Ref. [51], the values of a_j and b_j for Hg can be found in Table 1 of Ref. [53]. This gives

$$C(80) \simeq 1.441, \tag{.5}$$

which agrees with the value of $C(80)$ reported in Ref. [51].

Finally, with the values of a_j and b_j for He from the same table, the calculated value of $C(|\tilde{Z}|)$ for He ($Z = 2$) is

$$C(2) \simeq 1.386. \tag{.6}$$

A.2 Table of Parameters in the Electrostatic Finite Size Correction

The finite size correction described by Eq. 2.20 requires b_x-values provided in Table A-1:

Table A-1: Coefficients for the parameterization of $L_0(Z, W)$ for electrons copied from Ref. [3].

	b_1	b_2	b_3	b_4	b_5	b_6
a_{-1}	0.115	-1.8123	8.2498	-11.223	-14.854	32.086
a_0	-0.00062	0.007165	0.01841	-0.53736	1.2691	-1.5467
a_1	0.02482	-0.5975	4.84199	-15.3374	23.9774	-12.6534
a_2	-0.14038	3.64953	-38.8143	172.1368	-346.708	288.7873
a_3	0.008152	-1.15664	49.9663	-273.711	657.6292	-603.7033
a_4	1.2145	-23.9931	149.9718	-471.2985	662.1909	-305.6804
a_5	-1.5632	33.4192	-255.1333	938.5297	-1641.2845	1095.358

A.3 Order $Z\alpha^2$ Radiative Correction

A.3.1 Uniform Charge Distribution

For uniformly charged sphere of radius R [61],

$$\Delta_1^F = \ln\left(\frac{\Lambda}{m_p}\right) - \kappa_2 - \frac{3}{\sqrt{10}\pi}\frac{\Lambda}{m_p}\left[\frac{1}{2} + \gamma^E + \ln\sqrt{10} + \ln\left(\frac{m_p}{\Lambda}\right)\right], \tag{.7}$$

$$\Delta_2 = \frac{3}{2\sqrt{10}\pi}\frac{\Lambda}{m_p}\left(1 - \frac{\pi}{2\sqrt{10}}\frac{\Lambda}{m_p}\right), \tag{.8}$$

$$\Delta_3 = \frac{3}{\sqrt{10}\pi}g_A(1+\mu_V)\frac{\Lambda}{m_p}\left[\gamma^E - 1 + \ln\sqrt{10} + \ln\left(\frac{m_p}{\Lambda}\right) + \frac{\pi}{4\sqrt{10}}\frac{\Lambda}{m_p}\right], \tag{.9}$$

where $g_A = 1.27$, $1 + \mu_V = 4.70$, $\kappa_2 = \gamma^E - 4/3 + \ln\sqrt{10} = 0.395$, and $\Lambda \equiv \sqrt{10}/R$.

A.3.2 Modified Gaussian Charge Distribution

For modified Gaussian charge distribution, i.e., $\rho(r) = \text{const} \times (1 + Ak^2r^2/a^2)e^{-r^2k^2/a^2}$ [61],

$$\Delta_1^F = \ln\frac{\Lambda}{m_p} - \kappa_1(Z) - \frac{8}{\sqrt{6\pi^3}}\frac{k}{2+3A}\frac{\Lambda}{m_p}\left\{\left[1 + \frac{\gamma^E}{2} + \ln\left(\frac{\sqrt{6}}{k}\frac{m_p}{\Lambda}\right)\right](1+A) + \frac{A}{2}\right\}, \tag{.10}$$

$$\Delta_2 = \frac{4}{\sqrt{6\pi^3}}\frac{k}{2+2A}\frac{\Lambda}{m_p}\left[1 + A - \sqrt{\frac{\pi^3}{96}}k\frac{\Lambda}{m_p}\left(1 + \frac{A}{2}\right)\right], \tag{.11}$$

$$\Delta_3 = \frac{8}{\sqrt{6\pi^3}}g_A(1+\mu_V)\frac{k}{2+3\alpha}\frac{\Lambda}{m_p}\left\{\left[\frac{\gamma^E - 1}{2} + \ln\left(\frac{\sqrt{6}}{k}\frac{m_p}{\Lambda}\right)\right](1+A) + \frac{A}{2} + \sqrt{\frac{\pi^3}{6}}\frac{k}{8}\frac{\Lambda}{m_p}\right\}. \tag{.12}$$

where $A = (Z-2)/3$, $k^2 = \frac{3}{2}\frac{2+5A}{2+3A}$, and $\kappa_1(Z) = \frac{1}{2}\left[\gamma^E + \ln(3/2k^2) + 2A/(2+3A)\right]$.

A.4 Derivation from Eq. 2.58 to Eq. 2.62

Under the condition $k^{\max} = \mathcal{E} - 1$ it can be shown that

$$-2\frac{\sqrt{(\mathcal{E}-k^{\max})^2-1}}{\sqrt{\mathcal{E}-1}} = 0, \tag{.13}$$

$$\frac{2}{\beta}\ln\left(\frac{\mathcal{E}-k^{\max}-\sqrt{(\mathcal{E}-k^{\max})^2-1}}{\mathcal{E}-\sqrt{\mathcal{E}^2-1}}\right) = \frac{2}{\beta}\tanh^{-1}\beta, \tag{.14}$$

$$2\ln\left[\frac{\mathcal{E}^2-1-\mathcal{E}k^{\max}+\sqrt{\mathcal{E}^2-1}\cdot\sqrt{(\mathcal{E}-k^{\max})^2-1}}{2(\mathcal{E}^2-1)}\right] = -2\ln\left[2(\mathcal{E}+1)\right]. \tag{.15}$$

Replacing $\frac{1}{2}\ln\frac{1+\beta}{1-\beta}$ by $\tanh^{-1}\beta$ gives

$$\frac{1}{2}\beta\ln\frac{1+\beta}{1-\beta} = \beta\tanh^{-1}\beta, \tag{.16}$$

$$2\ln\lambda\left[\frac{1}{2\beta}\ln\left(\frac{1+\beta}{1-\beta}\right)-1\right]-2\left(1-\frac{\tanh^{-1}\beta}{\beta}\right)\ln\left(\frac{2k^{\max}}{\lambda}\right) = 2\ln(\mathcal{E}-1)\left(\frac{1}{\beta}\tanh^{-1}\beta-1\right), \tag{.17}$$

$$-\frac{1}{\beta}\left[\frac{1}{2}\ln\left(\frac{1+\beta}{1-\beta}\right)\right]^2 = -\frac{2}{\beta}(\tanh^{-1}\beta)^2. \tag{.18}$$

The three integrals I_k^{-1}, I_k^0, and I_k^1 can be rewritten in the following expressions

$$I_k^0 = \int_0^{k^{\max}} dk\ln\left(\frac{1+\beta_e}{1-\beta_e}\right) = 2\int_1^{\mathcal{E}} dE\ln(E+p), \tag{.19}$$

$$I_k^1 = \int_0^{k^{\max}} dk\,k\left(\frac{1+\frac{p}{E}}{1-\frac{p}{E}}\right) = 2\int_1^{\mathcal{E}} dE(\mathcal{E}-E)\ln(E+p), \tag{.20}$$

$$I_k^{-1} = \int_0^{k^{\max}} dk\frac{1}{k}\ln\left(\frac{1+\beta_e}{1-\beta_e}\cdot\frac{1-\beta}{1+\beta}\right) = 2\int_1^{\mathcal{E}}\frac{dE}{(\mathcal{E}-E)}\ln\frac{E+p}{\mathcal{E}(1+\beta)}. \tag{.21}$$

Here $I_k^{-1} = 2I^{-1}$, $I_k^0 = 2I^0$, and $I_k^1 = 2I^1$ in which I^{-1}, I^0, and I^1 are defined in Ref. [70]. Therefore,

$$\frac{1}{\beta}I_k^{-1} - \frac{1}{\mathcal{E}\beta}I_k^0 + \frac{1}{2\mathcal{E}^2\beta}I_k^1 = \frac{1}{\beta}\left(2I_{-1} + \frac{I_1}{\mathcal{E}^2} - \frac{2I_0}{\mathcal{E}}\right). \tag{.22}$$

Summing up the above terms and the constants in $g_v(\mathcal{E})$ and $g_b(\mathcal{E})$ gives the following expression

for $g(\mathcal{E})$:

$$\begin{aligned} g(\mathcal{E}) =& g_v(\mathcal{E}) + g_b(\mathcal{E}) \\ =& 2\ln 2[(\mathcal{E}-1)]\left(\frac{1}{\beta}\tanh^{-1}\beta - 1\right) - 2\ln\left[2(\mathcal{E}+1)\right] + \frac{3}{2}\ln m_p + \frac{13}{8} - \frac{2}{\beta}(\tanh^{-1}\beta)^2 \\ &+ \frac{2}{\beta}L\left(\frac{2\beta}{1+\beta}\right) + \beta\tanh^{-1}\beta + \frac{3}{\beta}\tanh^{-1}\beta + \frac{1}{\beta}\left(2I_{-1} + \frac{I_1}{\mathcal{E}^2} - \frac{2I_0}{\mathcal{E}}\right) \end{aligned} \tag{.23}$$

A.5 Derivation from Eq. 2.62 to Eq. 2.69

$g(\mathcal{E})$ can be rewritten by replacing the integrals in $g(\mathcal{E})$ by the closed forms from Eq. 2.65-2.67 and replacing $\tanh^{-1}\beta$ by $\frac{1}{2}\ln\frac{1+\beta}{1-\beta}$:

$$\begin{aligned} g(\mathcal{E}) =& \ln\frac{1+\beta}{1-\beta}\left\{\frac{1}{\beta}\ln\left[2(\mathcal{E}-1)\cdot 2(1+\frac{1}{\sqrt{1-\beta^2}})\cdot\frac{1+\beta}{1-\beta}\right] + \left(\frac{1}{2}-\frac{1}{8}\right)\beta + \left(\frac{3}{2}+\frac{3}{8}-1\right)\frac{1}{\beta}\right\} \\ &- 2\ln\left[2(\mathcal{E}-1)\cdot 2(\mathcal{E}+1)\right] - \frac{4}{\beta}\mathrm{Li}_2\left(\frac{2\beta}{1+\beta}\right) + \left(\frac{13}{8}-\frac{3}{4}+2\right) + \frac{3}{2}\ln m_p \\ =& \ln\frac{1+\beta}{1-\beta}\left\{\frac{1}{\beta}\ln\left[2(\mathcal{E}-1)\cdot 2(\mathcal{E}+1)\cdot\frac{1+\beta}{1-\beta}\right] + \frac{3}{8}\beta + \frac{7}{8\beta}\right\} \\ &- 2\ln\left[2(\mathcal{E}-1)\cdot 2(\mathcal{E}+1)\right] - \frac{4}{\beta}\mathrm{Li}_2\left(\frac{2\beta}{1+\beta}\right) + \frac{23}{8} + \frac{3}{2}\ln m_p. \end{aligned} \tag{.24}$$

As

$$2(\mathcal{E}-1)\cdot 2(\mathcal{E}+1) = 4\left(\frac{1}{\sqrt{1-\beta^2}}-1\right)\left(\frac{1}{\sqrt{1-\beta^2}}+1\right) = \frac{4\beta^2}{1-\beta^2}, \tag{.25}$$

$$\begin{aligned} g(\mathcal{E}) &= \ln\frac{1+\beta}{1-\beta}\left\{\frac{1}{\beta}\ln\left(\frac{4\beta^2}{1-\beta^2}\cdot\frac{1+\beta}{1-\beta}\right) + \frac{3}{8}\beta + \frac{7}{8\beta}\right\} - 2\ln\left(\frac{4\beta^2}{1-\beta^2}\right) - \frac{4}{\beta}\mathrm{Li}_2\left(\frac{2\beta}{1+\beta}\right) + \frac{23}{8} + \frac{3}{2}\ln m_p \\ &= \ln\frac{1+\beta}{1-\beta}\left\{\frac{2}{\beta}\ln\left(\frac{2\beta}{1+\beta}\right) + \frac{3}{8}\beta + \frac{7}{8\beta}\right\} - 2\ln\left(\frac{4\beta^2}{1-\beta^2}\right) - \frac{4}{\beta}\mathrm{Li}_2\left(\frac{2\beta}{1+\beta}\right) + \frac{23}{8} + \frac{3}{2}\ln m_p. \end{aligned} \tag{.26}$$

Replacing $-\mathrm{Li}_2[(2\beta)/(1+\beta)]$ by $\mathrm{L}[(2\beta)/(1+\beta)]$ gives

$$g(\mathcal{E}) = \ln\frac{1+\beta}{1-\beta}\left[\frac{2}{\beta}\ln\left(\frac{2\beta}{1+\beta}\right) + \frac{3}{8}\beta + \frac{7}{8\beta}\right] - 2\ln\left(\frac{4\beta^2}{1-\beta^2}\right) + \frac{4}{\beta}\mathrm{L}\left(\frac{2\beta}{1+\beta}\right) + \frac{23}{8} + \frac{3}{2}\ln m_p. \tag{.27}$$

BIBLIOGRAPHY

BIBLIOGRAPHY

[1] M. González-Alonso, O. Naviliat-Cuncic, and N. Severijns. New physics searches in nuclear and neutron β decay. *Progress in Particle and Nuclear Physics*, 104:165 – 223, 2019.

[2] NuDat2.7. `https://www.nndc.bnl.gov/nudat2/`.

[3] D.H. Wilkinson. Evaluation of beta-decay: II. finite mass and size effects. *Nuclear Instruments and Methods in Physics Research Section A: Accelerators, Spectrometers, Detectors and Associated Equipment*, 290(2):509 – 515, 1990.

[4] D. Dubbers and M. G. Schmidt. The neutron and its role in cosmology and particle physics. *Rev. Mod. Phys.*, 83:1111–1171, 2011.

[5] X. Huyan, O. Naviliat-Cuncic, D. Bazin, A. Gade, M. Hughes, S. Liddick, K. Minamisono, S. Noji, S. V. Paulauskas, A. Simon, P. Voytas, and D. Weisshaar. Toward a measurement of weak magnetism in ^{6}He decay. *Hyperfine Interactions*, 237(1):93, 2016.

[6] M. González-Alonso and O. Naviliat-Cuncic. Kinematic sensitivity to the Fierz term of β-decay differential spectra. *Phys. Rev. C*, 94:035503, 2016.

[7] T. Bjerge and K. J. BrostrÖm. β-ray spectrum of radio-helium. *Nature*, 138:400 EP, 1936.

[8] V. Perez-Mendez and H. Brown. The beta-spectrum of He^{6}. *Phys. Rev.*, 77:404–405, 1950.

[9] C. S. Wu, B. M. Rustad, V. Perez-Mendez, and L. Lidofsky. The beta-spectrum of He^{6}. *Phys. Rev.*, 87:1140–1141, 1952.

[10] B. M. Rustad and S. L. Ruby. Gamow-Teller interaction in the decay of He^{6}. *Phys. Rev.*, 97:991–1002, 1955.

[11] A. Z. Schwarzschild. *The Beta Spectrum of He^{6}: Limits on the Axial Vector and Pseudoscalar Coupling Constants of Beta Decay*. Ph.D thesis, Columbia University, 1957.

[12] D.W. Hetherington, A. Alousi, and R.B. Moore. The shape factor of the ^{20}F beta spectrum. *Nuclear Physics A*, 494(1):1 – 35, 1989.

[13] G. W. Severin, L. D. Knutson, P. A. Voytas, and E. A. George. ^{66}Ga ground state β spectrum. *Phys. Rev. C*, 89:057302, 2014.

[14] P. A. Voytas, E. A. George, G. W. Severin, L. Zhan, and L. D. Knutson. Measurement of the branching ratio for the β decay of ^{14}O. *Phys. Rev. C*, 92:065502, 2015.

[15] H. Behrens and J. Jänecke. *Numerical Tables for Beta-Decay and Electron Capture*. Springer, 1969.

[16] L. Hayen, N. Severijns, K. Bodek, D. Rozpedzik, and X. Mougeot. High precision analytical description of the allowed β spectrum shape. *Rev. Mod. Phys.*, 90:015008, 2018.

[17] X. Huyan, O. Naviliat-Cuncic, P. Voytas, S. Chandavar, M. Hughes, K. Minamisono, and S.V. Paulauskas. Geant4 simulations of the absorption of photons in CsI and NaI produced by electrons with energies up to 4 MeV and their application to precision measurements of the β-energy spectrum with a calorimetric technique. *Nuclear Instruments and Methods in Physics Research Section A: Accelerators, Spectrometers, Detectors and Associated Equipment*, 879:134 – 140, 2018.

[18] J. I. Collar, N. E. Fields, M. Hai, T. W. Hossbach, J. L. Orrell, C. T. Overman, G. Perumpilly, and B. Scholz. Coherent neutrino-nucleus scattering detection with a CsI[Na] scintillator at the SNS spallation source. *Nuclear Instruments and Methods in Physics Research Section A: Accelerators, Spectrometers, Detectors and Associated Equipment*, 773:56 – 65, 2015.

[19] V. Cirigliano, M. González-Alonso, and M. L. Graesser. Non-standard charged current interactions: beta decays versus the LHC. *Journal of High Energy Physics*, 2013(2):46, 2013.

[20] T. Bhattacharya, V. Cirigliano, S. D. Cohen, A. Filipuzzi, M. González-Alonso, M. L. Graesser, R. Gupta, and H. Lin. Probing novel scalar and tensor interactions from (ultra) cold neutrons to the LHC. *Phys. Rev. D*, 85:054512, 2012.

[21] T. D. Lee and C. N. Yang. Question of parity conservation in weak interactions. *Phys. Rev.*, 104:254–258, 1956.

[22] T. D. Lee and C. N. Yang. Question of parity conservation in weak interactions. *Phys. Rev.*, 106:1371–1371, 1957.

[23] C. Bouchard C. C. Chang M. A. Clark N. Garron B. Joo T. Kurth C. Monahan H. Monge-Camacho A. Nicholson K. Orginos E. Rinaldi P. Vranas A. Walker-Loud E. Berkowitz, D. Brantley. *arXiv:1704.01114 [hep-lat]*.

[24] M. González-Alonso and J. M. Camalich. Isospin breaking in the nucleon mass and the sensitivity of β decays to new physics. *Phys. Rev. Lett.*, 112:042501, 2014.

[25] T. Bhattacharya, V. Cirigliano, S. D. Cohen, R. Gupta, H. Lin, and B. Yoon. Axial, scalar, and tensor charges of the nucleon from $2+1+1$-flavor lattice QCD. *Phys. Rev. D*, 94:054508, 2016.

[26] J. D. Jackson, S. B. Treiman, and H. W. Wyld. Possible tests of time reversal invariance in beta decay. *Phys. Rev.*, 106:517–521, 1957.

[27] J. D. Jackson, S. B. Treiman, and H. W. Wyld. Coulomb corrections in allowed beta transitions. *Nuclear Physics*, 4:206 – 212, 1957.

[28] O. Naviliat-Cuncic and M. González-Alonso. Prospects for precision measurements in nuclear decay in the LHC era. *Annalen der Physik*, 525(8-9):600–619.

[29] N. Severijns, M. Beck, and O. Naviliat-Cuncic. Tests of the standard electroweak model in nuclear beta decay. *Rev. Mod. Phys.*, 78:991–1040, 2006.

[30] J. C. Hardy and I. S. Towner. Superallowed $0^+ \rightarrow 0^+$ nuclear β decays: 2014 critical survey, with precise results for V_{ud} and CKM unitarity. *Phys. Rev. C*, 91:025501, 2015.

[31] K. P. Hickerson, X. Sun, Y. Bagdasarova, D. Bravo-Berguño, L. J. Broussard, M. A.-P. Brown, R. Carr, S. Currie, X. Ding, B. W. Filippone, A. García, P. Geltenbort, J. Hoagland, A. T. Holley, R. Hong, T. M. Ito, A. Knecht, C.-Y. Liu, J. L. Liu, M. Makela, R. R. Mammei, J. W. Martin, D. Melconian, M. P. Mendenhall, S. D. Moore, C. L. Morris, R. W. Pattie, A. Pérez Galván, R. Picker, M. L. Pitt, B. Plaster, J. C. Ramsey, R. Rios, A. Saunders, S. J. Seestrom, E. I. Sharapov, W. E. Sondheim, E. Tatar, R. B. Vogelaar, B. VornDick, C. Wrede, A. R. Young, and B. A. Zeck. First direct constraints on Fierz interference in free-neutron β decay. *Phys. Rev. C*, 96:042501, 2017.

[32] D. Poĉanić, R. Alarcon, L.P. Alonzi, S. Baeßler, S. Balascuta, J.D. Bowman, M.A. Bychkov, J. Byrne, J.R. Calarco, V. Cianciolo, C. Crawford, E. Frlež, M.T. Gericke, G.L. Greene, R.K. Grzywacz, V. Gudkov, F.W. Hersman, A. Klein, J. Martin, S.A. Page, A. Palladino, S.I. Penttilä, K.P. Rykaczewski, W.S. Wilburn, A.R. Young, and G.R. Young. Nab: Measurement principles, apparatus and uncertainties. *Nuclear Instruments and Methods in Physics Research Section A: Accelerators, Spectrometers, Detectors and Associated Equipment*, 611(2):211 – 215, 2009.

[33] O. Naviliat-Cuncic. Searches for exotic interactions in nuclear beta decay. *AIP Conference Proceedings*, 1753(1):060001, 2016.

[34] N. Severijns. Correlation and spectrum shape measurements in β-decay probing the standard model. *Journal of Physics G: Nuclear and Particle Physics*, 41(11):114006, 2014.

[35] Barry R. Holstein and S. B. Treiman. Tests for second-class currents in nuclear beta decay. *Phys. Rev. C*, 3:1921–1926, 1971.

[36] B. R. Holstein. Recoil effects in allowed beta decay: The elementary particle approach. *Rev. Mod. Phys.*, 46:789–814, 1974.

[37] B. R. Holstein. Erratum: Recoil effects in allowed beta decay: The elementary particle approach. *Rev. Mod. Phys.*, 48:673–673, 1976.

[38] J. C. Bergstrom, I. P. Auer, and R.S. Hicks. Electroexcitation of the 0^+ (3.562 MeV) level of ^{6}Li and its application to the reaction ^{6}Li(γ, π+)^{6}He. *Nuclear Physics A*, 251(3):401 – 417, 1975.

[39] D. R. Tilley, C. M. Cheves, J. L. Godwin, G. M. Hale, H. M. Hofmann, J. H. Kelley, C. G. Sheu, and H. R. Weller. Energy levels of light nuclei A = 5, 6, 7. *Nuclear Physics A*, 708(1):3 – 163, 2002.

[40] B. J. Mount, M. Redshaw, and E. G. Myers. Atomic masses of ^{6}Li,^{23} Na,^{39,41} K,^{85,87} Rb, and ^{133}Cs. *Phys. Rev. A*, 82:042513, 2010.

[41] A. Knecht, R. Hong, D. W. Zumwalt, B. G. Delbridge, A. García, P. Müller, H. E. Swanson, I. S. Towner, S. Utsuno, W. Williams, and C. Wrede. Precision measurement of the ^{6}He half-life and the weak axial current in nuclei. *Phys. Rev. Lett.*, 108:122502, 2012.

[42] Y. K. Lee, L. W. Mo, and C. S. Wu. Experimental test of the conserved vector current theory on the beta spectra of B^{12} and N^{12}. *Phys. Rev. Lett.*, 10:253–258, 1963.

[43] C. S. Wu, Y. K. Lee, and L. W. Mo. β spectra of ^{12}B and ^{12}N reanalyzed. *Phys. Rev. Lett.*, 39:72–75, 1977.

[44] E. A. George, P. A. Voytas, G. W. Severin, and L. D. Knutson. Measurement of the shape factor for the β decay of ^{14}O. *Phys. Rev. C*, 90:065501, 2014.

[45] A. Knecht, R. Hong, D. W. Zumwalt, B. G. Delbridge, A. García, P. Müller, H. E. Swanson, I. S. Towner, S. Utsuno, W. Williams, and C. Wrede. Precision measurement of the ^{6}he half-life and the weak axial current in nuclei. *Phys. Rev. C*, 86:035506, 2012.

[46] L. D. Knutson, G. W. Severin, S. L. Cotter, Li Zhan, P. A. Voytas, and E. A. George. A superconducting beta spectrometer. *Review of Scientific Instruments*, 82(7):073302, 2011.

[47] D. E. Alburger. Intermediate-image pair spectrometer. *Review of Scientific Instruments*, 27(12):991–1004, 1956.

[48] F. P. Calaprice. Second class interactions and the electron-neutrino correlation in nuclear beta decay. *Phys. Rev. C*, 12:2016–2021, 1975.

[49] K. Siegbahn. *Beta and Gamma Ray Spectroscopy*. North-Holland Publishing Company, 1955.

[50] D.H. Wilkinson. Evaluation of beta-decay: I. the traditional phase space factors. *Nuclear Instruments and Methods in Physics Research Section A: Accelerators, Spectrometers, Detectors and Associated Equipment*, 275(2):378 – 386, 1989.

[51] W. Bühring. The screening correction to the fermi function of nuclear β-decay and its model dependence. *Nuclear Physics A*, 430(1):1 – 20, 1984.

[52] W. Bühring. Approximate, non-relativistic scattering phase shifts, bound state energies, and wave function normalization factors for a screened Coulomb potential of the Hulthén type. *Zeitschrift für Physik A Atoms and Nuclei*, 310(4):255–262, 1983.

[53] W. J. Byatt. Analytical representation of Hartree potentials and electron scattering. *Phys. Rev.*, 104:1298–1300, 1956.

[54] W. Bühring. An approximate phase shift formula applied to elastic scattering of electrons by mercury atoms. *Zeitschrift für Physik A Atoms and Nuclei*, 317(3):241–249, 1984.

[55] M. E. Rose. A note on the possible effect of screening in the theory of beta-disintegration. *Phys. Rev.*, 49:727–729, 1936.

[56] D. H. Wilkinson. Methodology for superallowed Fermi beta-decay Part II. Reduction of data. *Nuclear Instruments and Methods in Physics Research Section A: Accelerators, Spectrometers, Detectors and Associated Equipment*, 335(1):182 – 200, 1993.

[57] D. H. Wilkinson. The sensitivity of allowed β-decay to the nuclear radius. *Nuclear Physics A*, 205(2):363 – 366, 1973.

[58] H. Behrens and W. Bühring. *Electron Radial Wave Functions and Nuclear Beta-Decay*. Clarendon Press, 1982.

[59] A. Sirlin. General properties of the electromagnetic corrections to the beta decay of a physical nucleon. *Phys. Rev.*, 164:1767–1775, 1967.

[60] W. W. Repko and C. Wu. Radiative corrections to the end point of the tritium β decay spectrum. *Phys. Rev. C*, 28:2433–2436, 1983.

[61] A. Sirlin. Remarks concerning the $O(Z\alpha^2)$ corrections to fermi decays, conserved-vector-current predictions, and universality. *Phys. Rev. D*, 35:3423–3427, 1987.

[62] W. Jaus and G. Rasche. Radiative corrections to 0^+-0^+ β transitions. *Phys. Rev. D*, 35:3420–3422, 1987.

[63] A. Sirlin and R. Zucchini. Accurate verification of the conserved-vector-current and standard-model predictions. *Phys. Rev. Lett.*, 57:1994–1997, 1986.

[64] D. H. Wilkinson. Evaluation of beta-decay, part VI: The Z-dependent outer radiative corrections for allowed decay. *Nuclear Instruments and Methods in Physics Research Section A: Accelerators, Spectrometers, Detectors and Associated Equipment*, 401(2):275 – 280, 1997.

[65] J.K. Knipp and G.E. Uhlenbeck. Emission of gamma radiation during the beta decay of nuclei. *Physica*, 3(6):425 – 439, 1936.

[66] F. Bloch. On the continuous γ-radiation accompanying the β-decay. *Phys. Rev.*, 50:272–278, 1936.

[67] A. Kurylov, M. J. Ramsey-Musolf, and P. Vogel. Radiative corrections in neutrino-deuterium disintegration. *Phys. Rev. C*, 65:055501, 2002.

[68] I. S. Towner. Radiative corrections in neutrino-deuterium scattering. *Phys. Rev. C*, 58:1288–1297, 1998.

[69] S. Gardner, B. Véronique, and U. Meißner. Radiative tritium β-decay and the neutrino mass. *Physics Letters B*, 598(3):188 – 196, 2004.

[70] P. Vogel. Analysis of the antineutrino capture on protons. *Phys. Rev. D*, 29:1918–1922, 1984.

[71] S. A. Fayans. Radiative corrections and recoil effects in the $\bar{\nu}_e + p \rightarrow n + e^+$ reaction at low energies. *Sov. J. Nucl. Phys.*, 42:590, 1985. [Yad. Fiz.42,929(1985)].

[72] B. R. Holstein, W. Shanahan, and S. B. Treiman. Recoil effects in allowed nuclear beta decay. *Phys. Rev. C*, 5:1849–1855, 1972.

[73] M. Brodeur, T. Brunner, C. Champagne, S. Ettenauer, M. J. Smith, A. Lapierre, R. Ringle, V. L. Ryjkov, S. Bacca, P. Delheij, G. W. F. Drake, D. Lunney, A. Schwenk, and J. Dilling. First direct mass measurement of the two-neutron halo nucleus ^{6}He and improved mass for the four-neutron halo ^{8}He. *Phys. Rev. Lett.*, 108:052504, 2012.

[74] L. R. B. Elton. A semi-empirical formula for the nuclear radius. *Nuclear Physics*, 5:173 – 178, 1958.

[75] G. Ewald, W. Nörtershäuser, A. Dax, S. Götte, R. Kirchner, H.-J. Kluge, Th. Kühl, R. Sanchez, A. Wojtaszek, B. A. Bushaw, G. W. F. Drake, Z.-C. Yan, and C. Zimmermann. Nuclear charge radii of ^{8,9}Li determined by laser spectroscopy. *Phys. Rev. Lett.*, 93:113002, 2004.

[76] I. Angeli and K.P. Marinova. Table of experimental nuclear ground state charge radii: An update. *Atomic Data and Nuclear Data Tables*, 99(1):69 – 95, 2013.

[77] H. Daniel. Shapes of beta-ray spectra. *Rev. Mod. Phys.*, 40:659–672, 1968.

[78] G. Knoll. *Radiation Detection and Measurement, 4th edition*. Wiley, 2010.

[79] D. J. Morrissey, B. M. Sherrill, M. Steiner, A. Stolz, and I. Wiedenhoever. Commissioning the A1900 projectile fragment separator. *Nuclear Instruments and Methods in Physics Research Section B: Beam Interactions with Materials and Atoms*, 204:90 – 96, 2003. 14th International Conference on Electromagnetic Isotope Separators and Techniques Related to their Applications.

[80] D. J. Morrissey and NSCL staff. A new high-resolution separator for high-intensity secondary beams. *Nuclear Instruments and Methods in Physics Research Section B: Beam Interactions with Materials and Atoms*, 126(1):316 – 319, 1997. International Conference on Electromagnetic Isotope Separators and Techniques Related to Their Applications.

[81] O. B. Tarasov and D. Bazin. LISE++: radioactive beam production with in-flight separators. *Nuclear Instruments and Methods in Physics Research, Section B: Beam Interactions with Materials and Atoms*, 266(19-20):4657–4664, 2008.

[82] W. R. Leo. *Techniques for Nuclear and Particle Physics Experiments: A How-to Approach, 2nd edition*. Springer-Verlag, 1993.

[83] V. Avdeichikov, A.S. Fomichev, B. Jakobsson, A.M. Rodin, and G.M. Ter-Akopian. Range–energy relation, range straggling and response function of CsI(Tl), BGO and GSO(Ce) scintillators for light ions. *Nuclear Instruments and Methods in Physics Research Section A: Accelerators, Spectrometers, Detectors and Associated Equipment*, 439(1):158 – 166, 2000.

[84] J.F. Ziegler. *TRIM Code V. 95.4*. IBM Research, 1995.

[85] X. Fléchard, E. Liénard, O. Naviliat-Cuncic, D. Rodríguez, M. A. G. Alvarez, G. Ban, B. Carniol, D. Etasse, J. M. Fontbonne, A. M. Lallena, and J. Praena. Measurement of the ^{8}Li half-life. *Phys. Rev. C*, 82:027309, 2010.

[86] D. Weisshaar, A. Gade, T. Glasmacher, G. F. Grinyer, D. Bazin, P. Adrich, T. Baugher, J. M. Cook, C. Aa. Diget, S. McDaniel, A. Ratkiewicz, K. P. Siwek, and K. A. Walsh. CAESAR-a high-efficiency CsI(Na) scintillator array for in-beam γ-ray spectroscopy with fast rare-isotope beams. *Nuclear Instruments and Methods in Physics Research Section A: Accelerators, Spectrometers, Detectors and Associated Equipment*, 624(3):615 – 623, 2010.

[87] C.J. Prokop, S.N. Liddick, B.L. Abromeit, A.T. Chemey, N.R. Larson, S. Suchyta, and J.R. Tompkins. Digital data acquisition system implementation at the National Superconducting Cyclotron Laboratory. *Nuclear Instruments and Methods in Physics Research Section A: Accelerators, Spectrometers, Detectors and Associated Equipment*, 741:163 – 168, 2014.

[88] X. Huyan, O. Naviliat-Cuncic, and M. Hughes. Precision measurements of β-energy spectra in nuclear decays: Study of the sensitivity to the detector calibration. *Acta Physica Polonica B*, 49:249, 2018.

[89] S. Agostinelli, J. Allison, K. Amako, J. Apostolakis, H. Araujo, P. Arce, M. Asai, D. Axen, S. Banerjee, G. Barrand, F. Behner, L. Bellagamba, J. Boudreau, L. Broglia, A. Brunengo, H. Burkhardt, S. Chauvie, J. Chuma, R. Chytracek, G. Cooperman, G. Cosmo, P. Degtyarenko, A. Dell'Acqua, G. Depaola, D. Dietrich, R. Enami, A. Feliciello, C. Ferguson, H. Fesefeldt, G. Folger, F. Foppiano, A. Forti, S. Garelli, S. Giani, R. Giannitrapani, D. Gibin, J. J. Gómez Cadenas, I. González, G. Gracia Abril, G. Greeniaus, W. Greiner, V. Grichine, A. Grossheim, S. Guatelli, P. Gumplinger, R. Hamatsu, K. Hashimoto, H. Hasui, A. Heikkinen, A. Howard, V. Ivanchenko, A. Johnson, F. W. Jones, J. Kallenbach, N. Kanaya, M. Kawabata, Y. Kawabata, M. Kawaguti, S. Kelner, P. Kent, A. Kimura, T. Kodama, R. Kokoulin, M. Kossov, H. Kurashige, E. Lamanna, T. Lampén, V. Lara, V. Lefebure, F. Lei, M. Liendl, W. Lockman, F. Longo, S. Magni, M. Maire, E. Medernach, K. Minamimoto, P. Mora de Freitas, Y. Morita, K. Murakami, M. Nagamatu, R. Nartallo, P. Nieminen, T. Nishimura, K. Ohtsubo, M. Okamura, S. O'Neale, Y. Oohata, K. Paech, J. Perl, A. Pfeiffer, M.G. Pia, F. Ranjard, A. Rybin, S. Sadilov, E. Di Salvo, G. Santin, T. Sasaki, N. Savvas, Y. Sawada, S. Scherer, S. Sei, V. Sirotenko, D. Smith, N. Starkov, H. Stoecker, J. Sulkimo, M. Takahata, S. Tanaka, E. Tcherniaev, E. Safai Tehrani, M. Tropeano, P. Truscott, H. Uno, L. Urban, P. Urban, M. Verderi, A. Walkden, W. Wander, H. Weber, J.P. Wellisch, T. Wenaus, D.C. Williams, D. Wright, T. Yamada, H. Yoshida, and D. Zschiesche. Geant4—a simulation toolkit. *Nuclear Instruments and Methods in Physics Research Section A: Accelerators, Spectrometers, Detectors and Associated Equipment*, 506(3):250 – 303, 2003.

[90] Physics list electromagnetic constructors in Geant4 10.4. `https://geant4.web.cern.ch/node/1731#opt4`.

[91] Source code `physlistemstandard.cc`. `http://geant4.web.cern.ch/geant4/UserDocumentation/Doxygen/examples_doc/html_TestEm5/html/PhysListEmStandard_8cc_source.html`.

[92] Geant4 physics reference manual. `http://geant4.web.cern.ch/geant4/UserDocumentation/UsersGuides/PhysicsReferenceManual/fo/PhysicsReferenceManual.pdf`.

[93] H. D. Lemmel, S. T. Perkins, D. E. Cullen, and S. M. Seltzer. *EEDL. Evaluated Electron Data Library of the Lawrence Livermore National Laboratory, USA. Summary documentation*. 1994.

[94] V. N. Ivanchenko, O. Kadri, M. Maire, and L. Urban. Geant4 models for simulation of multiple scattering. *Journal of Physics: Conference Series*, 219(3):032045, 2010.

[95] R. Brun and F. Rademakers. Root — an object oriented data analysis framework. *Nuclear Instruments and Methods in Physics Research Section A: Accelerators, Spectrometers, Detectors and Associated Equipment*, 389(1):81 – 86, 1997. New Computing Techniques in Physics Research V.

[96] Numerical minimization. https://root.cern.ch/numerical-minimization.